How AI can read animals' faces—and feelings p. 710

Satiety neurons and high sugar intake pp. 717 & 750

Conserving nature, or just shifting problems elsewhere? p. 720

Science

$15
14 FEBRUARY 2025
science.org

AAAS



TRACKING THE DEEP

Elephant seals as sentinels of the ocean twilight zone p. 764

Congratulations to the 2025 winner of the

AAAS-MANI L. BHAUMIK AWARD FOR PUBLIC ENGAGEMENT WITH SCIENCE

Since 1987, this award has recognized an outstanding cadre of scientists and engineers who have demonstrated excellence in their contributions to public engagement with science.

To elevate the vital importance of effective science communication to promote public understanding and awareness of science and foster critical thinking, in 2019 this award was endowed in perpetuity with the generous financial support of distinguished physicist, Mani L. Bhaumik.

This year, we are honored to recognize theoretical physicist **Brian Greene** for his profound scholarly contributions to our understanding of the universe, and for his extraordinary ability to explain highly complex and abstract theories in ways that have captivated and educated audiences of all ages throughout the world.

Congratulations, Professor Greene!



PHOTO COURTESY OF WORLD SCIENCE FESTIVAL

Brian Greene

PROFESSOR & DIRECTOR,
CENTER FOR THEORETICAL PHYSICS
COLUMBIA UNIVERSITY

CO-FOUNDER
WORLD SCIENCE FESTIVAL

LEARN MORE AT **AAAS.ORG/AWARDS**

AAAS

CONTENTS

14 FEBRUARY 2025
VOLUME 387 • ISSUE 6735



710
Artificial intelligence can read feelings from an animal's face.

IMAGE: CHRISTA LESTÉ-LASSERRE

NEWS

IN BRIEF

702 News at a glance

IN DEPTH

704 U.S. aid freeze deals 'tectonic' blow to research
Scientists decry ethical violations as trials worldwide are paused and workers laid off
By C. Offord, J. Cohen, and M. Enserink

706 Judge's ruling leaves NIH's move to abruptly slash grants in limbo
Universities, states, and research groups attack plan to cut billions in "indirect cost" payments as illegal and unwise *By D. Malakoff*

707 Underwater light show heralds highest energy neutrino
Event promises "new energy window on the universe" *By D. Clery*

708 Retirement-age scientists just keep working
Desire to retain professional identity keeps Ph.D.s from stepping aside, survey shows
By K. Langin

709 Congressional Republicans take aim at recent Biden regulations
Climate, ocean archaeology rules could be reversed *By D. Charles*

FEATURES

710 Face readers
Artificial intelligence is becoming better than humans at scanning animals' faces for signs of stress and pain. Are more complex emotions next?
By C. Lesté-Lasserre
PODCAST

INSIGHTS

PERSPECTIVES

714 Where does all the water go?
Seismic noise measurements map out a deep groundwater recharge system
By T. Taira and R. Bürgmann
RESEARCH ARTICLE p. 758

716 Constrained roads to complex brains
Neural development and brain circuit evolution converged in birds and mammals
By G. Gattoni and M. A. Tosches
RESEARCH ARTICLES pp. 732, 733, & 734

717 Understanding the desire for dessert
A neural circuit in mice mediates the preference for high-sugar food after a meal
By S. Farooqi
RESEARCH ARTICLE p. 750

718 Thrifting iridium for hydrogen
Anchoring catalysts on an engineered oxide support enables stable water electrolysis
By A. D. Pendergast and S. W. Boettcher
RESEARCH ARTICLE p. 791

POLICY FORUM

720 Time to fix the biodiversity leak
The risk that locally successful nature conservation may be shifting problems elsewhere can no longer be ignored
By A. Balmford et al.

BOOKS *ET AL.*

723 Notes from the "politics factory"
A former government science adviser dissects the complex meshing of science and policy *By H. C. J. Godfray*

724 A scientific field, misled
Fraud undermines Alzheimer's disease research *By C. Elliott*

LETTERS

726 Jordan's electric vehicle growth drives trade-offs
By H. J. Khasawneh and H. Hussein

726 India's grasslands are not "wastelands"
By S. Lahiri and S. Reddy

727 India's ocean exploration undermines climate goals
By A. Mistry



716 & 732
Determining neuronal development in chick embryos

RESEARCH

IN BRIEF

728 From *Science* and other journals

REVIEW

731 Neuroscience
Neuroevolution insights into biological neural computation *R. Miikkulainen*
REVIEW SUMMARY; FOR FULL TEXT: DOI.ORG/10.1126/SCIENCE.ADP7478

RESEARCH ARTICLES

Brain evolution

732 Evolutionary convergence of sensory circuits in the pallium of amniotes *E. Rueda-Alaña* et al.
RESEARCH ARTICLE SUMMARY; FOR FULL TEXT: DOI.ORG/10.1126/SCIENCE.ADP3411

733 Developmental origins and evolution of pallial cell types and structures in birds *B. Zaremba* et al.
RESEARCH ARTICLE SUMMARY; FOR FULL TEXT: DOI.ORG/10.1126/SCIENCE.ADP5182

734 Enhancer-driven cell type comparison reveals similarities between the mammalian and bird pallium *N. Hecker* et al.
RESEARCH ARTICLE SUMMARY; FOR FULL TEXT: DOI.ORG/10.1126/SCIENCE.ADP3957
PERSPECTIVE p. 716

735 Enzymology
Conformational ensembles reveal the origins of serine protease catalysis *S. Du* et al.
RESEARCH ARTICLE SUMMARY; FOR FULL TEXT: DOI.ORG/10.1126/SCIENCE.ADO5068

736 Immunology
KLF2 maintains lineage fidelity and suppresses CD8 T cell exhaustion during acute LCMV infection *E. Fagerberg* et al.
RESEARCH ARTICLE SUMMARY; FOR FULL TEXT: DOI.ORG/10.1126/SCIENCE.ADN2337

737 Cancer
RNA polymerase II at histone genes predicts outcome in human cancer *S. Henikoff* et al.

744 Catalysis
Selective chemical looping combustion of acetylene in ethylene-rich streams *M. Jacob* et al.

750 Neuroscience
Thalamic opioids from POMC satiety neurons switch on sugar appetite *M. Minère* et al.
PERSPECTIVE p. 717

758 Geophysics
Depth-dependent seismic sensing of groundwater recovery from the atmospheric-river storms of 2023 *S. Mao* et al.
PERSPECTIVE p. 714

764 Marine conservation
Elephant seals as ecosystem sentinels for the northeast Pacific Ocean twilight zone *R. S. Beltran* et al.

769 Catalysis
Thermal catalytic reforming for hydrogen production with zero CO_2 emission *M. Peng* et al.

776 Membranes
Engineering grain boundaries in monolayer molybdenum disulfide for efficient water-ion separation *J. Shen* et al.

782 Hydrology
Variability of flowing stream network length across the US *J. P. Prancevic* et al.

786 Quantum materials
Good plasmons in a bad metal *F. L. Ruta* et al.

791 Electrochemistry
Ultrastable supported oxygen evolution electrocatalyst formed by ripening-induced embedding *W. Shi* et al.
PERSPECTIVE p. 718

DEPARTMENTS

701 Editorial
Breaking the silence
By H. H. Thorp and M. Phelan

798 Working Life
Rethinking success
By S. Mohammed

ON THE COVER

A mother elephant seal rests with her pup after returning from a 7-month, 10,000-kilometer foraging trip to the northeast Pacific Ocean, where she made ~75,000 attempts to feed on twilight zone fish. Seals' foraging success across decades reveals variation in fish abundance, which drives large fluctuations in the survival and reproductive success of their offspring. See page 764. *Photo: Bruce Lyon, under National Marine Fisheries Service (NMFS) research permit no. 23188*



IMAGE: FERNANDO GARCÍA-MORENO

Science Careers 797

SCIENCE (ISSN 0036-8075) is published weekly on Friday, except last week in December, by the American Association for the Advancement of Science, 1200 New York Avenue, NW, Washington, DC 20005. Periodicals mail postage (publication No. 484460) paid at Washington, DC, and additional mailing offices. Copyright © 2025 by the American Association for the Advancement of Science. The title SCIENCE is a registered trademark of the AAAS. Domestic individual membership, including subscription (12 months): $165 ($74 allocated to subscription). Domestic institutional subscription (51 issues): $2865; Foreign postage extra: Air assist delivery: $135. First class, airmail, student, and emeritus rates on request. Canadian rates with GST available upon request, GST #125488122. Publications Mail Agreement Number 1069624. **Printed in the U.S.A.**
Change of address: Allow 4 weeks, giving old and new addresses and 8-digit account number. **Postmaster:** Send change of address to AAAS, P.O. Box 96178, Washington, DC 20090–6178. **Single-copy sales:** $15 each plus shipping and handling available from backissues.science.org; bulk rate on request. **Authorization to reproduce** material for internal or personal use under circumstances not falling within the fair use provisions of the Copyright Act can be obtained through the Copyright Clearance Center (CCC), www.copyright.com. The identification code for *Science* is 0036-8075. *Science* is indexed in the *Reader's Guide to Periodical Literature* and in several specialized indexes.

EDITORIAL

Breaking the silence

H. Holden Thorp
is Editor-in-Chief of the *Science* journals.
hthorp@aaas.org

Meagan Phelan
is communications director of the *Science* journals.
mphelan@aaas.org

Research on science communication has largely focused on teaching scientists how to describe their studies in ways that interest the public while deepening their understanding of scientific exploration. However, there is another, often overlooked side to science communication—how scientists respond when questions arise about the integrity of their research. Often, the tendency has been to stay silent and wait for any controversy to pass or be resolved in professional forums. But in an age of growing, intense attacks on science, silence can be detrimental to both public trust and the careers of scientists who are under scrutiny. For better or worse, journalists, social media professionals, and the public may take a response of "no comment" as a concession that the critics are correct, so forthright communication about research questions is more urgent than ever.

Media and public interest in research integrity cases—spurred by online platforms like X, Bluesky, and PubPeer that give a front row seat to potential disputes in real time—is increasing. Although each case in the public eye may be different—ranging from no error to an honest mistake by a single author to a rare instance of intentional misconduct—public curiosity is not likely to dissipate in the contentious political environments prevailing around the world.

Science responds when questions are raised by the scientific community or the public about its published research papers and counsels authors and institutions to do the same, ensuring that legitimate concerns are addressed. This means being straightforward when there are problems while standing up for papers that are correct. Scientists should expect that publishing their findings in high-profile journals raises the odds that the work will be examined carefully. Authors sometimes naïvely think that once the paper is published, the discussion is over.

Science offers "tips for authors" on dealing with these situations (see the Editor's Blog). If contacted by the media, authors should discuss the issue with the press office and research integrity office at their university but cautiously consider any recommendations. A university is likely to opt for silence because of fear of litigation and damage to the institution's reputation. However, authors should ask themselves whether silence could be interpreted by the media and public as an admission of guilt. So, in addition to consulting with institutional professionals, authors should think about talking to the media directly. This can be an opportunity to provide the unvarnished truth in response to tough questions.

> **"...talking to the media...can be an opportunity to provide the unvarnished truth..."**

These days, journalists and other media specialists are increasingly asking authors of research papers about issues related to image irregularities, data availability, plagiarism, and more. Before responding, authors should seek an objective view by running answers past someone they trust who is not an expert on the topic and, ideally, not a scientist. This is crucial because that person would not be steeped in the details of the case or the intricacies of scholarly publishing. Attacking the motives or standing of those who question one's research, even though it may be justified, can often backfire. The public likely will not care about any agenda behind the critique or where it came from, but whether the questions are substantive. It's also helpful to examine what the inquiring media outlet has published on scientific integrity, as it could reveal questions that may come up. There are many examples of positive outcomes for authors who have engaged openly and honestly with media, but there are also instances where evasion has led to more digging and a prolonged drip of unwanted and perhaps unwarranted news. Time is hardly ever an advantage in these situations.

In the tense political environment for science around the world, authors and journals also will be called upon to defend scientific consensus on matters that have been considered closed for decades, such as whether vaccines cause autism, whether humans are causing climate change, and whether HIV causes AIDS. Attacking individual studies is a common tactic to undermine entire fields. The scientific community can respond effectively only if the public believes that when there is a problem, it will be quickly corrected. As difficult and scary as it is to talk to tough reporters and critics, the alternative can be far worse.

–H. Holden Thorp and Meagan Phelan

10.1126/science.adw5838

NEWS

> “It’s unethical, it’s unlawful, and it’s inhumane.”
>
> **George Washington University researcher Mandi Pratt-Chapman,** about the government’s cancellation of funding for her study on the sexual orientation and gender identity of cancer patients, following President Donald Trump’s ban on federal support for projects involving “gender ideology.”

IN BRIEF

Edited by
Jeffrey Brainard



A student (left) and a professor work in a chemistry lab at Occidental College, which held a now-canceled foundation award to make its science classes more inclusive.

PHOTO: CENTERS FOR DISEASE CONTROL AND PREVENTION; NATIONAL INSTITUTE OF ALLERGY AND INFECTIOUS DISEASES

WORKFORCE

Major research philanthropy kills $60 million diversity program

The Howard Hughes Medical Institute (HHMI) on 5 February abruptly terminated a $60 million program that funded universities to make science education more inclusive. Awardees of the Inclusive Excellence Program at 104 institutions received emails from HHMI announcing they will receive no more payments for 6-year awards now in their third years. These projects have supported systemic changes at colleges and universities to attract undergraduates from underrepresented groups to study science and retain them in those majors. HHMI, the United States’s largest private funder of medical research with an endowment of nearly $26 billion, offered no explanation and declined to answer questions from *Science*. HHMI has also recently removed words targeted by President Donald Trump’s administration—such as “disability,” “race,” and “gender”—from descriptions of still-existing institute programs that support scientists from underrepresented groups. In a 21 January executive order, under the heading “Encouraging the Private Sector to End Illegal [Diversity, Equity, and Inclusion] Discrimination,” Trump targeted foundations with endowments of more than $500 million, among other groups, for potential investigation by the Department of Justice.

NIH, FDA picks back ‘open’ journal

PUBLISHING | A new journal announced last week, co-founded by President Donald Trump’s pick to direct the U.S. National Institutes of Health (NIH), aims to “promote open and transparent scientific discourse” but quickly drew controversy. The board of the *Journal of the Academy of Public Health* includes NIH nominee Jay Bhattacharya, a physician and economist at Stanford University, and Trump’s pick to lead the Food and Drug Administration, Johns Hopkins University surgeon Martin Makary, both of whom made controversial arguments against vaccine mandates and other public health measures during the COVID-19 pandemic. Other people on the board have also been criticized for their views and research. Only members of a newly formed body, the Academy of Public

Health, chosen by existing members based on their research, can submit articles; all submitted articles are published, alongside peer reviews. Skeptics worry the publication will be used to sow doubt about scientific consensus on matters such as vaccine efficacy and safety.

Accused Alzheimer's scholar quits

RESEARCH INTEGRITY | Sylvain Lesné, a neuroscientist accused of image manipulation in a seminal Alzheimer's disease paper in *Nature*, resigned last week from his tenured professorship at the University of Minnesota Twin Cities (UMN). *Science* first reported his potential misconduct in 2022. UMN started an investigation, and the *Nature* study was retracted in June 2024; last week, a UMN spokesperson said the university found data-integrity problems with several other papers on which Lesné is an author and contacted journals to recommend they retract four more of them. His 2006 paper in *Nature* buoyed confidence in the hypothesis that a brain buildup of amyloid proteins may play a critical role in causing Alzheimer's, and the finding spurred multiple lines of new research by other investigators.

Cows get second bird flu virus

INFECTIOUS DISEASES | Dairy cows in Nevada have become infected by a second variant of the bird flu virus that has been decimating poultry and wild birds, a finding that could complicate efforts to control the disease and prevent it from spreading to humans. Since H5N1 began racing through dairy herds across the country in 2024, scientists had until now identified only a single viral lineage responsible, known as clade 2.3.4.4b, genotype B3.13. On 31 January, a national milk testing program discovered the Nevada cattle had become infected with the D1.1 genotype of the same clade, which has circulated widely in wild birds. It has caused three infections in humans, one of whom works at a Nevada dairy farm; but no evidence suggests D1.1 transmits between people or is more dangerous than other H5N1 variants. Scientists don't know whether a cow that has been infected with B3.13 and recovered will have immunity against D1.1.



IMAGE: MARC CAMPOS/OCCIDENTAL COLLEGE

The H5N1 avian flu virus, which has infected cows, forms rodlike shapes in this electron micrograph.

German groups win X data ruling

SOCIAL MEDIA | In a first, plaintiffs last week won a court order requiring the social media platform X to provide data sought by researchers wishing to study how posts on the social media platform may represent interference in Germany's upcoming national election. The lawsuit was brought under an EU law that took effect in 2022 and requires that large platforms release data to enable independent examination of social media's "systemic risks." Democracy Reporting International and the Society for Civil Rights alleged in a Berlin court that X, owned by billionaire Elon Musk, last year denied their request to supply data on details such as the number of likes and shares of posts. X charges $5000 a month for access to data at the scale researchers say is necessary for these studies. Researchers also want to analyze posts surrounding other recent elections in Europe. Musk has posted on X in support of the far-right Alternative for Germany Party, which is competing in the German national election to be held on 23 February.

Mexico squeezes research budget

FUNDING | Mexico's final spending plan for this year includes cuts for research that are expected to force staff layoffs and lower salaries. Funding for the new Secretariat of Science, Humanities, Technology, and Innovation will drop by 2% this year, to about $1.3 billion, while overall support for 24 government-funded research centers will decline by 11%. Some center directors have told scientists they have only enough money to operate until the end of September. Numerous scientists had hoped Claudia Sheinbaum Pardo, elected last year as the nation's president, would ease the austerity policies of her predecessor, Andrés Manuel López Obrador.

IN OTHER NEWS

REPORT SCUTTLED President Donald Trump's administration has killed a major scientific report about the condition of nature and the environment in the United States, just as a final draft was to be submitted this week. Organized by the U.S. Global Change Research Program, the *National Nature Assessment* was written by more than 150 researchers from federal agencies, universities, and organizations. Described as the first such comprehensive stocktaking by the government, it also detailed societal benefits from biodiversity and a healthy environment.

CENSUS RESIGNATION U.S. Census Bureau Director Robert Santos stepped down as of this week, 3 years into a 5-year appointment. The move will allow President Donald Trump to nominate his own choice to lead the agency in the run-up to the 2030 census, which will be used to allocate seats in the U.S. House of Representatives and distribute trillions of federal dollars. A statistician appointed by former President Joe Biden, Santos criticized the first Trump administration's failed effort to add a question about U.S. citizenship status to the 2020 census. As director, he worked with scientists to improve data collection, especially about undercounted groups, and lower costs.

ARGENTINA LEAVES WHO Argentine President Javier Milei announced plans to withdraw the country from the World Health Organization (WHO), following a similar decision by U.S. President Donald Trump. Milei criticized WHO's actions during the COVID-19 pandemic. The move will curb technical cooperation between WHO and local scientists, such as those at the Malbrán Institute, which specializes in infectious disease research and control.

UNUSED AI A majority of researchers say artificial intelligence (AI) outperforms humans in each of 23 research tasks, such as assisting the preparation of scholarly papers and handling large information sets, according to a survey by the publisher Wiley. But less than 40% of the nearly 5000 respondents, distributed globally and across disciplines, say they're using AI tools for such tasks. (Humans still lead or match AI in other areas, such as optimizing experimental designs, most respondents say.) Nearly two-thirds say a lack of guidance and training is stopping them from using AI as much as they'd like.



Workers scrub the name of the U.S. Agency for International Development from its Washington, D.C., headquarters on 7 February.

PHOTO: KAYLA BARTKOWSKI/GETTY IMAGES

GLOBAL HEALTH

U.S. aid freeze deals 'tectonic' blow to research

Scientists decry ethical violations as trials worldwide are paused and workers laid off

By **Catherine Offord**, **Jon Cohen**, *and* **Martin Enserink**

In 2023, a consortium of researchers launched a 3-year study among women in South Africa, Zimbabwe, Lesotho, Kenya, and Uganda to compare drugs for preventing HIV infection. The study, run by the U.S.-based nonprofit FHI 360 and named CATALYST, began by giving participants an anti-HIV drug via pills or vaginal rings. Then it added injections of a drug that lasts for 2 months. More than 3000 women were participating by early January.

The study is now in peril. Funded by the U.S. Agency for International Development (USAID), the trial was paused on 27 January after President Donald Trump's administration ordered a 3-month freeze on foreign aid and told recipients to halt their work immediately. Women enrolled in CATALYST lost access to drugs, information, and care. Research staff are shocked and angered. "The stop work order has forced us to walk away without meeting our most basic ethical obligations to study participants, placing them at risk and destroying the trust they and their communities placed in us," says a staffer on the project who, like several other people interviewed for this story, asked not to be identified.

The drama is just one of many that have played out in global health research because of the aid freeze. Clinical studies have suddenly been halted, in what scientists say is a violation of trial ethics. Data streams have also dried up, researchers and technical staff have been fired or put on leave, a system to predict food crises has been muzzled, and a USAID-supported global health journal has stopped reviewing manuscripts.

The collective impact is "tectonic, and that's an understatement," says Glenda Gray, chief scientific officer at the South African Medical Research Council. Gray leads the BRILLIANT Consortium, which at the last minute shelved plans for a phase 1 clinical trial of two new HIV vaccine candidates in response to the freeze.

"Important trials … are being potentially jeopardized by this," says Rachel Baggaley, an HIV specialist and former team lead for testing, prevention, and populations in the Department of Global HIV, Hepatitis and Sexually Transmitted Infections Programmes at the World Health Organization. "It's sad and incomprehensible that things have come to this."

Trump signed the order freezing foreign aid soon after he was sworn in on 20 January, and USAID—whose $40 billion annual budget not only provides food and medicines, but also supports clinical trials and many other types of research—has been subject to an unprecedented assault. The agency's website has gone dark, and on 4 February, USAID said all staff globally would be placed on administrative leave effective 7 February, with some exceptions for critical jobs. Agency staff posted overseas were ordered to return to the United States within 30 days. (A judge later issued a temporary restraining order partially blocking those moves.)

Trump ally Elon Musk branded the agency a "criminal organization" and boasted on X, the social media platform he owns, of "feeding USAID into the wood chipper." In an interview on 3 February, Secretary of State Marco Rubio argued that foreign aid spending does not support U.S. aims. USAID, the main conduit for foreign assistance, has a history of "deciding that they are somehow a global charity separate from the national interest. These are taxpayer dollars," Rubio said.

SOME SCIENTISTS REMAIN hopeful their projects will resume in weeks or months—counting on legal challenges to Trump's actions. But already, the freeze and USAID's

woes are disrupting research aimed at improving the health and lives of the world's poorest people, as well as efforts to help build research capacity in developing nations.

Stopping clinical trials is particularly troubling if it means participants are no longer monitored for adverse events or their medical care is interrupted, says bioethicist Nicholas Evans of the University of Massachusetts Lowell. "When a funder simply suspends a study out of the blue, that is a huge, huge ethics violation and probably illegal," says Arthur Caplan, a bioethicist at New York University's Grossman School of Medicine. It is also wasteful, says a USAID staffer. "Once you stop a trial you have to start from scratch to generate the data we need. That's millions of dollars wasted."

In the case of CATALYST, which aims to compare different strategies of preventing HIV infection using pre-exposure prophylaxis (PrEP), researchers worry about specific harms. When people stop taking the injectable PrEP drug, cabotegravir, they become vulnerable to infection, and low amounts of drug that linger in their body for up to 1 year could foster the emergence of drug-resistant HIV strains that they could transmit to others. To avoid this problem, people who stop taking injectable cabotegravir are asked to take oral PrEP pills for 1 year. It's not clear whether women who received injected cabotegravir in CATALYST will get access to those pills. A spokesperson for FHI 360 says the group is "deeply concerned" but does not have the money to continue the study itself.

Other HIV trials in Africa have been halted as well, including one in South Africa to test whether a vaginal ring can prevent infection and pregnancy. A study exploring how best to design future trials of HIV treatment and prevention in teenage girls and young women was paused after enrolling more than 1000 participants in South Africa, Kenya, Zambia, and Uganda.

The collapse of USAID has put the launch of other trials on indefinite hold. BRILLIANT's phase 1 study of HIV vaccine candidates was supposed to start enrolling dozens of volunteers in South Africa, Kenya, and Uganda in late January, with $45.6 million in support from USAID. Everything was ready to go, Gray says, but the team concluded that "it would be unethical to start a study that you can't guarantee you can continue."

Another trial now on hold planned to study whether the drug bedaquiline can prevent tuberculosis in people at high risk, including those living with HIV. It aimed to enroll 2530 people in Peru and South Africa. And IAVI, a U.S.-based nonprofit focused on HIV vaccines, has canceled a study of a therapeutic vaccine for people living with HIV in Uganda and Zambia. Even if the aid freeze is later lifted, "the delay meant that we wouldn't be able to vaccinate all of the participants before the clinical trial material expired," an IAVI spokesperson tells *Science*.

The disruption and uncertainty extends beyond Africa. The International Research Centre for Diarrhoeal Diseases Research, Bangladesh says it has laid off 1000 people and paused 10 U.S.-funded studies and projects "in compliance with the Stop-Work Order, pending further directives" according to a spokesperson. The halted projects focused on tuberculosis, nutrition, fungal infection surveillance, and the risk of viral spillover from animals to humans.

In Nepal, a U.S.-based nonprofit named the La Isla Network put on hold work funded by a $4 million grant from the U.S. Department of State on chronic kidney disease, a deadly condition believed to be linked to heat stress and dehydration that has emerged as a threat to manual laborers in hot climates. Nepal is a major source of construction workers for hot Middle Eastern countries. La Isla had been working to gauge the extent of the problem and which parts of the country are hardest hit, while also working to reform how Nepalese workers are screened for health conditions before they travel.

"It's sad and incomprehensible that things have come to this."

Rachel Baggaley, retired HIV specialist

SEEING THEIR AGENCY be dismantled in a matter of weeks has come as a shock to USAID staff overseeing research and aid programs. "I'm completely devastated," says Margaret McCluskey, who oversees an HIV vaccine research program that also funded BRILLIANT. McCluskey says she was told to hand in her badge, phone, and laptop on 29 January, after which she was escorted to her office to pick up six boxes' worth of material collected over the years. "The security guards had tears coming down their cheeks," McCluskey says. "I was maybe the 200th person that they had to take upstairs that day."

USAID-funded staff at the $800 million President's Malaria Initiative (PMI) were pushed out as well, even as they were trying to salvage some of their work, says a veteran malaria expert who has worked at various U.S. government agencies. PMI's disassembly began when USAID contract workers—who constitute most of its staff—were fired. On 3 February, the handful of actual USAID employees, including PMI's lead scientist, were "told to clear out their desks and be gone," the scientist says. "What a horrible time to have gotten training in public health to do God's work and all of a sudden your job is not there."

Key resources for global health are also vanishing. USAID has been the main funder of the Demographic and Health Surveys Program, which collects data in numerous developing countries every 3 to 5 years. It forms the basis for global child mortality estimates, for example, and helps track progress toward the United Nations Sustainable Development Goals. Its data show up in hundreds of papers every year, says a USAID staffer. Now, the collection of new data "will cease," the source says. A banner on the program's home page says it is "unable to respond to any data or other requests at this time."

The website of the Famine Early Warning Systems Network, a USAID-funded program that has forecast food crises since 1985, has disappeared along with all of its data. And *Global Health: Science and Practice* (*GHSP*), an open-access journal supported by USAID, has stopped reviewing manuscripts. Its future is unclear, but "if *GHSP* ceases to exist, effects will be felt at the level of policies and programs, particularly in countries currently experiencing the worst health outcomes, notably in Africa," says its editor, Stephen Hodgins, a physician and epidemiologist at the University of Alberta.

Some scientists are baffled that the U.S. seems ready to give up a major source of soft power and goodwill. Nepal, for example, is a strategically important part of the world, La Isla CEO Jason Glaser points out. "If we're not there as a country giving them an alternative to Chinese investment, I guarantee you [China] will start funding the hospitals for goodwill." And much of the research, including the HIV vaccine work, benefits the U.S. as well, McCluskey says. "Finding an HIV vaccine is fundamental to national security," she says.

Baggaley is still hopeful that relationships can be reestablished. The turmoil at USAID "comes after many years, if not decades, of U.S. funding for important research in various places around the globe," she says. "It's not only a huge benefit to the countries where they work, but there's also massive benefits to people from other countries, including from the U.S." ■

With reporting by Warren Cornwall, Phie Jacobs, Kai Kupferschmidt, Leslie Roberts, and Meredith Wadman.



The University of Alabama at Birmingham says it would lose $105 million under NIH's new indirect cost policy.

SCIENCE POLICY

Judge's ruling leaves NIH's move to abruptly slash grants in limbo

Universities, states, and research groups attack plan to cut billions in "indirect cost" payments as illegal and unwise

By **David Malakoff**

See you in court. That's the message 22 states and a coalition of research universities this week sent to President Donald Trump's administration after the National Institutes of Health (NIH) made a stunning announcement: The world's largest funder of biomedical research would immediately reduce by at least half the so-called indirect cost payments made to grantees' universities, hospitals, and research institutes to help cover facilities and administrative costs.

NIH estimates its move to apply a standard 15% indirect cost rate to all new and existing grants would reduce those payments, which totaled about $9 billion in 2023, by some $4 billion. But the policy, announced in a 7 February memo from NIH's director's office, drew immediate howls of protest from the U.S. biomedical community and some federal lawmakers. And states and universities quickly filed lawsuits to prevent the change from taking effect. The plaintiffs won an early victory on 10 February, when a federal judge ordered NIH to suspend the new policy, at least until a hearing on 21 February.

The rulings, issued late on Monday, capped a frenetic drama that began the previous Friday night with NIH's announcement of the new 15% indirect cost rate, which is far below the rate of roughly 50% or more of many current grants. The cut would force institutions to find billions of dollars from other sources to replace the agency's support for buildings, administrative staff, and other costs not directly related to the funded research.

"It is … vital to ensure that as many funds as possible go towards direct scientific research costs rather than administrative overhead," NIH wrote in its memo. The new rate would bring NIH into line with the maximum indirect cost rates allowed by private foundations, the memo stated, and would "allow grant recipients a reasonable and realistic recovery of indirect costs."

Researchers and university groups fiercely disagreed. NIH's shift was akin to dropping "a nuclear bomb on university budgets," says Morgan Polikoff, an education researcher at the University of Southern California.

"This is a surefire way to cripple lifesaving research and innovation. America's competitors will relish this self-inflicted wound," said the Council on Governmental Relations, which tracks federal policy for research universities.

The reduction would amount to a "generational restructuring of the US research and development ecosystem," Alondra Nelson of the Institute for Advanced Study, former head of the White House science office, lamented on Bluesky.

In the two lawsuits filed early this week, the plaintiffs argued the agency made a number of illegal missteps. They claimed, for example, that NIH not only violated the federal Administrative Procedures Act, which governs the process of how agencies issue new rules, but also defied a measure approved by Congress that, since 2018, has limited NIH's ability to alter indirect cost rates on its own. (In its memo, NIH cites federal rules, adopted nearly a decade ago, that the agency suggests allow unilateral imposition of a new rate.)

The NIH action, part of a cost cutting blitz by the Trump administration, was also seen as an attack on universities that it has deemed too liberal. Some observers also noted signs the NIH memo was not written by experienced agency staff. For example, they say it appears to incorrectly conclude from a 2021 budget document that the average indirect cost rate has hovered at about 27% to 28%, which is below the actual share.

The looming court and political battle has biomedical researchers suffering from a sense of déjà vu. In 2017, during Trump's first term, his administration tried to reduce indirect costs to 10% through the annual budget proposal process. Congress, then controlled by Republicans, responded by blocking that move and limiting NIH's power to change the rates. Slashing NIH's indirect costs rate was also proposed in Project 2025, a blueprint for an incoming Republican administration that Trump once disavowed but has since embraced.

The federal government has been adding indirect cost payments to research grants since 1947. Traditionally, each university has negotiated its own overhead rate—including one rate for facilities and one for administration—with the government every few years. Rates vary widely because of geography—costs are higher in urban areas—and because research expenses differ. Biomedical science, for example, often requires animal facilities, ethics review boards, and pricey equipment that aren't needed for social science. But universities have long complained that even the negotiated rates don't cover true research costs.

Both Republican and Democratic policymakers, in contrast, have tried to rein in

PHOTO: ZUMA VIA ALAMY

overhead payments. Most notably, in 1994 the U.S. government capped the administration rate for universities at 26% after several instances in which universities were found to have used the money for purposes outside the scope of the grant. Former President Barack Obama's administration also floated setting an unspecified flat rate, which economists said would increase efficiency and reduce paperwork.

Many who advocate for cutting NIH's indirect cost rate have argued that universities are willing to accept lower rates from private foundations. The NIH memo, for example, noted that the Bill & Melinda Gates Foundation limits indirect costs to 10%, whereas the David and Lucile Packard Foundation sets a 15% ceiling. But the Trump administration's reasoning is based on "perverse logic," says virologist Larry Corey of the Fred Hutchinson Cancer Center, who once led the $2 billion institution. Universities reluctantly accept such low indirect cost repayments from charitable donors, he and others say, because those grants amount to a relatively small fraction of their funding—and because the federal government has already provided the infrastructure used for the research.

In Congress, the NIH memo drew bipartisan pushback. Senator Susan Collins (R–ME), chair of the Senate Committee on Appropriations, expressed "strong opposition to these arbitrary cuts in funding for vital research." And she said she had gotten a promise from Robert F. Kennedy Jr., Trump's nominee to lead the Department of Health and Human Services, to "reexamine this initiative" if he is confirmed.

In Alabama, a deeply Republican state that Trump recently won by 30 percentage points, political leaders expressed concern about what the cut might mean for the University of Alabama at Birmingham (UAB), that state's largest employer. By one estimate, the university—which reports a 48.5% indirect cost rate on its NIH grants—would lose $105 million. "As it relates to our state's GDP [gross domestic product], as it relates to our economic growth, as it relates to our future … NIH research dollars play a massive, significant role," Birmingham Mayor Randall Woodfin told Al.com. "Those in the UAB family have a right to be concerned."

Alabama's junior Republican senator, Katie Britt, also expressed worry. "A smart, targeted approach," she told Al.com, "is needed in order to not hinder life-saving, groundbreaking research at high-achieving institutions like those in Alabama." ■

With reporting by Jon Cohen, Jessica Slater, Meredith Wadman, Jeffrey Mervis, and Jocelyn Kaiser.

ASTROPHYSICS

Underwater light show heralds highest energy neutrino

Event promises "new energy window on the universe"

By **Daniel Clery**

A flash of light 3.5 kilometers down in the Mediterranean Sea has signaled a record-breaking cosmic visitor: a neutrino with 30 times the energy of any previously recorded. Although researchers couldn't pinpoint where this elusive particle came from, its detection raises hopes that more will soon be captured, bearing clues to some of the universe's most violent events.

"We've opened a new energy window on the universe," says physicist Paschal Coyle of the Marseilles Particle Physics Centre, former spokesperson for the Cubic Kilometre Neutrino Telescope (KM3NeT), which captured the event, reported this week in *Nature*, on 13 February 2023. "It's the first time astronomy at this energy is possible."

Physicist Elisa Resconi of the Technical University of Munich agrees: "It's super-exciting."

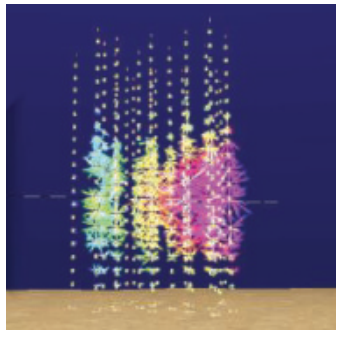
Neutrinos are elusive byproducts of many nuclear interactions, whizzing through space at near the speed of light, barely interacting with normal matter and unaffected by magnetic fields. Based on their arrival directions, physicists aim to trace the most energetic back to turbulent corners of the universe to resolve their origin.

Physicists can detect neutrinos by watching for their extremely rare collisions with atomic nuclei in large volumes of ice or water. The collisions spawn particles like electrons or their heavier cousins muons, which emit a cone of blue light as water or ice slow them. From the shape, brightness, and orientation of the cone, determined by an array of light detectors, physicists can estimate the direction and energy of the original neutrino.

IceCube, a U.S.-backed detector that monitors 1 cubic kilometer of ice below the South Pole, has detected some neutrinos with energies above 1 million billion electron-volts (PeV)—hundreds of times the collision energy of the world's most powerful accelerator. A few have been traced back to active galactic nuclei (AGNs)—distant galaxies that host gigantic black holes, consuming matter at a voracious rate and spewing out particles.

KM3NeT, a European project at two sites off the coasts of France and Sicily, relies on water instead, with strings of light detectors anchored to the seabed. In 2023, when the array was just 10% complete, it was flooded with light as a particle streamed horizontally through it. The brilliance "was a surprise to us and we didn't believe it at first," Coyle says. "But it passed all our many, many checks."

The group now believes the passing particle was a muon sparked by a neutrino that struck an atom in seawater or rock, possibly tens of kilometers away. "It's quite convincing, in my opinion, that this is a neutrino-induced event," Resconi says. The team estimated the energy of the original neutrino at a record-smashing 220 PeV.



A simulation depicts a new high-energy neutrino's detection by sensor strings rising from the seabed.

IMAGE: P. COYLE; CNRS; KM3NET COLLABORATION

The partial KM3NeT array can't yet trace neutrinos to sources. But if more such ultra–high-energy neutrinos can be found and tracked, they could reveal the locations of the universe's most powerful particle accelerators. AGNs are one candidate, whipping up particles, such as protons or small nuclei, to enormous speeds. Neutrinos are spawned when these so-called cosmic rays collide with other, slower moving particles.

Other possible sources include supernovae, merging neutron stars, or supermassive black holes tearing a star apart. More provocative is the idea that the neutrinos come from cosmic rays colliding with photons in the cosmic microwave background, the afterglow of the Big Bang. No one has confirmed such "cosmogenic" neutrinos, but one could be inferred if traced back to empty space.

"This is kind of the bleeding edge of science we're dealing with," says physicist Naoko Kurahashi Neilson of Drexel University, a member of the IceCube team. "We're starting to learn about it, which is, you know, the dawn before the daylight, right?" ■

WORKFORCE

Retirement-age scientists just keep working

Desire to retain professional identity keeps Ph.D.s from stepping aside, survey shows

By **Katie Langin**

Most Ph.D. scientists in the United States stay in the labor force notably longer than the average person—into their late 60s and in some cases beyond—according to new data from the National Science Foundation (NSF). Often they retire, only to return to work later. The finding won't surprise younger scientists trying to land faculty positions in departments heavy with older scientists. But by showing scientists often stay on because they want to preserve a professional identity, the findings point to the need for employers, such as universities, to develop and implement creative policies to help older scientists step aside without losing the sense of engagement they value.



For theoretical physicist Helen Quinn (right), volunteer work in science education policy has been a satisfying "retirement career."

The new peek into retirement patterns is based on responses from roughly 125,000 scientists and engineers ages 75 or younger to NSF's Survey of Doctorate Recipients. For the latest iteration of the long-running survey, NSF added new questions about the decision to retire or keep working. The findings, released last month, showed 40% of U.S.-based respondents between 71 and 75 years old continued to be employed in some capacity; that's roughly double the 19% figure for the general U.S. population. Among those still-working scientists, more than half had previously retired and returned to work, often part time.

Some went back to work because they wanted additional income and social connection, according to the survey; others were asked to return. But the most common reason cited was a desire to retain their professional identity. The findings make clear that many older professionals want to stay engaged with work, says Roger Baldwin, a professor emeritus of higher education at Michigan State University. "The old view of retirement is changing."

The data don't distinguish retirement patterns for scientists in academia from those in other sectors such as industry or government. But Donna Ginther, an economics professor at the University of Kansas who studies the academic workforce, suspects most of the older workers are academics.

Engineer Alison McCarthy, a postdoctoral fellow at the U.S. Naval Research Laboratory and chair of the National Postdoctoral Association's postdoc council, agrees. "There's a lot of older professors." She can understand where they're coming from. "They probably enjoy their jobs; they probably want to keep going." But the phenomenon can be discouraging for younger researchers hoping for tenure-track jobs, she adds. She asks older scientists, "Can you just donate your time, maybe, if you are in a good spot [financially] so that there can be new, fresh ideas and more jobs for people?"

Ginther agrees that tenured professors holding onto their positions may prevent early-career researchers from finding jobs. But there's no guarantee that an academic retiring will open up a new position, she adds. "Universities have been substituting non–tenure-track jobs for tenure-stream jobs for decades."

When Carole Goldberg, now a distinguished research professor at the University of California, Los Angeles, became vice chancellor 14 years ago, she was amazed by how many faculty members who were eligible for a full pension hadn't retired—especially given that many would have been better off financially if they had retired. She made it her mission to figure out what was holding people back and to devise strategies for meeting their needs. "I wanted to make it clear to people that retiring did not necessarily mean forgoing one's desired professional activities," she says. Instead, it "gave you the opportunity to cast off those that were less desired."

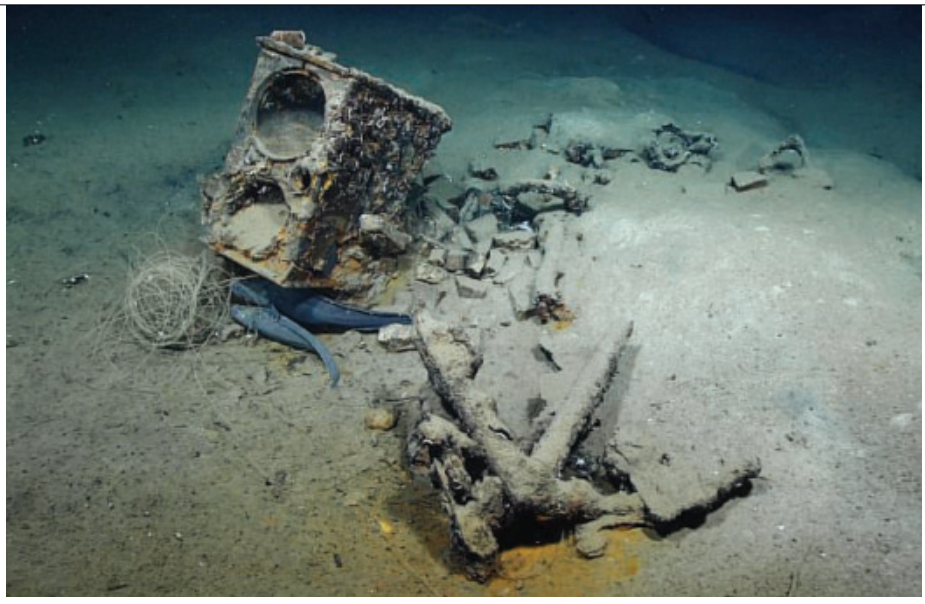
Some academics, she found, didn't want an "emeritus" title because they feared it would hinder their ability to get grants funded and receive speaking invitations. To remedy that, she asked the university to create a new "research professor" title for retired faculty who were still engaged with research. Goldberg's office also began to host panel discussions with retired faculty, highlighting how they were taking advantage of what the university offered. Such outreach, along with other adjustments to how the university engaged with professors on the issue, led to a spike in retirements, she says. "It was pretty dramatic."

Volunteering can be a source of fulfillment for those for whom it would be "shock to the system" to give up all work, says theoretical physicist Helen Quinn. When she retired in 2010, she transitioned to 2 years of full-time volunteer work chairing a report on K-12 science education for the National Academy of Sciences. Since then, the professor emeritus at Stanford University's SLAC National Accelerator Laboratory has continued to volunteer as a science education research and policy adviser. It was "a way to continue my work as a scientist, thinking about how science should be taught and learned," she says.

Baldwin did something similar for his own retirement, taking volunteer positions as the president of the Association of Retirement Organizations in Higher Education and on the board of trustees at his undergraduate institution. The continued access to professional activities has been key, he says. "I do feel a sense of continuing purpose and engagement."

"People are living longer and healthier lives," he adds, "and we as a society need to come to grips with the fact that retirement is not necessarily a period of leisure anymore." ■

PHOTO: DAN QUINN



A rule requiring oil companies to conduct surveys for shipwrecks, such as this one off Louisiana, is at risk.

PHOTO: NATIONAL OCEANIC AND ATMOSPHERIC ADMINISTRATION OCEAN EXPLORATION

SCIENCE POLICY

Congressional Republicans take aim at recent Biden regulations

Climate, ocean archaeology rules could be reversed

By **Dan Charles**

The new Republican-led U.S. Congress could soon move to revoke numerous environmental regulations adopted by former President Joe Biden's administration during its final months in office.

At-risk rules include one to protect archaeological sites on the ocean floor, such as shipwrecks, from oil and gas drilling. Others impose new fees for industry releases of methane, a potent warming gas; ban the manufacture of trichloroethylene, a toxic chemical solvent; and cut leaks of other warming gases, hydrofluorocarbons, from refrigeration equipment.

Unlike President Donald Trump's executive orders, some of which are being challenged in court, congressional resolutions to reverse such regulations have a clear legal basis under the 1996 Congressional Review Act (CRA). The CRA was championed by Republicans such as former House Speaker Newt Gingrich (R–GA) as a way to reverse "midnight regulations" that administrations rush to finalize before leaving office.

The law, which applies to regulations that Biden finalized after late May 2024, was rarely used until the first Trump administration. At that point, in early 2017, a Republican-controlled Congress passed 16 resolutions reversing regulations adopted by former President Barack Obama's administration. In 2021, after the election of Biden as president, a Democrat-controlled Congress reversed three rules promulgated under Trump. "Congress was very eager to use this tool," says Sarah Hay, a policy analyst at the George Washington University Regulatory Studies Center. "It's clearly a tool that they are well practiced with at this point."

According to the Coalition for Sensible Safeguards, a group that includes environmental and public health advocates, members of Congress have targeted 10 regulations so far.

Senator John Kennedy (R–LA) has introduced a resolution to reverse a rule on the Protection of Marine Archaeological Resources, which the Bureau of Ocean Energy Management (BOEM) adopted in September 2024. It requires oil companies to survey the ocean floor for shipwrecks or other cultural remains before undertaking development, something offshore wind facilities were already required to do.

Oil and gas companies previously had to conduct surveys only in places where computer models predicted higher odds of finding shipwrecks. "That model was not a good model," says Shawn Joy, vice president for archaeology at Deep Calm Seas Marine Services. He points to the example of a 19th century shipwreck that was only discovered in 2001 after ExxonMobil had already laid a pipeline straight through it.

The American Cultural Resources Association, which represents consulting firms, said in a statement to *Science* that the rule requires companies to spend only "a very small amount" of time and money, yet "helps prevent the permanent destruction of our history." But the Offshore Operators Committee, an industry group, had called the rule "far too ambiguous" when it was proposed, and asked BOEM to withdraw it.

Perhaps the most high-profile regulation facing potential repeal requires oil and gas companies to pay hefty fees for large releases of methane from their facilities. This regulation implements part of the Biden administration's landmark Inflation Reduction Act, which Trump has vowed to repeal.

Senator Ted Cruz (R–TX), meanwhile, wants to reverse the Department of Energy's new efficiency standards for gas-fired tankless water heaters. The rule "forces American families to choose between costly, high-end models or less efficient alternatives," Cruz said. Andrew deLaski, executive director of the Appliance Standard Awareness Project, called the repeal effort "a real danger," and said eliminating the standard would benefit only gas utilities and one manufacturer, Rinnai, which makes inefficient water heaters.

Half a dozen other new efficiency standards, covering appliances such as clothes dryers and dishwashers, are also vulnerable.

In all, according to an online CRA dashboard run by the Regulatory Studies Center, more than 1000 Biden regulations could theoretically be revoked using the CRA. The biggest obstacle, Hay says, may be a logjam of items on the legislative calendar. The law gives Congress a limited amount of time—typically just a few months—to vote on reversals, which need only a simple majority of both houses of Congress to succeed. But, "Floor time is a really valuable commodity in Congress," Hays says. "I'll be curious to see how much they end up spending on the CRA."

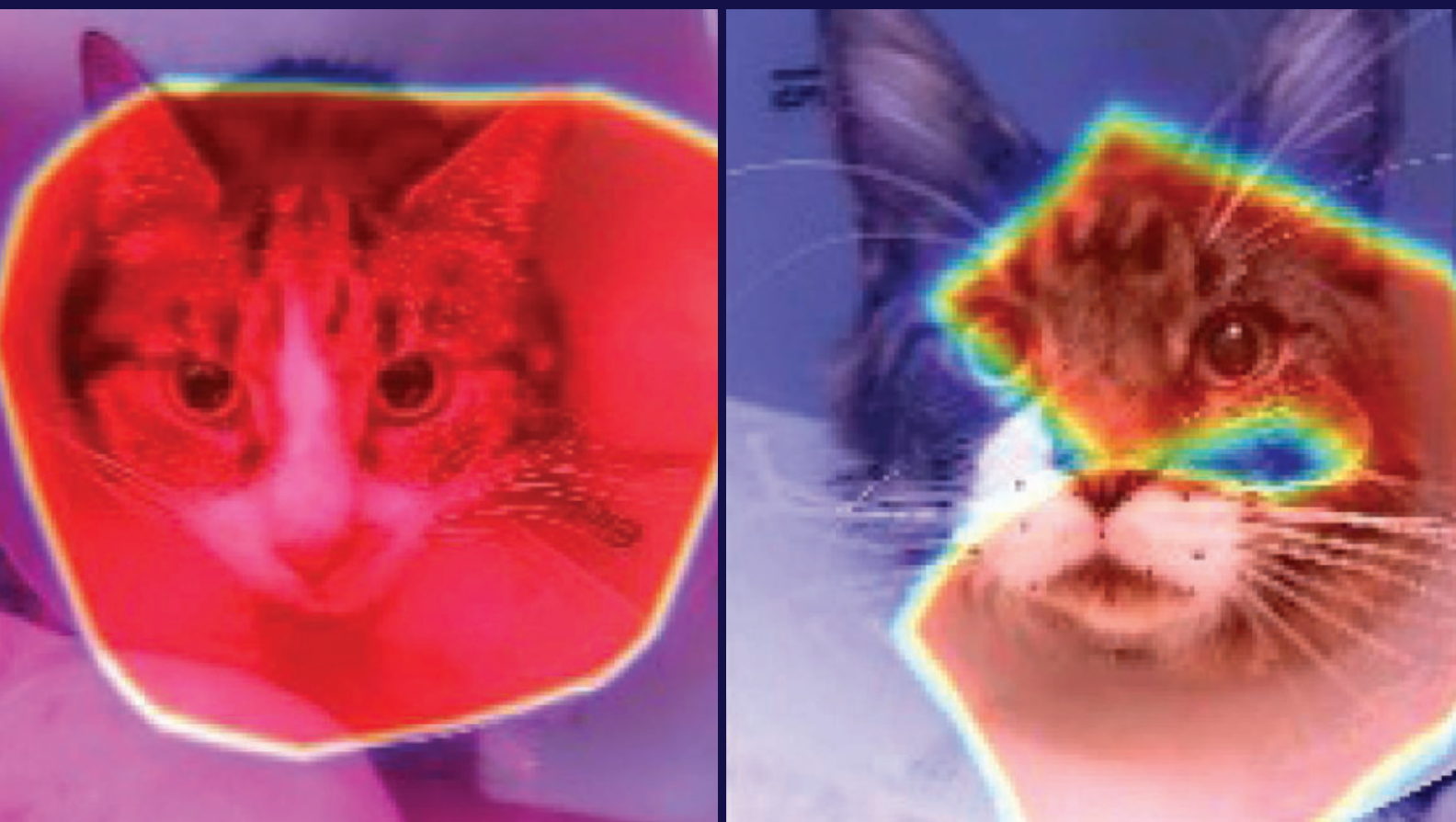
The CRA has one uniquely draconian aspect. If a regulation is successfully reversed, agencies are barred from proposing any similar regulation in the future unless Congress specifically authorizes it.

The Biden administration appears to have anticipated the risk that a future Congress might undo its regulations. Hay says there was an "unprecedented spike" in rules finalized during April and May 2024—early enough in the year to escape congressional review. ■



FEATURES

FACE READERS



Artificial intelligence is becoming better than humans at scanning animals' faces for signs of stress and pain. Are more complex emotions next?

By **Christa Lesté-Lasserre**

At 6 a.m. on a drizzly morning in the southeastern English countryside, hundreds of pinkish white sows are waking up for breakfast. Snorting and drooling, they trot impatiently toward dozens of feeding stalls, sideswiping each other in a mad rush to reach their morning meals.

But first, they have to get their pictures taken.

As each pig squeezes into her feeding stall, a tiny camera snaps a photo of her face. And in less than 1 second, an artificial intelligence (AI) system identifies her based on nothing but her snout, ears, eyes, and other facial features. Armed with that information, the AI orders a customized meal to shoot into the trough.

> **"My job is to be an agent for better lives for animals."**
> **Anna Zamansky**, University of Haifa

Meanwhile, the system continues to analyze her photo, looking for telltale signs in her facial expression that she might be in pain, sick, or in emotional distress. If it finds any, it sends an immediate alert to the farmer—the guy enjoying a morning coffee over in the next room.

These hungry piggies are the unsuspecting beta testers of Intellipig, a system being developed by scientists at the University of the West of England Bristol (UWE) and Scotland's Rural College (SRUC) to deal with a fundamental problem in animal welfare: We *Homo sapiens* are just not the best at understanding how animals are feeling.

The Intellipig team isn't alone. Scientists around the world are turning to AI to decipher the facial expressions of animals, from sheep to horses to cats. Some have already developed algorithms that are faster and more accurate at recognizing signs of pain and distress than the most attentive humans.

PHOTOS: (OPPOSITE PAGE) MARTVEL *ET AL.*

Heat maps reveal the facial regions an artificial intelligence considers most informative in cats.

These tools could usher in a new era of caring for animals that gives higher priority to their health, welfare, and protection, says Melvyn Smith, a machine vision engineer at UWE who led the design of the Intellipig system. There are tantalizing hints that they could go even further. Eventually, AI might even outshine humans in interpreting a range of more complex emotions akin to happiness, serenity, frustration, or fear, he says—feelings that are equally important to understand if we are to give animals the best possible lives.

But like most scientists contemplating the powers of AI, animal behavior researchers worry about putting too much stock in machines, especially when animal welfare is at stake. "Maybe a machine will end up being better than us; I don't know," says Emma Baxter, an animal behavior scientist at SRUC who collaborates with Smith. "I hope there's room for experts, to make sure that [the AI] is actually doing what it says it is."

SCIENTISTS HAVE LONG known that, like us, animals convey how they're feeling through their faces. In *The Expression of the Emotions in Man and Animals*, published in 1872, Charles Darwin suggested facial expressions were a sort of "shared language" among mammals, an ability that must have evolved deep in our evolutionary history.

He based that theory largely on anatomy, says Bridget Waller, a psychologist at Nottingham Trent University. Mammals—including humans—have many common facial muscles whose purpose is to create facial expressions. We share 38% of our facial movements with dogs, for instance, 34% with cats, and a full 47% with primates and horses.

Still, the anatomical similarities don't mean we can read animals' faces like those of fellow humans. So researchers studying animal communication often infer what an animal is experiencing through context.

Pain is the most obvious example: A horse that has just been castrated or a limping sheep with smelly, reddish footrot is undoubtedly feeling pain. Researchers studying animal expressions can also induce mild discomfort—tightening a blood pressure cuff around a leg, for instance, or dabbing a bit of hot chili extract onto the skin. Giving an animal painkillers, on the other hand, usually appears to make it feel better.

Likewise, it's easy to induce minor stress in many species, such as horses and cats, by taking them on a short drive or separating them from their friends for a few minutes. To study stress in young sows, Baxter simply brings in older ones, who intimidate them by acting dominant. Anxious behavior, such as calling out and defecating, and skyrocketing levels of the stress hormone cortisol can confirm that an animal is stressed.

Scientists have spent thousands of hours sitting in front of stalls and cages observing the faces of animals in these painful or stressful situations, then comparing them against animals who were most likely pain- or stress-free. As a result, they've developed "grimace scales" for a variety of species, which provide a measure of how much pain or stress an animal is experiencing based on the movements of its facial muscles.

For instance, a horse who rotates the ears outward while forming "worry wrinkles" above the eyes is more likely to be in pain than one who keeps both ears and eyes relaxed, says Pia Haubro Andersen, a horse surgeon at the Swedish University of Agricultural Sciences (see graphic, p. 712).

Experts in the field have become skilled at manually coding such facial movements in animals, which could—in theory—allow for welfare checks. But it's incredibly tedious work, Andersen says. Human coders need an average of 100 seconds to identify the various facial muscles and code their positions in a single image, or 2 to 3 hours for 30 seconds of video.

AI, on the other hand, can do the same task almost instantaneously—but first, it has to be taught.

FROM HER OFFICE at the University of Haifa, computer scientist Anna Zamansky spent many workdays drowning out the din of sirens and explosions from the Israel-Hamas war. On several occasions, she rushed her laptop and cherished chocolate poodle Becky—who also serves as her favorite research model—into a bomb shelter.

Unlike scientists in the rubble of Gaza's universities, however, Zamansky's team has been able to pursue its research. They are training AI systems to automatically read animals' faces—in the hope of making their lives better. "Putting our brains and our best abilities to do something so good as animal welfare? It truly helps us survive during these difficult times," she says. "It makes us feel hopeful."

Zamansky began by developing facial rec-

ognition software to help people find their lost dogs. Owners upload a picture of their dog's face to the software, which scans for a match in a database of images of strays submitted by concerned strangers. Zamansky and her co-developer George Martvel, a Ph.D. student who escaped the Russian draft in the war against Ukraine, have donated the technology to relief organizations working in Ukraine and in flood zones in Brazil, where it has helped reunite dozens of lost dogs with their owners.

More recently, the team has turned to a more difficult task: using AI to pinpoint the often subtle signs of discomfort in animals' faces. First, the AI system must learn to identify the parts of the face crucial to creating expressions. This involves manually flagging important "landmarks" associated with muscle movements—the top and bottom of an eye, say, or the sides of a nostril—on countless animal photos and converting the images into a mass of digital points, like a page in a child's connect-the-dots book. With the help of freelancers in Kenya, Martvel and his colleagues have landmarked "thousands and thousands" of faces from a variety of species, including cats, dogs, horses, and primates.

Scientists can then feed a plethora of landmarked photos into their AI, to teach it to find landmarks on new images all on its own. In pioneering work in 2016, for example, Peter Robinson, a computer scientist at the University of Cambridge, and his team built on research analyzing human faces to develop a tool that automatically finds the mouth, eyes, and ear tips on sheep faces. A year later, computer scientists at the University of California, Davis created a program trained on images of human faces that automatically places landmarks on horse and sheep faces once they've been warped into a more humanlike shape.

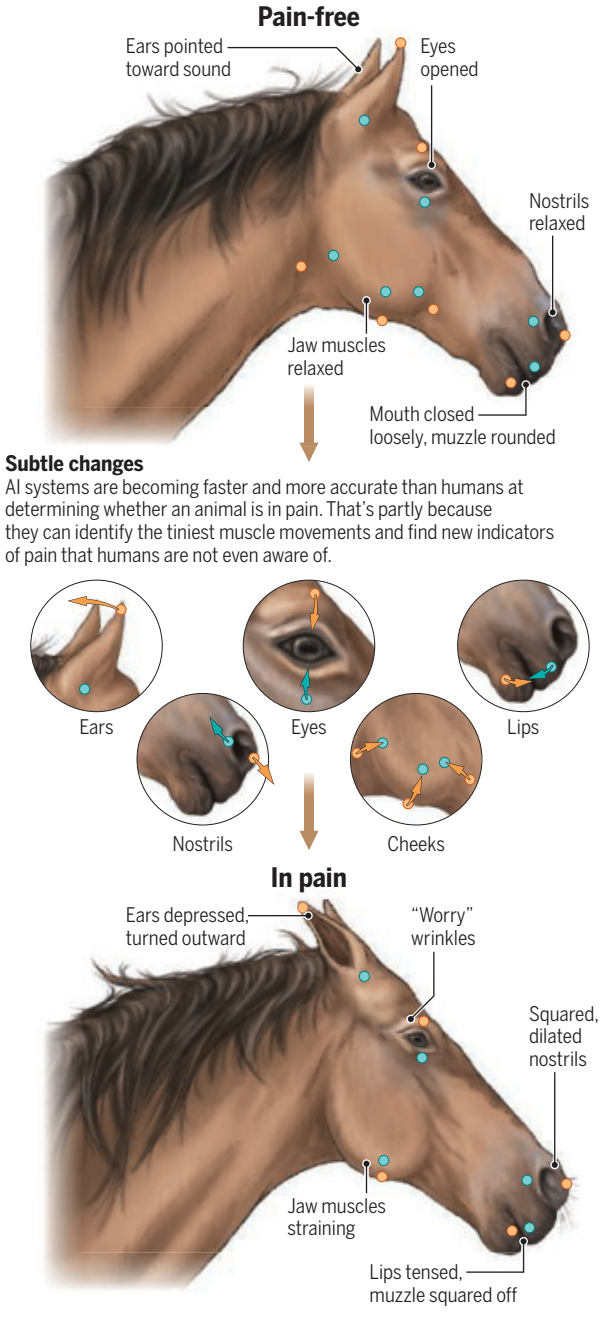
Martvel's AI has now gotten so good at automatic landmarking that it can even figure out where to place points on faces it can't fully see—such as when a dog buries his nose in a food bowl, or a cat peeps out from behind the couch, he says.

Once landmarking is complete, AI can identify specific facial expressions by analyzing the distances between those landmarks. For instance, if a cat widens and tenses up her muzzle—a sign she could be in pain—the distance between two points at the edges of the mouth broadens. By cross-referencing these expressions against the grimace scales researchers have already created, the AI can look for telltale signs of pain or distress.

The result of all this painstaking training is AI systems that can diagnose welfare issues with impressive precision. Robinson's AI, for instance, successfully picked out the handful of ewes within a herd that were suffering from footrot or mastitis. And in 2022, Zamansky and Martvel's AI was 77% accurate in determining whether a cat was in pain.

Pained expressions

Scientists assess an animal's level of pain by looking for telltale muscle movements around the eyes, ears, and other facial features. Artificial intelligence (AI) systems make similar judgments by measuring the distance between "landmarks" on the face (orange and teal dots).



Subtle changes
AI systems are becoming faster and more accurate than humans at determining whether an animal is in pain. That's partly because they can identify the tiniest muscle movements and find new indicators of pain that humans are not even aware of.

THOUGH EFFECTIVE, THESE TOOLS still rely on humans to make the initial call about what to look for in an animal's expression. So recently, researchers have been handing even more of the reins over to AI. Rather than teaching computer systems to look for predetermined expressions of pain or stress, some scientists are simply giving their AI images of animals in different situations and letting them spot telltale signs on their own, through a process called deep learning.

This is the approach used by Gabriel Lencioni, a veterinarian and Ph.D. student in horse behavior and welfare at the University of São Paulo. In recent work, he gave his AI system photos of horses' faces before and after surgery, and then before and after their regularly planned painkillers, instructing the machine to focus specifically on differences in the ears, eyes, and mouth. After training on 3000 images, "the AI learned by itself," he says; ultimately it was able to correctly diagnose whether an animal was in pain 88% of the time.

The Intellipig system being trialed on U.K. smart farms also uses deep learning. Not only does the AI trump humans in recognizing individual pigs, with an accuracy rate of 97%, but it has proved remarkably skilled at picking up on stress through facial features alone, Smith says.

And earlier this year, Zamansky's group published results showing a free-rein AI was consistently better at detecting pain in sheep than even highly skilled veterinarians and behavior experts. The algorithm correctly determined that a sheep had come out of a painful surgery in 82% of trials; four highly trained humans shown the sheep's faces only got it right 70% of the time.

Zamansky likens these AI wins to the historic 1997 triumph of Deep Blue, the IBM supercomputer that beat Russian chess master Garry Kasparov in front of millions of fans. "Like everyone reacting to AI nowadays, Kasparov's first reaction was panic. Everyone thinks, 'Oh my gosh, AI is going to take my job!'" Zamansky says. "But then they understand that AI is just a really powerful

GRAPHIC: A. FISHER/*SCIENCE*

tool that can enhance their own abilities."

Still, Zamansky cautions that a computer that's free to decide what to look for in images can seize on the wrong features. A classic example is a clock in the background. Imagine, for example, that researchers took photos of pain-free or happy animals every day at 10 a.m., as part of a standard scientific protocol, and then other photos of those animals in the opposite condition at 5 p.m. "If the machine sees an image of a clock at 10 a.m., it will say it's a nonpainful rabbit," she says—even if it's not.

Having no insight into how AI is actually making decisions unsettles researchers. "Everyone is concerned about the black box, because they don't know what the machine decides, or why," says Zamansky, whose student Tali Shitrit has devoted her dissertation to figuring out what, exactly, the group's AI looks for in animal faces. She uses a tool called gradient-weighted Class Activation Mapping, or GradCAM, which produces heat maps showing which areas of the face AI focuses on when making its decisions.

So far, she's found that the machine generally considers the eye area the most informative, across data sets and species. In cats, though, the maps are hottest around the nose and mouth, according to work done with veterinarian Holger Volk at the University of Veterinary Medicine Hannover.

Despite the kinks, some researchers are pushing further, striving toward systems that can read emotions more complex than stress and pain—those more akin to the human experiences of joy, anger, or grief.

BRITTANY FLORKIEWICZ, an evolutionary psychologist at Lyon College, has seen more than her fair share of cat videos. She and her team have spent hundreds of hours watching recordings of cats playing and scuffling in a Los Angeles cat café, meticulously coding every detail of the animals' facial expressions while looking for signs in their behavior that they are, essentially, "happy"—or not.

The work has revealed that cats make a whopping 276 distinct facial expressions. Now, Florkiewicz has teamed up with Martvel and Zamansky to apply AI to her data. Already the technology has shown that these café cats tend to subtly mimic each other's facial expressions—often in an invitation to bond through grooming or a playful romp.

In similar work, Zamansky's team trained their AI on photos of Labrador retrievers who were either eagerly anticipating a treat, or were able to see the treat but frustratingly prevented from reaching it. The AI was able to successfully detect whether a dog was "happy" or "frustrated" 89% of the time. It was equally successful at differentiating "happy" from "frustrated" horses. In the same experiment some horses were filmed as they discovered an anticipated treat wasn't there after all. The researchers found that their AI could correctly categorize a horse as "frustrated" or "disappointed" on 61% of trials—a modest success rate but better than chance.



AI systems like Intellipig could be deployed on "smart farms" to provide individualized care to animals.

PHOTO: HANSEN *ET AL.*

To build on these successes, Martvel and Zamansky are now constructing databases of dog, cat, horse, and primate faces in different emotional states. The team scours the internet for photos where owners have provided a clear description of the context—and therefore the animals' likely emotions. By running the photos through AI, they hope to decipher the distinct facial expressions that a species presents in each unique, emotional scenario.

Zamansky's "dream," she says, is to have a "dog face reader" that reveals basic emotional states such as happiness, sadness, and stress—a particular challenge for AI given the wide variety of facial and ear shapes across dog breeds. "It's not possible now, I know," she says. "But in a year, it will be possible. This is what we keep telling ourselves—and we're working hard on that." One day, Florkiewicz says, machines could even start to connect certain facial expressions with "intentionality"—discerning when an animal has a goal, such as going outside, grabbing a toy, or starting a fight.

One challenge is amassing the training data. "They trained ChatGPT with a volume of literature that's roughly equivalent to half the entire university library in Cambridge—which has a copy of every book ever published in the U.K.," Robinson says. "But it turns out there aren't that many pictures of dogs and cats and sheep on the internet"—at least not ones where it's clear how the animals are feeling, he says.

And facial expressions don't tell the whole story of an animal's emotions. For that, AI must look beyond the face to factors such as tail wagging or a hunched posture, says Suresh Neethirajan, an agricultural engineer at Dalhousie University. His own AI welfare check system for farm animals even analyzes body heat emissions—an important clue for chickens and other species that have limited facial expressions.

DESPITE THESE LIMITATIONS, facial AI already offers "pragmatic and realistic" opportunities, Zamansky says. Her team is about to release an AI-based app that will allow cat owners to scan their pets' faces for 30 seconds and immediately get easy-to-read messages such as "Considerable tension around the mouth detected; pain level moderate."

Researchers in the Netherlands have developed a similar app that scans resting horses' faces and bodies to estimate their pain levels. AI could eventually be used during equestrian competitions, Lencioni suggests, to reward riders of happy and comfortable horses and improve welfare and fairness in the sport.

More generally, labs and pet shelters could harness AI to monitor pain and emotional states in animals, Floriekwicz says. And "smart farms"—like those being trialed in the English countryside—promise to provide individualized care to animals through daily monitoring. Ultimately, Smith says, AI helpers could guide farmers in giving pigs not only a stress-free life, but a happy one.

For Zamansky, that prospect makes all her work worthwhile. "My job is to be an agent for better lives for animals," she says. "When we know our animal companions are happy, that makes us happy, too." ■

Christa Lesté-Lasserre is a journalist in Paris.

INSIGHTS

PERSPECTIVES



WATER MANAGEMENT

Where does all the water go?

Seismic noise measurements map out a deep groundwater recharge system

By **Taka'aki Taira**[1] *and* **Roland Bürgmann**[1,2]

Groundwater aquifers are extremely important sources and storage reservoirs of fresh water, especially in regions experiencing severe droughts that can rapidly diminish surface-water supplies. Unsustainable groundwater use can have detrimental effects such as aquifer depletion, loss of storage capacity, chemical and waste contamination, saltwater intrusion, and rapid land subsidence. Thus, it is essential to accurately track changes in the distribution of groundwater to manage the use and replenishment of these water systems below Earth's surface. However, conventional groundwater measurements are limited in their ability to map out the spatiotemporal state of aquifers, which makes it challeng-

A satellite image with simulated natural color shows the Los Angeles metropolitan area where groundwater is an important water supply.

IMAGE: NASA/GSFC/METI/ERSDAC/JAROS AND U.S./JAPAN ASTER SCIENCE TEAM

ing to track groundwater storage. On page 758 of this issue, Mao *et al.* (*1*) report how groundwater storage distribution can be monitored in both space and time through measurements of seismic ground vibrations or noise. This approach should enable surveillance of the amounts of subsurface water and enhance the management of sustainable groundwater use.

As severe droughts grow in duration (*2*), subsurface water storage becomes more important. For example, about one-third of the water supply in Los Angeles, California, which is prone to drought conditions, relies on groundwater. During droughts, human use of stored groundwater increases. However, it gets replenished from atmospheric rivers—that is, long, narrow regions in the atmosphere that transport large amounts of water vapor. Precipitation from atmospheric rivers infiltrates the soil and eventually recharges the groundwater aquifer. In 2023, after two decades dominated by drought conditions, a series of storms and Hurricane Hilary caused record precipitation and destructive flooding on the West Coast of the United States. These events replenished surface reservoirs in the Los Angeles area with nearly 90 billion gallons of stormwater over the course of just 7 months (*3*). However, it has not been clear how much of this excess water made its way into more enduring storage in deep aquifers. To address this question, it is essential to determine the temporal changes in the three-dimensional distribution of subsurface water.

Conventional groundwater measurements are typically performed in monitoring wells, which only provide sparsely distributed points of measurement. The sporadic well data cannot capture the heterogeneity across aquifers at different spatial scales to track subsurface flow from near Earth's surface down to several hundred meters beneath it. Alternatively, remote-sensing measurements of gravity changes, surface deformation, and shallow soil moisture only provide indirect estimates of subsurface water storage. Thus, the precise extent of groundwater loss during drought conditions and its recharge from precipitation are not clear.

Mao *et al.* demonstrate that analysis of seismic noise can capture changes in the state of groundwater storage with better depth resolution. Seismic interferometry with data from a network of seismometers (a device that measures ground vibrations) measures time-dependent properties of the seismic wavefield propagating through Earth's interior (*4, 5*). The seismic wave speed is perturbed by changes in the distribution of water that arise from fluctuations of pore pressure related to groundwater recharge. Thus, monitoring spatiotemporal changes in seismic wave speed in the subsurface (the area just beneath Earth's surface), in principle, can track changes in groundwater storage from the surface to deep underground (*6*). Drawing on the ability to monitor the spatiotemporal distribution of groundwater, Mao *et al.* propose a depth-dependent seismic drought index, which complements the existing indices of near-surface water availability or regional total storage change.

"Integrating different types of seismic data can provide a new perspective of the hydrological cycle..."

The seismic velocity changes documented by Mao *et al.* indicate that only about one-quarter of the groundwater lost in the past two decades in the Los Angeles region was replenished after the storms in 2023. This suggests that the recovery of deep aquifers is a very slow process. One thing to consider is the consequential and irreversible compaction of deep sedimentary layers. This results in permanent loss of water storage capacity as well as in land subsidence (*7*). Such irrecoverable reduction in the capacity of sediments to store valuable water resources is evident in the Central Valley of California (*8*), and in many groundwater basins around the world (*9*).

Beyond measuring variations of groundwater storage, the approach of Mao *et al.* could provide valuable information about in situ hydraulic dynamics and rock permeability, which may help validate models of groundwater flow. The spatial resolution of seismic interferometry could be further improved by incorporating direct waves that sample additional parts of Earth's interior (*10*). Energetic secondary waves excited by earthquakes could also help identify small-scale changes in fluid distributions (*11*). Further, field experiments generating continuous seismic signals could provide complementary information about fluid migration on time scales down to minutes (*12*). Integrating different types of seismic data can provide a new perspective of the hydrological cycle based on hydroseismology.

Although the seismic drought index proposed by Mao *et al.* can reveal temporal changes in groundwater amounts, validating these with other available data is crucial to understand and quantify groundwater recharge dynamics. This is because the seismic drought index relies on relative changes in the measured seismic velocity. It is also important to identify factors other than the flow of groundwater that could cause temporal variations in seismic velocity, such as shaking and deformation of rocks from major earthquake ruptures or thermoelastic strains (*13*). These effects may skew the inferred seismic drought index.

The spatial resolution in the approach by Mao *et al.* directly depends on the spacing of the available seismic stations installed in an area. Currently, only a few sedimentary basins, such as the Los Angeles basin that hosts multiple hazardous earthquake faults, are densely covered with seismometers. Thus, it may be worthwhile to establish new seismic stations near aquifers to explicitly monitor changes in groundwater depth. Alternatively, existing fiber-optic cables with distributed acoustic sensing (*14*) could provide continuous, real-time measurements of ground vibrations and strains. These cables could be used to capture changes in subsurface seismic velocity from the variations in soil moisture and groundwater (*15*). Integrating the seismic imaging techniques of Mao *et al.* with existing methods, such as in situ well monitoring and satellite-based or aerial remote-sensing observations, would allow for comprehensive tracking of groundwater. This will help to ensure the preservation of sustainable water supplies for future generations. ■

[1]Berkeley Seismological Laboratory, University of California, Berkeley, Berkeley, CA, USA. [2]Department of Earth and Planetary Science, University of California, Berkeley, Berkeley, CA, USA. Email: taira@berkeley.edu; burgmann@berkeley.edu

REFERENCES AND NOTES

1. S. Mao, W. L. Ellsworth, Y. Zheng, G. C. Beroza, *Science* **387**, 758 (2025).
2. K. Strzepek, G. Yohe, J. Neumann, B. Boehlert, *Environ. Res. Lett.* **5**, 044012 (2010).
3. Los Angeles County Press Release, (2024); https://lacounty.gov/2024/05/08/la-county-ends-storm-season-with-96-3-billion-gallons-of-captured-stormwater/.
4. K. Aki, *Bull. Earthq. Res. Inst. Univ. Tokyo* **35**, 415 (1957).
5. M. Campillo, A. Paul, *Science* **299**, 547 (2003).
6. C. Sens-Schönfelder, U. Wegler, *Geophys. Res. Lett.* **33**, L21302 (2006).
7. B. Riel, M. Simons, D. Ponti, P. Agram, R. Jolivet, *Water Resour. Res.* **54**, 3557 (2018).
8. G. Carlson, S. Werth, M. Shirzaei, *Remote Sens. Environ.* **311**, 114303 (2024).
9. M. F. Hasan, R. Smith, S. Vajedian, R. Pommerenke, S. Majumdar, *Nat. Commun.* **14**, 6180 (2023).
10. N. Nakata, J. P. Chang, J. F. Lawrence, P. Boué, *J. Geophys. Res. Solid Earth* **120**, 1159 (2015).
11. F. Niu, P. G. Silver, R. M. Nadeau, T. V. McEvilly, *Nature* **426**, 544 (2003).
12. T. M. Daley, R. D. Solbau, J. B. Ajo-Franklin, S. M. Benson, *Geophysics* **72**, A57 (2007).
13. T. Clements, M. A. Denolle, *J. Geophys. Res. Solid Earth* **128**, e2022JB025553 (2023).
14. N. Lindsey, E. R. Martin, *Annu. Rev. Earth Planet. Sci.* **49**, 309 (2021).
15. V. Rodríguez Tribaldos, J. B. Ajo-Franklin, *J. Geophys. Res. Solid Earth* **126**, e2020JB021004 (2021).

10.1126/science.adv4928

EVOLUTION

Constrained roads to complex brains

Neural development and brain circuit evolution converged in birds and mammals

By **Giacomo Gattoni** and **Maria Antonietta Tosches**

During the arms race for survival on Earth, highly intelligent biological systems have emerged only a few times. Among vertebrates, mammals and birds can solve complex problems, use tools, and engage in elaborate social behaviors. These sophisticated tasks involve the pallium, the brain region most implicated in cognition, which includes the neocortex in mammals. However, it is unclear whether complex brains evolved multiples times through similar or different mechanisms. On pages 733, 734, and 732 of this issue, Zaremba *et al.* (*1*), Hecker *et al.* (*2*), and Rueda-Alaña *et al.* (*3*), respectively, provide evidence for the convergent development and evolution of neurons and their connections in the bird and mammalian pallia, highlighting the need for multiple perspectives in brain comparative studies.

Department of Biological Sciences, Columbia University, New York, NY, USA. Email: mt3353@columbia.edu

Neural circuits in the bird pallium and mammalian neocortex are remarkably similar (*4*), leading to the suggestion that neurons in these regions are homologous, that is, inherited from the last common ancestor of birds and mammals (*5*, *6*). However, neurons belonging to these similar circuits develop from molecularly and spatially distinct regions of the pallium—the ventral pallium in birds and the dorsal pallium in mammals—which argues against homology (*7*, *8*). This has led to contrasting views on pallium evolution, with the debate hampered by the lack of detailed characterizations of the diversity of cell types in the avian pallium.

Zaremba *et al.* and Hecker *et al.* expanded on previous work (*9*) and used single-cell and spatial omics, enhancer prediction, connectivity, and developmental analyses to characterize neuron types in the chicken pallium. Their studies show that, from a molecular perspective, ventral pallium neurons in birds are more similar to mammalian ventral pallium neurons than to mammalian dorsal pallium (neocortex) neuron types. Rueda-Alaña *et al.* compared neural circuit development across mammals (mouse), reptiles (gecko), and birds (chicken) and noted substantial differences in the generation and molecular identity of the input, integrative, and output neurons in bird cortical-like circuits and mammalian neocortex. Collectively, these results show that the similarity of neural circuits in birds and mammals is the result of evolutionary convergence, rather than common ancestry.

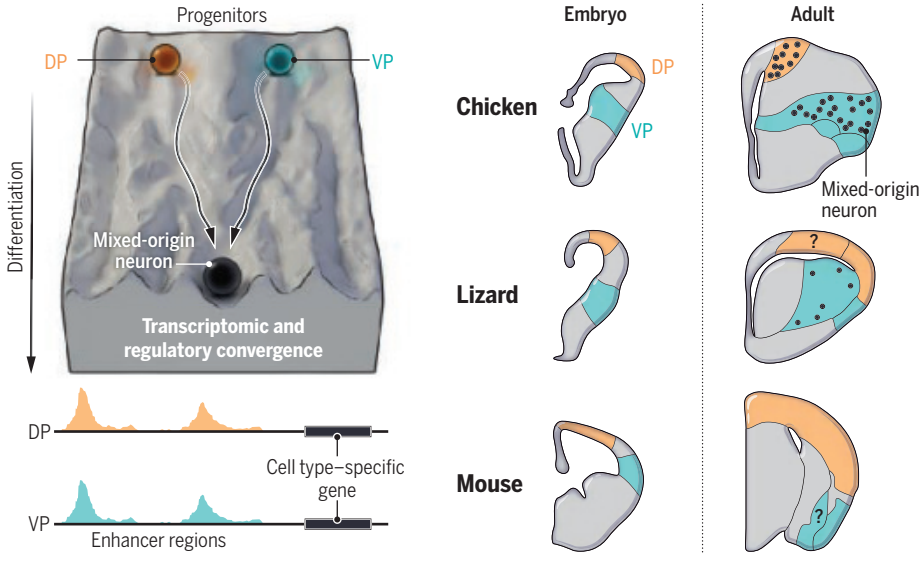
Like mammals, birds also have a dorsal pallium, called the hyperpallium, which has previously been compared to the neocortex because of its similar position in the brain. However, Zaremba *et al.*, Hecker *et al.*, and Rueda-Alaña *et al.* show that bird hyperpallium cell types do not closely resemble mammal neocortical neurons. Instead, some of the hyperpallium cells are similar to neurons in other mammalian cortical areas, such as the subiculum, echoing results from amphibian and fish studies (*10*, *11*).

Zaremba *et al.* and Hecker *et al.* also discovered new neuron types that map spatially to both the hyperpallium and ventral pallium and that lack clear counterparts in mammals. Although these neurons are part of two different pallial regions, they are indistinguishable at the transcriptome level (abundance of specific RNA transcripts) (*12*). This raises the question of whether the same gene expression in these neurons is established by distinct regulatory programs in the dorsal and ventral pallia. Zaremba *et al.* and Hecker *et al.* thus analyzed chromatin accessibility and the use of enhancers (DNA sequences that activate transcription) in the chicken genome and found that these dorsal and ventral pallium neurons are largely indistinguishable at the chromatin level as well and can therefore be regarded as the same cell type. In the absence of strong evidence of neuronal migration between pallial regions, these results contradict the assumption that distinct regions of the embryonic pallium must generate different types of neurons, a pillar of popular hypotheses on pallium evolution.

In analyzing neural development, Zaremba *et al.* determined that cells in the embryonic dorsal and ventral pallia initially have distinct transcriptomes, reflecting their origin from different neural progenitors. However, they acquire the same molecular identity with maturation, erasing any trace of separate developmental origins (see the figure). These observations suggest that "mixed-origin" neuron types mature late in development and raise the possibility that extrinsic cues might direct transcriptomic convergence. Notably, the closest counterparts of

One neuron type, two developmental origins

In the chicken pallium, distinct progenitors give rise to the same neuron types in the dorsal pallium (DP) and ventral pallium (VP) of the adult brain, as represented in the Waddington landscape of differentiation and gene expression profiles. These mixed-origin neurons in birds appear more similar to VP cells in lizards than to cells in mammals.



GRAPHIC: A. FISHER/*SCIENCE*

these neurons are found in the ventral pallium of lizards and turtles. If confirmed, this would suggest that the dorsal pallium in birds may have recruited gene regulatory programs that were ancestrally restricted to cell types in the ventral pallium.

Evolutionary change in the brain can occur at every level of organization, from cell types to neural circuits and brain regions. Zaremba *et al.*, Hecker *et al.*, and Rueda-Alaña *et al.* illustrate how comparisons across multiple levels are critical to understand brain evolution. Single-cell profiling is a powerful tool for reconstructing the evolution of neuron types while also characterizing brain regions. However, cell type comparisons may be insufficient to clarify the evolution of brain regions, particularly without developmental context. This is because the same cell identity program—the gene expression program that establishes and maintains type-specific characteristics (*13*)—can be activated in different developmental contexts. Astrocytes, for example, are the same cell type regardless of whether they develop from forebrain or hindbrain progenitors. In the chicken pallium, ignoring the transcriptomic convergence of mixed-origin neuron types during development would lead to the erroneous conclusion that the bird dorsal and ventral pallia are homologous to the lizard ventral pallium. Developmental analyses indicate that distinct dorsal and ventral pallia already existed in the last common ancestor of birds, lizards, and mammals.

Extending beyond the molecular comparison of cell types is even more critical to infer the evolution of neural circuits. As Rueda-Alaña *et al.* show, nonhomologous neuron types can be part of neural circuits with remarkably similar architecture across regions and species. Conversely, Hecker *et al.* and Zaremba *et al.* identified neuron types in birds and mammals with similar transcriptomes but diverging connectivity. Integrating cell type molecular and connectivity data to resolve the evolution of neural circuits is one of the biggest challenges for future research. ■

GRAPHIC: A. MASTIN/*SCIENCE*

REFERENCES AND NOTES

1. B. Zaremba *et al.*, *Science* **387**, eadp5182 (2025).
2. N. Hecker *et al.*, *Science* **387**, eadp3957 (2025).
3. E. Rueda-Alaña *et al.*, *Science* **387**, eadp3411 (2025).
4. M. Stacho *et al.*, *Science* **369**, eabc5534 (2020).
5. H. J. Karten, *Ann. N. Y. Acad. Sci.* **167**, 164 (1969).
6. J. Dugas-Ford, J. J. Rowell, C. W. Ragsdale, *Proc. Natl. Acad. Sci. U.S.A.* **109**, 16974 (2012).
7. G. F. Striedter, *Brain Behav. Evol.* **49**, 179 (1997).
8. L. Puelles *et al.*, *J. Comp. Neurol.* **424**, 409 (2000).
9. B. M. Colquitt, D. P. Merullo, G. Konopka, T. F. Roberts, M. S. Brainard, *Science* **371**, eabd9704 (2021).
10. J. Woych *et al.*, *Science* **377**, eabp9186 (2022).
11. M. Tibi *et al.*, *Sci. Adv.* **9**, eadh7693 (2023).
12. G. Gedman *et al.*, *J. Comp. Neurol.* **529**, 3222 (2021).
13. D. Arendt *et al.*, *Nat. Rev. Genet.* **17**, 744 (2016).

10.1126/science.adv2609

NEUROSCIENCE

Understanding the desire for dessert

A neural circuit in mice mediates the preference for high-sugar food after a meal

By **Sadaf Farooqi**

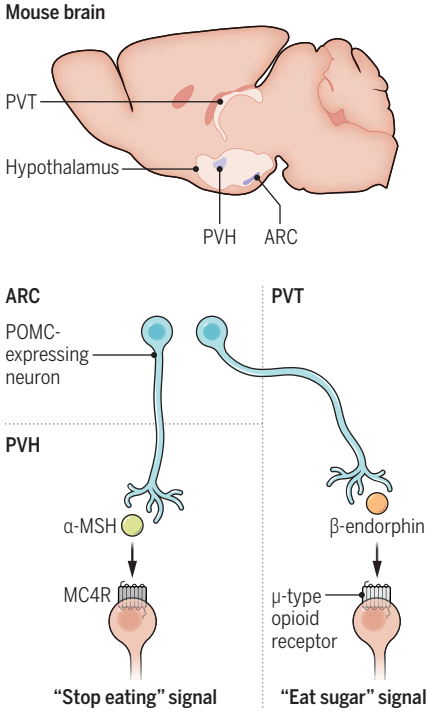
Overeating is a major cause of obesity, type 2 diabetes, cardiovascular disease, and some cancers (*1*). Although in many societies, readily available, cheap foods promote overconsumption, the sensory properties of food also influence the amount and type of food eaten. Sensory-specific satiety (fullness) describes the decline in pleasantness of a food as it is eaten, relative to uneaten foods that have different sensory qualities—for example, the desire for a sweet dessert after a meal (*2*). However, the neural mechanisms that mediate this preference for sweet food are incompletely understood. On page 750 of this issue, Minère *et al.* (*3*) report a neural circuit that regulates the preference for sweet food after the consumption of a standard meal in mice (*Mus musculus*). This circuit is formed by neurons that project from the hypothalamus to the paraventricular thalamus, a region involved in sensing pleasantness and driving motivated behaviors. This work advances understanding of the drive to eat sweet food when already full.

Eating behavior is modified by external environmental cues (visual appearance, smell, and availability of food) and internal drives, such as hunger and satiety (*4*). These external and internal cues are detected and integrated by highly conserved neural circuits, the functions of which are to defend against starvation and adapt to changing energy demands during growth and reproduction. Food also has rewarding properties that drive consumption. The desire for sweet foods is an innate behavior evident in multiple mammalian species; even newborn humans will consume a greater volume of a solution that tastes sweeter (*5*). In nonhuman species, naturally occuring plant sugars (for example, glucose, sucrose, fructose, and maltose) and lactose in milk induce the sensory quality of sweetness.

A more comprehensive understanding of the molecular mechanisms that underpin these highly conserved eating behaviors is now emerging. Neural circuits in the hypothalamus—a deep subcortical brain region surrounded by a relatively leaky blood-brain barrier—respond to changes in hormones and nutrients that circulate in the blood. A key circuit involves neurons in the arcuate nucleus of the hypothalamus that respond to the hormone leptin, which is released by adipose tissue and signals nutrient availability to the brain.

Signaling sweet preference

Pro-opiomelanocortin (POMC)–expressing neurons are activated in the satiated (full) state and project from the arcuate nucleus of the hypothalamus (ARC) to the paraventricular hypothalamus (PVH) and the paraventricular thalamus (PVT). In the PVH of mice, these neurons release α-melanocyte–stimulating hormone (α-MSH) that binds to the melanocortin 4 receptor (MC4R), reducing hunger and increasing satiety. POMC-expressing neurons that project to the PVT release β-endorphin, which binds to the μ-type opioid receptor, resulting in a desire for sugar.



Institute of Metabolic Science, University of Cambridge, Cambridge, UK. Email: isf20@cam.ac.uk

These neurons express pro-opiomelanocortin (POMC) and connect to neurons in the paraventricular hypothalamus that express the melanocortin 4 receptor (MC4R). In the fed state, leptin stimulates the expression of POMC, which is processed into smaller peptides, including α-melanocyte–stimulating hormone (α-MSH) and β-endorphin. Binding of α-MSH to MC4R leads to reduced hunger, increased satiety, and a reduction in food intake. Conversely, β-endorphin activates δ-type and μ-type opioid receptors in limbic nuclei and other brain regions to give food a hedonic quality, and it can also affect the motivational properties, or wanting, of food (*6*).

Minère *et al.* investigated the role of β-endorphin in the response to fullness in mice. They found that β-endorphin–positive POMC-expressing neurons project to the paraventricular thalamus (PVT) (see the figure). Optogenetic stimulation of these neurons evoked β-endorphin release in the PVT. To understand whether this circuit has a role in the desire for sweet foods when full, the authors offered mice either a high-sugar diet or standard chow (with comparatively low sugar content) after a 90-min bout of feeding. In control conditions, mice offered the high-sugar diet ate more than those offered the chow. However, optogenetic inhibition of POMC neuron terminals in the PVT reduced the consumption of the high-sugar diet, indicating that this behavioral response was mediated by the POMC-PVT circuit.

Minère *et al.* suggest that therapies that reduce the preference for sweet food might be effective in the treatment of obesity. However, it is important to consider that the feeling of pleasure relating to food is closely linked to mood. Anhedonia (the reduced ability to experience pleasure) is a cardinal sign of depression, and sucrose preference tests are used as measures of anhedonia, depressive behavior, and the response to antidepressant treatment in mice and humans. Clinical trials of the antiobesity medication rimonabant (a cannabinoid 1 receptor antagonist targeting neural circuits involved in reward) showed significant weight loss. However, once the drug was licensed and larger numbers of people with obesity were treated, the risks of severe depression and suicidal ideation became evident, leading to its withdrawal from clinical use. These findings suggest that although medications that suppress sucrose preference might reduce total food intake, the ability to sense some pleasure from food is important for health.

Understanding food preference in humans is further complicated by the observation that sweet foods are often also high in fat. Genetic disruption and pharmacological inhibition of melanocortin signaling in mice as well as MC4R deficiency in humans are associated with reduced desire for, and consumption of, high-sucrose solutions (mice) and food (humans) but an increased preference for high-fat diets (*7*, *8*). Preference for foods high in fat might in part be mediated by MC4R-expressing neurons in the amygdala because the inhibition of MC4R in this brain region increases fat consumption in mice. Neurons in the central nucleus of the amygdala project to the parabrachial nucleus, which responds to gustatory and visceral signals and is involved in sucrose preference (*9*). Cumulatively, these findings and the data from Minère *et al.* suggest that interactions between melanocortin and opioid receptor–mediated signaling have a critical role in food preference.

"The desire for sweet foods is an innate behavior evident in multiple mammalian species..."

A comprehensive understanding of the neural mechanisms involved in mediating the preference for dietary fat, sucrose, and other nutrients is needed to understand the drivers of overconsumption—a major cause of obesity and metabolic disease. Further studies are required to evaluate the relative contribution of sweet taste and type of sugar or sweeteners to liking, wanting, food seeking, and consumption, particularly when combined with fat. Understanding how neural circuits are affected by food intake after a single meal and after repeated consumption of a particular food (habituation) will also be important. Ultimately, policies aimed at improving the quality of food and tackling its adverse effects on health should be informed by an awareness of the powerful biological drives that shape sweet preference, sugar consumption, and eating behavior. ■

REFERENCES AND NOTES

1. F. Rubino *et al.*, *Lancet Diabetes Endocrinol.* 10.1016/S2213-8587(24)00316-4 (2025).
2. B. J. Rolls, E. T. Rolls, E. A. Rowe, K. Sweeney, *Physiol. Behav.* **27**, 137 (1981).
3. M. Minère *et al.*, *Science* **387**, 750 (2025).
4. A. A. van der Klaauw, I. S. Farooqi, *Cell* **161**, 119 (2015).
5. D. A. Yarmolinsky, C. S. Zuker, N. J. P. Ryba, *Cell* **139**, 234 (2009).
6. M. D. Hayward, J. E. Pintar, M. J. Low, *J. Neurosci.* **22**, 8251 (2002).
7. B. L. Panaro, R. D. Cone, *Proc. Natl. Acad. Sci. U.S.A.* **110**, 7050 (2013).
8. A. A. van der Klaauw *et al.*, *Nat. Commun.* **7**, 13055 (2016).
9. B. P. Shah *et al.*, *Proc. Natl. Acad. Sci. U.S.A.* **111**, 13193 (2014).

10.1126/science.adv4359

HYDROGEN PRODUCTION

Thrifting iridium for hydrogen

Anchoring catalysts on an engineered oxide support enables stable water electrolysis

By **Andrew D. Pendergast**[1,2,3] *and* **Shannon W. Boettcher**[1,2,3,4]

Using renewable electricity to produce hydrogen fuel reduces reliance on fossil fuels. Proton exchange membrane water electrolyzers (PEMWEs) are the highest-performing commercialized technology (*1*). These devices split water into oxygen gas and hydrogen ions (protons) at the anode. The protons then migrate through an ion-conducting polymer membrane (ionomer) to be reduced to hydrogen gas at the cathode. The anode reaction's harsh environment requires the use of precious-metal catalysts, such as iridium oxide (IrO_x). Given the expense and scarcity, the design of electrodes that minimize the use of precious metals without compromising the requisite stability and activity is desired for large-scale hydrogen production (*2*, *3*). On page 791 of this issue, Shi *et al.* (*4*) report that anchoring IrO_x catalysts onto porous cerium-oxide (CeO_x) supports maintains performance even with much reduced precious metal use.

Although many materials have been explored (*5*), IrO_x remains the only practical catalyst for oxygen evolution in PEMWEs because of its stability under acidic oxidizing conditions. Known degradation mechanisms include catalyst dissolution (*2*, *3*), detachment, agglomeration, Ostwald ripening (dissolution and redeposition of small particles into large particles), active-site blocking by oxygen bubbles, and electrical or ionic isolation of catalyst particles (see the figure) (*1*, *6*). To circumvent these issues, commercial PEMWE anodes are loaded with a high mass of IrO_x (2 to 3 mg cm^{-2}), despite the cost and scarcity of iridium (*1*).

[1]Energy Storage and Distributed Resources Division, Lawrence Berkeley National Laboratory, Berkeley, CA, USA. [2]Department of Chemical and Biomolecular Engineering, University of California, Berkeley, CA, USA. [3]Department of Chemistry, University of California, Berkeley, CA, USA. [4]Oregon Center for Electrochemistry, Department of Chemistry and Biochemistry, University of Oregon, Eugene, OR, USA. Email: boettcher@berkeley.edu

To achieve a levelized cost of hydrogen of US$1 per kilogram by 2031 from PEMWEs, the US Department of Energy (DOE) targets a platinum group metal loading below 0.125 mg cm^{-2} while improving the hydrogen production rate and extending device lifetime beyond a decade (*7*). To achieve this goal, new interfacial engineering strategies are necessary to reduce catalyst mass loading by increasing catalyst utilization (proportion of catalyst's metal sites involved in the reaction) while maintaining stability. Previous approaches include using core-shell titanium dioxide (TiO_2)–IrO_x nanoparticles and placing IrO_x nanoparticles on conductive TiO_2 supports (*6*). So far, these methods appear insufficient to meet the aggressive DOE targets.

To decrease degradation rates at low IrO_x catalyst loading, Shi *et al.* embedded IrO_x nanoparticles within porous CeO_x supports. These anchored IrO_x particles were formed during a sonication-induced Ostwald ripening pathway in which the CeO_x surface partially dissolves and redeposits around the nucleating IrO_x particles. This process buried the IrO_x particles by ~1 nm into the CeO_x support. The CeO_x support was also found to have both ionic and electronic conductivity—properties that may improve catalyst utilization by facilitating proton transport from IrO_x active sites to the ionomer and electrical connectivity between IrO_x particles in the anode, respectively.

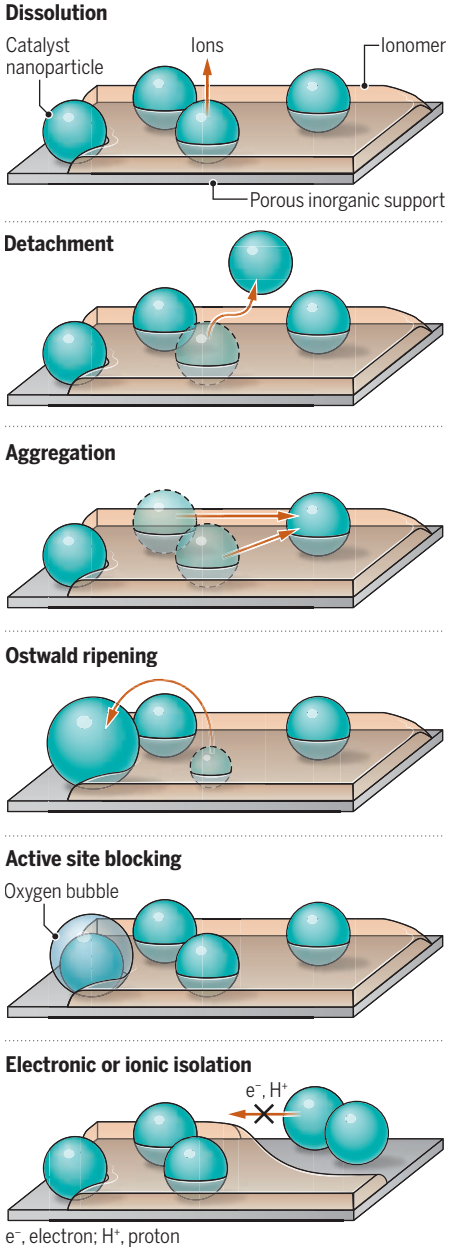
The anchoring approach of Shi *et al.* produced a PEMWE cell with current densities of 3.0 A cm^{-2} at 1.72 V at iridium loadings of 0.3 mg cm^{-2}. This outperforms the 2026 interim DOE targets. The cell voltage increased by only 1.3 μV $hour^{-1}$, which surpasses the final DOE target.

In addition to physical stabilization through the embedding approach, Shi *et al.* attributed the durability of the electrolyzer to electronic stabilization of the catalyst. Oxygen vacancies in CeO_x were proposed to slow catalyst dissolution by mitigating the formation of high oxidation state iridium species during oxygen evolution. Direct confirmation of such interactions between the catalyst and the support is challenging because of the dynamic structure of hydrated catalysts formed during electrolysis (*8*). Further study of embedded IrO_x catalysts in various model oxide supports (other than CeO_x) would help elucidate potential mechanisms of electronic stabilization.

Complete suppression of catalyst dissolution during oxygen evolution is probably impossible. The stability number—a metric for catalyst stability—relates the amount of oxygen produced to the amount of catalyst dissolved. This figure is used to compare the intrinsic activity and stability of catalysts (*3*). An inverse correlation between catalytic activity and stability number has been reported for IrO_x. This is likely due to common intermediates along the reaction pathways for oxygen evolution and IrO_x dissolution (*9*). By contrast, the IrO_x/CeO_x catalysts reported by Shi *et al.* show that interface design can break this inverse correlation. Simultaneous improvements in catalyst activity and durability are indeed possible.

How catalysts deactivate during hydrogen production

Harsh reaction conditions in a water electrolyzer deactivate catalysts in various ways. The method of Shi *et al.* addresses this issue by embedding catalysts in a porous inorganic support.



e^-, electron; H^+, proton

GRAPHIC: N. BURGESS/*SCIENCE*

Understanding the precise degradation mechanisms for catalysts in PEMWEs is complicated by multiscale transport phenomena. Electron microscopy (*10*) and mass-balance analyses (*11*) have shown that more than 90% of dissolved iridium redeposits within the electrochemical cell, including on the cathode and within the ionomer membrane. Although it is not explicitly demonstrated by Shi *et al.*, the IrO_x/CeO_x structure may effectively confine dissolved molecular iridium species for subsequent redeposition in productive locations within the anode.

To better understand the catalyst dynamics during operation, a realistic model system that captures reaction and transport processes across the multiple phases and length scales is required. A combination of factors affects the overall stability of catalysts, including the amount of catalyst, the type of electrolyte (solid versus liquid), the porous transport layer design, and electrode passivation architectures. This necessitates further analyses with a full electrochemical cell in various conditions (*12*), in addition to the existing PEMWE models based on half-cells (*13*) and gas-diffusion electrodes (*14*). High-throughput analytical platforms that are compatible with operando spectroscopy and scanning probe microscopy techniques could complement existing platforms to understand processes in complex electrochemical systems such as PEMWEs. The resulting insight would enable electrode and electrocatalyst redesign, building on the work by Shi *et al.*, to reach the ambitious goal of producing hydrogen at scale at a cost that outcompetes fossil fuels on a subsidy-free basis. ■

REFERENCES AND NOTES

1. C. Wang *et al.*, *Int. Mater. Rev.* **69**, 3 (2024).
2. C. Spöri, J. T. H. Kwan, A. Bonakdarpour, D. P. Wilkinson, P. Strasser, *Angew. Chem. Int. Ed.* **56**, 5994 (2017).
3. S. Geiger *et al.*, *Nat. Catal.* **1**, 508 (2018).
4. W. Shi *et al.*, *Science* **387**, 791 (2025).
5. L. Li, P. Wang, Q. Shao, X. Huang, *Adv. Mater.* **33**, e2004243 (2021).
6. M. Bernt *et al.*, *Chem. Ing. Tech.* **92**, 31 (2020).
7. DOE, Technical targets for PEM electrolysis; https://www.energy.gov/eere/fuelcells/technical-targets-proton-exchange-membrane-electrolysis.
8. N. Danilovic *et al.*, *J. Phys. Chem. Lett.* **5**, 2474 (2014).
9. O. Kasian, J. P. Grote, S. Geiger, S. Cherevko, K. J. J. Mayrhofer, *Angew. Chem. Int. Ed.* **57**, 2488 (2018).
10. H. R. Yu, L. Bonville, J. Jankovic, R. Maric, *Appl. Catal. B* **260**, 118194 (2020).
11. M. Milosevic *et al.*, *ACS Energy Lett.* **8**, 2682 (2023).
12. J. Knöppel *et al.*, *Nat. Commun.* **12**, 2231 (2021).
13. T. Imhof, R. K. F. Della Bella, B. M. Stühmeier, H. A. Gasteiger, M. Ledendecker, *Phys. Chem. Chem. Phys.* **25**, 20533 (2023).
14. M. Geuß *et al.*, *ACS Catal.* **14**, 11819 (2024).

ACKNOWLEDGMENTS

The authors acknowledge support from the DOE, Office of Science Energy Earthshot Initiative as part of the Center for Ionomer-based Water Electrolysis at Lawrence Berkeley National Laboratory under contract DE-AC02-05CH11231.

10.1126/science.adv4929

POLICY FORUM

CONSERVATION

Time to fix the biodiversity leak

The risk that locally successful nature conservation may be shifting problems elsewhere can no longer be ignored

By **Andrew Balmford[1,2], Thomas S. Ball[1,2], Ben Balmford[3], Ian J. Bateman[3], Graeme Buchanan[4], Gianluca Cerullo[1,2,5], Francisco d'Albertas[1,2], Alison Eyres [1,2], Ben Filewod[6], Brendan Fisher[7,8], Jonathan M. H. Green[9], Kyle S. Hemes[10,11], Jody Holland[1,2], Miranda S. Lam[1,2], Robin Naidoo[12], Alexander Pfaff[13], Taylor H. Ricketts[7,8], Fiona Sanderson[14], Timothy D. Searchinger[15,16], Bernardo B. N. Strassburg[17], Thomas Swinfield[1,2], David R. Williams[18]**

As momentum builds behind hugely ambitious initiatives like the Global Biodiversity Framework (GBF) 30 x 30 target and the European Union's (EU's) Biodiversity and Forestry Strategies, there is a danger that hard-won local conservation gains will be dissipated through leakage, the displacement of human activities that harm biodiversity away from the site of an intervention to other places (*1*). These off-site damages may be less than on-site gains—in which case the action is still beneficial but less so than it superficially seems. However, if activities are displaced to more biodiverse (or less productive) places, leakage impacts may exceed local benefits, so that well-intentioned efforts cause net harm. There is a pressing need for leakage effects like this to be acknowledged and as far as possible avoided or mitigated—through demand reduction, careful selection of conservation or restoration sites, or compensatory increases in production in lower-impact areas.

Conservation interventions on land or at sea are intrinsically vulnerable to leakage because most threatened species are in trouble from farming, fishing, hunting, or wood harvesting. It follows, then, that effective conservation or restoration actions generally lower current or future food or fiber production—by preventing habitat conversion, reducing the intensity of production, or stopping it altogether. Under local, so-called activity-shifting leakage, actors directly affected by an intervention then relocate to farm, log, hunt, or fish elsewhere. But as supply chains become more globalized and area-based conservation efforts expand in scale, it is increasingly likely that they lead to what is termed market leakage (*2*). Here, by reducing local production and so raising prices, conservation actions inadvertently incentivize the expansion of harmful production by other actors, sometimes after a delay, and even in other countries.

As one carefully analyzed example, although US government actions to conserve old-growth forests in the Pacific Northwest reduced annual timber harvests there by ~2.1 billion board-feet, they incentivized a 1.7 billion board-feet increase in softwood harvesting elsewhere in North America (*3*), where it is likely to have had substantial biodiversity impacts. Currently, there are growing concerns that as large-scale conservation and wider environmental initiatives accelerate in temperate regions such as Europe and China, resulting production shortfalls are stimulating accelerated land conversion in more biodiverse, less well regulated parts of the world (*4*, *5*).

LEAKY CONSERVATION

It appears that, as in the market for forest-carbon credits (*2*, *6*–*8*), leakage is seriously underrecognized in the biodiversity sector. At the site level, preliminary results from a new survey of 100 managers responsible for tropical conservation projects found that 37% said they were unaware of the concept of leakage, and less than half reported undertaking efforts to mitigate its extent (*9*). At larger scale there is, extraordinarily, no mention of the problem of leakage in the recent Global Biodiversity Framework goals or targets, where the text calling for at least 30% of Earth's land and sea "to be effectively conserved and managed" says nothing about whether this might simply shift the negative impacts of food and wood production elsewhere. Likewise, the Japanese government's plans for a pesticide-free Green Food System and the EU's Biodiversity and Forestry Strategies (*5*) are mute on how the leakage of forgone production will affect biodiversity and other environmental outcomes farther afield; in Europe, the EU's Anti-Deforestation Regulation signals an intention to consider impacts beyond its borders but is undermined by trade regulations (*10*).

So why is leakage still largely overlooked in conservation? We think there are several reasons. Biodiversity projects, programs, and policies focus largely on local, national, or regional targets; impacts induced outside the defined domain of interventions are then not considered. Additionally, quantifying leakage and its biodiversity impacts robustly is hard—and what is not measured is often ignored. Also, mitigating leakage can be a daunting and costly challenge. Finally, incorporating leakage effects will generally lead to conservation impacts being revised downward, creating perverse incentives to instead be unduly optimistic about leakage.

Yet as with carbon projects (*6*–*8*), there is widespread evidence that biodiversity interventions often cause leakage. As one example, an assessment of deforestation in and around 423 East African protected areas (PAs) reported that rates of forest loss in their buffer zones often exceeded average regional losses, particularly for the National Parks that successfully slowed deforestation within their boundaries (*11*). Attributing causality in cases of apparent activity-shifting leakage like this is difficult, but market leakage too is challenging to analyze (*2*). Because of the dispersed and interlinked nature of many markets, the actors who respond to such price signals may be far from the intervention site and thus difficult to track. Most assessments of market leakage therefore rely on hard-to-parameterize equilibrium models of how consumers and suppliers react to the price

[1]Department of Zoology, University of Cambridge, Cambridge, UK. [2]Conservation Research Institute, University of Cambridge, Cambridge, UK. [3]Land, Environment, Economics and Policy Institute, Economics Department, University of Exeter Business School, Exeter, UK. [4]Royal Society for the Protection of Birds (RSPB) Centre for Conservation Science, RSPB Scotland, Edinburgh, UK. [5]Department of Forest Ecosystems and Society, Oregon State University, Corvallis, OR, USA. [6]Canadian Forest Service, Ottawa, Canada. [7]Gund Institute for Environment, University of Vermont, Burlington, VT, USA. [8]Rubenstein School of Environment and Natural Resources, University of Vermont, Burlington, VT, USA. [9]Stockholm Environment Institute York, Department of Environment and Geography, University of York, York, UK. [10]Woods Institute for the Environment, Stanford University, Stanford, CA, USA. [11]Amazon Worldwide Sustainability, Seattle, WA, USA. [12]World Wildlife Fund, Washington, DC, USA. [13]Sanford School of Public Policy, Duke University, Durham, NC, USA. [14]RSPB Centre for Conservation Science, RSPB The Lodge, Sandy, UK. [15]World Resources Institute, Washington, DC, USA. [16]School of Public and International Affairs, Princeton University, Princeton, NJ, USA. [17]Rio Conservation and Sustainability Science Centre, Department of Geography and the Environment, Pontifícia Universidade Católica, Rio de Janeiro, Brazil. [18]Sustainability Research Institute, School of Earth and Environment, University of Leeds, Leeds, UK. Email: apb12@cam.ac.uk

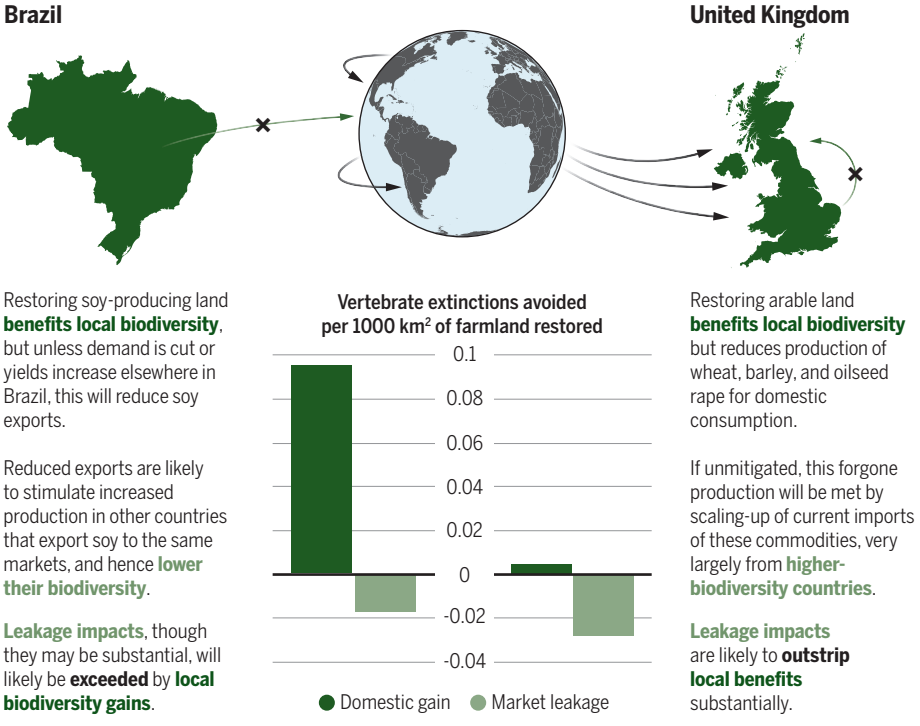
changes caused by reduced production (*2*, *8*). The resulting estimates of the magnitude of leakage are inevitably uncertain (*2*) but potentially major (*3*). Nevertheless, using available data on production, trade, and species' distributions, it is possible to make some inferences about the range of likely biodiversity impacts of market leakage arising from conservation projects in different regions (see the figure).

Consider two hypothetical but plausible restoration programs in agricultural landscapes, assessed using real-world data and preliminary, simplified analyses. In one (see the figure, left), restoring natural habitats on soy-producing land in a high-biodiversity region causes market leakage, but mostly to less biodiverse countries. In this case, local biodiversity gains probably exceed losses elsewhere: The intervention is less beneficial than it might first seem but still generates net conservation gains. In marked contrast, in a second example (see the figure, right), restoration of currently productive arable farmland in a wealthy but low-biodiversity country boosts local biodiversity but raises food imports from higher-biodiversity countries. In this case, local gains would be exceeded by overseas losses, so that in net terms, the intervention harms global biodiversity.

Several conclusions about leakage from area-based conservation or restoration thus appear valid. First, despite the difficulties in robust assessment of displaced production from such efforts, off-site biodiversity damage from leakage may be considerable. Second, real-world efforts to mitigate leakage or even acknowledge its importance in conservation are limited. This raises concerns that reported benefits of conservation actions will be overestimated—potentially weakening future political support for efforts to greatly increase the extent of area-based conservation and undermining the emerging market for biodiversity credits (*12*). Third, as illustrated by our restoration examples, we should be especially concerned about leakage from output-reducing conservation interventions in biodiversity-poor but wealthy parts of the world (such as Northwestern Europe), which can readily replace forgone production through imports. The resulting rises in imports can stimulate increased production in higher-biodiversity regions (*4*, *10*), causing damage there that may exceed domestic conservation gains. And finally, it seems likely that problems of leakage and its quantification will increase—as conservation and restoration efforts grow, as the footprint of food and fiber production expands, and as markets become increasingly interconnected.

Regional variation in biodiversity impacts net of leakage

Worked examples of market leakage from two hypothetical programs restoring 1000 km^2 of farmland to natural habitat. See supplementary materials for details of methods, assumptions, and results.



GRAPHIC: N. CARY/*SCIENCE* AND M. HERSHER/*SCIENCE*

FIXING THE LEAK

There is no single solution for tackling leakage from conservation interventions, but we summarize five possible approaches (see supplementary materials for more details).

Recognize and report forgone production and potential for leakage as rigorously as possible

Tracking changes in food or wood production in intervention areas is in principle relatively straightforward and should be integrated into routine program monitoring. Projects that report near-zero losses in production should be examined further to distinguish those with effective leakage mitigation from those with little or no conservation impact. National or international conservation policies or targets affecting land use should include explicit consideration of local and longer-range leakage. But environmental accounting rules that ignore production impacts incurred beyond country or regional boundaries, as well as poor-quality agricultural, timber, and trade data and the challenges of assessing consumer and producer dynamics, all mean that translating forgone production into leakage impacts will continue to be problematic (*2*). Data improvements and a shift to include jurisdictional assessment of interventions will help. However, we suggest that precise estimates of leakage should be treated with caution, and that most focus should instead be on its mitigation.

Reduce demand for high-leakage goods and improve efficiencies in line with decreases in production

If demand is cut as output falls, leakage is less likely. Actions that reduce waste or improve the efficiency of resource use may be particularly promising. For instance, an intervention coupling restrictions in unsustainable fuelwood harvesting with provision of more fuel-efficient stoves might prevent wood collection shifting elsewhere. More ambitiously, lowering demand for meat by encouraging uptake of lower-footprint alternatives may be possible in some contexts (*10*). But demand-side interventions raise several concerns, including the risks of reducing incomes and access to essential goods, and the possibility that any savings achieved through efficiency gains may stimulate increased purchases of other products with their own biodiversity impacts. There is also the question of who is best placed to tackle demand. Some actions—working to reduce farm-level food losses in an inter-

vention area, for instance—might plausibly be delivered by conservation projects. But others, such as infrastructure improvements to cut retail food waste, or shifting high-footprint diets, will require much larger scale programs and necessitate partnerships with other sectors, such as food and farming, forestry, transport, and health.

Target conservation actions to places where conserving or restoring substantial biodiversity will cause limited displacement of production

One possibility here is the restoration of currently degraded areas that produce little food or wood but require help to restore their biodiversity value. An example could be tropical forests that are repeatedly cut in part to maintain land tenure, but never farmed (*13*) (so-called "Peter Pan" forests because, like the fictional character, they never grow up). Another could be the restoration of mangroves that were cleared to establish now-abandoned aquaculture operations. A second, broader option for limiting leakage is to focus interventions in areas (as in the figure, left) that are much higher in potential biodiversity value or where yields (production per unit area) are substantially lower than in areas to which forgone production is likely to be displaced. However, a general limitation to all these approaches is that conservation is most often needed in biodiverse landscapes with considerable current or future potential for producing food or wood: These are the areas where nature is at greatest risk.

Increase yields within or near project areas

If the yields of products can be sustainably increased nearby, land can be conserved or restored with little or no reduction in overall production, local food security, or livelihoods. The Gola Rainforest Project in Sierra Leone, for example, slows deforestation while limiting activity-shifting leakage by providing wide-ranging agronomic support to local farmers to boost cocoa and staple crop yields (*14*). In Spiti Valley, India, villagers received training and financial incentives for herding practices that reduce losses to snow leopards (and so boost yields) in exchange for setting aside land for wild ungulates. Given the marked yield gaps commonly observed in production systems in the tropics (*15*), there would appear to be widespread scope for locally targeted support for sustainable yield increases to be integrated into conservation projects, through actions ranging from provision of improved seeds and fertilizer to better access to credit and insurance. Even in intensively farmed regions such as Europe, innovative practices and technologies can increase yields sustainably (*10*). Safeguards are needed to limit the risk of rebound effects, whereby yield increases lower prices or raise profits and so stimulate increased production. Moreover, increasing yields sustainably and over the long run can be challenging and often requires several simultaneous interventions, which conservation-focused agencies or nongovernmental organizations may not have the capacity to deliver; again, other partners—in farming, forestry, and development—may be needed.

Direct displaced production to lower-impact areas beyond intervention sites

If increasing yields in or near a project area is not practical or cost-effective, large-scale programs or policies could encourage conservation organizations—or, more likely, agriculture or forestry specialists they might partner with—to replace forgone production by narrowing yield gaps in other places that supply the same markets but are less important for biodiversity. A new generation of restoration approaches is seeking to make this possible. Another option might be to allow limited habitat conversion in areas with high yield potential but low value for biodiversity. In either case, the environmental impacts and possible rebound effects of intentionally displaced production need to be tracked and deducted from estimates of intervention performance. It will also be important to assess and mitigate any negative socioeconomic effects of shifts in the location where goods are produced. However, deliberate displacement of production to known areas makes tracking and addressing such impacts more feasible than under unconstrained market leakage.

PROGRESS BY PREVENTION

Leakage can undo the hard work of otherwise successful conservation actions. We believe it demands far greater attention from a sector that seeks to shape how 30% of an ever-hungrier and more connected planet is managed. Several technological and research developments already underway—high-resolution data on farm and forestry yields, trade flows, and the distribution and sensitivity of biodiversity, and better methods for estimating displaced production—will help improve quantification of leakage. But much greater efforts are also needed to prevent leakage in the first place—by making measures such as demand reduction and sustainable compensatory yield increases (on or away from conservation sites) integral to biodiversity interventions in production landscapes, and by being cautious about expanding conservation efforts in high-yielding areas of lower-biodiversity regions of the world that can readily import replacement commodities.

For locally successful actions to be globally beneficial, conservation must recognize and address its unintended but increasingly wide-reaching impacts on production of the food, timber, and other goods that people need. Where the conservation sector focuses on site-level outcomes and ignores activity-shifting and especially market leakage, demands for forgone production will in many cases simply be met elsewhere, in some instances at net cost to biodiversity as a whole. Of course, tackling leakage effectively necessitates change not just within conservation but among commodity producers and traders too, which in turn requires regulatory support from governments so that businesses are operating on a level playing field. Fortunately, many of these actors share in the ambition of halting global biodiversity loss. Taking coordinated action to limit leakage is essential if this common goal is to be achieved. ■

REFERENCES AND NOTES

1. R. M. Ewers, A. S. L. Rodrigues, *Trends Ecol. Evol.* **23**, 113 (2008).
2. B. Filewod, G. McCarney, *One Earth* **6**, 790 (2023).
3. D. N. Wear, B. C. Murray, *J. Environ. Econ. Manage.* **47**, 307 (2004).
4. Y. Zhang, S. Chen, *For. Policy Econ.* **122**, 102339 (2021).
5. H. Zhong *et al.*, *Nat. Sustain.* **7**, 1501 (2024).
6. W. Pan, M.-K. Kim, Z. Ning, H. Yang, *For. Policy Econ.* **115**, 102161 (2020).
7. S. S. Atmadja *et al.*, *Environ. Res. Lett.* **17**, 044038 (2022).
8. B. K. Haya *et al.*, "Quality assessment of REDD+ carbon credit projects" (Berkeley Carbon Trading Project, 2023); https://gspp.berkeley.edu/assets/uploads/page/Quality-Assessment-of-REDD+-Carbon-Crediting.pdf.
9. M. Lam, T. Swinfield, J. Lyons-White, A. Balmford, Conservation practitioners' perceptions of leakage, Zenodo (2025); https://doi.org/10.5281/zenodo.14780198.
10. R. Fuchs, C. Brown, M. Rounsevell, *Nature* **586**, 671 (2020).
11. M. Pfeifer *et al.*, *PLOS ONE* **7**, e39337 (2012).
12. T. Swinfield, S. Shrikanth, J. W. Bull, A. Madhavapeddy, S. O. S. E. zu Ermgassen, *Nat. Sustain.* **7**, 1217 (2024).
13. P. H. S. Brancalion *et al.*, *Nat. Ecol. Evol.* **8**, 179 (2024).
14. M. Malan *et al.*, *Nat. Sustain.* **7**, 120 (2024).
15. B. B. N. Strassburg *et al.*, *Glob. Environ. Change* **28**, 84 (2014).

ACKNOWLEDGMENTS

The authors thank the Biotechnology and Biological Sciences Research Council, the Gund Institute for the Environment of the University of Vermont, the Tezos Foundation, and Tarides for support. B.Filewood has provided paid consulting services to a company interested in providing tools to improve leakage quantification. T.S. has been a consultant to the World Wildlife Fund on nature-based credits. B.B.N.S. is the founder of re.green, a company dedicated to restoring native ecosystems, and has an equity stock.

SUPPLEMENTARY MATERIALS

science.org/doi/10.1126/science.adv8264

10.1126/science.adv8264



BOOKS *et al.*

Diana Morant speaks at Spain's Science, Technology and Innovation Policy Council in 2023.

PHOTO: EUROPA PRESS NEWS VIA GETTY IMAGES

SCIENCE AND SOCIETY

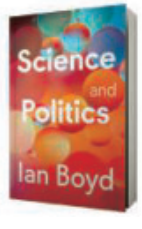
Notes from the "politics factory"

A former government science adviser dissects the complex meshing of science and policy

By **H. Charles J. Godfray**

The British government includes around 25 departments, each of which has a chief scientific adviser (CSA). In most cases, these are not career civil servants but rather academics and other scientists seconded for 3 to 5 years. Their job is to give dispassionate advice on all things scientific. Not being part of the permanent civil service gives them more freedom to speak truth to power but also means that they are outsiders, at least initially unversed in the culture and practices of government decision-making.

No one I know who has taken on such a role has come out completely unscathed, but few have exposed their yet-to-heal wounds in such a public way as does Ian Boyd in his engaging new book, *Science and Politics*. Boyd served as CSA in the UK's Department for Environment, Food and Rural Affairs (Defra) from 2012 to 2019, a ministry that deals with more than its fair share of science-related political hot potatoes, from culling badgers (beloved British nature icons but reservoirs of bovine tuberculosis), to insecticides that harm pollinators, to restrictions on urban driving to reduce air pollution. If that is not enough, his department was responsible for clearing up after a state-terrorism nerve-agent incident.



Science and Politics
Ian Boyd
Polity, 2025. 304 pp.

Successful CSAs simultaneously maintain a distance from the policy mill and know how to inject scientific arguments where they have the most effect. Boyd had a reputation as someone who pulled off this difficult balancing act. (Full disclosure: I chaired Defra's external Science Advisory Council for most of Boyd's tenure as CSA.)

Science and Politics explores the pathologies of integrating science into policy-making, provides valuable advice on how best to do so, and makes suggestions about how the "troubled marriage" of science and politics might be fixed. Boyd talks of the frustration of having to deal with politicians looking for evidence to support a prior view and of interest groups cherry-picking data to advance a particular position. He despairs that the constraints imposed by nature and the environment are so often ignored in setting long-term goals. A particular gripe is the tick-box and performative way in which evidence can appear to be collected and acted on without it genuinely informing policy.

Anyone taking up a science advisory position will greatly benefit from reading this book. It will lessen the culture shock of being thrust into what Boyd calls the "politics factory" and the challenges to scientific objectivity. He talks about the skill of interjecting science at the appropriate juncture in policy formation, in a way that can be assimilated by nonspecialists. Science is only one input into policy-making, and he describes his efforts to keep it center stage and the importance of being in "the room where it happens."

How might the dysfunction be reduced? Boyd argues that scientists are poor at developing compelling narratives that can forge coalitions to bring about change. (Economists are increasingly making the same point about their subject.) Science advisers need to acknowledge the complexity of policy issues, the limitations of interventions, and the frequency of unexpected outcomes. They should be more willing to manage issues adaptively (facilitated by artificial intelligence) and open about the need for course corrections.

Boyd wants more attention paid to the science that may set boundary conditions to policy and less emphasis on science as a driver of growth, although I would argue that it is more "and" than "or." He also calls for a body to regulate science advice to governments and to accredit those who proffer advice. I am less convinced by this suggestion, which I suspect will have its own unintended consequences, but agree with his call for more transparency in policy advice and for policy-makers to explain why advice is not followed. Finally, he, like many others, laments the lack of people with science backgrounds among politicians and in the senior echelons of most civil services.

Boyd does not pull punches in describing those who ignore or distort the science: the words "charlatan" and "hocus-pocus" together appear more than 10 times in the first three pages of the preface. Some may see this as science hauteur and be put off, but the arguments are made with good humor and optimism and with frequent excursions into his backstory as a marine biologist and his broad readings in the natural and social sciences.

Science and Politics is a book about ideas—there is no score settling and (to this reviewer, a tad disappointingly) not much gossip. This is an important book that should be read by anyone who cares about how government can better integrate the best science into policy. ■

The reviewer is at the Oxford Martin School and the Department of Biology, University of Oxford, Oxford, UK. Email: charles.godfray@oxfordmartin.ox.ac.uk

10.1126/science.adv3163

RESEARCH MISCONDUCT

A scientific field, misled

Fraud undermines Alzheimer's disease research

Doctored: Fraud, Arrogance, and Tragedy in the Quest to Cure Alzheimer's
Charles Piller
Atria/One Signal, 2025.
352 pp.



By **Carl Elliott**

If you are looking for an inspirational story about the triumph of medical science, Charles Piller's *Doctored* is not the book for you. *Doctored* is a dark, cautionary tale of the way frauds, cheats, and hustlers have undermined research into Alzheimer's disease. Along the way, Piller catalogs an array of academic sins worthy of Augustine: greed, arrogance, self-deception, and hypocrisy, not to mention a healthy dose of hubris. That Piller pursues the story with the clear-eyed tenacity of a private detective does little to lighten the mood. It is an impressively demoralizing achievement.

Piller, an investigative journalist for *Science*, stumbled onto the fraud in December 2021. A credible source claimed to have inside information on a simmering controversy at Cassava Sciences, the maker of the experimental Alzheimer's drug simufilam. Working with a group of data sleuths, Piller would go on to report a web of possible research misconduct, implicating Lindsay Burns of Cassava Sciences, Hoau-Yan Wang of the City University of New York, Steven Arnold of Harvard University, Eliezer Masliah of the National Institute on Aging, and Berislav Zlokovic of the University of Southern California, among others.

Chief among those others is Sylvain Lesné, an Alzheimer's researcher at the University of Minnesota. Data sleuths flagged more than 70 suspect images in at least 20 of Lesné's papers, including a highly influential 2006 paper in *Nature*. The 2006 paper was fundamental to the hypothesis that Aβ*56, an oligomer of the amyloid beta protein, causes memory impairment in Alzheimer's. What made these findings doubly shocking was that some of Lesné's work had come from the lab of Karen Ashe, one of the most acclaimed neuroscientists in the field.

If there is a heroic figure in *Doctored*, it is Matthew Schrag, a junior professor at Vanderbilt University. Schrag was drawn into the Cassava Sciences story in 2021 when he was introduced to neuroscientist investors who believed that some simufilam research might be fraudulent. They wanted Schrag to investigate. "You think I'm stupid enough to do that?" Schrag responded, knowing that his career could be destroyed in the process. Yet simufilam was already being tested on human subjects. The possibility that they might be harmed persuaded him to cooperate. What Schrag discovered was enough to convince him that research misconduct is far more pervasive than he had ever suspected.

Piller portrays Schrag as an exceptionally honorable figure: morally committed, careful in his conclusions, and reluctant to accuse yet deeply devoted to the truth. One of the most painful episodes in the book comes when Schrag feels compelled to confront a mentor and close friend after discovering evidence of misconduct in his papers.



Perhaps the most striking element of the story Piller tells is the pervasive atmosphere of fear. Virtually everyone Piller tries to speak to is terrified—of blowing the whistle on misconduct, of speaking to a reporter on the record, of being fired, sued, blackballed, or financially destroyed. Even researchers who have behaved honorably are terrified of being wrongly accused or vilified for honest mistakes.

Almost as striking is how differently the researchers react when presented with evidence that images in papers they authored may have been doctored. Although a few own up to their mistakes, most seem far more concerned with protecting their reputations. They hide behind attorneys and refuse to answer questions.

Yet it would be misleading to lay all the blame on individual researchers. They work in a system that gives them powerful incentives to cheat and little risk of being punished. Scientific journals resist retracting flawed papers. Understaffed oversight bodies operate at a glacial pace. High-profile researchers add their names to papers they have not properly examined and join the boards of questionable companies. Perhaps most damaging of all is the behavior of research institutions, many of which do their best to cover up misconduct and protect the researchers responsible.

In June 2024, *Nature* retracted the 2006 paper by Lesné and Ashe. The University of Minnesota claims it investigated Lesné and cleared him of misconduct for that article, but it has said nothing about the other 19 suspicious papers. The timing of the retraction was noteworthy, coming only a week after *Nature* retracted yet another influential article from the same institution, a 2002 paper on adult stem cells from the lab of Catherine Verfaillie. Today, according to Retraction Watch, the University of Minnesota holds the dubious distinction of producing two of the five most highly cited scientific papers ever to be retracted. That distinction caps an extraordinary string of research scandals that have plagued the institution at regular intervals since the early 1990s: conflicts of interest, financial crimes, and, most disturbing of all, abuses of human subjects (*1*). All of which raises an uncomfortable question that lies at the heart of *Doctored*: Why do some institutions become incubators for fraud and abuse while others manage to stay clean? ■

The reviewer is at the Department of Philosophy, University of Minnesota, Minneapolis, MN, USA. Email: ellio023@umn.edu

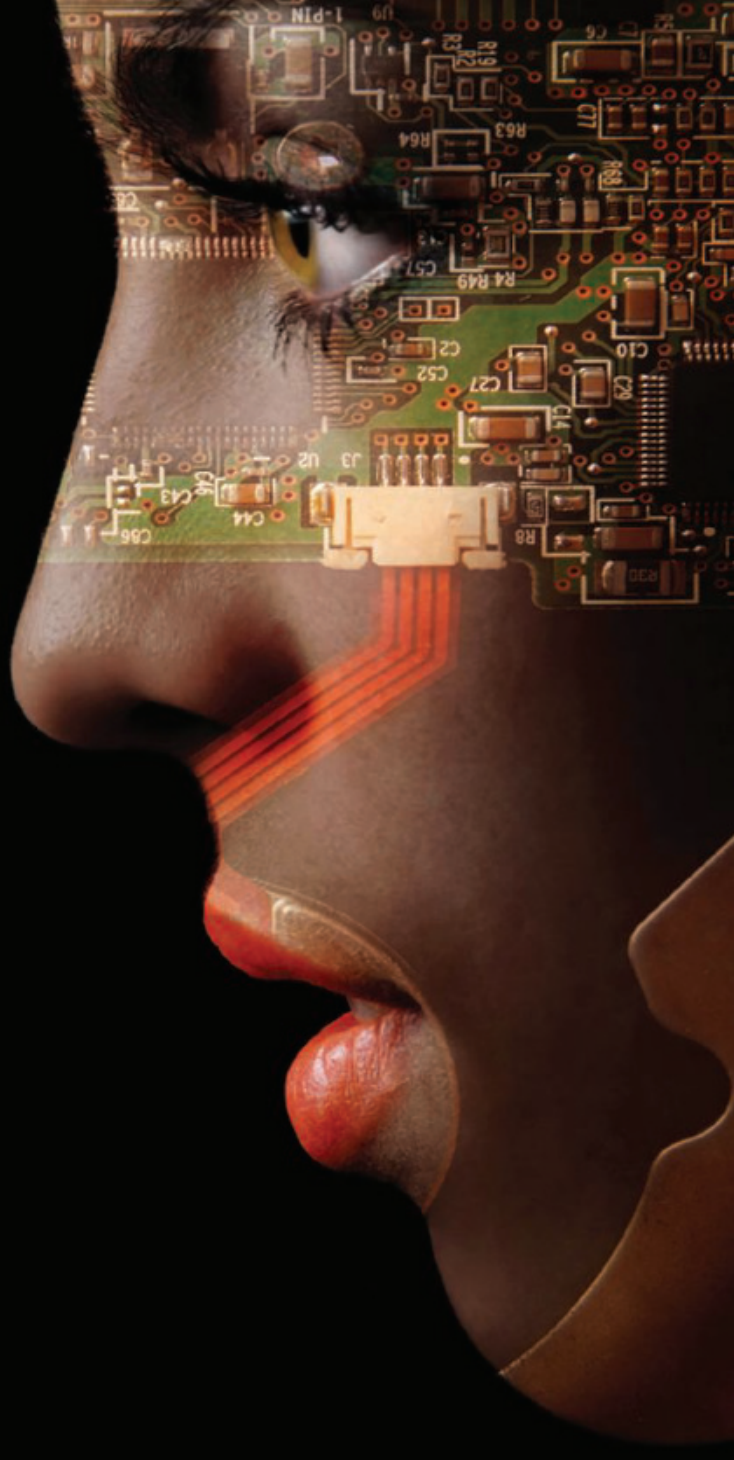
REFERENCES AND NOTES

1. C. Elliott, *The Occasional Human Sacrifice: Medical Experimentation and the Price of Saying No* (Norton, 2024).

10.1126/science.adv3711

ILLUSTRATION: NUTHAWUT SOMSUK/ISTOCK PHOTO

Share **Your Robotics Research** with the **World**.



Shaping the future of robotics with high impact research!

As a multidisciplinary online-only journal, *Science Robotics* publishes original, peer-reviewed, research articles that advance the field of robotics. The journal provides a central forum for communication of new ideas, general principles, and original developments in research and applications of robotics for all environments.

Submit your research today. Learn more at: **science.org/journal/scirobotics**

Twitter: @SciRobotics
Facebook: @ScienceRobotics

Science Robotics
AAAS



Jordan has implemented a range of policies regulating the import of Chinese vehicles, such as these cars staged for loading in Jiangsu Province.

Edited by **Jennifer Sills**

Jordan's electric vehicle growth drives trade-offs

Jordan is a regional leader in electric vehicle (EV) adoption, with EVs accounting for 45% of vehicle sales in 2023 (*1*). By August 2024, more than 120,000 EVs were registered on Jordanian roads (*2*), a remarkable increase from just 900 in 2016 (*3*). Reduced import tariffs, rising fuel prices, and the growing availability of affordable Chinese-manufactured EV models have driven this surge (*4*). Jordan's transition to EVs is a crucial component of its climate strategy, which includes reducing greenhouse gas emissions by 30% by 2030, as outlined in its Nationally Determined Contributions (*5*). However, the rapid shift to EVs has led to a substantial reduction in fuel tax revenues, a critical source of public funding. Jordan must find a way to balance economic and environmental sustainability as it makes this transition.

In 2024, Jordan introduced several regulatory changes in an attempt to decrease the uptake of EVs and increase taxes on their use. The government banned the import of Chinese-standard EVs in June (*6*) but amended the decision 2 months later to allow used Chinese EV imports (*7*). In July, the government introduced a time-based electricity tariff for EV charging (*8*). In September, increased taxes on EV purchases went into effect, with rates reaching up to 50% (*9*).

Jordan's efforts to recover lost fuel tax revenue have slowed the rate of EV adoption, particularly among middle-income households (*10*). In response, Jordan's new cabinet introduced a 50% reduction in taxes on EVs in November 2024 (*11*) and then approved a graduated tax mechanism in December. The revised tax structure focuses on higher-value EVs, rightly prioritizing the affordability of lower-cost models (*12*).

To ensure that Jordan meets both its fiscal needs and its climate targets, the government should maintain consistent policies on EVs and consider alternative revenue streams. In addition to taxes on luxury vehicles, distance-based taxes, in which EV owners are charged per kilometer driven, and expanded electricity tariffs during peak charging hours could increase revenue without reducing EV purchases. Public-private partnerships to build more charging infrastructure could further support the long-term growth of the EV market, ensuring both economic and environmental sustainability.

Hussam J. Khasawneh[1,2]* and Hussam Hussein[3]
[1]Department of Electrical Engineering, Al Hussein Technical University, Amman, Jordan.
[2]Department of Mechatronics Engineering, The University of Jordan, Amman, Jordan.
[3]Department of Politics and International Relations, University of Oxford, Oxford, UK.
*Corresponding author. Email: hussam.khasawneh@htu.edu.jo

REFERENCES AND NOTES

1. "Global EV outlook 2024: Moving towards increased affordability" (International Energy Agency, 2024); https://www.iea.org/reports/global-ev-outlook-2024.
2. "From vision to reality: Jordan's EV surge and the road to sustainability" (EcoMENA, 2024).
3. "Electric vehicles take charge in Jordan's market, up by 35%," *Jordan News*, 11 March 2024.
4. "Jordan EV profile: Segment to grow on reduced import taxes and arrival of new affordable models" (Fitch Solutions, 2023).
5. Jordan Ministry of Environment, "The Kingdom's target to reduce greenhouse gas emissions by 31 per cent by the year 2030 requires an estimated JD7.5 billion in investments, according to Secretary-General of the Ministry of Environment, Mohammed Khashashneh" (Government of Jordan, 2024).
6. "Amman, Jordan Chambers of Commerce oppose new tax on electric vehicles," *Roya News*, 15 September 2024.
7. "What are the conditions for electric vehicles to enter Jordan? Explanation," *Country News* (2024); https://www.assawsana.com/article/639979 [in Arabic].
8. "Time-based electricity tariff to go into effect Monday—EMRC," *Jordan Times*, 2 July 2024.
9. Jordan News Agency Petra, "Cabinet implements measures to promote EV adoption in Jordan," *Petra News*, 12 September 2024; https://www.petra.gov.jo/Include/InnerPage.jsp?ID=63404&lang=en&name=en_news.
10. "Quick view: Jordan's EV adoption to face more challenges after special tax changes" (Fitch Solutions, 2024).
11. "Government lowers tax on e-vehicles by half until end of year," *Jordan Times*, 23 November 2024).
12. Jordan News Agency Petra, "Cabinet approves new graduated special tax mechanism for electric vehicles," *Petra News*, 31 December 2024.

10.1126/science.adu1313

India's grasslands are not "wastelands"

For decades, India's open biomes, including old-growth grasslands and savannas, have been misclassified (*1*, *2*). The British colonial government converted large tracts of open habitats into plantations to maximize the benefits of silviculture (*3*). The widespread land-use changes reduced the size and quality of grassland and savanna habitats (*4*), led to a loss of biodiversity, and deprived marginalized communities of their rights and livelihoods (*3*). The colonial government classified savannahs and grasslands that were unsuitable for plantations as "wastelands" (*1*), and the term has persisted (*1*). To promote environmentally responsible land-use decisions, India must acknowledge the biodiversity and cultural value of

PHOTO: JI HAIXIN/VCG VIA GETTY IMAGES

grasslands and savannas, starting by classifying them as ecologically distinct biomes (*2*) rather than wastelands.

Outdated terms such as "wasteland" not only undermine the ecological value of open biomes but also affect policy by providing a justification to convert the land. India has made international and national commitments to combat climate change by increasing green cover to 33% of the country's total land area (*1*). However, lands that are categorized and thus perceived as wastelands are often the first sites designated for afforestation initiatives (*2*, *3*, *5*). Converting open ecosystems, rather than restoring degraded forests, undermines ecosystem services, including habitats for endemic species such as the Bengal florican and swamp grass babbler (*1*, *6*).

The systemic misclassification of open habitats has also impeded scientific research (*7*). India's biodiversity is already understudied (*8*), and research is focused primarily on biodiverse forests (*7*, *9*). As a result, the ecosystems and biodiversity in grasslands and savannas are not well understood (*9*, *10*). The lack of such knowledge widens the conservation gap between forested and open biomes and could lead to the implementation of conservation measures that are unsuitable for open biome diversity. Given that in recent decades grassland fauna has declined more markedly than that of other biomes (*11*), conservation missteps could have severe ramifications.

To protect the distinct ecosystems and biodiversity in open habitats, India must remove the misleading use of "wasteland" from government parlance and invest in baseline biodiversity studies in open biomes. Researchers should aim to understand the origin and maintenance of open biome diversity and to create a thorough map of old-growth grasslands and savannas (*12*). These data can inform India's decisions as the government prioritizes areas for grassland conservation and restoration.

Sutirtha Lahiri[1,2]* and Sushma Reddy[1,3]
[1]Department of Fisheries, Wildlife, and Conservation Biology, University of Minnesota, St. Paul, MN, USA. [2]Interdisciplinary Center for the study of Global Change, University of Minnesota Twin Cities, St. Paul, MN, USA. [3]Bell Museum of Natural History, University of Minnesota, St. Paul, MN, USA.
*Corresponding author. Email: lahir022@umn.edu

REFERENCES AND NOTES

1. S. Lahiri, A. Roy, F. Fleischman, *Restor. Ecol.* **31**, e13858 (2023).
2. M. D. Madhusudan, A. T. Vanak, *J. Biogeogr.* **50**, 1377 (2022).
3. A. A. Joshi, M. Sankaran, J. Ratnam, *Biol. Conserv.* **224**, 144 (2018).
4. M. Arasumani *et al.*, *PLOS ONE* **13**, e0190003 (2018).
5. J. W. Veldman *et al.*, *Science* **366**, eaay7976 (2019).
6. A. T. Vanak *et al.*, *Managing Open Natural Ecosystems for People, Climate and Biodiversity* (Centre for Policy Design, Ashoka Trust for Research in Ecology and the Environment, 2024).
7. F. A. O. Silveira *et al.*, *J. Appl. Ecol.* **59**, 1967 (2022).
8. S. Reddy, *Mol. Phylogenet. Evol.* **77**, 159 (2014).
9. N. Stevens, W. Bond, A. Feurdean, C. E. R. Lehmann, *Annu. Rev. Environ. Resour.* **47**, 261 (2022).
10. J. Ratnam, K. W. Tomlinson, D. N. Rasquinha, M. Sankaran, *Phil. Trans. R. Soc. B* **371**, 20150305 (2016).
11. K. V. Rosenberg *et al.*, *Science* **366**, 120 (2019).
12. A. N. Nerlekar, A. Munje, P. Mhaisalkar, A. J. Hiremath, J. W. Veldman, *J. Ecol.* **112**, 98 (2024).

10.1126/science.adu0193

India's ocean exploration undermines climate goals

In July 2024, India began seeking additional deep-sea exploration licenses from the International Seabed Authority for the purpose of mining metals such as nickel, manganese, and copper from the Clarion-Clipperton Zone in the Pacific Ocean (*1*). These metals are central to the development of a green-energy economy (*2*). However, deep-sea mining disrupts marine ecosystems and could reduce marine carbon sequestration. India should not expand its mining activities until its effects on deep-sea biodiversity, and deep-sea species' effects on carbon sequestration, are better understood.

Deep-sea mining harms marine life by polluting the water with suspended sediments and heavy metal discharge such as mercury and by making noise that disrupts foraging and organismal survival (*3*–*5*). Such individual-level effects translate to broader ecosystem-level changes. Although less is known about mining's effects on species in the deep ocean, it may disrupt the daily migration of zooplankton between the ocean's surface (epipelagic zone) and the deeper layers (the twilight zone) (*6*). Zooplankton facilitate the flow of energy and matter, including carbon, from the epipelagic layer to the abyssal seabed (*7*, *8*), contributing to a substantial carbon capture mechanism (*9*, *10*).

India already has two licenses for mining in the Indian Ocean (*11*). Before expanding these activities, India should invest in research to understand the interplay between mining, deep-sea marine ecosystems, and carbon sequestration. Communicating accessible information about the ocean's carbon capture cycle to the public could also bolster awareness and attract research interest. If India continues to expand mining according to its current plans, obtaining the metals needed to power green energy could undermine the progress toward carbon mitigation goals that green energy is intended to make possible.

Ayush Mistry
Department of Biochemistry and Molecular Biology, Saint Louis University School of Medicine, St. Louis, MO, USA. Email: ayush.mistry@slu.edu

REFERENCES AND NOTES

1. N. Arora, M. Bhardwaj, *Reuters*, 22 July 2024; https://www.reuters.com/world/india/india-seek-licences-scout-pacific-ocean-critical-minerals-2024-07-22.
2. J. R. Hein, A. Koschinsky, T. Kuhn, *Nat. Rev. Earth Environ.* **1**, 158 (2020).
3. K. R. Conley, F. Lombard, K. R. Sutherland, *Proc. R. Soc. B* **285**, 20180056 (2018).
4. B. Christiansen, A. Denda, S. Christiansen, *Marine Pol.* **114**, 103442 (2020).
5. S. Fuchida *et al.*, *Geochem. Trans.* **19**, 15 (2018).
6. Ocean Twilight Zone, "Migration in the Ocean Twilight Zone" (Woods Hole Oceanographic Institution); https://twilightzone.whoi.edu/explore-the-otz/migration.
7. D. Bianchi, E. D. Galbraith, D. A. Carozza, K. a. S. Mislan, C. A. Stock, *Nat. Geosci.* **6**, 545 (2013).
8. P. C. Davison, D. M. Checkley, J. A. Koslow, J. Barlow, *Prog. Oceanogr.* **116**, 14 (2013).
9. M. R. Stukel *et al.*, *Nat. Commun.* **14**, 2024 (2023).
10. A. J. R. Smith, *Science* **387**, eadq5564 (2025).
11. International Seabed Authority, Exploration contracts (2022); https://www.isa.org.jm/exploration-contracts.

10.1126/science.adt6347



PHOTO: SUTIRTHA LAHIRI

Reclassifying India's grasslands as valuable areas instead of "wastelands" would help protect ecosystems in the Himalayan foothills, where tree species such as *Bombax ceiba* are overtaking native habitats.

RESEARCH

IN *SCIENCE* JOURNALS

Edited by **Michael Funk**



HYDROLOGY

Now you see it, now you don't

Ephemeral streams flow only sporadically and are dry the rest of the time. How much does their coming and going affect overall stream network length? Prancevic *et al.* used a semimechanistic model combined with stream gauge measurements and topographical data to estimate the variability of stream network length across the entire contiguous United States. This approach allowed them to conclude that the median US stream network is six times longer during annual high-flow conditions than during annual low-flow conditions. —Jesse Smith

Science p. 782, 10.1126/science.ado2860

Ephemeral streams, such as Salt Creek in Death Valley National Park, pictured here, contribute greatly to stream network length.

CANCER

Predictive histone gene hypertranscription

Cancer often exhibits genome-wide hypertranscription, but the mechanisms driving this phenomenon remain unclear. To understand how increased transcription might contribute to cancer progression, Henikoff *et al*. investigated RNA polymerase II (RNAPII) activity across different tumor types. Mapping RNAPII activity across the whole genome in tumor and normal tissues, the authors found widespread transcriptional changes. They also discovered that RNAPII occupancy at histone genes correlated with tumor aggressiveness, particularly in meningiomas and breast cancers. Elevated RNAPII at histone genes predicted rapid cancer recurrence and corresponded to chromosome losses, suggesting that histone gene hypertranscription may drive overproliferation and genomic instability in cancer. —Di Jiang

Science p. 737, 10.1126/science.ads2169

CATALYSIS

Reforming hydrogen reforming

A thermal catalytic process converts ethanol and water into hydrogen and acetic acid at low temperatures with near-zero carbon dioxide production, unlike the conventional methane-reforming process used to make hydrogen. Peng *et al*. developed a catalyst with a high density of atomically dispersed platinum and iridium species on reactive α-molybdenum carbide that facilitates reforming at the metal-support interfaces. The absence of larger metal nanoparticle surfaces avoids unwanted carbon–carbon bond cleavage. —Phil Szuromi

Science p. 769, 10.1126/science.adt0682

MARINE CONSERVATION

Marine canaries

Most of the ocean fish biomass exists in the "twilight zone," an important region of the open ocean that is notoriously difficult to sample and monitor. Beltran *et al*. tested whether an important predator in this ecosystem, the northern elephant seal, could be used as an indicator of fish abundance, and thus ecosystem health, in this zone. Using foraging patterns and success linked to ocean conditions, the authors were able to successfully hindcast twilight zone fish abundance. Such hindcasting success facilitated future predictions. Elephant seals can thus provide insight into how this hidden but essential system responds to external changes. —Sacha Vignieri

Science p. 764, 10.1126/science.adp2244

CATALYSIS

Purifying ethylene by combustion

Trace acetylene can be removed from ethylene feedstocks by selective combustion of acetylene. Jacob *et al*. found that the lattice oxygen of bismuth oxide can combust acetylene with more than 99% selectivity for gas streams containing equimolar or dilute amounts acetylene in ethylene. Lattice oxygen removed by combustion could be regenerated over many cycles by reaction with molecular oxygen. This alternative purification route to semihydrogenation of acetylene does not require elevated pressures and

PHOTO: TIM FITZHARRIS/MINDEN PICTURES

is tolerant to carbon dioxide and water impurities. —Phil Szuromi

Science p. 744, 10.1126/science.ads3181

QUANTUM MATERIALS

Electronic correlations and plasmons

Plasmonics offers a route to shrink light wavelengths down to the nanoscale using collective electronic excitations. Intuitively, highly conducting metals are the materials of choice, providing for long plasmon lifetime. Ruta *et al*. looked at the so-called "bad metal" molybdenum oxide dichloride, in which electronic correlations give rise to high resistivity. Surprisingly, they observed plasmons with very long lifetimes. The unexpected finding of long-lifetime plasmons may provide a route to expanding the choice of materials for nanophotonic applications. —Ian S. Osborne

Science p. 786, 10.1126/science.adr5926

MEMBRANES

Uniform pores over large areas

A key challenge in the field of membrane technology for separating water from ions is the formation of uniform nanopores over large areas on robust two-dimensional materials. Shen *et al*. prepared molybdenum disulfide membranes by aligning seeds along the 60-degree grain boundaries (also known as mirror twin boundaries) during the chemical vapor deposition process to form eight-membered ring pores. The physical size of the intrinsic eight-membered rings allows only water molecules to pass through while blocking a wide range of hydrated ions due to their larger size. The performance can be tuned by controlling the density of the eight-membered rings. Optimized membranes demonstrate both ultrahigh water-to-sodium chloride selectivity and exceptional water permeance. —Marc S. Lavine

Science p. 776, 10.1126/science.ado7489

CANCER IMMUNOLOGY

Mapping multiple myeloma ecosystems

Multiple myeloma (MM) is a plasma cell malignancy that develops in the bone marrow but can form "breakout lesions" that expand into the soft tissues surrounding bone as the disease progresses. Using single-cell and spatial multiomics, Lutz *et al.* compared the cellular composition of bone marrow–confined MM and breakout lesions in patients with newly diagnosed MM. Breakout lesions contained a distinct microenvironment characterized by plasma cell–dominated regions infiltrated by macrophages and natural killer cells and focal regions rich in immune cells. T cell clonal expansion was heterogeneous and coincided with tumor genomic diversification, suggesting that MM breakout lesions represent an important site for tumor–immune cell interactions. —Claire Olingy

Sci. Immunol. (2025) 10.1126/sciimmunol.adp6667

CANCER THERAPY

Taking indirect aim at cancer drivers

Many cancers of the head and neck, referred to as head and neck squamous cell carcinomas (HNSCCs), are driven by the undruggable transcription factors c-MYC or mutant p53. Funk *et al*. found that these oncogenes might be targeted indirectly through the kinase LZK. They found that LZK stabilized c-MYC through kinase-dependent activity, whereas LZK stabilized mutant p53 through a kinase-independent interaction. A drug that causes degradation of LZK resulted in destabilization of both proteins, and a catalytic inhibitor of LZK slowed the growth of certain HNSCCs in mice, showing potential for further clinical development. —Leslie K. Ferrarelli

Sci. Signal. (2025) 10.1126/scisignal.ado2857

IN OTHER JOURNALS

Edited by **Corinne Simonti** and **Jesse Smith**



RADIO ASTRONOMY

Outrigger locates a fast radio burst

Fast radio bursts (FRBs) are unpredictable and only last a few milliseconds, so their exact positions are difficult to determine. Some FRBs have been precisely located by staring at a patch of sky with a radio interferometer and waiting for a burst to occur, but these instruments have narrow fields of view. Shah *et al.* identified an FRB using a wide-field radio survey telescope equipped with an outrigger station 66 kilometers away. When the main telescope detected a sufficiently bright burst, it sent a signal to the outrigger, so both detectors saved raw data spanning the FRB. Subsequent interferometric analysis allowed the authors to localize the FRB to the outskirts of an elliptical galaxy. —Keith T. Smith

Astrophys. J. Lett. (2025) 10.3847/2041-8213/ad9ddc

The origin of a series of fast radio bursts, measured by very long baseline interferometry, likely is a distant elliptical galaxy (perhaps one like the elliptical Sombrero Galaxy pictured).

IMAGE: NASA/JPL-CALTECH

PLANT BIOTECHNOLOGY

Prime editing in plants makes progress

Genome editing has transformed plant genetic engineering and is used in many crop species. However, large insertions, deletions, and chromosomal inversions are still challenging to engineer. Zhao *et al.* developed dual prime editing to achieve large chromosome structural changes in wheat, tomato, and *Nicotiana*. The authors used a fused reverse transcriptase and Cas9 nickase with mutations to optimize efficacy in plants. Together with two prime editing guide RNAs, the system could produce genetic substitutions and inversions of more than 200 kb with high precision and efficiency. This work opens up greater capacities for prime editing in plant systems for



CONSERVATION

Protection for the noble pen shell

Human-induced declines in animal populations has made animals more susceptible to natural forms of mortality such as parasites and pathogens. Such has been the case for the second largest bivalve in the world, the noble pen shell, whose already shrinking distribution in the Mediterranean has been decimated by a parasite over the past few decades. No known populations remain in the open sea. Foulquié *et al.* surveyed one of the last residual populations within France's Thau lagoon from 2020 to 2024. They found a relatively healthy and large population, likely due to local conditions limiting parasite spread or even potential resistance. This makes protection of this lagoon of paramount conservation importance. —Sacha Vignieri

Endanger. Species Res. (2024) 10.3354/esr01357

A French lagoon may be the last refuge for the critically endangered noble pen shell (*Pinna nobilis*)

PHOTO: MATHIEU FOULQUIE/BIOSPHOTO/MINDEN PICTURES

research and crop improvement. —Madeleine Seale

Nat. Plants (2025)
10.1038/s41477-024-01898-3

CELL BIOLOGY

Breaking and entering

In the cell, the nuclear pore complex allows the import and export of proteins, nucleic acids, and even viruses between the cytosol and the nucleoplasm. HIV-1 has a cone-shaped capsid that needs to traverse the nuclear envelope and release the viral genome for integration into the host cell genome. Kreysing *et al*. combined high-resolution imaging of human macrophages with molecular simulations to study the nuclear entry of HIV. They found that the capsid enters the central channel of the nuclear pore with its narrow end first. The movement of the capsid strains the ring scaffold of the nuclear pore and ultimately cracks it open, thus physically defeating the guardians of the human genome. —Stella M. Hurtley

Cell (2025)
10.1016/j.cell.2024.12.008

PREGNANCY

Pregnancy brain in the making

During pregnancy, the brain undergoes substantial remodeling. However, longitudinal characterization of these changes is lacking. Servin-Barthet *et al.* analyzed magnetic resonance imaging scans before, during, and after pregnancy in 127 women undergoing their first pregnancy. Gray matter volume decreased rapidly during pregnancy and partially recovered (albeit slowly and only partially) postpartum. Volume changes were correlated with alterations in estrogens and were particularly evident in high-order cognitive networks. At the behavioral level, stronger gray matter volume recovery was associated with reduced hostility toward the newborn. Understanding brain adaptation during pregnancy could be leveraged to promote well-being during the postpartum period. —Mattia Maroso

Nat. Commun. (2025)
10.1038/s41467-025-55830-0

CATALYST DESIGN

New descriptor for catalysis

Recent advances show that understanding correlations between adsorption energies can expedite the discovery of efficient, cost-effective, and heterogeneous catalysts for various industrial chemical processes. Developing comprehensive atomistic models manually, unlike black box machine learning, allows for a more precise integration of inputs based on local structure, directly linking these properties to catalyst performance. Using a coordination-based model initially proposed for platinum, Mandal and Abild-Pedersen observed metal-independent strong linear scaling relations between site-specific metal binding energies (DE_Ms) and adsorption energies of the CH and O groups of hydrocarbon-based adsorbate across different transition metals. The proposed descriptor DE_M can also be implemented for alloy and intermetallic systems and, because of its versatility, it holds potential for further expansion and broader applications. —Yury Suleymanov

JACS Au. (2024)
10.1021/jacsau.4c00759

PHOTOCATALYSIS

Controlling carbon dot chemistry

Carbon nanoparticles (carbon dots) synthesized in water have higher photocatalytic activity for an atom transfer radical addition reaction when they are more graphitic. Morbiato *et al.* performed a microwave synthesis of carbon dots from citric acid and urea at various temperatures. After extensive purification, they showed that the highest-temperature conditions formed carbon dots with more double bonds, fewer side chains, and longer-lived photoexcited states. The most graphitic carbon dots achieved yields of up to 83% for the photoreaction between 1-hexene and carbon tetrabromide. —Phil Szuromi

ACS Nano (2025)
10.1021/acsnano.4c16538

REVIEW SUMMARY

NEUROSCIENCE

Neuroevolution insights into biological neural computation

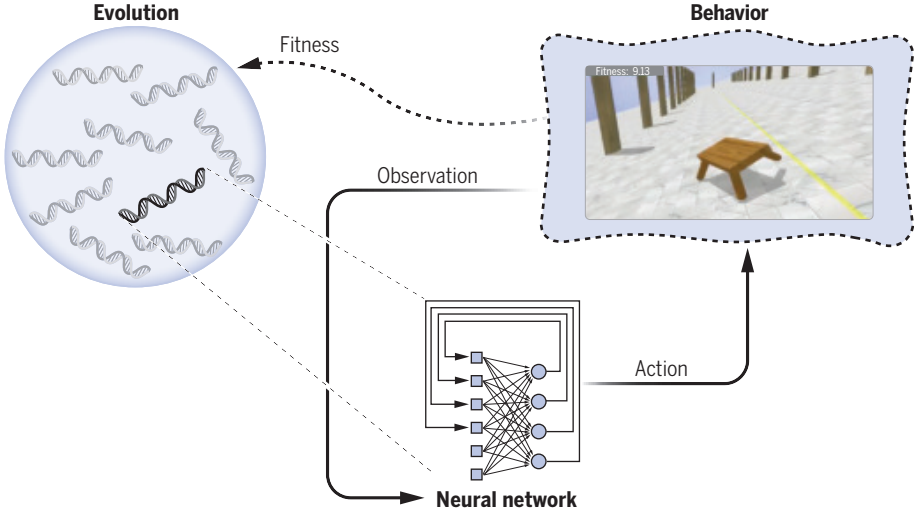
Risto Miikkulainen*

BACKGROUND: Neuroevolution is a computational modeling technique in which an artificial neural network architecture and/or parameters are optimized through evolutionary computation. Much of current work in neural networks and artificial intelligence (AI) in general builds on gradient descent methods, i.e. learning a statistical model of a large training set. However, intelligent behavior in nature is instead learned through search processes based on survival of the fittest in an evolutionary scale and reinforcement during an individual's lifetime. Neuroevolution offers a computational approach for constructing such behavior. Similar to biological evolution, it is a population-based search process. It provides a way to explore a diverse set of alternatives to discover stepping stones and eventually solutions that balance multiple objectives and can be surprising and creative. It can therefore be used to formulate and evaluate hypotheses about the evolutionary origins of neural circuits, not only about what the circuitry does and how it does it, but also why that particular circuitry exists, what the alternatives are, and how the circuits could be repaired.

ADVANCES: This approach has led to biologically relevant advances at four levels. First, it has been possible to demonstrate the possible evolutionary origins of particular neural circuits and elements, such as command neurons, facilitating synapses, neuromodulation, emergence of network motifs, and pattern generators. It is also possible to optimize the design of complex, hand-constructed models, such as those of spiking neural networks. Neuroevolution thus helps to derive and evaluate functional hypotheses for observed neural circuits. Second, neuroevolution can be combined with models of development, including cell chemistry and grammatical rewriting approaches, as well as learning mechanisms. Such approaches can demonstrate how principled neural structures can arise from cellular growth and genetic regulatory processes. They also demonstrate how complexity arises from a synergy of evolution and learning: Evolution provides a starting point and a learning mechanism, and the actual structure is derived from the interaction with the environment. Thus, neuroevolution can help to delineate the role of evolution and development in neuroscience and help us understand their synergy. Third, neuroevolution can be used to identify and understand the constraints that lead to the emergence of a particular neuroscience structure or function. These include resource limitations, wiring length and complexity, coevolution of the physical structure and its control, and competitive and cooperative coevolution with other agents. By varying the physical, environmental, cooperative, and competitive constraints systematically, it may be possible to develop a deeper understanding of what is essential in the observed neural structure and function and what the alternatives are. Fourth, the approach can provide insight into the evolutionary origins of behavior. This includes robust, nonlinear control through recurrent circuitry and trajectory noise, as well as behavioral strategies that consist of accurate orchestration of multiple behaviors. It is possible to identify challenges in constructing cognitive facilities such as memory, learning, and communication and the role that multiple objectives play in discovering them. Neuroevolution simulations can thus be used to understand how intelligent behaviors emerged as a response to survival pressure in a way that other computational techniques, such as supervised learning and reinforcement learning, cannot.

OUTLOOK: Given these advances and modern computational resources, it may now be possible to address large questions such as the origin of language and other major transitions in the development of intelligence. There is enough computing power to set up virtual worlds with different conditions, and it is possible to evolve networks to perform many different tasks at once. The representations for these tasks can be mapped to different areas in the brain. For instance, to what extent do the structures for language depend on structures for other cognitive behaviors? Similar combinations of neuroevolution and neuroscience can then be used to understand other cognitive behaviors as well, and, eventually, such progress should allow us to build more capable artificial agents.

Of course, neuroevolution experiments can only provide computational evidence into neuroscience questions, not actual proof. They can create insight and new ideas, but the results still need to be verified experimentally. In this manner, neuroevolution, like computational modeling in general, can be seen as a way of expanding thinking and creativity in neuroscience. ■



In neuroevolution, a population's neural network encoding is evolved based on how well each network's behavior solves a task. Neuroevolution experiments can provide insight into the evolutionary origins of neural circuits, behavior, and cognitive processes.

The list of author affiliations is available in the full article online.
*Email: risto@cs.utexas.edu
Cite this article as R. Miikkulainen, *Science* 387, eadp7478 (2025). DOI: 10.1126/science.adp7478

READ THE FULL ARTICLE AT
https://doi.org/10.1126/science.adp7478

RESEARCH ARTICLE SUMMARY

BRAIN EVOLUTION

Evolutionary convergence of sensory circuits in the pallium of amniotes

Eneritz Rueda-Alaña, Rodrigo Senovilla-Ganzo, Marco Grillo, Enrique Vázquez, Sergio Marco-Salas, Tatiana Gallego-Flores, Aitor Ordeñana-Manso, Artemis Ftara, Laura Escobar, Alberto Benguría, Ana Quintas, Ana Dopazo, Miriam Rábano, María dM Vivanco, Ana María Aransay, Daniel Garrigos, Ángel Toval, José Luis Ferrán, Mats Nilsson, Juan Manuel Encinas-Pérez, Maurizio De Pittà, Fernando García-Moreno*

INTRODUCTION: For decades, scientists have debated the homologies between the mammalian neocortex and the pallium of other vertebrates. Claims of homology are often based on gene expression patterns in embryonic brains or neuronal connectivity patterns in adult brains. We sought to understand pallial evolution because its homologies provide insights into the evolutionary and developmental pathways of brain structures across species.

RATIONALE: We tackled this debate from alternative perspectives by investigating the developmental formation of pallial circuitry through neurogenic, transcriptional, and mathematical analyses in three selected species: chick, mouse, and gecko. By examining the development of their pallial circuits, we aimed to determine whether similarities in sensory processing circuits are due to conserved homology or convergent evolution.

RESULTS: Our study revealed that neurons that form the three stations of the pallial circuit are generated at different times and in distinct brain regions across species. The avian dorsal ventricular ridge (DVR) circuit develops in a different order than the neocortical circuit, whereas the avian hyperpallial circuit follows previously unknown neurogenic rules that are not seen in either the avian DVR or the mouse neocortex. Geckos exhibit a dual sequence: Their dorsal circuit forms like the mammalian neocortex, whereas their ventral circuit develops like the avian DVR. These findings indicate unexpected diversification in amniote pallial sensory circuit developmental programs.

On the molecular level, single-cell RNA sequencing depicted different evolutionary trends for equivalent cell types, produced in homologous pallial regions and at equivalent neurogenic times. Glutamatergic pallial neurons mature into divergent neuronal types in chick and mouse, whereas γ-aminobutyric acid–releasing (GABAergic) pallial neurons showed strong conservation, underscoring their fundamental role in pallial sensory circuits.

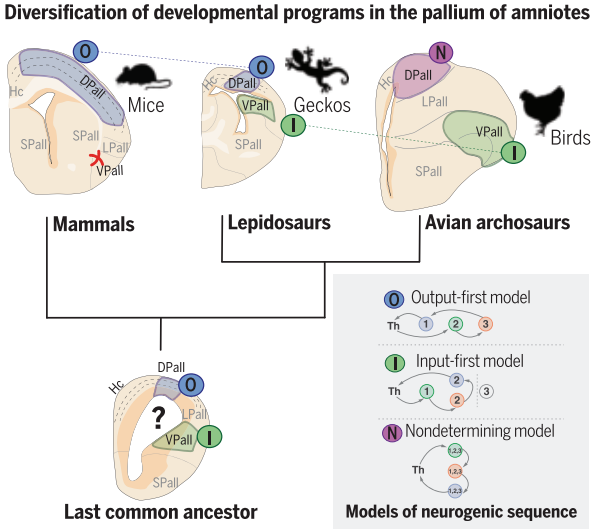
By means of spatially resolved transcriptomic analysis, we inferred the pallial location and transcriptional type of early neurons generated in the pallium of both chick and mouse. This analysis showed greater conservation of GABAergic cells and indicated that the only similarity in the glutamatergic class was mesopallial neurons of the chick brain and deep, lateral mammalian cortical neurons.

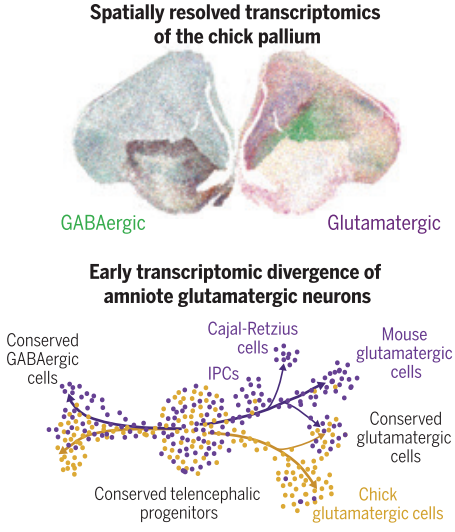
The developmental differences were also notable in progenitors and other cells. Whereas pallial radial glial cells displayed similarities between species, their neurogenic behaviors differed markedly. Additionally, the population of intermediate progenitor cells that expanded neuronal numbers in the mammalian neocortex had no clear homolog in the avian developing pallium. Cajal-Retzius cells were not found in the chick pallium. Furthermore, mathematical modeling suggests that components of sensory circuits in birds and mammals were shaped by similar functional constraints.

CONCLUSION: Our study demonstrates that high-order sensory processing circuits have evolved separately in different vertebrate taxa, converging into a functionally similar circuit. The differences in the developmental rules, progenitor cells, and transcriptomic profiles support a nonhomologous character of the amniote pallial circuits. The strong conservation of GABAergic neurons indicates their crucial role in pallial sensory circuits, whereas the divergent development of glutamatergic neurons suggests a flexible evolution of this neuronal class. Evolution tinkered with pallial circuit development, structure, and function. And likely, convergent evolution sculpted the formation of the components of the sensory circuits in amniote species. ■

The list of author affiliations is available in the full article online.
***Corresponding author. Email: fernando.garcia-moreno@achucarro.org**
Cite this article as E. Rueda-Alaña *et al.*, *Science* 387, eadp3411 (2025). DOI: 10.1126/science.adp3411

READ THE FULL ARTICLE AT
https://doi.org/10.1126/science.adp3411





Evolutionary history of pallial development in amniotes. (Left) Illustrations depicting the varied sequences of neurogenesis found in the pallial circuits of amniotes. (Top right) Spatially resolved transcriptomics allowed us to identify a wide neuronal diversification in the chick pallium. (Bottom right) Single-cell RNA sequencing of early born neurons revealed conservation in the differentiation of GABAergic neurons in amniotes, which contrasted with the diversification of most glutamatergic neurons. DPall, dorsal pallium; Hc, hippocampus; IPCs, intermediate precursor cells; LPall, lateral pallium; SPall, subpallium; Th, thalamus; VPall, ventral pallium.

RESEARCH ARTICLE SUMMARY

BRAIN EVOLUTION

Developmental origins and evolution of pallial cell types and structures in birds

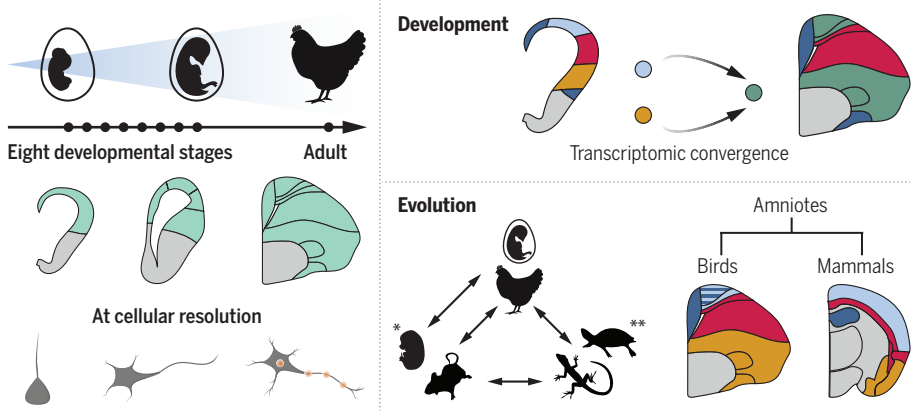
Bastienne Zaremba*, Amir Fallahshahroudi, Céline Schneider, Julia Schmidt, Ioannis Sarropoulos, Evgeny Leushkin, Bianka Berki, Enya Van Poucke, Per Jensen, Rodrigo Senovilla-Ganzo, Francisca Hervas-Sotomayor, Nils Trost, Francesco Lamanna, Mari Sepp, Fernando García-Moreno*†, Henrik Kaessmann*†

INTRODUCTION: Some avian species have advanced cognitive abilities that rival those of great apes, likely facilitated by evolutionary innovations in the avian forebrain, including the pallium. The pallium, equivalent to the dorsal telencephalon, has undergone substantial morphological changes during amniote evolution since their last common ancestor ~320 million years ago. In mammals, the pallium primarily includes layered structures such as the isocortex, whereas in birds and reptiles, it mostly comprises the nuclear-organized dorsal ventricular ridge (DVR). Unlike other reptiles, birds lack a layered cortex and instead have another nuclear-organized region, the hyperpallium. Because of these extensive differences, diverse views on amniote pallium evolution exist, some assuming homology of cell types with similar roles in the neural circuitry, and others suggesting homologous developmental territories.

RATIONALE: Recent single-cell molecular studies in adult reptiles and restricted areas of the pallium of songbirds have provided evidence for homology of specific pallial cell types, suggested to originate from shared embryonic regions but diverging considerably in their transcriptomic profiles across amniote lineages. However, cell type–level data for several key regions of the avian pallium, such as the hyperpallium, have been lacking. Moreover, despite the recognized importance of development in understanding evolutionary cell type relationships, the development of the pallium in nonavian reptiles and birds has never been studied at the single-cell level. To explore the developmental origins and evolution of pallial structures and cell types in birds, we generated spatially resolved cell type atlases of the entire adult chicken pallium and across in ovo development using single-nucleus RNA sequencing (snRNA-seq) and spatial transcriptomics technologies and compared them to corresponding atlases from mammals and nonavian reptiles.

RESULTS: We detected conserved expression patterns in inhibitory neurons across amniotes, with an expansion of one cell type in birds, which is predominantly located in the mammalian amygdala but present throughout the avian pallium. We also show evolutionary conservation of excitatory neuron types in the hippocampal regions of amniotes and identify homologs of excitatory neurons in the mammalian claustrum in the avian anterior DVR. Avian cell populations related to claustrum-like neurons resemble neurons in deep layers of the mammalian cortex, challenging current developmental and circuitry-focused hypotheses. Several excitatory neuron repertoires diverged substantially in birds, especially in the hyperpallium and ventral DVR (called the nidopallium). Our findings clarify the borders of the hyperpallium and reveal that only a fraction of cells in this region are homologous to neurons in the mammalian isocortex. Whereas adult comparisons support the functional equivalence of the DVR to the mammalian isocortex, developmental data reveal correspondences of cell types in ventral pallial areas between birds and mammals, illustrating the pronounced gene expression divergences of adult cell types in these regions. We also identify an extensive developmental convergence of gene expression programs between excitatory cell populations from the hyperpallium and nidopallium, accounting for their previously observed similarity in adults. This functional convergence occurs during late developmental stages, suggesting that, in birds, the topological location within the pallium is not always a determinant factor for adult gene expression programs underlying functional properties.

CONCLUSION: Our study provides key insights into the anatomy and development of the avian pallium, paving the way for research on the molecular mechanisms underlying advanced avian behaviors. We elucidate the evolutionary history of the amniote pallium, confirming previous notions and findings, such as the transcriptomic conservation of inhibitory neurons or of excitatory neurons in the hippocampus, while also identifying novel relationships, for example, that of cell populations in the anterior DVR and deep layers of the mammalian isocortex. We also show that adult transcriptomic similarities within the avian pallium may result from developmental convergence rather than reflecting homology. Our work thus emphasizes the need for updated models of amniote pallial evolution and the importance of considering developmental data in evolutionary comparisons. Overall, our study resolves long-standing debates on the amniote pallium, offering valuable insights into the evolutionary trajectory and diversification of neural cell types and structures crucial for advanced behaviors. ■



Cellular development and evolution of the chicken pallium. snRNA-seq delineates the development and cellular composition of the chicken pallium (left). During development, glutamatergic neuron populations from dorsal and ventral pallial areas converge in their transcriptomic profiles (top right). Comparisons of cell types across all major lineages of amniotes (mammals, birds, nonavian reptiles) in adults and development reveal cell type and potential regional homologies in the pallium. Single and double asterisks indicate external datasets.

The list of author affiliations is available in the full article online.
*Corresponding author. Email: b.zaremba@zmbh.uni-heidelberg.de (B.Z.); fernando.garcia-moreno@achucarro.org (F.G.-M.); h.kaessmann@zmbh.uni-heidelberg.de (H.K.)
†These authors contributed equally to this work.
Cite this article as B. Zaremba *et al.*, *Science* **387**, eadp5182 (2025). DOI: 10.1126/science.adp5182

READ THE FULL ARTICLE AT
https://doi.org/10.1126/science.adp5182

RESEARCH ARTICLE SUMMARY

BRAIN EVOLUTION

Enhancer-driven cell type comparison reveals similarities between the mammalian and bird pallium

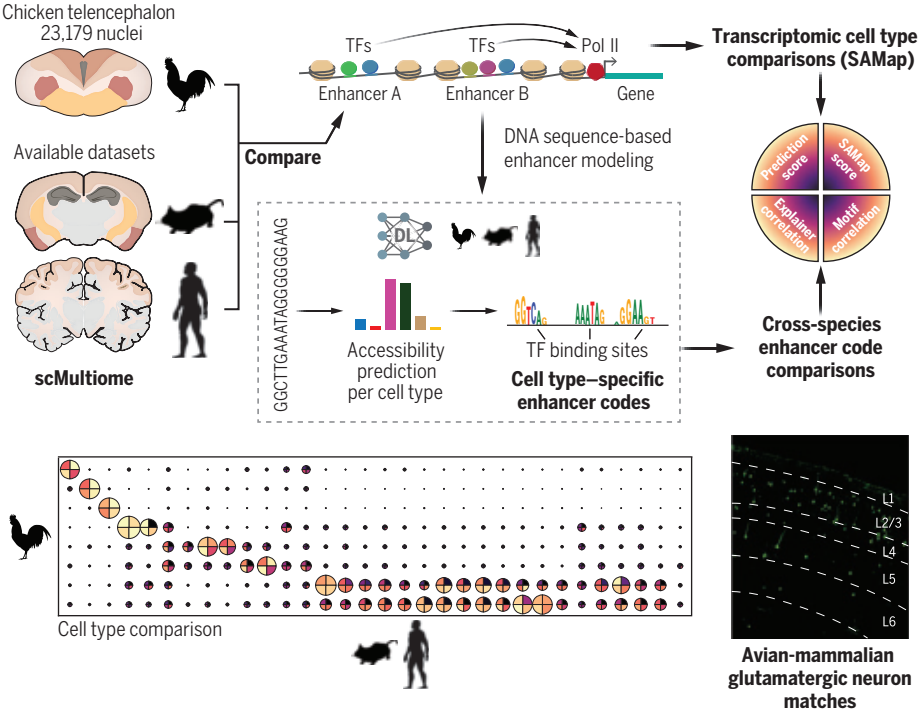
Nikolai Hecker†, Niklas Kempynck†, David Mauduit, Darina Abaffyová, Roel Vandepoel, Sam Dieltiens, Lars Borm, Ioannis Sarropoulos, Carmen Bravo González-Blas, Julie De Man, Kristofer Davie, Elke Leysen, Jeroen Vandensteen, Rani Moors, Gert Hulselmans, Lynette Lim, Joris De Wit, Valerie Christiaens, Suresh Poovathingal, Stein Aerts*

INTRODUCTION: The identity of cell types is governed by gene regulatory networks, which comprise cell type–specific combinations of transcription factors (TFs) that bind to genomic enhancer regions. The arrangements of TF binding sites form cell type–specific enhancer codes. Deep learning models trained on single-cell data provide the means to model and characterize enhancer codes at nucleotide resolution. Enhancer codes at such resolution have not yet been characterized for the mammalian telencephalon, which constitutes a major part of the forebrain, including the pallium. The pallium displays notable neuroanatomical differences between mammals and nonmammalian vertebrates. Most noticeable, the mammalian pallium contains a six-layered neocortex that is absent in all nonmammalian vertebrates, such as birds. Homologies between the mammalian and bird pallium are subject to a decades-long debate. It is currently unknown whether enhancer codes are conserved across vertebrate brains and whether they are informative to resolve homology relationships between species at the cell type level.

RATIONALE: To characterize and compare the enhancer codes of brain cell types between the mammalian and bird pallium, we generated single-cell multiome (scMultiome) and spatially resolved transcriptomics data of the chicken telencephalon. As a baseline to map cell type similarities between species, we compared the transcriptomes of telencephalon cell types between human, mouse, and chicken. We then used variable chromatin accessibility as a proxy to identify potential genomic enhancer regions and to assess their cell type specificity. Next, we trained sequence-based deep learning models on these regions to infer cell type–specific enhancer codes for the human, mouse, and chicken telencephalon. We implemented three metrics that exploit enhancer codes to compare cell types between species.

RESULTS: Excitatory neurons of the chicken telencephalon distinctly localize to pallial neuroanatomical regions, including the mesopallium, entopallium, hyperpallium, and nidopallium. Based on the transcriptomic and enhancer code comparisons, nonneuronal and γ-aminobutyric acid–mediated (GABAergic) cell types show a high degree of similarity across birds and mammals, which is reflected by conserved TF combinations for these cell types. On the other hand, the enhancer codes of excitatory neurons in the mammalian and avian pallium exhibit a higher degree of divergence. These matches only partially agree with existing evolutionary models for homologies between vertebrate pallial cell types based on developmental trajectories and brain circuitry. We found that the mammalian deep-layer excitatory neurons are most similar to mesopallial neurons, and mammalian neocortical upper-layer, piriform cortex, and amygdalar neurons are most similar to hyper- and nidopallial neurons. As a validation for the predicted correspondences between mammalian and bird cell types, we performed in vivo enhancer reporter assays. We show that chicken enhancer sequences exhibit activity in the corresponding mammalian telencephalic cell types when assayed in mouse brains.

CONCLUSION: Our study shows that enhancer codes can be exploited to infer cell type correspondences between species that are in line with transcriptomic comparisons. Joint comparisons of transcriptomes and deep learning–based enhancer codes reveal both expected and unexpected correspondences between cell types in the mammalian and avian telencephalon, indicating conserved regulatory programs that likely originated in the common amniote ancestor and have been co-opted or diversified. The proposed enhancer code–based approaches are generally applicable and can be used to characterize and compare cell types across species using the genomic regulatory code. ■



Correspondences between avian and mammalian telencephalic regulatory codes hint at ancestral conservation. We generated a scMultiome and spatial chicken telencephalon dataset and compared chicken, mouse, and human telencephalic cell types by comparing their transcriptomic profiles and their inherent enhancer codes through sequence-based deep learning models. Pol II, polymerase II.

The list of author affiliations is available in the full article online.
*Corresponding author. Email: stein.aerts@kuleuven.be
†These authors contributed equally to this work.
Cite this article as N. Hecker *et al.*, *Science* **387**, eadp3957 (2025). DOI: 10.1126/science.adp3957

READ THE FULL ARTICLE AT
https://doi.org/10.1126/science.adp3957

RESEARCH ARTICLE SUMMARY

ENZYMOLOGY

Conformational ensembles reveal the origins of serine protease catalysis

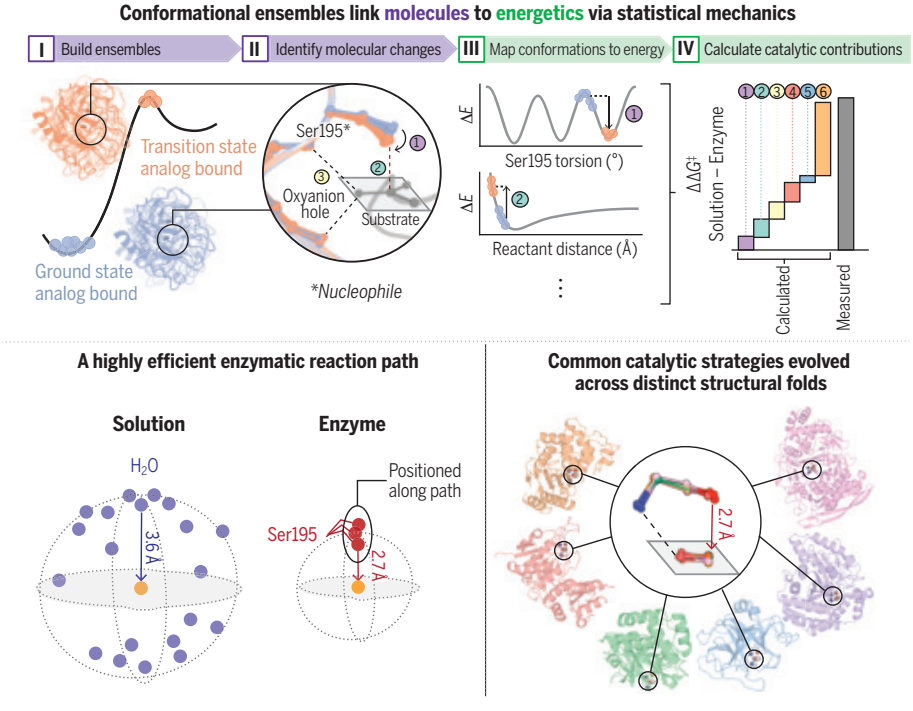
Siyuan Du, Rachael C. Kretsch, Jacob Parres-Gold, Elisa Pieri, Vinícius Wilian D. Cruzeiro, Mingning Zhu, Margaux M. Pinney, Filip Yabukarski, Jason P. Schwans, Todd J. Martínez, Daniel Herschlag*

INTRODUCTION: Enzymes are central to all biological functions. A century of enzymology has established chemical mechanisms and roles of active-site residues and cofactors for almost all known enzymes. Yet, we still lack the ability to account for the enormous rate enhancements provided by enzymes. Although serine proteases are often used as examples in biochemistry textbooks to illustrate enzyme catalysis, it remains unclear how their active sites accelerate the peptide bond cleavage reaction. The serine nucleophile is a hydroxyl group that is similar to water in reactivity; the oxyanion hole typically consists of amide groups, which are also similar to water as hydrogen bond donors. The general base in the catalytic triad does facilitate proton transfer but not nearly enough to account for serine protease catalysis. A deepened understanding of how such enzymes work requires an approach that can identify catalytic features, uncover the physical basis of their function, and quantify their catalytic contributions.

RATIONALE: Reaction rates—and catalysis—are determined by the probability of achieving the reaction's transition state, and these probabilities are defined by free energies. Conformational ensembles encode states and their probabilities, thereby providing a means to access the free energies that define catalysis. We therefore moved beyond traditional structure-function relationships to develop an ensemble-function approach that identifies catalytic features and quantifies the catalytic contribution from each individual feature. We applied this approach to serine proteases to address the following questions: (i) What are the molecular changes between the enzymatic reaction states? (ii) How does the enzymatic reaction differ from that in solution? and (iii) What are the energetic consequences of these differences?

RESULTS: We brought together >1000 x-ray crystallographic structures from 17 serine proteases to build pseudo-ensembles, and we obtained ensemble information for the uncatalyzed solution reaction from small-molecule structures and computation. Pseudo-ensembles for enzymes bound to ground state analogs, transition state analogs, or no substrates revealed an altered energy landscape for the enzymatic reaction, where shorter and more efficient reaction paths are favored relative to those in solution. The enzymes position reactants within a short distance and use a side-chain rotation of the catalytic serine to facilitate reaction, removing much of the translational motion needed in solution and increasing the reaction probability. The enzymatic reaction is further accelerated by multiple interactions that are destabilized in the ground state and relieved in the transition state. We quantified catalytic contributions from these features using knowledge-based energy functions to provide a minimal model that accounts for serine protease catalysis within error. The same catalytic features are commonly used by enzymes from distinct structural folds to catalyze reactions that involve nucleophilic addition on carbonyl compounds, suggesting convergent evolution under the same mechanistic constraints and high evolvability of the identified strategies.

CONCLUSION: Ensemble-function analyses identified precise catalytic features and established an experimentally based, quantitative model for serine protease catalysis. This model is grounded in the most basic concepts of chemistry and physics—torsion angles, van der Waals interactions, hydrogen bonds, and conformational entropy—and thus is accessible to researchers and students alike. The ensemble-function approach connects these fundamental physicochemical properties to the emergent functions of macromolecules, a connection that is needed to understand enzyme catalysis and still more complex protein functions, such as allostery and molecular machines. ■



The ensemble-function approach provides a quantitative catalytic model for serine proteases and identifies repeatedly evolved catalytic strategies. (Top) The four steps of the ensemble-function approach. (Bottom left) Reactants on serine proteases are highly positioned and at shorter distances relative to those in solution, simplifying the reaction path and increasing reaction probability. (Bottom right) Enzymes from multiple structural folds use the catalytic strategies identified here.

The list of author affiliations is available in the full article online.
*Corresponding author. Email: herschla@stanford.edu
Cite this article as S. Du *et al.*, *Science* **387**, eado5068 (2025).
DOI: 10.1126/science.ado5068

READ THE FULL ARTICLE AT
https://doi.org/10.1126/science.ado5068

RESEARCH ARTICLE SUMMARY

IMMUNOLOGY

KLF2 maintains lineage fidelity and suppresses CD8 T cell exhaustion during acute LCMV infection

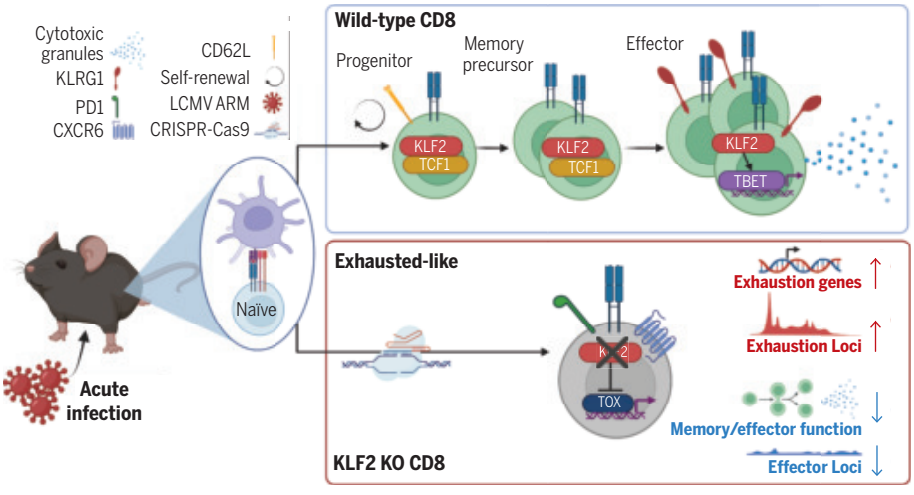
Eric Fagerberg, John Attanasio, Christine Dien, Jaiveer Singh, Emily A. Kessler, Leena Abdullah, Jian Shen, Brian G. Hunt, Kelli A. Connolly, Edward De Brouwer, Jiaming He, Nivedita R. Iyer, Jessica Buck, Emily R. Borr, Martina Damo, Gena G. Foster, Josephine R. Giles, Yina H. Huang, John S. Tsang, Smita Krishnaswamy, Weiguo Cui, Nikhil S. Joshi*

INTRODUCTION: Naïve CD8 T cells have the potential to differentiate into a variety of effector and memory CD8 T cell states during an immune response. These states reflect the cells' functional potential to fight infection, respond to immunotherapies, or cause immunopathology. Acute T cell responses are associated with highly functional effector and memory states. Conversely, chronic antigen environments, as seen in tumors and chronic infection, drive dysfunctional T cell fate decisions, termed generally as T cell exhaustion.

RATIONALE: Despite recent insights into how these divergent T cell differentiation states determine physiological outcomes, it remains uncertain how fate decisions are made and what mechanisms exist to suppress differentiation towards alternative fates and maintain lineage fidelity. High-dimensional single-cell studies have enabled deep inquiry into the spectrum of T cell differentiation states across different immune challenges, and, from this, efforts have been made to infer differentiation trajectories and their underlying transcriptional regulation. Yet, testing these predictions has traditionally been accomplished through lower-throughput knock-out and/or lineage-tracing experiments. PerturbSEQ is a technique that couples CRISPR perturbations of target genes with single-cell RNA sequencing (scRNA-seq) and enables mechanistic dissection of differentiation processes. In this study, we used perturbSEQ with the goal of understanding factors that regulate fate decisions and preserve T cell lineage fidelity.

RESULTS: We generated a differentiation space map (DSM) of the spectrum of CD8 T cell states in acute and chronic lymphocytic choriomeningitis virus (LCMV) infection across time points using scRNA-seq. Analyses across four time points revealed a linear differentiation trajectory in acute infection, whereas a bifurcation between effector and exhausted trajectories was observed in chronic infection. We then performed in vivo perturbSEQ in LCMV-specific CD8 T cells for a library of ~40 genes [largely transcription factors (TFs) and epigenetic modulators] in the context of acute LCMV infection. This experiment identified proteins that could regulate the extent to which cells differentiated along an expected memory to effector trajectory, thereby highlighting their role as a suppressor or promoter of specific T cell functions. Moreover, it elucidated KLF2 as a transcription factor that maintains effector lineage fidelity. KLF2 knockout (KO) T cells aberrantly acquired distinct features of exhaustion during acute LCMV infection. This included impaired effector and memory differentiation and function during both primary and secondary viral challenge. Epigenetic changes, both at sites of KLF2 binding and globally throughout the genome, overlapped with loci accessibility changes seen in chronic infection. Mechanistic studies showed that KLF2 was downregulated upon T cell receptor stimulation and was intrinsically required for suppression of the exhaustion-defining TF, TOX. Epistasis experiments revealed that KLF2 was also critical for enabling the function of the effector-defining TF, TBET. Investigation in tumor models pointed to a role for KLF2 in the early bifurcation of effector and exhausted differentiation trajectories as KLF2 was required to maintain a polyfunctional TCF1$^+$ CD62L$^+$ precursor state. KO cells less potently controlled tumors and exhibited enhanced differentiation with features of exhaustion and residence. Overexpression of KLF2 was sufficient to rescue this precursor state in tumor-draining lymph nodes as well as suppress features of exhaustion and induce effector differentiation in acute and chronic viral infection.

CONCLUSION: Our study highlighted the role of many TFs in regulating the extent to which CD8 T cells differentiate along a defined linear trajectory and revealed KLF2's distinct role in enabling cells to remain on this effector lineage. This adds to our mechanistic understanding of T cell fate decisions and demonstrates that differentiation toward the exhaustion lineage is suppressed in acute infection. It additionally opens new questions regarding maintenance of lineage fidelity across immune contexts, where little is still known. Further, modulation of KLF2 proved useful in driving or suppressing distinct T cell functional states with potential implications for immunotherapy. ■



KLF2 prevents aberrant CD8 T cell differentiation in acute LCMV infection. Naïve CD8 T cells undergo functional effector differentiation in acute LCMV infection. This effector differentiation involves KLF2-dependent TBET activity. KLF2 KO in this setting results in aberrant CD8 T cell differentiation to a TOX$^+$ exhausted-like state. This is characterized by an epigenetic and transcriptional signature resembling hallmark features of CD8 T cells in chronic infection and results in reduced cytolytic potential and memory recall capacity. [Figure created with BioRender.com]

The list of author affiliations is available in the full article online.
*Corresponding author. Email: nikhil.joshi@yale.edu
Cite this article as E. Fagerberg *et al.*, *Science* **387**, eadn2337 (2025). DOI: 10.1126/science.adn2337

READ THE FULL ARTICLE AT
https://doi.org/10.1126/science.adn2337

RESEARCH ARTICLES

CANCER

RNA polymerase II at histone genes predicts outcome in human cancer

Steven Henikoff[1,2]*†, Ye Zheng[1]†‡, Ronald M. Paranal[3], Yiling Xu[1], Jacob E. Greene[1,4], Jorja G. Henikoff[1], Zachary R. Russell[3], Frank Szulzewsky[3]¶, H. Nayanga Thirimanne[3], Sita Kugel[3], Eric C. Holland[3], Kami Ahmad[1]

Genome-wide hypertranscription is common in human cancer and predicts poor prognosis. To understand how hypertranscription might drive cancer, we applied our formalin-fixed paraffin-embedded (FFPE)–cleavage under targeted accessible chromatin method for mapping RNA polymerase II (RNAPII) genome-wide in FFPE sections. We demonstrate global RNAPII elevations in mouse gliomas and assorted human tumors in small clinical samples and discover regional elevations corresponding to de novo HER2 amplifications punctuated by likely selective sweeps. RNAPII occupancy at S-phase-dependent histone genes correlated with WHO grade in meningiomas, accurately predicted rapid recurrence, and corresponded to whole-arm chromosome losses. Elevated RNAPII at histone genes in meningiomas and diverse breast cancers is consistent with histone production being rate-limiting for S-phase progression and histone gene hypertranscription driving overproliferation and aneuploidy in cancer, with general implications for precision oncology.

Global increase in transcriptional output, or hypertranscription, is associated with poor prognosis in cancer (*1*). However, it is difficult to reconcile promiscuous incremental up-regulation of thousands of genes with the presumed direct action of oncogenic transcription factors in activating expression of target genes to drive tissue-specific malignancies. Alternatively, hypertranscription in cancer may be relevant only to the subset of genes for products that are rate-limiting for cell doubling. Histones are rate-limiting for proliferation (*2*–*4*), insofar as all newly synthesized DNA must be packaged into nucleosomes in every cell cycle, and the 64 genes encoding all five histone subunits must produce ~5% of a human cell's total protein during S-phase (*5*). RNA polymerase II (RNAPII) is so abundant over histone genes during replication that S-phase–specific, genome-wide depletion of RNAPII at other genes has been observed in mouse embryonic stem cells (*4*). S-phase–dependent histone messenger RNAs are not polyadenylated and so are essentially absent from RNA-sequencing libraries, and the possibility that they drive overproliferation has been overlooked.

[1]Basic Sciences Division, Fred Hutchinson Cancer Center, Seattle, WA, USA. [2]Howard Hughes Medical Institute, Chevy Chase, MD, USA. [3]Human Biology Division, Fred Hutchinson Cancer Center, Seattle, WA, USA. [4]Molecular Medicine and Mechanisms of Disease PhD Program, University of Washington, Seattle, WA, USA.
*Corresponding author. Email: steveh@fredhutch.org
†These authors contributed equally to this work.
‡Present address: Department of Bioinformatics and Computational Biology, University of Texas MD Anderson Cancer Center, Houston, TX, USA.
¶Present address: Huntsman Cancer Institute, University of Utah Health Sciences Center, Salt Lake City, UT, USA.

RNAPII hypertranscription varies between tumors

We recently adapted cleavage under targeted accessible chromatin (CUTAC) for formalin-fixed paraffin-embedded (FFPE) sections to directly map RNAPII in fixed tissue samples (*6*). This provides a DNA-based method for measuring transcription, instead of RNA-based methods that are limited by RNA instability and variable transcript half-lives. We assessed RNAPII across 343,731 candidate cis-regulatory elements (cCREs) defined by the Encyclopedia of DNA Elements (ENCODE) project (*7*) and compared normal mouse brain tissue to adjacent tumors induced by different transgene drivers (*8*–*10*). We observed that significantly up-regulated cCREs were more frequent than down-regulated cCREs (fig. S1). To sensitively detect RNAPII hypertranscription (Fig. 1A), in which the absolute change is important, we first counted the number of mapped fragments spanning each base pair in a cCRE scaled to the mouse genome coverage and averaged the normalized counts over that cCRE. We then plotted tumor minus normal (T–N) counts on the *y*-axis versus the average RNAPII signal (*11*) on a $\log_{10}$ scale on the *x*-axis for clarity. This revealed clear hypertranscription (tumor >> normal RNAPII) for the RELA-driven tumor (Fig. 1B). Two platelet-derived growth factor B (PDGFB)–driven tumors differed in hypertranscription, high in PDGFB-1 (Fig. 1C) and low in PDGFB-2 (Fig. 1D), whereas the YAP1-driven tumor showed weak hypotranscription (Fig. 1E). To determine whether hypertranscription is specific to any particular class of regulatory element(s), we divided the data into the five ENCODE-annotated cCRE categories and observed that the five RNAPII hypertranscription profiles are highly consistent with one another (fig. S2). This suggests that RNAPII abundance differences between tumors and normal brains affect all regulatory element classes.

We next expanded our findings to a diverse sample of human tumors and matched normal sections from the same patient (fig. S3). We performed FFPE-CUTAC and rank-ordered each pair by T–N differences to test for RNAPII hypertranscription based on the 984,834 ENCODE-annotated human cCREs. We observed clear hypertranscription in five of the seven tumors (breast, colon, liver, rectum, and stomach) and for the composite of all samples (Fig. 1, F to M, and fig. S4). By contrast, the kidney and lung tumor samples tested showed essentially no hypertranscription, which implies that hypertranscription is a common, but not a defining, feature of cancer (*1*, *12*). We also applied a computational method independent of annotations using the sparse enrichment analysis for CUT&RUN (SEACR) peak caller (*13*), customized by replacing the background control with the normal sample in each pair. SEACR reported a median of 4483 peaks that were elevated in tumors, whereas when tumor and normal were exchanged, only a median of 15 peaks elevated in normal tissue were identified, demonstrating that RNAPII hypertranscription is more common than RNAPII hypotranscription in these cancer samples.

We next asked whether SEACR tumor-versus-normal peak calls corresponded to the 100 top cCREs ranked by T–N in the overall list representing all seven tumors. All 100 cCREs at least partially overlapped one or more SEACR tumor-versus-normal peak calls, and in addition, the majority of the 100 top-ranked cCREs intersected with overlapping SEACR peak calls from multiple tumor-versus-normal pairs (table S1). Each of the #1-ranked cCREs in the breast, colon, liver, lung, and rectum tumor samples respectively intersected MSL1, RFFL, PABPC1, CLTC, and SERINC5 genes and overlapped SEACR peak calls in 4 or 5 of the 7 tumors (Fig. 1, N to S, and fig. S5). We concluded that the most strongly RNAPII-hypertranscribed regulatory elements tend to be strongly hypertranscribed in multiple human cancers of different types, including liver cancers from different individuals (fig. S6).

We observed a much lower level of mitochondrial DNA (mtDNA) in most tumor samples than in their matched normal samples for both mice and humans (fig. S7, A and B), suggesting that these tumors contain fewer mitochondria. To test this interpretation, we mined publicly available assay for transposase-accessible chromatin with sequencing (ATAC-seq) data from both the Cancer Genome Atlas Program (TCGA) and ENCODE projects and observed similar reductions in cancer samples (fig. S7, C and D).

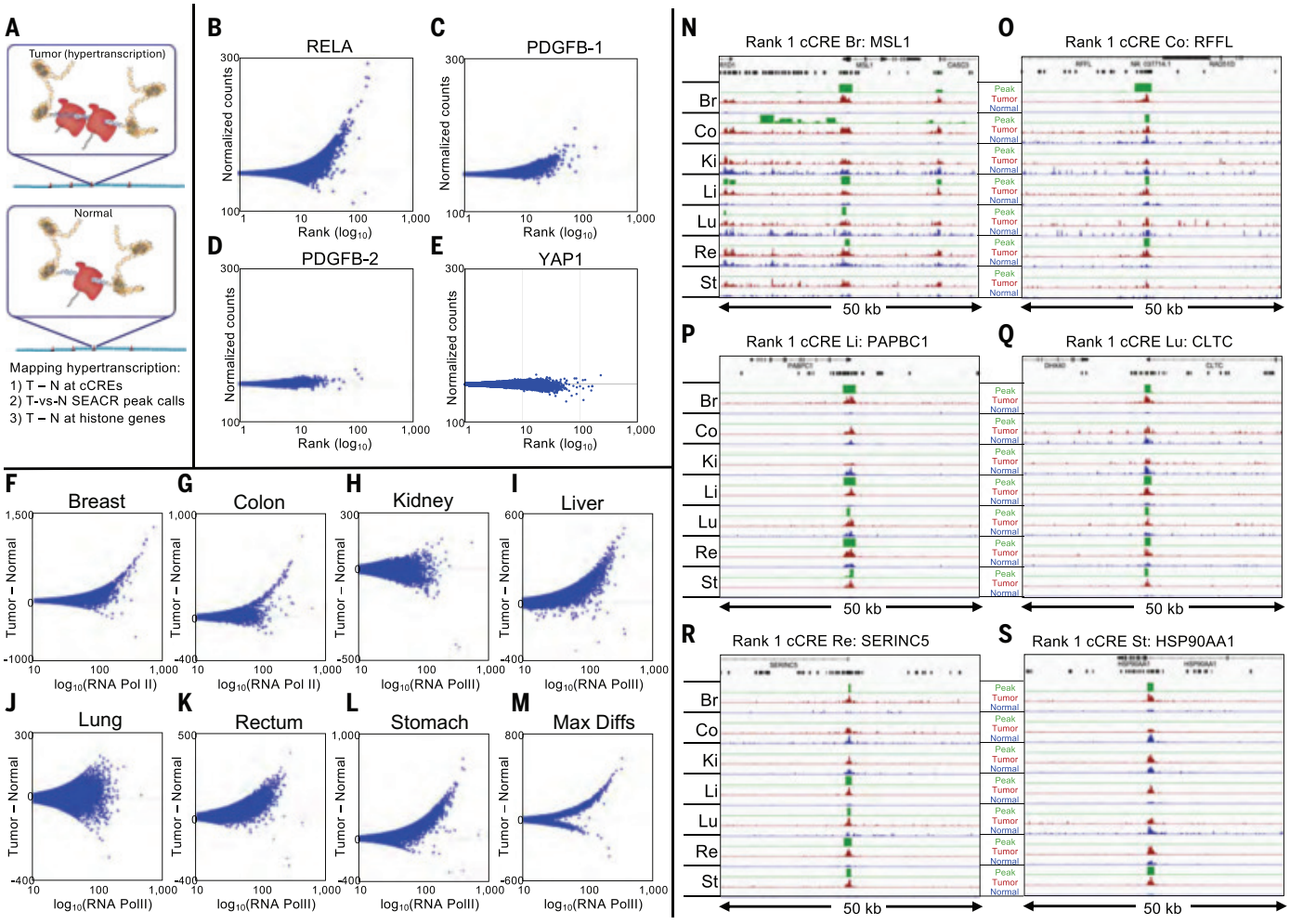


Fig. 1. RNAPII-Ser5p FFPE-CUTAC directly maps hypertranscription. (**A**) Model for hypertranscription in cancer: Paused RNA polymerase II (RNAPII) at active gene regulatory elements such as promoters and enhancers typically increases through the cell cycle, resulting in a net proportional gain in RNAPII occupancy across the genome. Using RNAPII FFPE-CUTAC, we can map hypertranscription genome-wide using three complementary approaches: (i) genome-scaled tumor (T) minus normal (N) counts at cCREs; (ii) T–N at S-phase–dependent histone genes; and (iii) SEACR tumor peak calls using normal as the background control. (**B** to **E**) T–N versus log(T + N)/2 plots showing hypertranscription mapped over the 343,731 annotated mouse cCREs for tumor and normal sections dissected post tagmentation from a 10-μm FFPE slice from each of four different paraffin blocks. Hypertranscription of a cCRE is defined as the excess of RNAPII-Ser5p in the indicated tumor over normal (tumor minus normal in normalized count units for mm10-mapped fragments pooled from the same slide). (**F** to **M**) All fragments were pooled from four slides from the same paraffin block and the number of fragments equalized between tumor and normal for each of the seven cancers. T–N versus log(T + N)/2 plots showing hypertranscription mapped over the 984,834 annotated human cCREs for tumor and matched normal sections from five micron FFPE slices. Max diffs displays the tumor minus normal maximum of the seven samples for each cCRE. (**N** to **S**) For each of the indicated tumors, tracks are shown for 50-kb regions around the #1-ranked cCRE based on tumor (dark red) and normal (blue) counts. Raw data tracks were group-autoscaled together for tumor (red) and normal (blue), where SEACR tumor peak calls (green) use normal as the negative control. Gene annotations and cCREs (black rectangles) are shown at the top.

Such reductions in mtDNA have been reported based on whole-genome sequencing (*14*).

HER2 amplifications with selective sweeps

All but one of the top 25 cCREs are located on Chromosome 17 (table S1). Eight of these cCREs are within Chr17q12 and 13 are within Chr17q21, each spanning a few hundred kilobases in length in breast and colon tumors not seen in normal tissue (Fig. 2, A and B, and fig. S8). High RNAPII occupancy over the cCREs in Chr17q12-21 can account for most of the RNAPII hypertranscription signal in the breast and colon samples, centered over the ERBB2 gene (fig. S9). ERBB2 encodes human epidermal growth factor receptor 2 (HER2) and is commonly amplified in cancer and is a target of breast cancer therapy (*15*).

To confirm that the broad regions of RNAPII enrichment around the ERBB2 promoter correspond to HER2 amplifications in the breast and colon patient samples, we applied SEACR, which densely tiled a ~150-kb region centered over the ERBB2 promoter (Fig. 2, A and B). To ascertain whether dense tiling using SEACR can detect amplification events, we called SEACR broad peaks on our published K562 RNAPII-Ser5p CUTAC datasets (*16*, *17*). We observed a single region heavily tiled with broad SEACR peaks corresponding to an annotated amplification specific for K562 cells. Zooming in revealed that the end of the densely tiled region corresponded precisely to the t(9;22)(q34;q11) translocation breakpoint of BCR-ABL (fig. S10, A and B), which we confirmed by observing a broad SEACR peak on the ABL1 side of the translocation breakpoint (fig. S10C). Thus, our approach using RNAPII-Ser5p CUTAC and SEACR can identify and precisely map regional

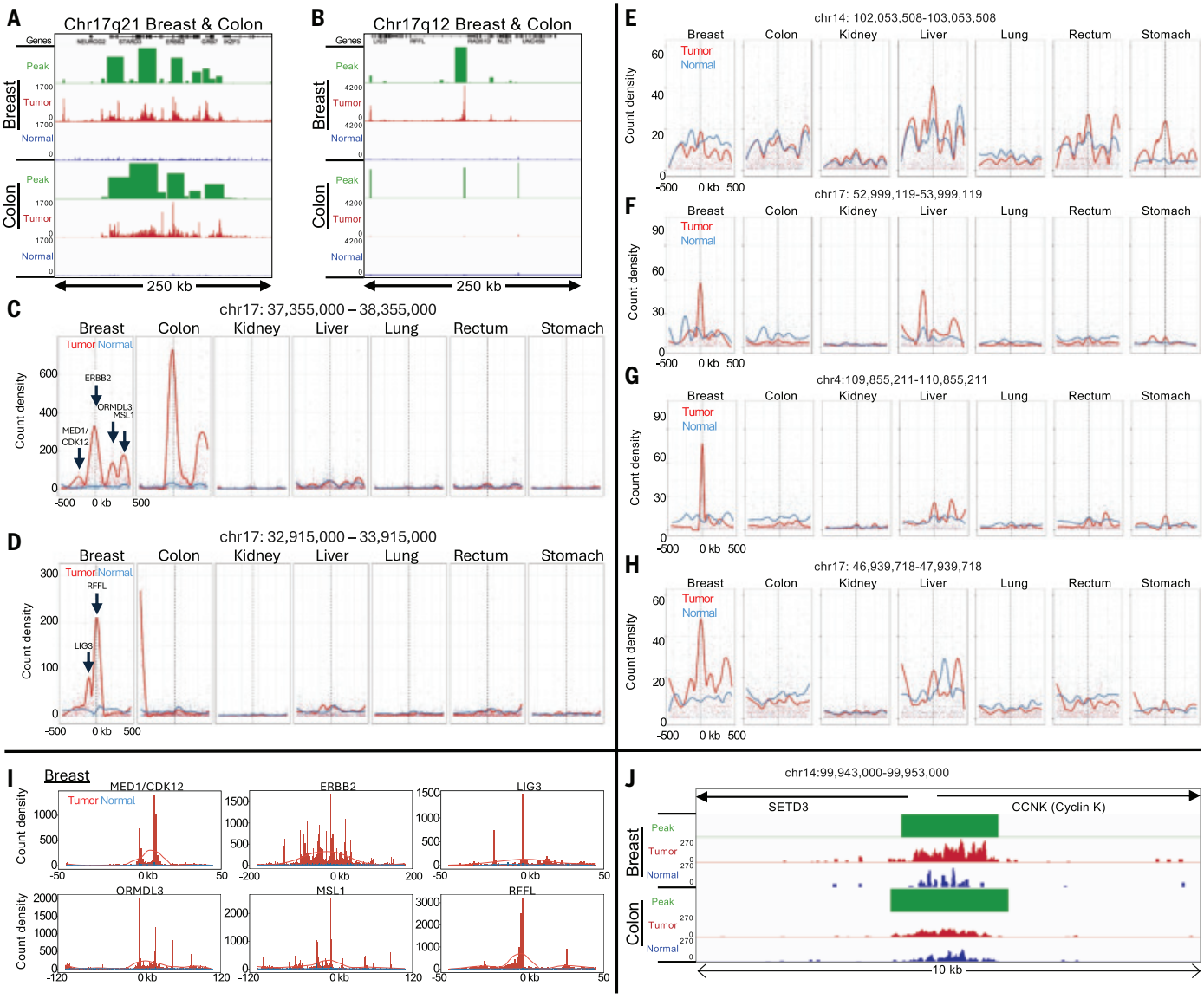


Fig. 2. RNAPII levels identify likely HER2 amplifications and regions of linkage disequilibrium. (**A**) and (**B**) Normalized count tracks and SEACR peak calls for the 250-kb region on Chromosome 17q21 (A) and for the 250-kb 17q12 region (B) amplified in the breast tumor but evidently not in the colon tumor. Tracks were group-autoscaled together for tumor (red) and normal (blue), where SEACR tumor peak calls (green) use normal as the negative control. Broad regions of prominent RNAPII hypertranscription indicate likely HER2 amplifications in both tumors. (**C**) and (**D**) 1-kb bins were tiled over each 1-Mb region centered on the highest peak in Chr17q21 (C) corresponding to the ERBB2 promoter in Chr17q21, and the RFFL promoter in Chr17q12 (D); count density within each bin is plotted with curve-fitting and smoothing. Each of the six summits in the breast tumor sample is centered over the promoter peak indicated by an arrow. (**E** to **H**) Same as (C) and (D) for top-ranked loci outside of the HER2 amplicon. (**I**) Individual broad summits in (C) to (D) were zoomed in and rescaled on the *x*-axis centered over the indicated promoter peak and superimposed over data tracks scaled to the height of the central peak. (**J**) Data tracks for the *CCNK* promoter region, where the normalized count increase in the breast tumor relative to normal over the 10-kb region shown is 5.4-fold and for colon is 2.1-fold. The range for the other five tumors is 0.9- to 2.5-fold.

amplifications such as are found in tumors with BCR-ABL and HER2 amplifications.

To delineate possible RNAPII hypertranscription features within Chr17q12-21, we binned successive 1-kb tiles over each 1-Mb region centered on the highest peak, corresponding to the ERBB2 promoter in Chr17q21 and the RFFL promoter in Chr17q12, and plotted count density within each bin with curve-fitting and smoothing. Multiple broad summits appeared in both breast and colon tumor-versus-normal tracks, and the six summits in the breast tumor sample accounted for the six highest ranked Chr17 promoter peaks (Fig. 2, C and D). We similarly plotted count densities of the four highest ranking cCREs outside of Chr17q12-21 (table S1), but tumor peaks in these regions were at least one order of magnitude lower than the ERBB2 peaks in the breast and colon tumor samples (Fig. 2, E to H). Of the six summits in the breast tumor sample, ERBB2 and MSL1 also appeared in the colon tumor sample, whereas no other samples showed prominent summits above normal in Chr17q12-21 (Fig. 2, C and D). MSL1 encodes a subunit of a histone H4-lysine-16 acetyltransferase complex required for up-regulation of the mammalian X chromosome (*18*).

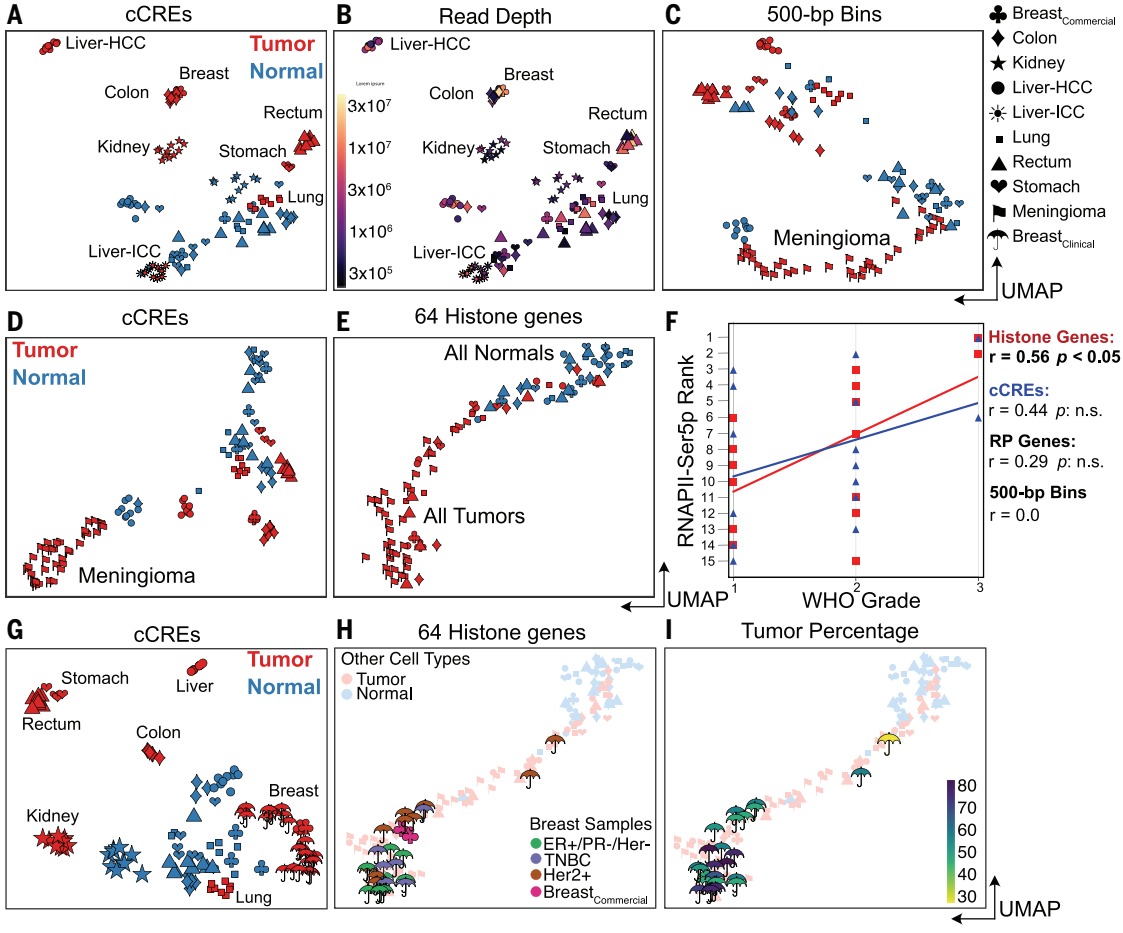


Fig. 3. RNAPII over histone genes correlates with aggressiveness in meningiomas and breast tumors. (**A**) UMAP of commercial tumor and normal patient samples and replicates. HCC, Hepatocellular carcinoma; ICC, Intrahepatic cholangiocarcinoma. (**B**) Same as (A) colored for sequencing depth and indicating homogeneous tumor clusters. (**C**) UMAP of RNAPII FFPE-CUTAC data including samples and replicates from 30 meningiomas based on 500-bp bins over the human genome. (**D**) Same as (C) for cCREs. (**E**) Same as (C) for the 64 S-phase–dependent histone genes. (**F**) WHO grade correlates best with RNAPII occupancy over histone genes. (**G**) Same as (D) excluding meningiomas but including samples and replicates from 13 additional breast tumors. (**H**) Same as (E) for breast tumor samples and replicates, colored for tumor type. (**I**) Same as (H) colored for tumor percentage.

We next superimposed each of the six summits in the Chr17q12-21 region in the breast tumor sample over the genomic tracks on expanded scales for clarity, centered over the highest promoter peak in the region (Fig. 2I). For ERBB2, the ~100-kb broad summit is almost precisely centered over the ~1-kb-wide ERBB2 promoter peak. Although the other summits are less broad, each is similarly centered over a promoter peak. Insofar as there are multiple summits much broader than the promoter peaks that they are centered over, our results are inconsistent with independent up-regulation of promoters over the HER2-amplified regions. Rather, it appears that a HER2 amplification event was followed by clonal selection for broad regions around ERBB2 and other loci within each amplicon, consistent with the observation of clonally heterogeneous HER2 amplifications in primary breast tumors by whole-genome sequencing (*19*). Clonal selection may be driven by selective sweeps (*20*) following amplification events that generate extrachromosomal DNA in double-minute acentric chromosomes, which partition unequally during each cell division (*21*–*23*). Such copy number gains within a tumor can result in intratumor heterogeneity (*23, 24*) and are potential factors for resistance to therapy (*25*). FFPE-CUTAC thus potentially provides a general diagnostic strategy for detection and analysis of amplifications and clonal selection during cancer progression and therapeutic treatment.

One of the summits in the breast tumor sample absent from the colon tumor sample corresponds to the bidirectional promoters of MED1 and CDK12, both of which have been shown to functionally cooperate with co-amplified ERBB2 in aggressive breast cancer (*26*, *27*). CDK12 is the catalytic subunit of the CDK12/Cyclin K kinase heterodimer complex, which phosphorylates RNAPII for productive transcriptional elongation (*28*, *29*). As Cyclin K is the regulatory subunit of the CDK12 kinase, we would expect that the *CCNK* gene that encodes Cyclin K would be strongly up-regulated in the breast tumor but not necessarily in the colon tumor. Indeed, we saw a 5.4-fold increase in RNAPII-S5p over the *CCNK* promoter in the breast tumor relative to adjacent normal tissue, whereas in the colon tumor there was a 2.1-fold increase (Fig. 2J), and a 0.9- to 2.5-fold increase for the other five tumors, consistent with RNAPII hypertranscription driven in part by CDK12 amplification in this tumor.

RNAPII over histone genes predicts aggressiveness in meningiomas and breast tumors

To evaluate how effectively FFPE-CUTAC can resolve differences between the seven tumor samples, we constructed a cCRE-based uniform manifold approximation and projection (UMAP) of commercial tumor and normal patient samples. Normal samples produced mixed clusters whereas tumor samples formed tight homogeneous clusters separated by tissue type (Fig. 3A). This implies that paused RNAPII at regulatory elements is more discriminating between tumors than between the tissues that the tumors emerge from. Relatively few samples and shallow sequencing depths were needed for tight clustering (Fig. 3B).

As the exceptionally S-phase–dependent histone loci are expressed in proportion to the amount of replicated DNA, we wondered whether cancer cell hypertranscription functions to increase engaged RNAPII at these loci to load

up on histones at S-phase for more rapid cell proliferation. For both the mouse and human clustered histone genes we observed differences between tumor samples consistent with RNAPII hypertranscription at cCREs differing between samples (fig. S11). If histone production at S-phase is rate-limiting for proliferation, then we would observe a correlation between cancer aggressiveness and RNAPII, specifically over histone genes. As a test of this hypothesis, we applied FFPE-CUTAC to 30 meningioma patient samples and constructed a UMAP that also included the tumor and normal pairs described above. Using RNAPII abundance within cCREs, we found that the meningiomas clustered separately from other tumors and from normal samples (Fig. 3, C and D). When we performed the same UMAP construction using only RNAPII abundance over the 64 S-phase–dependent histone genes, we found that all tumors regardless of type clustered together in a cline that overlapped normal clusters at one end (Fig. 3E). This suggested that RNAPII at histone genes can distinguish cancer from normal but is insensitive to cancer type differences. In a double-blind test of whether the cline overlapping normal samples in multidimensional space is an indication of tumor aggressiveness, we rank-ordered the 15 samples with World Health Organization (WHO) grades based on distance from normal samples for RNAPII occupancy in 500-bp bins, cCREs, histone genes, or ribosomal protein genes (Fig. 3F). Best performance was for the histone genes ($r = 0.56$, $P < 0.05$), consistent with our hypothesis that high RNAPII levels at histone genes drive proliferation in cancer.

To determine whether S-phase–dependent histone genes can predict cancer aggressiveness in an invasive tumor type, we performed FFPE-CUTAC on a set of 10-μm breast tumor FFPEs from 13 patients representing three major subtypes. When we included these samples with the seven diverse tumor and normal samples (Fig. 1, F to L) and used cCREs for UMAP construction, we observed tight clustering according to tumor type (Fig. 3G). However, when we used histone genes for UMAP construction, we observed a single large cluster at one end of a cline that overlapped normal clusters at the other end (Fig. 3, H to I). We conclude that histone genes alone can predict cancer aggressiveness in both noninvasive meningiomas and multiple invasive breast cancer subtypes.

RNAPII over histone genes accurately predicts rapid recurrence in meningiomas

WHO grade is a coarse predictor of recurrence (*30*), so to predict recurrence for each patient sample, we integrated FFPE-CUTAC data with RNA-sequencing (RNA-seq) data using canonical correlation analysis in multidimensional space, based on normalized counts over each RefSeq-annotated human gene (fig. S12). We defined a gene as spanning from the 3′-most transcript end through the 5′-most end, stopping

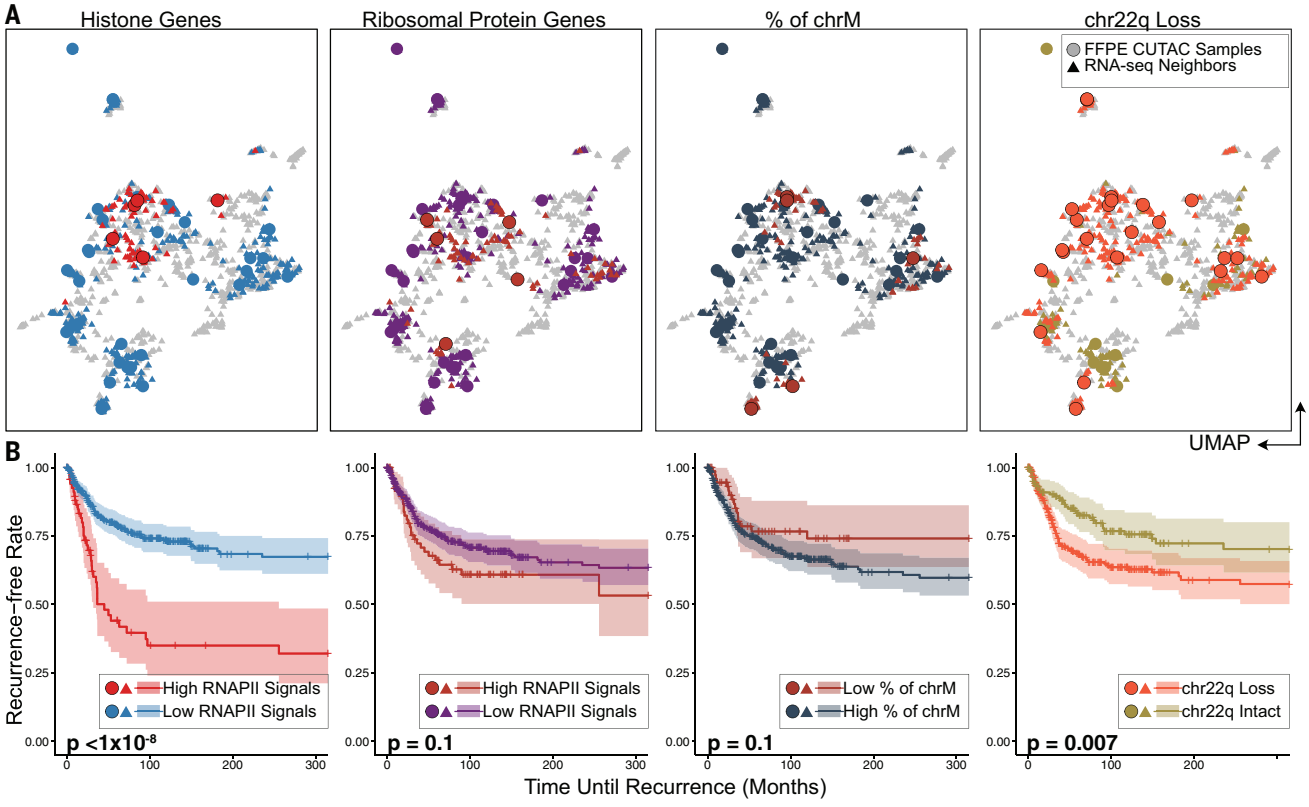


Fig. 4. RNAPII over histone genes predicts recurrence in meningiomas. (**A**) UMAPs of FFPE-CUTAC and frozen RNA-seq meningioma patient samples grouped by different biomarkers. (Left to right) RNAPII over S-phase–dependent histone genes; RNAPII over ribosomal protein genes; percent of chromosome M (chrM) (mitochondrial DNA); Chr22q loss. UMAPs are based on integrating FFPE-CUTAC (circles) with frozen-RNA-seq (triangles) samples (fig. S12) using the canonical correlation analysis. For histone and ribosomal protein genes, points are colored by high (red) or low (blue for histone genes and purple for ribosomal protein genes) RNAPII enrichment over the corresponding genes for FFPE-CUTAC samples or their shared nearest neighbor RNA-seq samples. For chrM, points are colored by low (red) or high (dark gray) fractions of chrM fragments, with the hypothesis that a low chrM fraction predicts malignancy. For chr22q loss, the FFPE-CUTAC samples with chr22q loss and their RNA-seq neighbors are red and those with chr22q intact are green. (**B**) Kaplan-Meier (KM) plots of recurrence-free rate as a function of time in months based on each grouping strategy using the biomarkers shown in (A). For fair comparisons between histone genes, ribosomal protein genes and chrM, the same number of samples, i.e., the top five patients, are selected in the malignant group. The fraction of the chrM predictor has settings (6 to 18 samples in the malignant group) with small *P*-values. However, the KM curve order is in the wrong direction for the hypothesis that a low fraction of chrM predicts fast recurrence (fig. S13D).

when either end of the next gene or LINE element is reached. We observed near-coincidence for 17 of 19 matched RNA-seq and FFPE-CUTAC samples.

To predict meningioma patient recurrence, we classified FFPE-CUTAC samples by the histone genes signal and used the top 20 RNA-seq nearest neighbors to compare the patient recurrences (Fig. 4A and fig. S13A). Indeed, we found a highly significant association between high histone signals in FFPE-CUTAC samples and rapid patient recurrence ($P < 10^{-8}$) (Fig. 4B, left, and fig. S13B). Using only the normalized FFPE-CUTAC counts at the 64 histone genes, we could distinctly separate the five most rapidly recurring from the 25 other tumors, which aligns with the generally low recurrence rate of meningiomas, and are predominantly benign tumors (*31*). By contrast, levels of RNAPII over ribosomal protein genes or mtDNA failed to significantly separate rapidly recurring from benign tumors, regardless of the thresholds applied (Fig. 4B and fig. S13, C and D). Although we did observe significant separation of rapidly

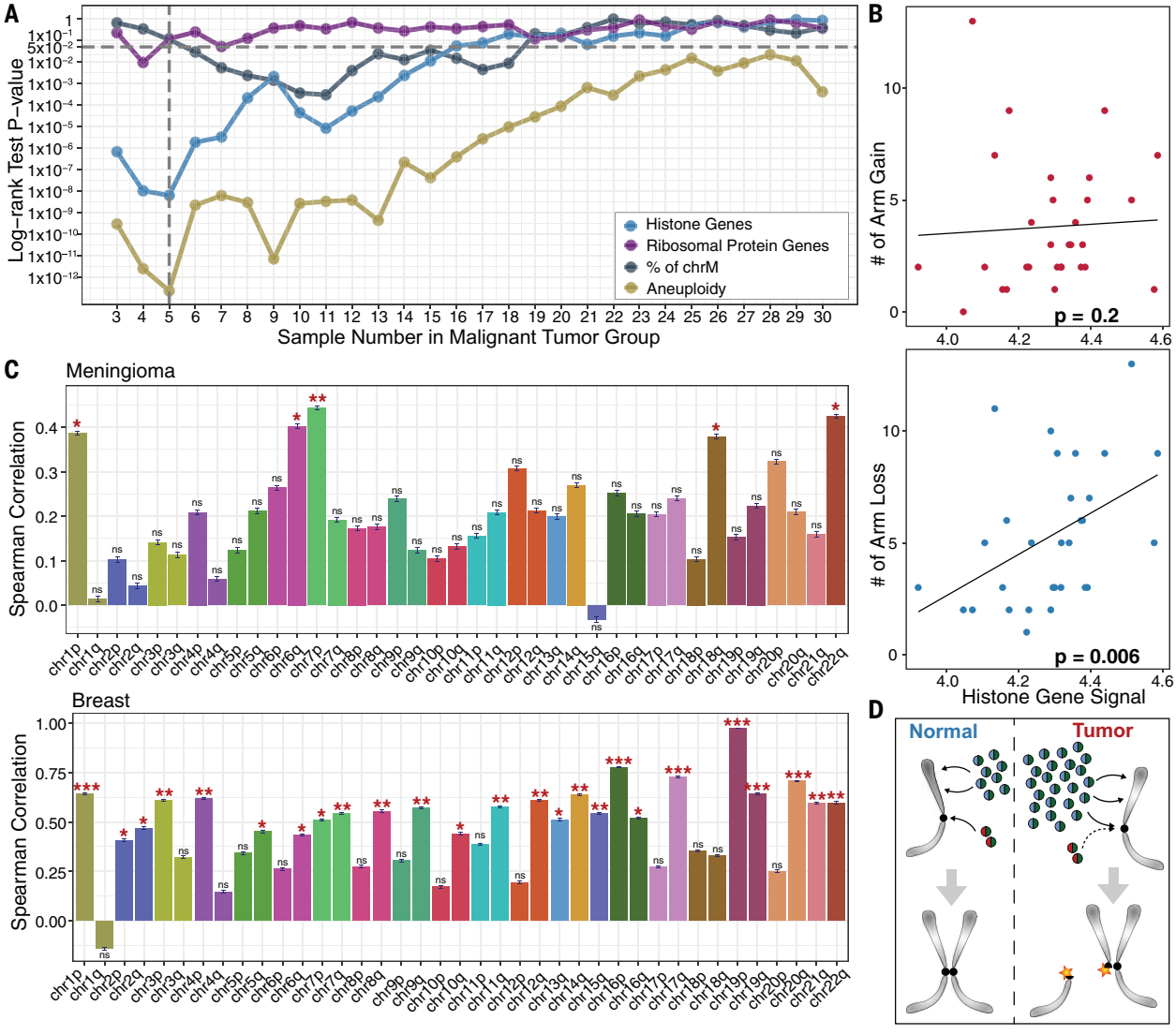


Fig. 5. RNAPII over histone genes predicts whole-arm chromosome losses. (**A**) *P*-values from the log-rank test for the KM separation of malignant from benign tumors for all thresholds of the 30 meningioma patients and the corresponding 36 FFPE-CUTAC samples for histone genes (blue), ribosomal protein genes (purple) and percent of mitochondrial DNA (gray) (Fig. 4), also including the combined aneuploidy data for all 39 chromosome arms (gold). (**B**) Scatterplots and Spearman correlations between RNAPII over histone genes and number of whole-arm gains (upper panel) and losses (lower panel) for each of the 30 meningioma patient samples. (**C**) Spearman correlations between the signal for RNAPII over histone genes and null RNAPII occupancies at cCREs for all 39 autosomal arms for meningiomas (upper panel) and breast tumors (lower panel). This summarizes correlation coefficients and significances on the correlation scatterplot in fig. S14. A negative correlation is expected if gains are more frequent than losses (i.e., chromosome arm gain will lead to a lower percentage of cCREs with zero RNAPII signals) with increasing histone gene signals and a positive correlation if losses are more frequent than gains. The error bar describing the standard deviation of the Spearman correlation coefficient is based on a 1000 bootstrap estimation. The significance level is indicated by the stars on the top of each bar with **P*-value < 0.05, ***P*-value < 0.01, and ****P*-value < 0.001. (**D**) Model for induction of centromere breaks and aneuploidy by histone gene hypertranscription. Histone H3|H4 dimers (blue-green spheres) are deposited along chromosome arms during DNA replication for chromatin duplication, while CENPA|H4 dimers (red-green spheres) are deposited at centromeres and maintain centromere identity. H3|H4 and CENPA|H4 histone dimers are preferentially deposited (black arrows) by the CAF1 and HJURP assembly factors, respectively. However, the excess H3|H4 dimers produced by hypertranscription in cancer cells compete with CENPA|H4 for centromere assembly, reducing centromere function and creating DNA breaks (*38*, *39*). Segregation of broken chromosomes leads to whole-arm aneuploidies.

recurring from benign tumors using Chr22q, the most frequently lost whole-arm (*30*) (Fig. 4B, right), and significant separation for Chr1q gains and Chr6p losses (fig. S13, E and F), the levels of significance were much lower than for separation using RNAPII at the histone genes. Our finding that high levels of RNAPII over histone genes accurately predicts poor outcomes in meningioma could imply a causal basis.

RNAPII over histone genes predicts whole-arm chromosome losses

As a positive control for separation of malignant from benign tumors, we counted total aneuploidies from RNA-seq data and observed the best separation for five malignant and 25 benign tumors, closely matching our prediction based on RNAPII at histone genes over the range of 3 to 7 malignant (Fig. 5A). This led us to ask whether there is a relationship between overproduction of histones and total aneuploidy by plotting RNAPII levels over the histone genes for each patient as a function of the total number of whole-arm chromosome gains or losses. We observed a weak, nonsignificant positive Spearman correlation with gains ($P < 0.2$), but a highly significant correlation with losses ($P < 0.006$) (Fig. 5B). To test whether this excess of losses over gains applied to all chromosome arms, for each patient we asked whether there was a net increase or decrease in the level of RNAPII over histone genes. Indeed, 38 out of 39 autosomal arms showed a net positive correlation for the meningioma patient population (Fig. 5C and fig. S14A), suggesting that RNAPII at histone genes predicts whole-arm losses in meningiomas. We confirmed this excess of whole-arm losses for the breast cancer samples, in which we also observed excesses of losses over gains for 38 out of 39 autosomal whole-arm aneuploids (Fig. 5C and fig. S14B), as expected if overexpression of histones drives both over-proliferation and whole-arm chromosome losses in cancer.

Discussion

We have demonstrated that elevated RNAPII over genes and regulatory elements is a direct measure of hypertranscription in diverse human cancers and identifies and precisely maps amplifications and selective sweeps in small clinical samples. Likewise, we observed a close correspondence between high RNAPII at the 64 S-phase-dependent histone genes consistent with cytological evidence of exceptionally high levels of RNAPII at mouse histone genes (*4*) and both RNAPII (*2*, *3*) and Myc (*32*) at Drosophila histone locus bodies exclusively during S-phase. This led us to hypothesize that the single functional role of hypertranscription in cancer is to produce enough histones to keep up with the requirement for packaging new DNA in cancer cells to proliferate faster than normal. We confirmed this prediction by performing FFPE-CUTAC on a set of 30 human meningiomas and showing that RNAPII at the 64 S-phase–dependent histone genes, which comprise only 1/100,000th of the human genome, successfully estimated WHO grade and accurately predicted rapid recurrence, which corresponds to elevated expression of proliferation genes (*30*). Although meningiomas are not invasive, elevated RNAPII at histone genes was also observed in invasive breast tumors. The ability of RNAPII FFPE-CUTAC at only the 64 histone genes to predict aggressiveness in a common intracranial tumor and in multiple breast cancer subtypes implies that a rapid polymerase chain reaction assay for histone gene RNAPII or transcription (*33*) may become an inexpensive general cancer diagnostic tool, revolutionizing precision oncology.

We also found that levels of RNAPII at the S-phase–dependent histone genes correlated with total aneuploidies, which are present in nearly all meningioma patient samples (*30*), consistent with the occurrence of ~90% whole-arm imbalances in pan-cancer data from the TCGA (*34*). Whole-arm losses were observed to be in excess of gains for 38 of the 39 autosomal arms for both meningiomas and breast tumors representing multiple subtypes. To explain how overproduction of histones might account for this notable whole-arm loss bias in patient tumors, we propose that excess H3 histones compete with CENP-A histones at S-phase for nucleosome assembly at centromeres (*35*, *36*) (Fig. 5D). Production of S-phase histones is tightly regulated (*37*) and overproduction in cancer and displacement of CENP-A nucleosomes are known to result in the generation of DNA–RNA hybrids, likely due to transcription–replication conflicts causing delayed DNA replication, centromere breakage, and loss of whole chromosome arms (*38*, *39*). Thus, RNAPII excess over histone genes at S-phase provides a mechanistic basis for understanding not only how cancer cells can proliferate faster than their neighbors but also how this process might generate centromeric breaks and whole-arm imbalances that drive most cancers.

REFERENCES AND NOTES

1. M. Zatzman *et al*., *Sci. Adv.* **8**, eabn0238 (2022).
2. F. Lu *et al*, Integrator-mediated clustering of poised RNA polymerase II synchronizes histone transcription. bioRxiv 2023.10.07.561364 [Preprint] (2023).
3. S. K. Huang, P. H. Whitney, S. Dutta, S. Y. Shvartsman, C. A. Rushlow, *Curr. Biol.* **31**, 5102–5110.e5 (2021).
4. D. B. Mahat *et al*., *Nature* **631**, 216–223 (2024).
5. R. Milo, R. Phillips, *Cell Biology by the Numbers* (Garland Science, 2016).
6. S. Henikoff *et al*., *Nat. Commun.* **14**, 5930 (2023).
7. J. E. Moore *et al*., *Nature* **583**, 699–710 (2020).
8. T. Ozawa *et al*., *Cell Rep.* **23**, 3787–3797 (2018).
9. F. Szulzewsky *et al*., *Genes Dev.* **34**, 1051–1064 (2020).
10. C. Dai *et al*., *Genes Dev.* **15**, 1913–1925 (2001).
11. D. G. Altman, J. M. Bland, *Statistician* **32**, 307 (1983).
12. S. Patange *et al*., *Cell Rep.* **38**, 110292 (2022).
13. M. P. Meers, D. Tenenbaum, S. Henikoff, *Epigenetics Chromatin* **12**, 42 (2019).
14. E. Reznik *et al*., *eLife* **5**, e10769 (2016).
15. H. Zhang *et al*., *Histopathology* **85**, 3–19 (2024).
16. S. Henikoff, J. G. Henikoff, K. Ahmad, *bio-protocol* **11**, e4043 (2021).
17. D. H. Janssens *et al*., *Genome Biol.* **23**, 81 (2022).
18. X. Deng *et al*., *Dev. Cell* **25**, 55–68 (2013).
19. Y. Fan *et al*., *BMC Genomics* **24**, 391 (2023).
20. D. Yang *et al*., *Cell* **185**, 1905–1923.e25 (2022).
21. X. Yan, P. Mischel, H. Chang, *Nat. Rev. Cancer* **24**, 261–273 (2024).
22. R. J. Kaufman, P. C. Brown, R. T. Schimke, *Proc. Natl. Acad. Sci. U.S.A.* **76**, 5669–5673 (1979).
23. P. C. Nowell, *Science* **194**, 23–28 (1976).
24. J. R. M. Black, N. McGranahan, *Nat. Rev. Cancer* **21**, 379–392 (2021).
25. D. L. Schaff, A. J. Fasse, P. E. White, R. J. Vander Velde, S. M. Shaffer, *Cell Syst.* **15**, 213–226.e9 (2024).
26. M. Forster-Sack *et al*., *J. Pathol. Clin. Res.* **10**, e12362 (2024).
27. M. Marotta *et al*., *Sci. Rep.* **7**, 41921 (2017).
28. B. Bartkowiak *et al*., *Genes Dev.* **24**, 2303–2316 (2010).
29. M. Tellier *et al*., *Nucleic Acids Res.* **48**, 7712–7727 (2020).
30. H. N. Thirimanne *et al*., *Cell Genom.* **4**, 100566 (2024).
31. S. Goebel, H. M. Mehdorn, *Support. Care Cancer* **21**, 1365–1372 (2013)
32. K. Daneshvar, A. Khan, J. M. Goodliffe, *PLOS ONE* **6**, e23928 (2011).
33. R. Sun, H. Qi, *Gene Expr. Patterns* **14**, 30–41 (2014).
34. J. Shih *et al*., *Nature* **619**, 793–800 (2023).
35. C. C. Chen *et al*., *Dev. Cell* **34**, 73–84 (2015).
36. M. D. Blower, B. A. Sullivan, G. H. Karpen, *Dev. Cell* **2**, 319–330 (2002).
37. W. F. Marzluff, R. J. Duronio, *Curr. Opin. Cell Biol.* **14**, 692–699 (2002).
38. S. Giunta *et al*., *Proc. Natl. Acad. Sci. U.S.A.* **118**, e2015634118 (2021).
39. A. Scelfo *et al*., *Mol. Cell* **84**, 1003–1020.e10 (2024).
40. S. Henikoff *et al*., Genomic Data for: RNA Polymerase II at histone genes predicts outcome in human cancer, Version v1, Zenodo (2024); https://doi.org/10.5281/zenodo.13138686.
41. S. Henikoff *et al*., Customized Codes for Manuscript: RNA Polymerase II at histone genes predicts outcome in human cancer, Version v1, Zenodo (2025); https://doi.org/10.5281/zenodo.14649635.

ACKNOWLEDGMENTS

We thank C. Codomo and T. Bryson for technical assistance, the Fred Hutch Genomics Shared Resource for sequencing and data processing and the Fred Hutch Experimental Histopathology Shared Resource for FFPE processing and analysis, Oregon Health Sciences University Knight Biolibrary for breast tumor FFPEs, and R. Corces for advice on ATAC-seq data availability. **Funding:** This work was supported by the Howard Hughes Medical Institute (to S.H.), National Institutes of Health grant HG012797 (to Y.Z.), and grant T32CA009515 from the National Cancer Institute (to R.M.P.). **Author contributions:** Conceptualization: S.H., Y.Z., and K.A. Methodology: S.H., Y.Z., J.E.G., J.G.H., and H.N.T. Investigation: S.H., Y.Z., R.M.P., Y.X., J.E.G., J.G.H., Z.R.R., F.S., H.N.T., K.A. Funding acquisition: S.H. Supervision: S.H., E.C.H., S.K., K.A. Writing – original draft: S.H. Writing – review and editing: S.H., Y.Z., J.G.H., S.K., E.C.H., K.A. **Competing interests:** S.H., Y.Z., and K.A. have applied for patents (USPTO application numbers 63/505,964 and 63/683,342) on related work. All other authors declare no competing interests. **Data and materials availability:** The sequencing data generated in this study have been deposited in the NCBI GEO database under accession code GSE261351. The raw sequencing data generated from the University of Washington samples are not made available due to data privacy laws. Processed FFPE-CUTAC data for these samples have been deposited on Zenodo (*40*). Custom scripts used in this study are also available from Zenodo (*41*). **License information:** Copyright © 2025 the authors, some rights reserved; exclusive licensee American Association for the Advancement of Science. No claim to original US government works. https://www.science.org/about/science-licenses-journal-article-reuse. This article is subject to HHMI's Open Access to Publications policy. HHMI lab heads have previously granted a nonexclusive CC BY 4.0 license to the public and a sublicensable license to HHMI in their research articles. Pursuant to those licenses, the Author Accepted Manuscript (AAM) of this article can be made freely available under a CC BY 4.0 license immediately upon publication.

SUPPLEMENTARY MATERIALS

science.org/doi/10.1126/science.ads2169
Materials and Methods
Supplementary Text
Figs. S1 to S14
Tables S1 and S2
References (*42*–*50*)

Submitted 2 August 2024; resubmitted 5 November 2024
Accepted 15 January 2025
10.1126/science.ads2169

CATALYSIS

Selective chemical looping combustion of acetylene in ethylene-rich streams

Matthew Jacob[1], Huy Nguyen[1], Rishi Raj[1], Javier Garcia-Barriocanal[2], Jiyun Hong[3], Jorge E. Perez-Aguilar[3], Adam S. Hoffman[3], K. Andre Mkhoyan[1], Simon R. Bare[3], Matthew Neurock[1], Aditya Bhan[1]*

The requirement for C_2H_2 concentrations below 2 parts per million (ppm) in gas streams for C_2H_4 polymerization necessitates its semihydrogenation to C_2H_4. We demonstrate selective chemical looping combustion of C_2H_2 in C_2H_4-rich streams by Bi_2O_3 as an alternative catalytic pathway to reduce C_2H_2 concentration below 2 ppm. Bi_2O_3 combusts C_2H_2 with a first-order rate constant that is 3000 times greater than the rate constant for C_2H_4 combustion. In successive redox cycles, the lattice O of Bi_2O_3 can be fully replenished without discernible changes in local Bi coordination or C_2H_2 combustion selectivity. Heterolytic activation of C–H bonds across Bi–O sites and the higher acidity of C_2H_2 results in lower barriers for C_2H_2 activation than C_2H_4, enabling selective catalytic hydrocarbon combustion leveraging differences in molecular deprotonation energies.

C_2H_2 concentrations in C_2H_4 must be <2 parts per million (ppm) to prevent deactivation of C_2H_4 polymerization catalysts (*1*–*3*). Industrially, the most common route to produce C_2H_4 involves steam cracking of saturated hydrocarbon feedstocks such as naphtha, which results in C_2H_2 formation as a by-product up to 2.5 wt % (*4*, *5*). C_2H_2 semihydrogenation on Pd-based catalysts at temperatures ranging from 373 to 523 K and moderate pressures of ~5 bar is used to enhance C_2H_4 yields and reduce C_2H_2 concentrations to <2 ppm (*6*). To enable C_2H_2 semihydrogenation at appreciable rates, the catalyst must be proficient in adsorbing H_2 and C_2H_2 but must desorb C_2H_4 before it can be further hydrogenated or oligomerized. Alloying Pd-based catalysts with other metals such as Ag (*7*–*10*), Ga (*11*), or Cu (*12*, *13*) improves C_2H_4 yields by modifying the electronic properties of the active site to either bind C_2H_2 or H_2 more strongly, thus enhancing rates, or by lowering the barrier for C_2H_4 desorption relative to the barrier for the thermodynamically favored hydrogenation to C_2H_6, thus enhancing selectivity. However, modification of the electronic properties of the active site to decrease the barrier for C_2H_4 desorption typically results in weaker adsorption of C_2H_2, leading to lower rates (*7*, *8*, *10*).

An alternative strategy to selectively remove C_2H_2 from C_2H_4-rich gas streams uses a reducible oxide to selectively activate the C–H bonds of C_2H_2, initiating a reaction cascade that results in combustion. Hydrocarbon combustion at high temperatures (>1000 K) with O_2 cofeeds is a radical-mediated process that results in the indiscriminate activation of hydrocarbons and in limited selectivity to combustion of one hydrocarbon in a mixture (*14*, *15*). The use of a solid oxygen carrier as the active oxidant for hydrocarbon combustion in the absence of gaseous O_2 has been demonstrated with numerous material formulations, but no selective hydrocarbon combustion processes have been reported.

By using an oxide with active sites that selectively activate C–H bonds of C_2H_2, lattice O can be discharged stoichiometrically to combust C_2H_2 in mixtures with C_2H_4 during reduction half-cycles and replenished by air during oxidation half cycles. Separation of the reduction and oxidation half-cycles avoids flammability concerns associated with high-temperature combustion and the formation of unselective oxygen species upon the conversion of molecular oxygen (O_2). The viability of such a process is predicated upon the selectivity for C_2H_2 combustion during reduction half–cycles and the regenerability of the oxide after redox cycling.

Bi_2O_3, a post-transition metal oxide with highly reducible (*16*) and mobile lattice O (*17*, *18*) that has been used in fuel cells as a solid electrolyte (*18*, *19*), in gas-sensing applications (*20*, *21*), and as a selective hydrogen combustion catalyst (*22*–*25*), is reported herein to reduce C_2H_2 concentrations to <2 ppm in C_2H_4-rich streams in a chemical looping operation. The regenerability of C_2H_2 combustion rates in successive stoichiometric redox cycles in which 20 to 30% of O atoms in Bi_2O_3 are removed during each reduction step and fully replenished with O_2 demonstrates the feasibility of removing trace quantities of C_2H_2 in mixtures with excess C_2H_4. Kinetic analyses show that the rate constant for C_2H_2 combustion, which is unconvoluted by diffusion of O to catalytically relevant surfaces, exceeds the C_2H_4 combustion rate constant by a factor of 3000, a property afforded by heterolytic C–H activation on Bi–O sites. Redox cycling alters Bi_2O_3 surface morphology without the formation of new Bi or Bi_2O_3 phases with lower selectivity to C_2H_2 combustion.

Reaction studies

We exposed C_2H_2 and C_2H_4 to bulk Bi_2O_3 with a Brunauer-Emmett-Teller (BET) surface area of 0.2 $m^2\ g^{-1}$ in an air-free recirculating batch reactor system (see fig. S1 for a reactor schematic). The mass loading of Bi_2O_3, and thus the amount of O available for reaction, was modulated to ensure that <20% of lattice O atoms were removed during reduction half-cycles in a recirculating batch reactor. Upon exposure of an equimolar mixture of C_2H_2 and C_2H_4 to Bi_2O_3 at 773 K (Fig. 1A), the C_2H_2 partial pressure dropped from 28,000 to 3 ppm within 20 min, whereas the C_2H_4 partial pressure dropped from 2.48 to 2.40 kPa. The C_2H_2 concentration dropped <1 ppm within 1 hour, and the C_2H_4 partial pressure remained at 2.40 kPa.

The feasibility of selective C_2H_2 combustion was examined with a 65:1 C_2H_4:C_2H_2 molar ratio gas mixture representative of naphtha steam-cracking effluent gas compositions containing up to 1.4 wt % C_2H_2 (*4*). In the dilute mixture (Fig. 1B), the conversions of C_2H_2 and C_2H_4 after 2.5 hours at 673 K were 99.8% and <2%, respectively, before the C_2H_2 concentration was too low to measure due to overlap with the peak for C_2H_4 in the gas chromatograph. Even after redox cycling, in which 20 to 30% of O atoms were removed from the oxide by C_2H_2 combustion and fully replenished by reoxidation with O_2 in 10 successive redox cycles, the redox-cycled Bi_2O_3 sample exposed to an equimolar mixture of C_2H_2 and C_2H_4 at 773 K could reduce the C_2H_2 concentration from 26,600 to <1 ppm in <50 min at 773 K whereas C_2H_4 conversion remained <3% (Fig. 1C).

The selectivities to C_2H_2 combustion, as evaluated by comparison of the pseudo-first-order rate constants for C_2H_2 and C_2H_4 consumption in each mixture examined in Fig. 1, A to C, are shown in Fig. 1D. The selectivity to C_2H_2 combustion exceeded 99% in every case, with no change in selectivity observed for a redox-cycled Bi_2O_3 sample relative to a fresh sample, showing that redox-cycled Bi_2O_3 remained as effective as fresh Bi_2O_3 in removing C_2H_2 from gas streams containing C_2H_4. These high selectivities persisted despite the transient evolution of the ensemble of exposed active sites during stoichiometric reduction cycles that removed O atoms from the oxide. This suggests that, on average, the difference in activation barriers for C_2H_2 and C_2H_4 did not change appreciably on the ensemble of Bi–O active sites available for combustion. These results were corroborated computationally (see below) by observation of the same difference in transition state energy for the C–H activation of C_2H_2 and C_2H_4 on Bi–O sites with varying

[1]Department of Chemical Engineering and Materials Science, University of Minnesota, Minneapolis, MN, USA. [2]Characterization Facility, University of Minnesota, Minneapolis, MN, USA. [3]Stanford Synchrotron Radiation Lightsource, SLAC National Accelerator Laboratory, Menlo Park, CA, USA.
*Corresponding author. Email: abhan@umn.edu

Bi–O bond lengths to simulate real catalysts that were partially reduced to expose active sites with varying coordination environments and surface terminations.

The longevity of Bi_2O_3 used for selective C_2H_2 combustion with repeated redox cycling was evaluated in a flow reactor (see fig. S2 for a reactor schematic). During reduction half-cycles, Bi_2O_3 was exposed to an equimolar mixture of C_2H_2 and C_2H_4 at 673 K to remove lattice O atoms as CO_2 and H_2O. After an intervening purge of the system with inert He, the partially reduced Bi_2O_3 was exposed to O_2 to replenish lattice O in the bulk metal oxide abstracted during the reduction cycle. Samples referred to hereafter as redox-cycled were prepared during this experiment. Figure 1E shows the integrated amounts of O removed from the oxide as CO_2 and H_2O and added to the oxide from O_2 consumption during reduction and oxidation cycles, respectively, relative to the total amount of O in fully stoichiometric Bi_2O_3.

During the oxidation cycles, all lattice O atoms removed by reduction in equimolar C_2H_2 or C_2H_4 could be fully regenerated, as illustrated by O removed during the reduction step being equal to the O added during the subsequent oxidation step. Differences in O removed or added reflect slight variations in the length of the reduction step; the last reduction step was allowed to progress for slightly longer and removed 30% of O atoms from the oxide, all of which were replenished by oxidation.

Figure 1F compares the rates of C_2H_2 consumption during each reduction half-cycle and shows that when the Bi_2O_3 catalyst was not over-reduced during reduction, C_2H_2 consumption rates were regenerable for 10 redox cycles. Additional experimental details of the reduction and oxidation half cycles can be found in figs. S3 to S5; an analogous experiment is shown in fig. S6 that exposed Bi_2O_3

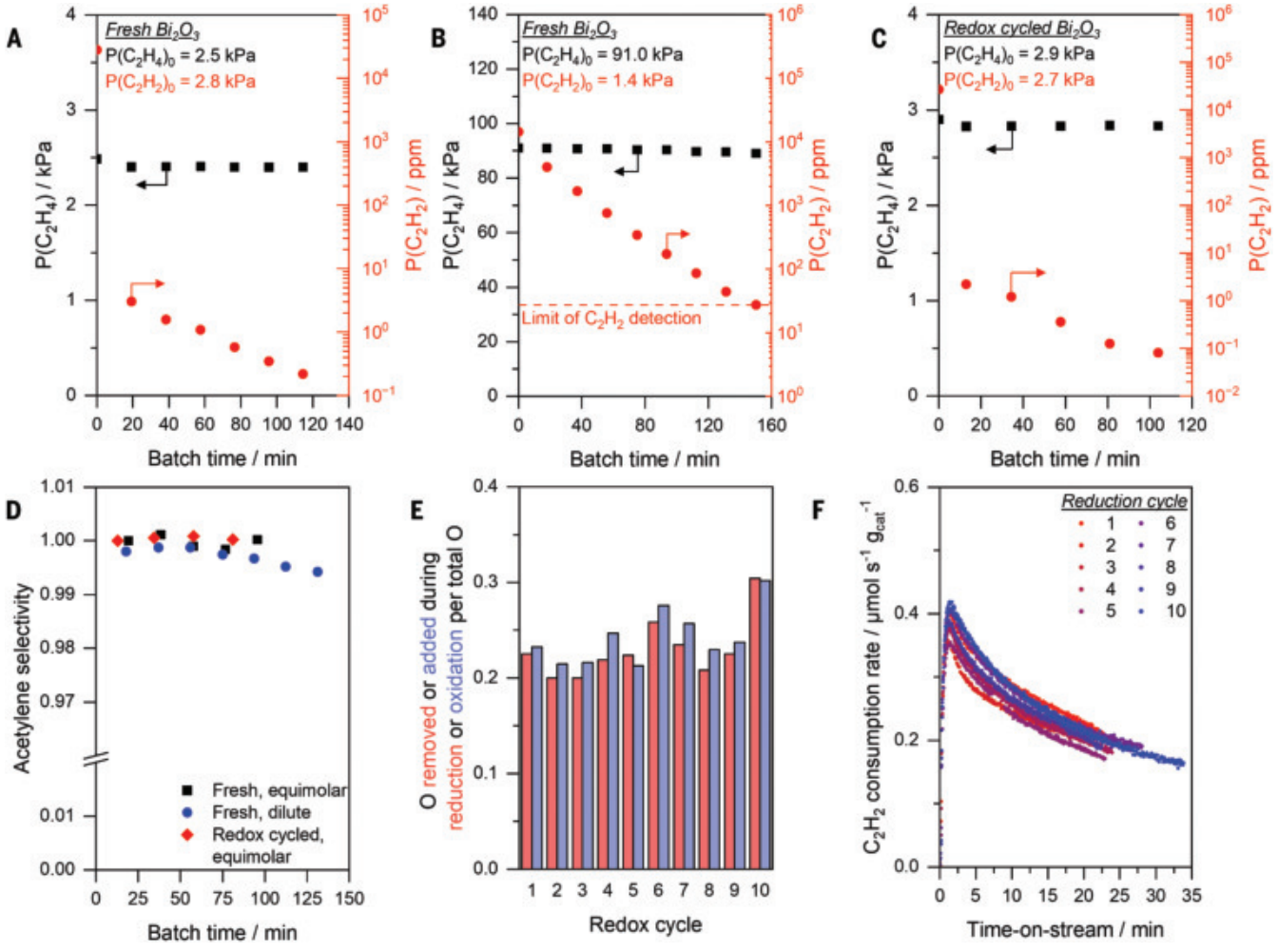


Fig. 1. Demonstration of selective removal of C_2H_2 from C_2H_4 streams. (**A** to **C**) Selective catalytic combustion of C_2H_2 in C_2H_4 for fresh Bi_2O_3 in an equimolar mixture (A) and a dilute mixture (B) and for redox-cycled Bi_2O_3 in an equimolar mixture (C). (**D**) C_2H_2 selectivity as a function of batch time for the data shown in (A) to (C), ($S = \frac{\hat{k}(C_2H_2)}{\hat{k}(C_2H_2)+\hat{k}(C_2H_4)}$, where $\hat{k}$ denotes the first-order rate constant for the consumption of C_2H_2 or C_2H_4, in μmol s^{-1} g_{cat}^{-1} kPa^{-1}). (**E** and **F**) Amount of oxygen removed or added from the catalyst in each redox cycle relative to the total number of O atoms in fresh Bi_2O_3 (E) and rates of C_2H_2 consumption in the reduction cycles of successive chemical looping reduction/oxidation cycles (F). Batch reaction conditions for (A): m(Bi_2O_3) = 251.1 mg, T = 773 K, $P(C_2H_4)_0$ = 2.5 kPa, $P(C_2H_2)_0$ = 2.8 kPa, $P(He)_0$ = 6.4 kPa, balance N_2. Batch reaction conditions for (B): m(Bi_2O_3) = 254.7 mg, T = 663 K, $P(C_2H_4)_0$ = 91 kPa, $P(C_2H_2)_0$ = 1.4 kPa, $P(He)_0$ = 6.4 kPa, balance N_2. Batch reaction conditions for (C): m(redox-cycled Bi_2O_3) = 261.0 mg, T = 773 K, $P(C_2H_4)_0$ = 2.9 kPa, $P(C_2H_2)_0$ = 2.7 kPa, $P(CH_4)_0$ = 5.3 kPa, $P(He)_0$ = 45.9 kPa, balance N_2. Flow reaction conditions for (E) and (F): m(Bi_2O_3) = 1004.2 mg, T = 673 K. Reduction conditions: $P(C_2H_4)_0$ = $P(C_2H_2)_0$ = 1.1 kPa, $P(CH_4)_0$ = 1.4 kPa, $P(N_2)_0$ = 20.9 kPa, balance Ar, total flow rate = 1.67 cm^3_{STP} s^{-1}. Oxidation conditions: $P(O_2)_0$ = 2.4 kPa, $P(He)_0$ = 21.8 kPa, balance Ar, total flow rate = 1.67 cm^3_{STP} s^{-1}. The catalyst was isolated in 0.17 cm^3_{STP} s^{-1} He between reduction and oxidation treatments.

to only C_2H_4 as a reductant to demonstrate the low reactivity of C_2H_4. The reproducibility of C_2H_2 combustion rates and full reoxidation of partially reduced Bi_2O_3 in repeated reduction and oxidation cycles were also verified in redox cycling experiments removing only 10% of O atoms in each reduction step, as shown in figs. S7 and S8.

Kinetic studies

Chemical looping reduction and oxidation cycles necessarily involve simultaneous kinetic rate processes involving lattice O abstraction by the reacting hydrocarbon and physical rate processes involving diffusion of lattice O to O-deficient regions on the surface of the catalyst. The surface coverage of lattice O atoms during redox half-cycles is dictated by the rate at which lattice O is supplied to surface O vacancies relative to the rate at which surface O is removed by combustion. We investigated the contributions of lattice O diffusion to measured C_2H_2 combustion kinetics with a dwell experiment (*26*). During a stoichiometric reduction cycle, an inert dwell step was used to redistribute lattice O atoms throughout the oxide and alleviate any gradients in O concentration. Equal combustion product evolution rates before and after the inert dwell step indicated that the reductant contacted a surface with equal chemical potential of the oxidant before and after the inert dwell step, showing that lattice O diffusion is fast relative to surface lattice O abstraction by combustion. Figure 2A depicts the results of a dwell experiment with an intervening He purge lasting 25 min after removal of 7% of lattice O atoms in Bi_2O_3 in 1:10 C_2H_2:C_2H_4. The same H_2O and CO_2 evolution rates were observed before and after the inert dwell step, indicating that lattice O diffusion was faster than surface reaction kinetics; therefore, the measured C_2H_2 combustion kinetics

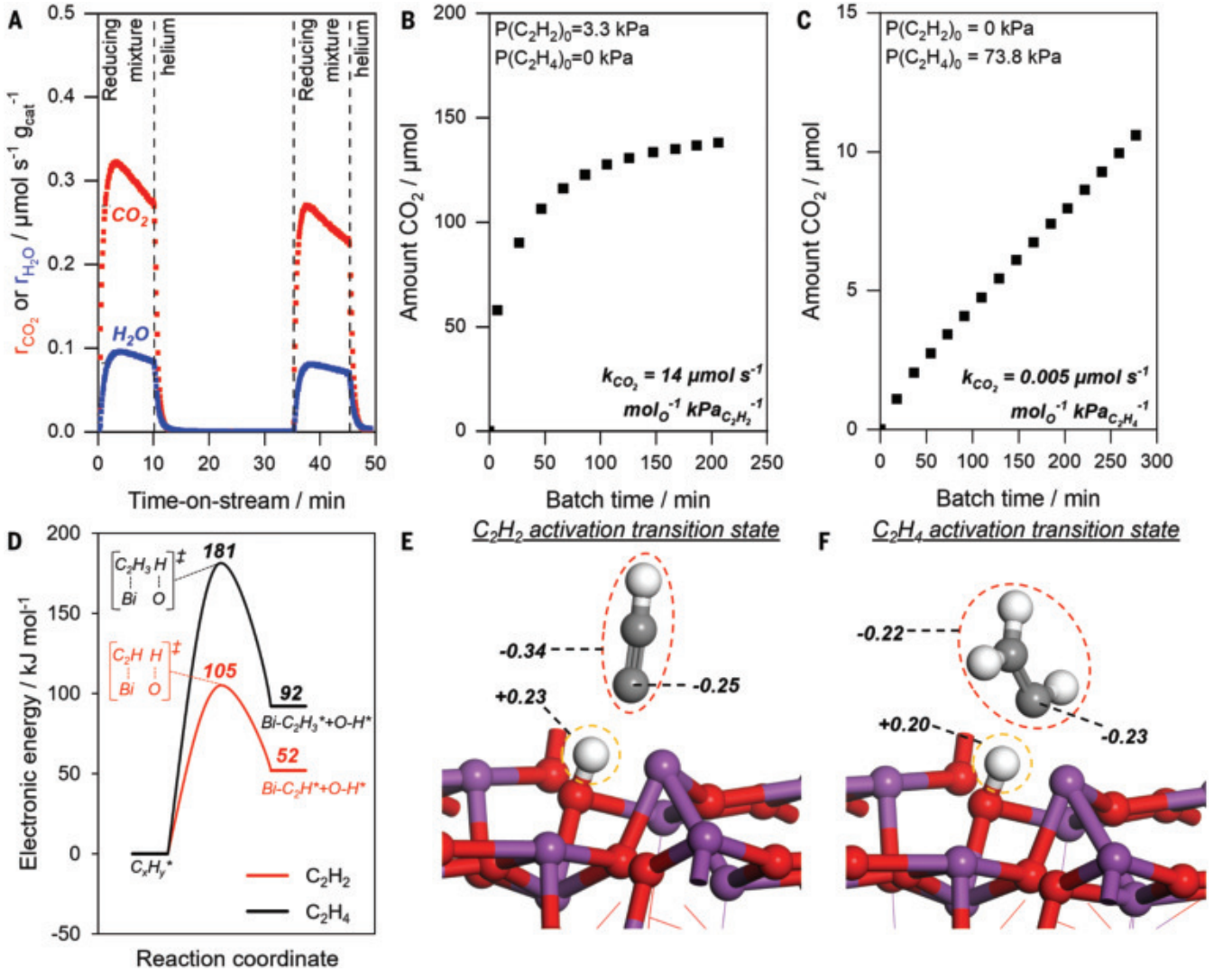


Fig. 2. Kinetics of C_2H_2 and C_2H_4 activation. (**A**) Dwell experiment showing combustion product evolution rates upon exposure of Bi_2O_3 to 1:10 C_2H_2:C_2H_4 before and after He treatment. (**B** and **C**) Amount of CO_2 formed upon exposure of Bi_2O_3 to C_2H_2 with no C_2H_4 (B) and C_2H_4 with no C_2H_2 in a recirculating batch reactor at 663 K (C). (**D** to **F**) Reaction energy diagram for C–H activation of C_2H_2 and C_2H_4 across a nonbonded Bi–O site (D) and the corresponding transitions states for C_2H_2 (E) and C_2H_4 (F). Transition state and product state energies are referenced to the physisorbed state. The numbers correspond to charges on C and H atoms and the C_xH_y fragment formed in the C–H scission transition state. Bi atoms are purple, O atoms are red, C atoms are gray, and H atoms are white. Flow reaction conditions for (A): m(Bi_2O_3) = 1.0 g, T = 673 K, $P(C_2H_2)$ = 2.2 kPa, $P(C_2H_4)$ = 21.5 kPa, $P(CH_4)$ = 2 kPa, P(Ar) = 34.8 kPa, balance N_2, total flow rate = 0.83 cm^3_{STP} s^{-1}. During the dwell step, the catalyst was exposed to He with a flow rate of 0.83 cm^3_{STP} s^{-1}. Batch reaction conditions for (B): m(Bi_2O_3) = 258.4 mg, T = 663 K, $P(C_2H_2)_0$ = 3.3 kPa, $P(C_2H_4)_0$ = 0 kPa, $P(CH_4)_0$ = 2.1 kPa, $P(He)_0$ = 51.4 kPa, balance N_2. Batch reaction conditions for (C): m(Bi_2O_3) = 250.0 mg, T = 663 K, $P(C_2H_2)_0$ = 0 kPa, $P(C_2H_4)_0$ = 73.8 kPa, $P(Ar)_0$ = 2.5 kPa, balance He.

were not convoluted by lattice O diffusion at 673 K. Equivalent rates of C_2H_2 consumption before and after the dwell step (fig. S9) corroborated this result.

Dwell experiments were repeated at a range of viable process conditions. Bi_2O_3 combusted C_2H_2 at temperatures as low as 555 K (fig. S10). Dwell experiments at 573 K (fig. S11) and 773 K (fig. S12) showed that lattice O diffusion constraints only became relevant at 773 K. At 673 K, however, comparison of the rate of lattice O removal by C_2H_2 combustion and a lower bound on the rate of lattice O diffusion revealed that lattice O diffusion rates exceeded rates of lattice O abstraction by C_2H_2 combustion by a factor >12 (figs. S13 and S14), indicating that C_2H_2 activation kinetics measured at 663 K were limited solely by rates of surface reactions. Further discussion on the barrier for O diffusion in Bi_2O_3 is provided in the text accompanying fig. S15.

Rate constants for C_2H_2 and C_2H_4 combustion, free from O diffusion limitations, were assessed independently to determine whether the lack in reactivity of C_2H_4 in the presence of C_2H_2 was caused by suppression or occupancy of C_2H_4 combustion sites by C_2H_2. During a batch reaction with C_2H_2 exposed to Bi_2O_3, C_2H_2 combusted to produce CO_2 (Fig. 2B); however, the rate at which CO_2 was produced decreased as the reaction progressed because of stoichiometric consumption of lattice O by C_2H_2, resulting in a lower C_2H_2 concentration and in fewer lattice O atoms remaining.

After accounting for the decrease in lattice O during stoichiometric reduction half-cycles by normalizing combustion rates by remaining O atoms, we found that C_2H_2 combustion was first order in C_2H_2 pressure with a rate constant for CO_2 formation of 14 μmol CO_2 s^{-1} mol_O^{-1} $kPa_{C_2H_2}^{-1}$ at 663 K and an apparent barrier for C_2H_2 activation of 113 ± 8 kJ mol^{-1} (fig. S16) in absence of heat and mass transport limitations (see Eqs. S7 to S19 and the accompanying discussion). The individual rate constant for C_2H_4 combustion assessed in the absence of C_2H_2 was 0.005 μmol CO_2 s^{-1} mol_O^{-1} $kPa_{C_2H_4}^{-1}$ (Fig. 2C), 3000× smaller than the C_2H_2 combustion rate constant, demonstrating that occupancy of catalytically relevant sites for C_2H_4 combustion by C_2H_2 was not responsible for the high selectivity to C_2H_2 observed in molecular mixtures. The measured apparent barrier for C_2H_4 activation of 165 ± 20 kJ mol^{-1} (fig. S17) led to a difference between the experimentally measured apparent activation barriers for C_2H_2 and C_2H_4 of 52 kJ mol^{-1}, supporting the hypothesis that activation of C_2H_4 on bare Bi_2O_3 surfaces was energetically disfavored relative to activation of C_2H_2. Enumeration of the rate constants for C_2H_2 activation with CO_2, C_2H_4, and H_2O cofeeds (figs. S18 to S20) showed that C_2H_2 activation rates were not inhibited by surface coverages of CO_2, C_2H_4, or H_2O. A rate constant for H_2 combustion on Bi_2O_3 at 663 K of 5.6 μmol H_2 s^{-1} mol_O^{-1} kPa_{H2}^{-1} (fig. S21) indicated that H_2 present in real feeds containing C_2H_2 and H_2 may combust to remove lattice O as well.

Theoretical studies

First-principles density functional theory (DFT) calculations were performed to examine the adsorption and activation of C_2H_2 and C_2H_4 over a model (010) surface of α-Bi_2O_3 and in turn elucidate the mechanistic origin for the high reactivity of C_2H_2 on Bi_2O_3. Previous calculations showed that the (010) surface is the lowest-energy α-Bi_2O_3 surface (*27*) and provided valuable insights into the oxidation of hydrogen on Bi_2O_3 (*28*). Calculations herein showed that C_2H_2 as well as C_2H_4 weakly adsorbed on exposed Bi sites with an energy of −11 kJ mol^{-1}. The C–H bonds of C_2H_2 and C_2H_4 could be cleaved homolytically on O–O or Bi–Bi site pairs or heterolytically across Bi–O site pairs. Homolytic activation of C_2H_2 on undercoordinated Bi sites proceeded through metal insertion into the C–H bond, resulting in an activation energy of 148 kJ mol^{-1} (see figs. S22 and S23 for details of the Bi_2O_3 models used for the periodic and cluster calculations, respectively; fig. S24, A to C, for reactant, transition state, and product state geometries; and table S1 for Bi–H and Bi–C bond lengths). Attempts to activate C_2H_2 across O–O site pairs instead converged to a heterolytic transition state across a Bi–O site.

In the heterolytic C–H activation of C_2H_2 and C_2H_4 over Bi–O site pairs, a proton and a negatively charged carbanion formed that were stabilized by the negative O^{2-} and positive Bi^{3+} charged surface sites, respectively. We investigated C–H activation of C_2H_2 and C_2H_4 on different active sites on the (010) α-Bi_2O_3 surface composed of undercoordinated Bi_{3c}^{3+} and O^{2-} site pairs involving: (i) bonded Bi_{3c}–O and (ii) nonbonded Bi_{3c}–O site pairs, with respective Bi–O distances of 2.16 and 3.09 Å. Given the ensemble of Bi–O sites exposed on α-Bi_2O_3 surfaces during reaction, these sites represented limiting cases of sites with varying Bi–O distances across which C–H bonds may be activated.

The C–H activation barrier for C_2H_2 over the nonbonded Bi–O site was calculated to be slightly higher at 105 kJ mol^{-1} (Fig. 2D; fig. S24, D to F; and table S1) than over the bonded Bi–O site at 87 kJ mol^{-1} (fig. S24, G to I, and table S1), with overall reaction energies of 52 and 77 kJ mol^{-1}, respectively. Activation of C_2H_4 on the nonbonded and bonded Bi–O sites proceeded with transition state energies of 181 kJ mol^{-1} (Fig. 2D; fig. S25, A to C; and table S2) and 162 kJ mol^{-1} (fig. S25, D to F, and table S2) and overall reaction energies of 92 and 140 kJ mol^{-1}, respectively.

The transition state geometries that contribute to the differences in transition state energies on Bi–O sites are illustrated in fig. S26. Although C–H activation of C_2H_2 and C_2H_4 over nonbonded Bi–O sites resulted in transition state energies that were 18 and 19 kJ mol^{-1} higher, respectively, than on bonded Bi–O sites, these limiting cases resulted in C–H activation barriers for C_2H_2 that were 75 and 76 kJ mol^{-1} more favorable than C_2H_4, respectively, as illustrated in Fig. 2D over nonbonded Bi–O sites. Chemical looping reduction cycles may lead to a distribution of sites that contribute unequally to measured rates of hydrocarbon activation, but we do not expect that evolution of the ensemble of exposed sites would lead to changes in selectivity to C_2H_2 activation. Experimentally, no changes in the >99% selectivity to C_2H_2 activation were observed in redox-cycling experiments during removal of up to 20% of total lattice O atoms in Bi_2O_3 (Fig. 1D).

The results in Fig. 2, E and F, provide additional evidence for the heterolytic nature of the activation steps for C_2H_2 and C_2H_4, respectively, by showing the charges on the H atoms and C_xH_y fragments in the transition state (enumerated by cluster calculations). The hydrogen atoms formed upon the C–H scission of both molecules become protonic, with positive atomic charges of +0.23 e and +0.20 e for C_2H_2 and C_2H_4 activation, respectively. The electrons in the C–H bond localized in the residual hydrocarbon fragment, yielding anionic CH≡C(−) and CH_2=CH(−) fragments with overall charges of −0.34 e and −0.22 e, respectively.

The preferential stabilization of the C_2H_2 activation transition state appeared to be the result of C_2H_2 tending to cleave heterolytically with energy given by the deprotonation energy (DPE), rather than homolytically with energy given by the bond dissociation energy (BDE). Although C_2H_2 is more difficult to activate homolytically in the gas phase than C_2H_4 [BDE = 558 kJ mol^{-1} versus 464 kJ mol^{-1} (*29*)], heterolytic dissociation of the C–H bond in C_2H_2 is 125 kJ mol^{-1} more favorable than C_2H_4 [DPE = 1580 kJ mol^{-1} versus 1705 kJ mol^{-1} (*30*)]. The higher acidity of the C–H bond in C_2H_2 results from the higher stability of the resulting CH≡C(−) anion, which has more s character (50%) than the resulting CH_2=CH(−) anion (33.3%), and thus allows the excess electron density to lie closer to the nuclei.

Despite differences in transition state lateness on bonded and nonbonded Bi–O sites, the C–H activation transition states for both C_2H_2 and C_2H_4 were late as assessed by the O-H and Bi–C bond lengths relative to the reactant and product states (tables S1 and S2) and involved the near complete dissociation of the C–H bonds. The transition state energies reflect, in part, contributions from the DPEs of C_2H_2 and C_2H_4, resulting in a lower barrier for C_2H_2 activation on Bi–O than C_2H_4. Based on the hypothesis that rates of hydrocarbon combustion initiated by rate-determining heterolytic C–H scission will scale with molecular DPEs, we investigated the viability of extrapolating this concept to other

hydrocarbon mixtures by examining selective combustion of 1,3-butadiene in propane on Bi_2O_3. 1,3-butadiene has a DPE [1672 kJ mol^{-1} (*30*)] that is 83 kJ mol^{-1} lower than that of propane [1755 kJ mol^{-1} (*30*)] but a BDE [445 kJ mol^{-1} (*31*)] that is 34 kJ mol^{-1} higher than propane [411 kJ mol^{-1} (*29*)].

At 773 K, Bi_2O_3 selectively combusted 1,3-butadiene with > 98% selectivity (fig. S27), consistent with selective combustion of the more acidic C–H bonds in 1,3-butadiene in mixtures with propane. Further discussion on the use of Bi_2O_3 as a combustion catalyst for 1-butene and 1,3-butadiene is provided in the discussion accompanying figs. S28 and S29. Low BDE values for molecules that may form stable radical species upon C–H scission may enable alternate homolytic reactivity pathways that limit the use of DPE as a sole molecular descriptor for catalytic cycles initiated by C–H activation. These homolytic C–H activation routes are inaccessible for activation of C_2H_2 or C_2H_4 on Bi_2O_3 due to their high BDE values of 558 and 464 kJ mol^{-1}, respectively (*29*).

Catalyst characterization

The DFT results are predicated on the persistence of α-Bi_2O_3 surfaces during reaction and after repeated redox cycling, especially considering the redistribution of lattice O consequent from the removal and full replenishment of 20 to 30% of O atoms during redox cycles. We used a suite of characterization techniques to develop a better understanding of the catalytically relevant surfaces after partial reduction by C_2H_2 combustion and the effects that redox cycling has on phase, particle morphology, and local Bi coordination. Temperature-programmed oxidation (TPO) of a partially reduced Bi_2O_3 sample was used to assess the absence or presence of coke on particle surfaces after partial reduction by C_2H_2 combustion (fig. S30). After reduction of Bi_2O_3 to θ_O = 0.84, 7.1 μmol C g_{cat}^{-1} were removed as CO_2 during the subsequent TPO, relative to the 430 μmol C g_{cat}^{-1} reacted during the preceding reduction step, indicating minimal coke formation during reduction half cycles.

X-ray diffraction (XRD) was used to evaluate the presence of other Bi_2O_3 polymorphs or crystalline Bi metal domains in fresh, partially reduced, and redox-cycled Bi_2O_3 samples. In situ XRD diffraction patterns of fresh Bi_2O_3 heated to 773 K in flowing air (fig. S31) illustrated that no other polymorphic Bi_2O_3 phases form up to 773 K; all shifts in peak positions with increasing temperature could be attributed solely to anisotropic lattice expansion (fig. S32), as has been observed by Yashima *et al.* (*32*). A series of partially reduced Bi_2O_3 samples were prepared by removal of 8, 17, and 28% of O atoms by C_2H_2 combustion at 673 K, followed by cooling to ambient conditions in Ar. The XRD patterns of partially reduced Bi_2O_3 samples exhibited peaks for α-Bi_2O_3 and Bi metal, which increased monotonically with extent of reduction (fig. S33). The discussion accompanying figs. S33 to S41 provides further details regarding the phase and composition of partially reduced Bi_2O_3 samples. Heating of a partially reduced Bi_2O_3 sample above the melting point of Bi metal (544 K) resulted in the disappearance of diffraction peaks for Bi metal (fig. S34). Figure 3A compares the XRD patterns of the redox-cycled Bi_2O_3 sample with simulated XRD patterns for α-Bi_2O_3 and Bi metal. After cooling to ambient conditions following full reoxidation by O_2, the redox-cycled Bi_2O_3 catalyst exhibited high crystallinity and was composed of the α polymorph of Bi_2O_3, with only trace peaks from Bi metal and no other Bi_2O_3 polymorphs detected, illustrating that reoxidation steps in redox cycling experiments can regenerate partially reduced Bi_2O_3 particles with minimal changes in catalytic activity (Fig. 1, C and F).

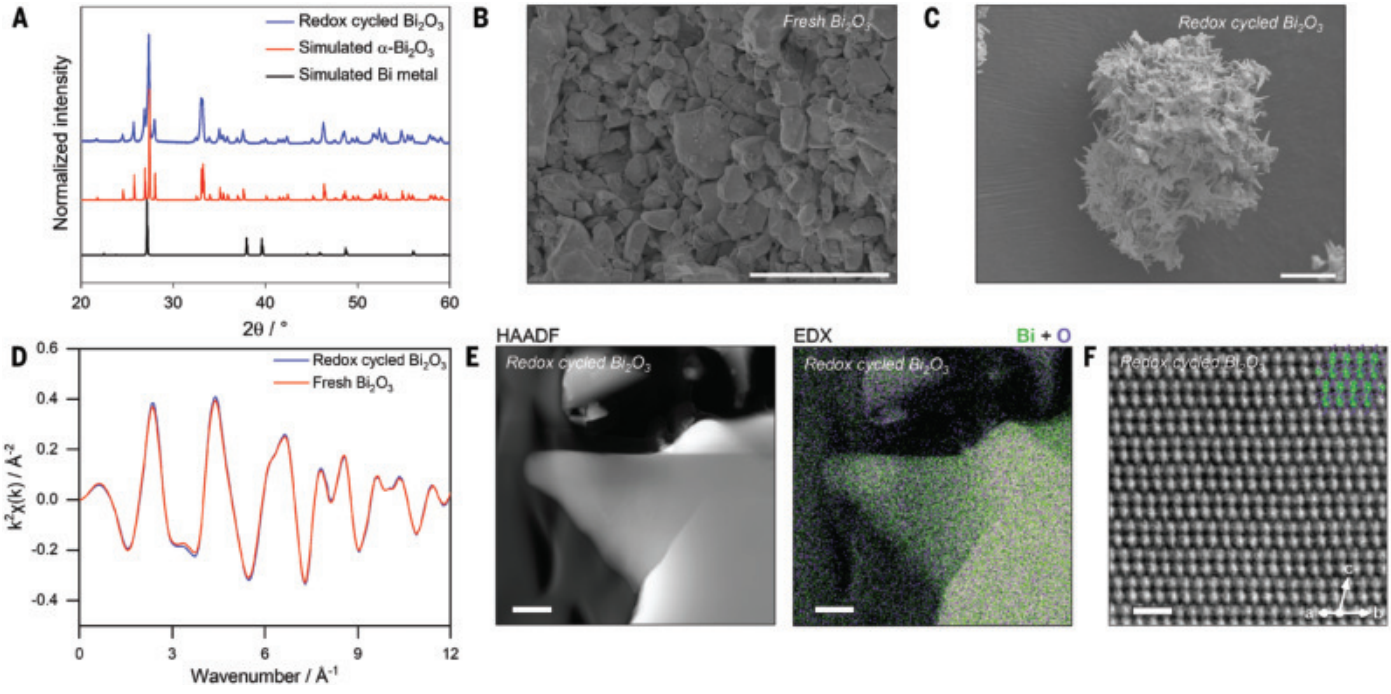


Fig. 3. Characterization of fresh and redox-cycled Bi_2O_3. (**A**) XRD patterns of redox-cycled Bi_2O_3 referenced against XRD patterns of α-Bi_2O_3 (*33*) and Bi metal (*34*) simulated from their corresponding crystallographic information files. (**B** and **C**) SEM images of the Bi_2O_3 catalyst before (B) (scale bar, 20 μm) and after (C) (scale bar, 100 μm) 10 successive reduction and oxidation cycles. (**D**) Bi L_3-edge XAS k^2-weighted χ(k) oscillations of fresh Bi_2O_3 and redox-cycled Bi_2O_3. (**E**) Low-magnification HAADF-STEM image of a needle-like feature on the redox-cycled Bi_2O_3 with STEM-EDX elemental map. The map is overlayed over the HAADF image showing the distribution of Bi and O everywhere in the structure. Scale bars, 200 nm. (**F**) Atomic-resolution HAADF-STEM image from the redox-cycled sample showing the crystal structure of Bi_2O_3 viewed along the [110] direction. The image was low-pass filtered for clarity. The atomic model of the α-Bi_2O_3 structure is overlayed to show the match. Scale bar, 1 nm.

Despite the phase purity of redox-cycled Bi_2O_3 observed by XRD, the textural properties of Bi_2O_3 particles were altered by redox cycling; Fig. 3, B and C, compare scanning electron microscopy (SEM) images of fresh and redox-cycled Bi_2O_3 particles, respectively. The fresh catalyst exposed large, flat facets, whereas the redox-cycled Bi_2O_3 sample adopted a surface with needle-like structures. These textured surfaces were observed on all redox-cycled particles; additional SEM images are shown in fig. S42. These changes in morphological properties were also observed on the Bi_2O_3 sample subjected to five successive redox cycles in which <10% of O atoms were removed from the oxide during each reduction step (fig. S43).

We determined the phase and stoichiometry of these needle-like structures relative to fresh Bi_2O_3 samples using ex situ x-ray absorption spectroscopy (XAS) and x-ray photoelectron spectroscopy (XPS) to determine changes in local Bi coordination and oxidation state, energy-dispersive x-ray (EDX) to assess the Bi:O stoichiometry in these needles (specifically to address if these features were composed of Bi metal that was unable to be reoxidized), and high-angle annular dark-field scanning transmission electron microscopy (HAADF-STEM) to determine differences in the facets exposed on the needle-like structures. Comparisons of the Bi 4f and O 1s XPS spectra of fresh and redox-cycled Bi_2O_3 samples (figs. S44 and S45) indicated that all near-surface Bi cations exhibited the +3 oxidation state with only minor differences in the O 1s spectra. Figure 3D shows negligible differences in k^2-weighted (k)-space oscillations for fresh and redox-cycled Bi_2O_3 (see fig. S46 for comparisons of the normalized absorbances of the Bi-L_{III} edge and the magnitude and imaginary components of Fourier-transformed EXAFS for the fresh and redox-cycled Bi_2O_3 samples). These results qualitatively indicated that the redox-cycled Bi_2O_3 sample contains Bi cations with the same local environment as fresh α-Bi_2O_3 samples.

Extended x-ray absorption fine structure (EXAFS) modeling of the structures of fresh and redox-cycled Bi_2O_3 samples (shown in fig. S47, with fitting parameters for the fresh and redox-cycled samples shown in tables S6 and S7, respectively) indicated that the effective bond lengths of the three Bi–O bonds and one Bi–Bi bond included in the fits, bond length disorder (σ^2) parameters, and amplitude reduction factors were the same when we used fitting procedures that fixed the coordination numbers of each of the paths included. These EXAFS fitting parameters reflected contributions of Bi particles throughout the bulk of the oxide particles and were not specific to Bi atoms on the catalytically relevant surfaces.

We used STEM to probe the phase and stoichiometry of the needle-like structures directly without convolution by Bi atoms subsiding in the bulk of Bi_2O_3 particles. Figure 3E shows a set of HAADF-STEM images of the dendritic growth on redox-cycled Bi_2O_3 along with STEM-EDX compositional maps. The needle-like spikes were composed of Bi and O, with no apparent phase segregation or formation of Bi metal cores (fig. S48). The even distribution of Bi and O seen in STEM-EDX maps was consistent with the maps obtained from fresh Bi_2O_3 particles (fig. S49). The crystal structure of the needle-like structures was further corroborated by the observation of α-Bi_2O_3, as shown in Fig. 3F (see fig. S49 for images obtained from fresh Bi_2O_3 samples). These observations further support the formation of α-Bi_2O_3 in the needle-like structures during redox cycling.

Discussion

We demonstrate selective chemical-looping C_2H_2 combustion as an alternative to C_2H_2 semihydrogenation to purify C_2H_4-rich gas streams with an inexpensive bulk Bi_2O_3 catalyst that does not require elevated pressures; is tolerant to CO_2, H_2O, and C_2H_4; and retains reactivity for C_2H_2 combustion with high selectivity across multiple redox cycles after full reoxidation. The rate constant for C_2H_2 combustion was ~3000× the rate constant for C_2H_4 combustion, consistent with the ~75 kJ mol^{-1} difference in DFT-derived transition state energies on Bi–O sites. DFT results indicated that the high selectivity of Bi_2O_3 to C_2H_2 combustion in C_2H_4 mixtures could be attributed to the formation of heterolytic C–H activation transition states on Bi–O sites of α-Bi_2O_3 that favored the activation of molecules with more acidic C–H bonds, such as C_2H_2. After redox cycling, the catalyst exhibited no changes in local Bi coordination and only trace amounts of Bi metal. The drastic changes in particle morphology observed after redox cycling are ascribed to recrystallization of the O-deficient reduced state upon exposure to O_2 to regenerate crystalline α-Bi_2O_3 domains. This application of selective hydrocarbon combustion has the potential to circumvent conventional separation methods for the removal of molecules with more acidic C–H bonds, such as alkynes, from multicomponent hydrocarbon mixtures.

REFERENCES AND NOTES

1. I.-T. Trotuş, T. Zimmermann, F. Schüth, *Chem. Rev.* **114**, 1761–1782 (2014).
2. A. Borodziński, G. C. Bond, *Catal. Rev., Sci. Eng.* **48**, 91–144 (2006).
3. A. Borodziński, G. C. Bond, *Catal. Rev., Sci. Eng.* **50**, 379–469 (2008).
4. P. Pässler *et al.*, in *Ullmann's Encyclopedia of Industrial Chemistry* (Wiley, 2011); https://doi.org/10.1002/14356007.a01_097.pub4.
5. S. Seifzadeh Haghighi, M. R. Rahimpour, S. Raeissi, O. Dehghani, *Chem. Eng. J.* **228**, 1158–1167 (2013).
6. X. Zhao *et al.*, *ACS Omega* **7**, 17–31 (2021).
7. N. A. Khan, S. Shaikhutdinov, H.-J. Freund, *Catal. Lett.* **108**, 159–164 (2006).
8. P. A. Sheth, M. Neurock, C. M. Smith, *J. Phys. Chem. B* **109**, 12449–12466 (2005).
9. G. X. Pei *et al.*, *ACS Catal.* **5**, 3717–3725 (2015).
10. F. Studt *et al.*, *Angew. Chem. Int. Ed.* **47**, 9299–9302 (2008).
11. A. Ota *et al.*, *J. Phys. Chem. C Nanomater. Interfaces* **115**, 1368–1374 (2011).
12. F. Huang *et al.*, *J. Am. Chem. Soc.* **144**, 18485–18493 (2022).
13. G. Kyriakou *et al.*, *Science* **335**, 1209–1212 (2012).
14. C. K. Westbrook, F. L. Dryer, *Pror. Energy Combust. Sci.* **10**, 1–57 (1984).
15. D. Hucknall, *Chemistry of Hydrocarbon Combustion* (Springer, 2012).
16. Y. Hinuma *et al.*, *J. Phys. Chem. C Nanomater. Interfaces* **122**, 29435–29444 (2018).
17. S. Boyapati, E. D. Wachsman, N. Jiang, *Solid State Ion.* **140**, 149–160 (2001).
18. N. M. Sammes, G. A. Tompsett, H. Näfe, F. Aldinger, *J. Eur. Ceram. Soc.* **19**, 1801–1826 (1999).
19. A. M. Azad, S. Larose, S. A. Akbar, *J. Mater. Sci.* **29**, 4135–4151 (1994).
20. M. Hussain *et al.*, *Sens. Actuators B Chem.* **192**, 429–438 (2014).
21. A. Cabot, A. Marsal, J. Arbiol, J. R. Morante, *Sens. Actuators B Chem.* **99**, 74–89 (2004).
22. J. G. Tsikoyiannis, D. L. Stern, R. K. Grasselli, *J. Catal.* **184**, 77–86 (1999).
23. R. K. Grasselli, D. L. Stern, J. G. Tsikoyiannis, *Appl. Catal. A Gen.* **189**, 1–8 (1999).
24. R. K. Grasselli, D. L. Stern, J. G. Tsikoyiannis, *Appl. Catal. A Gen.* **189**, 9–14 (1999).
25. L. Låte, W. Thelin, E. A. Blekkan, *Appl. Catal. A Gen.* **262**, 63–68 (2004).
26. A. Hwang, J. Wu, A. Getsoian, E. Iglesia, *J. Phys. Chem. C Nanomater. Interfaces* **127**, 2936–2952 (2023).
27. Y.-H. Lei, Z.-X. Chen, *J. Chem. Phys.* **138**, 054703 (2013).
28. M. Jacob, H. Nguyen, M. Neurock, A. Bhan, *ACS Catal.* **14**, 4568–4580 (2024).
29. W. M. Haynes, Ed., *CRC Handbook of Chemistry and Physics* (CRC Press, ed. 95, 2014).
30. P. Linstrom, "NIST Chemistry WebBook, NIST Standard Reference Database 69" (NIST, 1997); https://doi.org/10.18434/T4D303.
31. P. C. St. John, Y. Guan, Y. Kim, S. Kim, R. S. Paton, *Nat. Commun.* **11**, 2328 (2020).
32. M. Yashima, D. Ishimura, K. Ohoyama, *J. Am. Ceram. Soc.* **88**, 2332–2335 (2005).
33. S. A. Ivanov, R. Tellgren, H. Rundlof, V. G. Orlov, *Powder Diffr.* **16**, 227–230 (2001).
34. R. W. G. Wyckoff, *Crystal Structures*, vol. 1 (Interscience Publishers, ed. 2, 1963).

ACKNOWLEDGMENTS

Funding: This work was primarily supported by the US Department of Energy Office of Basic Energy Sciences under award DE-SC0025321 and partially under award DE-SC0024710. Parts of this work were performed in the Characterization Facility, University of Minnesota, which receives partial support from the National Science Foundation through the Materials Research Science and Engineering Centers (MRSEC award DMR-2011401) and the National Nanotechnology Coordinated Infrastructure (NNCI award ECSS-2025124) programs. H.N. and M.N. gratefully acknowledge the Minnesota Supercomputing Institute (MSI) at the University of Minnesota for computational resources. M.N. was also supported by US Department of Energy award DE-SC0023383. Use of the Stanford Synchrotron Radiation Lightsource, SLAC National Accelerator Laboratory, is supported by the US Department of Energy, Office of Science, Office of Basic Energy Sciences under contract DE-AC02-76SF00515. Co-ACCESS, part of the SUNCAT Center for Interface Science and Catalysis, is supported by the US Department of Energy, Office of Basic Energy Sciences, Chemical Sciences, Geosciences and Biosciences Division. **Author contributions:** Conceptualization: M.J., A.B.; Funding acquisition: A.B., S.R.B., K.A.M., M.N.; Investigation: M.J., H.N., R.R., J.G.; Methodology: M.J., H.N., R.R., J.G., J.H., J.P., A.H.; Project administration: A.B.; Supervision: J.G., K.A.M., S.R.B., M.N., A.B.; Visualization: M.J., H.N., R.R.; Writing – original draft: M.J.; Writing – review & editing: all authors. **Competing interests:** M.J. and A.B. are listed as inventors on a provisional patent that has been filed for this work (US nonprovisional patent application 18/743,688). The authors declare no competing interests. **Data and materials availability:** All data are available in the main manuscript or in the supplementary materials.

License information: Copyright © 2025 the authors, some rights reserved; exclusive licensee American Association for the Advancement of Science. No claim to original US government works. https://www.science.org/about/science-licenses-journal-article-reuse

SUPPLEMENTARY MATERIALS

science.org/doi/10.1126/science.ads3181
Materials and Methods
Supplementary Text
Figs. S1 to S49
Tables S1 to S7
References (*35*–*57*)

Submitted 7 August 2024; accepted 15 January 2025
10.1126/science.ads3181

NEUROSCIENCE

Thalamic opioids from POMC satiety neurons switch on sugar appetite

Marielle Minère[1,2], Hannah Wilhelms[1], Bojana Kuzmanovic[3], Sofia Lundh[4], Debora Fusca[5,6], Alina Claßen[1], Stav Shtiglitz[7], Yael Prilutski[7], Itay Talpir[7], Lin Tian[8], Brigitte Kieffer[9], Jon Davis[10], Peter Kloppenburg[5,6], Marc Tittgemeyer[3,5,11], Yoav Livneh[7], Henning Fenselau[1,2,5]*

High sugar–containing foods are readily consumed, even after meals and beyond fullness sensation (e.g., as desserts). Although reward-driven processing of palatable foods can promote overeating, the neurobiological mechanisms that underlie the selective appetite for sugar in states of satiety remain unclear. Hypothalamic pro-opiomelanocortin (POMC) neurons are principal regulators of satiety because they decrease food intake through excitatory melanocortin neuropeptides. We discovered that POMC neurons not only promote satiety in fed conditions but concomitantly switch on sugar appetite, which drives overconsumption. POMC neuron projections to the paraventricular thalamus selectively inhibited postsynaptic neurons through mu-opioid receptor signaling. This opioid circuit was strongly activated during sugar consumption, which was most notable in satiety states. Correspondingly, inhibiting its activity diminished high-sugar diet intake in sated mice.

Satiety, the sensation of being sated or full, is an important neurobiological process for the maintenance of a stable body weight. Satiety is triggered by caloric surplus and in response to the resolution of caloric deficiency, such as after eating a meal (*1*, *2*). However, although feeding behavior and overall food intake are attenuated in these states of satiety, they are directly associated with an increased desire to eat sweet, high sugar–containing foods. This paradoxical increase in appetite for sugar is most notable after meals, which accounts for the widespread consumption of desserts. Brain pathways that encode reward-driven behavior critically contribute to food intake regulation and can drive consumption of palatable food beyond homeostatic needs (*3*). However, activity manipulations have shown that these pathways also control food intake in states of energy deprivation as well as the consumption of fat (*4*, *5*). Thus, despite considerable interest for the development of new obesity therapeutics, the specific mechanisms that switch on the appetite for sugar in states of satiety are unknown.

[1]Research Group Synaptic Transmission in Energy Homeostasis, Max Planck Institute for Metabolism Research, Cologne, Germany. [2]Policlinic for Endocrinology, Diabetes, and Preventive Medicine, University Hospital Cologne, Cologne, Germany. [3]Translational Neurocircuitry Group, Max Planck Institute for Metabolism Research, Cologne, Germany. [4]Global Drug Discovery, Novo Nordisk A/S, Måløv, Denmark. [5]Excellence Cluster on Cellular Stress Responses in Aging Associated Diseases (CECAD), University of Cologne, Cologne, Germany. [6]Institute of Zoology, Department of Biology, University of Cologne, Cologne, Germany. [7]Department of Brain Sciences, Weizmann Institute of Science, Rehovot, Israel. [8]Max Planck Florida Institute for Neuroscience, Jupiter, FL, USA. [9]INSERM U1114, Centre de Recherche en Biomédecine de Strasbourg, Université de Strasbourg, Strasbourg, France. [10]Global Drug Discovery, Novo Nordisk A/S, Lexington, MA, USA. [11]Faculty of Medicine, University of Cologne, Cologne, Germany.
*Corresponding author. Email: henning.fenselau@sf.mpg.de

Pro-opiomelanocortin (POMC) neurons of the arcuate nucleus (ARC) of the hypothalamus are a core element of the neurocircuitry that controls satiety. POMC neurons are activated in fed conditions and release alpha-melanocyte–stimulating hormone (α-MSH), a neuropeptide that binds to the melanocortin-4 receptor (MC4R) (*6*). Genetic deficiency of *Pomc* or *Mc4r* causes hyperphagia and massive obesity (*7*–*10*), whereas administration of α-MSH into the paraventricular hypothalamus (PVH) or activating second-order MC4R-expressing PVH neurons potently reduce feeding (*11*, *12*). These findings have led to the general consensus that POMC neurons promote satiety through excitatory α-MSH–MC4R signaling in the downstream PVH (*1*). However, POMC also serves as the precursor of β-endorphin, an opioid peptide whose action on the mu-opioid receptor (MOR) stimulates appetite (*13*, *14*). Moreover, blocking β-endorphin–MOR signaling with centrally acting opioid receptor antagonists decreases sugar intake, which is particularly prominent in ad libitum fed conditions (*15*–*17*). Because of the widespread projections of POMC neurons (*18*), we hypothesized that they might be the source of the endogenous opioid signal that actuates this sugar appetite in satiety states through a downstream brain region other than the PVH.

POMC neurons selectively inhibit paraventricular thalamic neurons

We first analyzed expression of the MOR in the projection sites of POMC neurons (Fig. 1A). We reasoned that high levels of MOR expression on postsynaptic neurons could predict POMC neuron–innervated regions with facilitated β-endorphin–MOR signaling. We performed fluorescence in situ hybridization (FISH) with a probe for the MOR gene (*Oprm1*) followed by immunohistochemistry (IHC) staining with a POMC antibody. MOR expression was detectable in all brain regions that contained POMC-expressing terminals (Fig. 1, A and B, and fig. S1, A and B). However, the paraventricular nucleus of the thalamus (PVT), a midline thalamic structure that has emerged as an important relay station of signals for feeding and motivated behavior (*19*–*22*), showed both the densest number of MOR-positive cells and the highest MOR expression intensity among all POMC-innervated sites (Fig. 1, A and B, and fig. S1, A and B). The high expression of MOR and POMC was found throughout the anterior to posterior extent of the PVT (fig. S1, C and D). Immunostainings in mice expressing an mCherry-tagged MOR (*23*) revealed the close proximity of β-endorphin–positive POMC neuron terminals and MORs in the PVT (fig. S2A).

To test how postsynaptic PVT neurons respond to POMC neuron terminal activation, we used an optogenetic-electrophysiology approach (Fig. 1C). Because neuropeptide release is favored during high-frequency firing (*24*–*26*), we virally expressed the kinetically fast optogenetic activator ChETA in POMC neurons (Fig. 1C and fig. S2B). High-frequency (20 Hz) photostimulation of ChETA-expressing POMC neuron terminals inhibited PVT neurons, as determined by a reduction in spontaneous firing rate and membrane hyperpolarization (Fig. 1, D and E, and fig. S2C). To assess the contribution of MOR signaling, we performed recordings in the presence of the opioid receptor antagonist naloxone or the selective MOR antagonist CTAP. Addition of either drug blocked the inhibitory action of POMC neuron terminal stimulation (Fig. 1E and fig. S2C), which demonstrates that MOR activation underlies the inhibitory action of the POMC→PVT circuit.

Because many POMC neurons express markers for glutamate and γ-aminobutyric acid (GABA) (*27*), we additionally investigated PVT neuron responses in the presence of blockers for these fast-acting neurotransmitters. Addition of synaptic blockers had no influence on PVT neuron inhibition upon POMC neuron terminal stimulation (Fig. 1E and fig. S2C). Consistent with the postsynaptic inhibition of PVT neurons upon MOR activation, bath application of the selective MOR agonist DAMGO hyperpolarized PVT neurons and decreased firing frequency (Fig. 1F and fig. S2D), without causing significant alterations in spontaneous glutamate and GABA release (fig. S2E).

We next measured the release of β-endorphin from POMC neuron terminals in the PVT. In ChETA-expressing mice, high-frequency optogenetic stimulation of POMC→PVT projections evoked β-endorphin secretion as assessed by enzyme-linked immunosorbent assay (ELISA) (fig. S2F). To examine the temporal features of β-endorphin–MOR signaling in the PVT, we used an optogenetic-imaging approach (Fig. 1G).

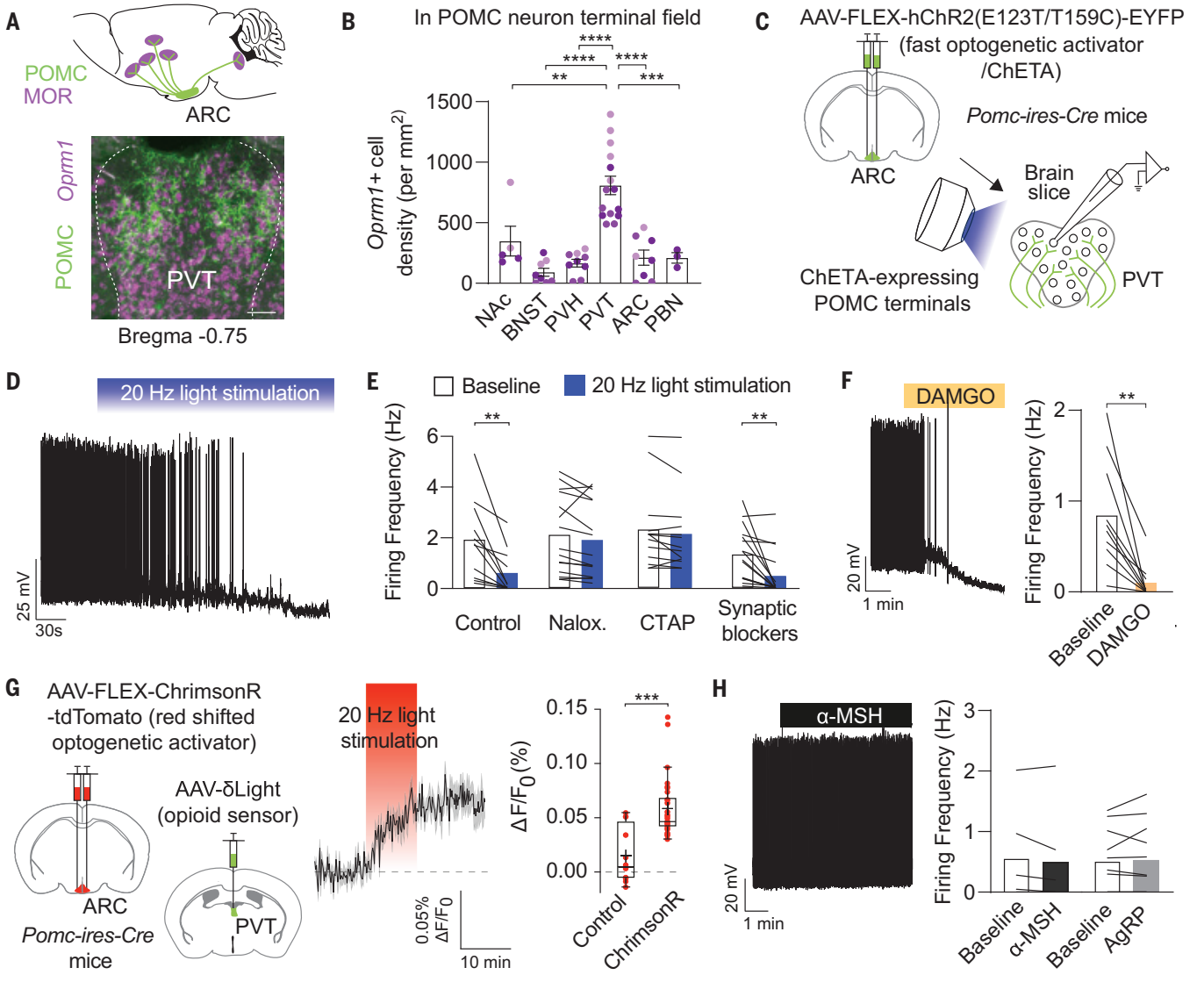


Fig. 1. POMC neurons silence PVT neurons through opioid signaling. (**A**) (Top) Schematic of the histological approach to characterize POMC neuron projection sites. (Bottom) Fluorescence image showing dense MOR expression (*Oprm1*) in the field of POMC neuron terminals in the PVT. Scale bar, 50 μm. (**B**) Analysis of MOR-expressing (*Oprm1*+) cells in POMC-innervated brain regions. BNST, bed nucleus of the stria terminalis; PBN, parabrachial nucleus. (**C**) (Top) A Cre-dependent viral approach to express the kinetically fast optogenetic activator ChETA for selective activation of POMC neuron terminals in the PVT. (Bottom) Patch clamp recordings were performed from PVT neurons in the field of ChETA-expressing terminals (EYFP+). EYFP, enhanced yellow fluorescent protein. (**D**) Current-clamp recordings from PVT neurons. Blue light (473 nm)–evoked photostimulation (20 Hz) of POMC neuron terminals inhibited action-potential firing and induced hyperpolarization. (**E**) Summary of firing frequency shows that POMC neuron terminal stimulation silenced PVT neurons. Addition of naloxone (Nalox.) or CTAP (D-Phe-Cys-Tyr-D-Trp-Arg-Thr-Pen-Thr-NH2) blocked the light-evoked inhibition of PVT neurons, whereas antagonists of glutamate and GABA-A receptors (CNQX, D-AP5, and bicuculline; synaptic blockers) had no effects. (**F**) Trace and summary of DAMGO-induced silencing of PVT neurons. DAMGO is a selective MOR agonist. (**G**) (Left) Viral approach to express the red-shifted, kinetically fast optogenetic activator ChrimsonR in POMC neurons and the opioid sensor δLight in the PVT. (Right) δLight responses to photostimulation of POMC neuron terminals in the PVT in the absence (control) and presence of ChrimsonR. (**H**) Trace and summary of firing frequency changes in PVT neurons in response to α-MSH or AgRP application. Data presented in the graphs in (B), (E), (F), and (H) represent means ± SEMs. Horizontal lines in box plots in (G) indicate medians, and crosses indicates means; whiskers were calculated using the Tukey method. Statistical analysis was performed using ordinary one-way analysis of variance (ANOVA), Tukey's multiple comparisons test (B), two-tailed paired Student's *t* test [(E), (F), and (H)], or Mann-Whiney *U* test (G). $^{**}P \leq 0.005$; $^{***}P \leq 0.001$; $^{****}P \leq 0.0001$. Number of mice for experiments: $N = 3$ (B); $N = 4$ (E); $N = 4$ (F); $N = 3$ (control) or 5 (ChrimsonR) (G); $N = 3$ (α-MSH) or 7 (AgRP) (H). (B) Data from each mouse are represented in the same shading (light purple for mouse 1, purple for mouse 2, and dark purple for mouse 3).

Stimulation of POMC neuron terminals in the PVT using the red light–shifted, kinetically fast optogenetic activator ChrimsonR produced a spatially restricted increase in fluorescence of the opioid sensor δLight (*28*) in a frequency-dependent manner (Fig. 1G and fig. S2, G to J).

We then considered the possibility that concomitant release of melanocortin neuropeptides could also be involved in transmission across the POMC→PVT synapse. We first analyzed the distribution of the MC4R, whose activation by POMC neuron–derived α-MSH activates postsynaptic neurons in the PVH (*11*, *29*, *30*). The PVT, unlike other POMC neuron projection sites,

showed a near-complete absence of MC4Rs (fig. S3, A and B). In support of our histological findings, bath applications of α-MSH, or the endogenous MC4R antagonist agouti-related protein (AgRP), did not acutely alter the membrane potential or firing frequency of PVT neurons (Fig. 1H and fig. S3, C and D).

POMC neuron activity stimulates sated sugar intake

We next investigated the role of the POMC→PVT opioid circuit in feeding behavior regulation. In humans, surplus intake of high sugar–containing foods is particularly prominent as dessert. We therefore designed a behavioral paradigm that captures this phenomenon in mice (Fig. 2A). After an overnight fast, mice were provided access with chow diet for a refeeding period of 90 min, after which they were given access to either chow or a high sugar–containing diet (HSD) for 30 min. When chow was given during this 30-min dessert period, mice consumed an expected small amount, confirming the enhanced satiety state induced by the large amount of chow that they consumed during the 90-min refeeding period (Fig. 2B). By contrast, access to HSD during the dessert period potently stimulated feeding, increasing the caloric intake by more than sixfold (Fig. 2B). This vigorous stimulation of consumption of the high sugar–containing food was consistent across all mice.

To investigate the activity dynamics of the POMC→PVT circuit during the refeeding-dessert paradigm, we used fiber photometry and recorded GCaMP6s dynamics in POMC neuron terminals as a proxy for presynaptic activity (Fig. 2C and fig. S3E). During the initial 90-min refeeding period, presynaptic activity was only modestly increased, albeit the mice voraciously consumed chow (Fig. 2, D to F, and fig. S3F). By contrast, HSD consumption during the dessert period was accompanied by a strong activation of POMC→PVT neuron terminals (Fig. 2, D to F, and fig. S3F). The increase in presynaptic activity occurred rapidly upon HSD presentation and remained elevated during consumption (Fig. 2, D and E, and fig. S3F). Video analysis of head orientation revealed that presynaptic activity increased before the start of HSD consumption and aligned with the behavioral orientation toward the food pellet (Fig. 2F and fig. S3G). This suggests that activation of the POMC→PVT opioid circuit may be necessary for driving the appetitive and consummatory aspects of high sugar–containing food.

POMC neurons are strongly activated upon chow diet presentation and consumption in fasted mice—although at the level of their cell bodies in the ARC (*31*, *32*). To reexamine this, we recorded GCaMP6s dynamics in POMC neurons with optical fibers implanted above the ARC (fig. S3H). Consistent with previous observations (*31*, *32*), refeeding fasted mice

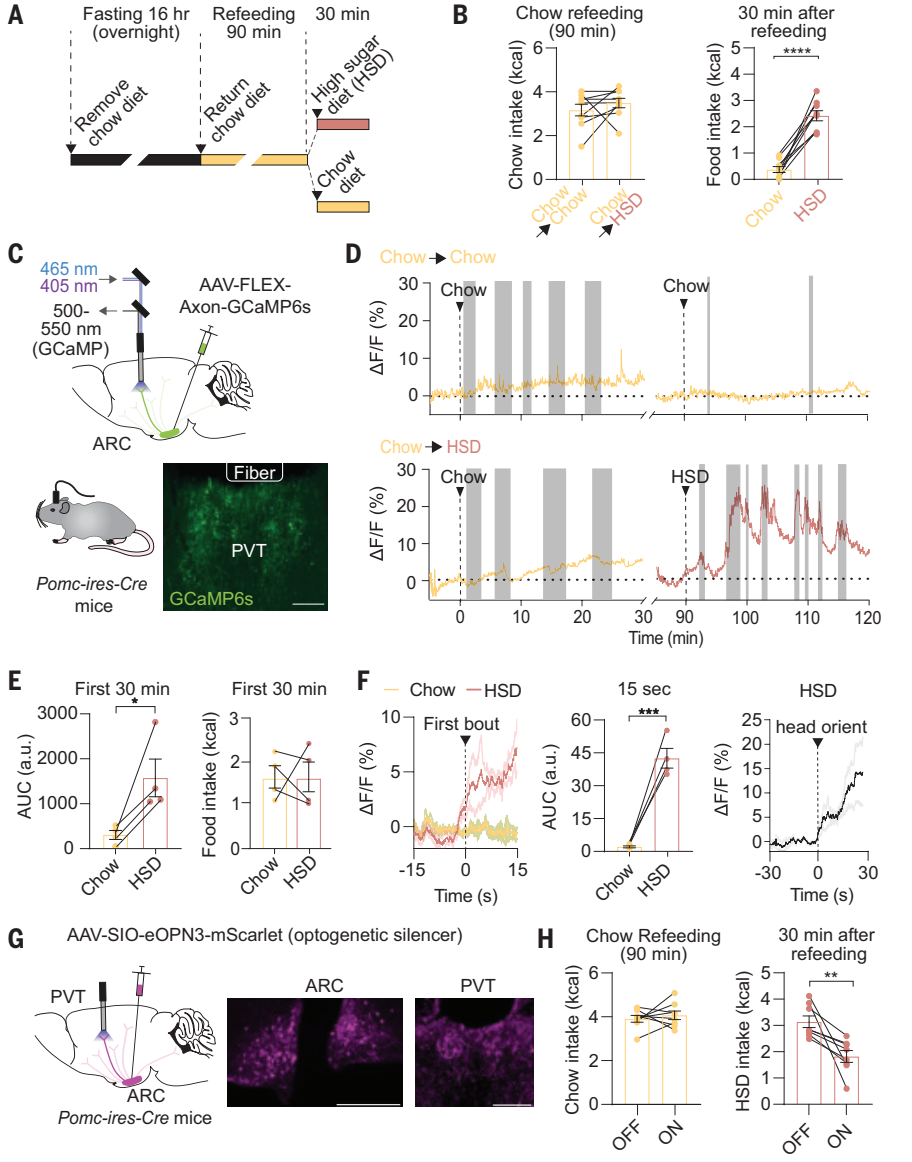


Fig. 2. POMC neuron activity drives sugar consumption after refeeding. (**A**) Schematic of experimental design for the refeeding-dessert paradigm to assess HSD intake in acutely sated mice. (**B**) (Left) Chow diet consumption (in calories) during the 90-min refeeding period was not altered when mice received either chow diet (Chow→Chow) or the HSD (Chow→HSD) during the 30-min dessert period. (Right) Caloric intake was significantly higher when mice received HSD instead of chow diet during the dessert period (30 min after refeeding). (**C**) (Top) A Cre-dependent viral approach to express the axon-targeted GCaMP6s construct in POMC neurons. The photometry fiber was implanted above the PVT for measuring GCaMP6s signals in POMC neuron terminals. (Bottom) Fluorescence image showing GCaMP6s expression in the PVT. Scale bar, 50 μm. (**D**) GCaMP6s fluorescence traces. (Top) A mouse received chow during both the refeeding period and the dessert period. (Bottom) A mouse received a chow during the refeeding period and HSD during the dessert period. Gray areas indicate eating bouts. (**E**) (Left) Quantification of fiber photometry responses during the first 30 min of chow diet consumption in the refeeding period and during the 30-min dessert period when mice consumed the HSD. AUC, area under the curve; a.u., arbitrary units. (Right) Chow diet intake during the first 30 min of the refeeding period and HSD intake during the first 30 min of the dessert period, assessed during the fiber photometry recordings. (**F**) (Left) POMC→PVT terminal fiber photometry responses aligned to time of the first feeding bout of chow diet and HSD. (Middle) Quantification of responses 15 s after alignment to the first feeding bout. (Right) Photometry responses aligned to the head orientation movement. (**G**) Cre-dependent viral approach to express the optogenetic inhibitor eOPN3 in POMC neurons. The optic fiber was implanted above the PVT. Fluorescence image shows eOPN3 (mScarlet) expression in the ARC and PVT. Scale bars, 100 μm (ARC) and 50 μm (PVT). (**H**) eOPN3-mediated inhibition of POMC→PVT projections reduced HSD intake during the dessert period after refeeding ("off," no light; "on," light stimulation). All data presented in the graphs represent means ± SEMs. Statistical analysis was performed using two-tailed paired Student's *t* test [(B), (E), (F), (H)]; $^{*}P \le 0.05$; $^{**}P \le 0.005$; $^{***}P \le 0.001$; $^{****}P \le 0.0001$.

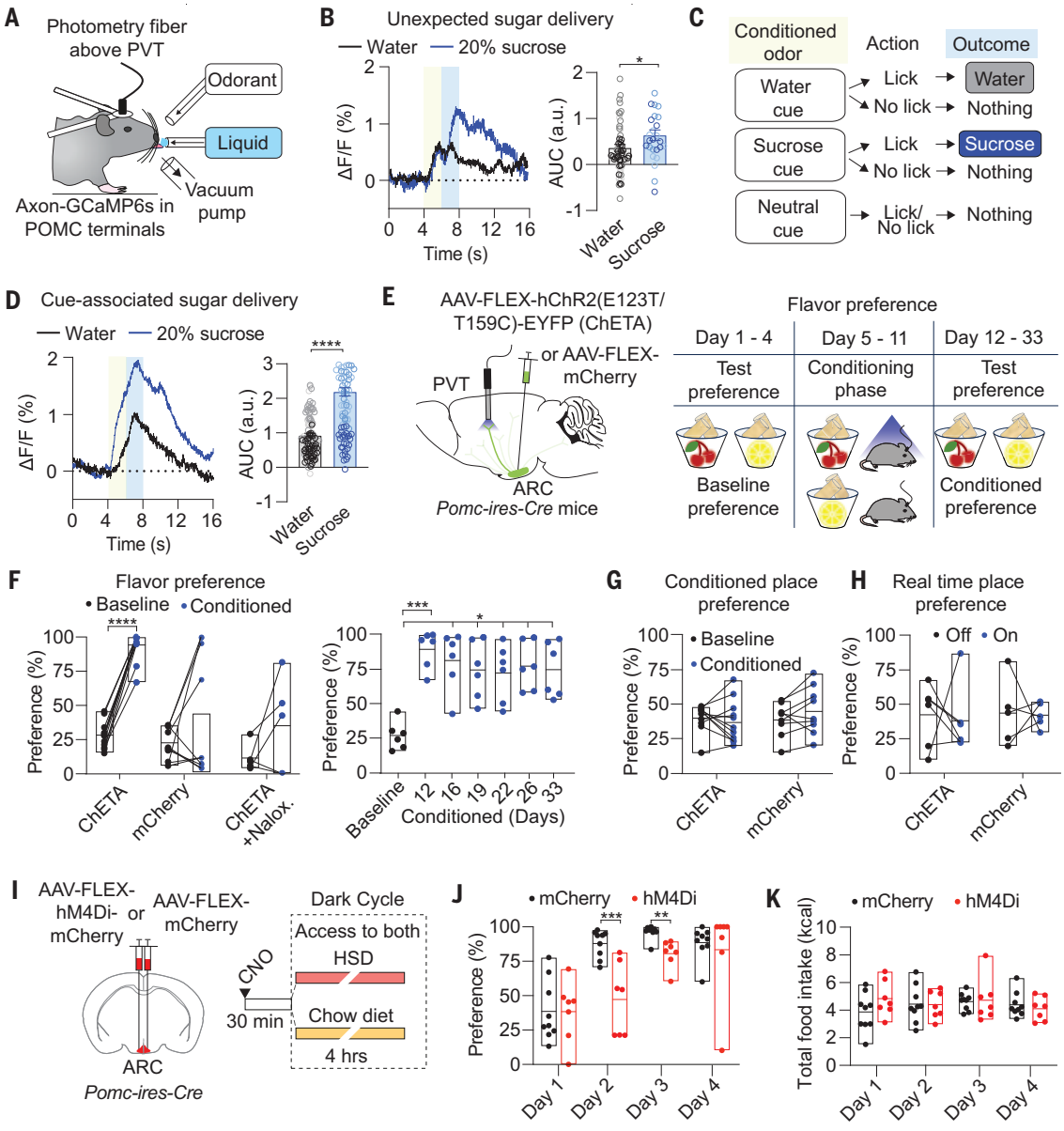


Fig. 3. The POMC→PVT circuit promotes the formation of sugar preference. (**A**) Schematic of the setup for in vivo measurement of fiber photometry responses in POMC→PVT terminals in head-fixed mice. The presented olfactory cues were removed by a vacuum pump. Licking was detected by a lickometer. (**B**) (Left) GCaMP6s fluorescence traces of water and sugar solution delivery within the same animal when completely naïve to the sugar solution. Yellow area indicates 2-s cue presentation window. Blue area indicates 2-s response window. (Right) Quantification of responses during olfactory cue presentation and delivery of solution (between 4 and 8 s). (**C**) Design of the go/no-go olfactory discrimination task for measuring responses to learned sugar-predicting cues. The cues were presented for 2 s followed by a 2-s response window. If mice responded with licking after offset of the water or sucrose predictive olfactory cue, they received 4 μl of water or the sugar solution (20% sucrose), respectively; they received nothing after the neutral olfactory cue. (**D**) (Left) Traces of water and sugar solution delivery within the same animal after training. (Right) Quantification of responses during cue presentation and delivery of solution (between 4 and 8 s) in trained mice. Colored areas indicate the 2-s presentation and 2-s response windows. (**E**) Experimental design for optogenetic stimulation of the POMC→PVT circuit (left). ChETA or mCherry was expressed in POMC neurons, and optical fibers were implanted above the PVT. Experimental design of the CFP assay is shown (right). (**F**) ChETA-expressing mice exhibited a significant preference for the flavored diet that was paired with blue light during the conditioning period, as compared with mCherry-expressing mice (day 12, first day of assessment; left). Naloxone administration before light illumination during the conditioning phase inhibited the diet preference change in ChETA-expressing mice. Preference changes for the flavored diet that was paired with light lasted until the end of the assessment (day 33). (**G**) Changes in preference for the chamber that was paired with light illumination during the conditioning period in mice expressing ChETA or mCherry in POMC neurons. (**H**) Place preference changes during a real-time place preference assay. (**I**) Experimental design for chemogenetic inhibition of POMC neurons. Mice expressing hM4Di or mCherry (control) were injected with CNO before being given access to HSD and chow diet during the first 4 hours of the dark cycle. (**J**) hM4Di-expressing mice exhibited a time delay in preference for consuming the HSD, as compared with mCherry-expressing mice (all mice received CNO). (**K**) hM4Di- and mCherry-expressing mice consumed the same total amount of food (in calories). All data presented in the graphs represent means ± SEMs. Statistical analysis was performed using two-tailed paired Student's *t* test [(B), (D), (G), (H), (J), and (K)], two-way ANOVA with Sidak's multiple comparisons test [(F), left], or ordinary one-way ANOVA followed by Tukey's multiple comparisons test [(F), right]; $^{*}P \le 0.05$; $^{**}P \le 0.01$; $^{****}P \le 0.0001$. Number of mice for fiber photometry experiments: $N = 3$. Number of trials: water (72), sucrose (26) (B); water (98), sucrose (97) (D).

with chow diet potently increased POMC neuron activity in the ARC (fig. S3I).

The activation of POMC→PVT projections during HSD consumption and subsequent postsynaptic opioid signaling should inhibit PVT neurons, which has been associated with driving food consumption (*19*, *20*, *22*). To explore this, we optogenetically inhibited POMC neuron terminals in the PVT (Fig. 2G and fig. S4A). Photoinhibition of POMC→PVT projections in fasted, eOPN3-expressing mice reduced HSD intake during the dessert period without altering chow diet intake during the 90-min refeeding period (Fig. 2H and fig. S4B). Chemogenetic inhibition of POMC neurons expressing hM4Di

using clozapine *N*-oxide (CNO) similarly reduced HSD intake (fig. S4, C to E). In contrast to this acute sugar appetite–suppressing effect, 48-hour intake of chow diet was increased by continuous chemogenetic inhibition of POMC neurons (fig. S4F). This finding is consistent with the previously reported, delayed anorexigenic function of POMC neurons and the melanocortin neuropeptides that they release (*29*, *33*, *34*).

Sugar cues rapidly activate POMC→PVT projections

We next sought to precisely determine the relationship between activation of the POMC→PVT circuit and sugar consumption. Because mice were acclimated to the HSD for our refeeding-dessert paradigm (Fig. 2A) before the experiments to avoid food neophobia, we considered the possibility that the immediate increase in presynaptic activity upon HSD detection is preingestive and that its rapid activation involves a learning process. We therefore recorded presynaptic activity in head-fixed animals, which were trained to perform a go/no-go discrimination task (Fig. 3A). We first investigated how delivery of a sugar solution to an olfactory cue that predicts water access influences presynaptic POMC→PVT terminal activity. Water-deprived mice were presented with one of two distinct olfactory cues, after which licking to the correct (water) cue led to delivery of a water reward (4-μl drop) (fig. S5, A and B). In well-trained mice that selectively licked to the water cue (fig. S5, A and B), unexpected delivery of a high sugar–containing solution (20% sucrose) resulted in a rapid increase in POMC→PVT terminal activity (Fig. 3B). This response emerged during the onset of solution delivery (Fig. 3B), which indicates that signals from the oral cavity rapidly reach POMC neurons that project to the PVT.

We also observed a small, yet consistent increase in presynaptic activity to the water cue, which emerged shortly after stimulus onset (Fig. 3B). This unexpected rapid activation suggests that POMC neurons, which regulate various metabolic processes in addition to feeding (*35*), also integrate water-related signals, at least in a state of mild dehydration. Furthermore, the increased activity preceding water access indicates that the thirsty mice learned to associate the otherwise arbitrary (olfactory) cue with water availability.

We next recorded presynaptic activity in response to cues predicting sugar access by including an additional olfactory cue after which licking led to the delivery of the high sugar–containing solution (Fig. 3C). In trained mice, activity of POMC→PVT terminals profoundly increased to sugar cue presentation and solution consumption (Fig. 3D). This increase in activity immediately emerged during presentation of the cue and consistently exceeded the response to the water cue (Fig. 3D). This difference was not because of differential

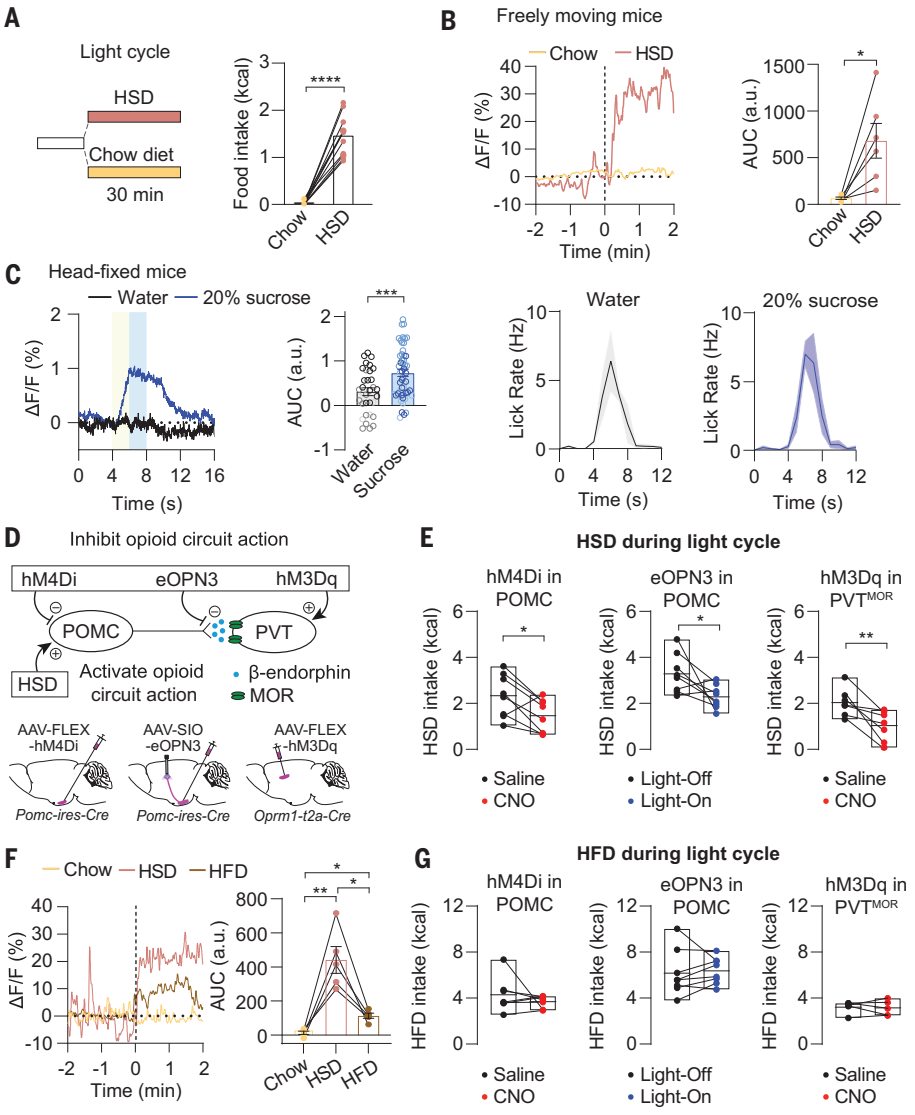


Fig. 4. POMC→PVT circuit activity drives sated sugar—but not fat—consumption. (**A**) Providing HSD at the onset of the light cycle resulted in voracious feeding in mice. (**B**) POMC→PVT terminals are profoundly activated upon HSD presentation and consumption in freely behaving mice. (Left) Fiber photometry recordings from POMC→PVT terminals expressing GCaMP6s from the same mouse. (Right) Mean responses to chow diet and HSD presentation demonstrating increased presynaptic activity within the first 2 min after food presentation. (**C**) In fed and hydrated mice, presentation of sugar cues and sugar solution consumption evoked rapid responses in POMC→PVT neuron terminals in head-fixed mice. (Left) Traces of water and sugar solution delivery within the same animal. (Middle) Quantification of fiber photometry responses upon delivery of water and the sugar solution between 4 and 8 s. (Right) Licking behavior during the response window using 1-s bins. Mice licked similarly to both sugar and water cues. (**D**) Schematic of chemo- and optogenetic manipulations of the POMC→PVT circuit. (**E**) HSD intake in fed mice is significantly reduced by hM4Di-mediated inhibition of POMC neurons, eOPN3-mediated optogenetic inhibition of POMC→PVT projections, and hM3Dq-mediated activation of PVT^{MOR} neurons. (**F**) POMC→PVT terminals are activated upon HFD presentation and consumption in fed mice, but to a much lesser extent than for HSD. (Left) Fiber photometry recordings from POMC→PVT terminals expressing GCaMP6s from the same mouse. (Right) Mean responses to chow diet, HSD, and HFD within the first 2 min after food presentation. (**G**) Effects of chemo- and optogenetic manipulations of the POMC→PVT circuit on HFD consumption in fed mice. All data presented in the graphs represent means ± SEMs. Statistical analysis was performed using two-tailed paired Student's *t* tests [(A) to (C), (E), and (G)] or one-way ANOVA followed by Tukey's multiple comparisons test (F). Number of head-fixed mice for fiber photometry experiments: $N = 3$. Number of trials: water (50), sucrose (49). $^{*}P \le 0.05$; $^{**}P \le 0.01$; $^{***}P \le 0.001$; $^{****}P \le 0.0001$.

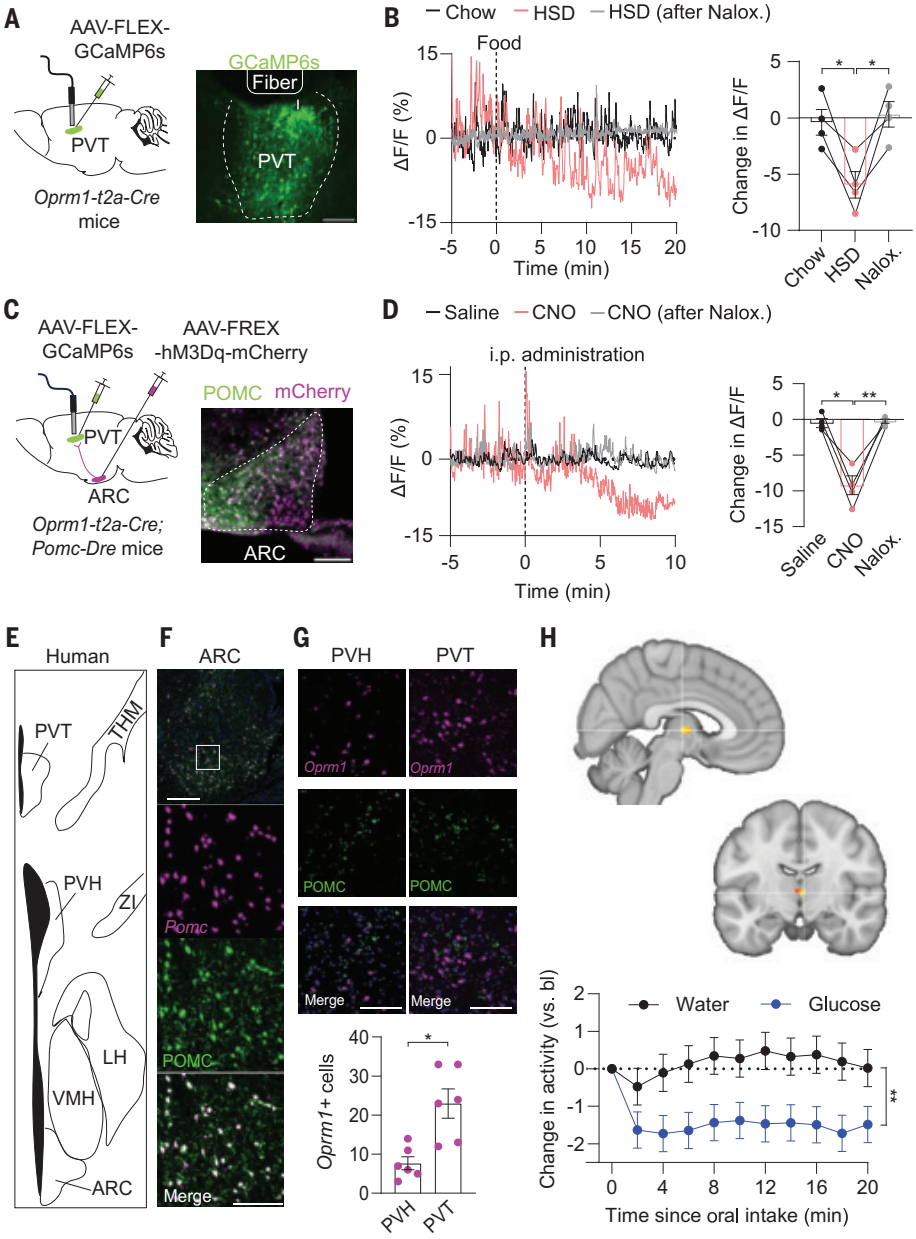


Fig. 5. Sugar-evoked responses in the PVT in mice and humans. (**A**) AAV-FLEX-GCaMP6s was injected into the PVT of *Oprm1-t2a-Cre* mice to determine real-time activity changes of PVT^{MOR} neurons using fiber photometry. Fluorescence image shows GCaMP6s expression and photometry fiber placement in the PVT. Scale bar, 50 μm. (**B**) (Left) GCaMP6s fluorescence traces in a single mouse upon delivery of chow or HSD recorded during the onset of the light cycle, and upon delivery of HSD with prior naloxone administration. (Right) Comparison of PVT^{MOR} neuron responses 20 min after food presentation. (**C**) AAV-FLEX-GCaMP6s was injected into the PVT and AAV-FREX-hM3Dq-mCherry was injected into the ARC of *Oprm1-t2a-Cre; Pomc-Dre* mice to activate POMC neurons while measuring PVT^{MOR} neuron activity. Fluorescence image shows hM3Dq (mCherry) and POMC expression in the ARC. Scale bar, 50 μm. (**D**) GCaMP6s fluorescence traces in a single hM3Dq-expressing mouse upon injection of saline or CNO and upon injection of CNO after naloxone injection. i.p., intraperitoneal. (Right) Comparison of PVT^{MOR} neuron responses 10 min after injection of saline or CNO. (**E**) Diagram derived from the human brain atlas. THM, thalamus; ZI, zona incerta; LH, lateral hypothalamus; VMH, ventromedial hypothalamic nucleus. (**F**) Fluorescence images showing POMC protein and *Pomc* mRNA expression in the ARC. (**G**) (Top) POMC protein (terminals) and *Oprm1* mRNA expression in the PVH and PVT. (Bottom) Quantification of *Oprm1*+ cells in POMC-innervated areas in human brain samples is shown. (**H**) Change in human PVT activity after oral intake of water (black) or glucose solution (blue), relative to the baseline (bl) before the intake. The consumption of a glucose solution relative to water reduced the BOLD signal in the PVT across 10 consecutive 2-min time intervals (up to 20 min after oral intake; $P < 0.05$, FWE-corrected at the voxel level within the PVT mask; bars show means and standard errors; activity maps overlayed on MNI152 brain template). All data presented in the graphs represent means ± SEMs. Statistical analysis was performed using ordinary one-way ANOVA followed by Tukey's multiple comparisons test [(B) and (D)] or two-tailed Student's *t* test (G) and t-contrasts followed by an omnibus test (H); $^{*}P \leq 0.05$; $^{**}P \leq 0.01$. Scale bars, 300 μm (F) and 50 μm (G). (G) Number of human donors: $N = 2$; number of brain slices per brain area: $n = 6$. (H) Number of human subjects, $N = 30$.

licking behavior (fig. S5C). Thus, although oral sugar sensing is initially sufficient to increase presynaptic activity, sugar cues and associated consumption expedite and strongly potentiate the synaptic response. The activation of POMC→PVT terminals scaled with the amount of sucrose in the solution, and even a 0.7% sucrose solution evoked an increase in presynaptic activity similar to that evoked by the 20% sucrose solution (fig. S5, D to F).

The POMC→PVT circuit promotes the formation of sugar preference

The learning-induced increase in presynaptic activity suggests that activation of the POMC→PVT opioid circuit may contribute to creating a sugar preference and inducing sugar consumption. We used a conditioned flavor preference (CFP) test combined with optogenetic manipulation (Fig. 3E). Mice expressing ChETA in POMC neurons and control mice expressing mCherry were habituated to lemon- and cherry-flavored chow diets, which were isocaloric, had no added sugar, and were identical in their nutrient composition. After determining the initial preference, POMC→PVT terminals were photostimulated during consumption of the diet with the initially less-preferred flavor (Fig. 3E). This approach, where circuit activation is paired with a flavored chow diet, circumvents potential confounding effects of sweet taste or postingestive sugar sensing on preference formation (*36*–*38*). ChETA-expressing mice showed a robust increase in preference for the photostimulation-paired diet after conditioning (Fig. 3F and fig. S6, A and B). This preference formation required opioid signaling because naloxone administration before the conditioning sessions prevented the behavioral change induced by photostimulation in ChETA-expressing mice (Fig. 3F). Measurement of diet preference over the following weeks demonstrated that the behavioral change persisted until the end of assessment (Fig. 3F and fig. S6C).

We additionally investigated the possibility that activation of the POMC→PVT opioid circuit is sufficient in eliciting a general preference behavior analogous to the activation of midbrain dopamine neurons. We first used the conditioned place preference paradigm to test the behavioral conditioning effects of photostimulation on environmental cues. After habituation and determining the initial preference, optogenetic stimulation of POMC→PVT terminals was paired with the initially less-preferred chamber of the apparatus (fig. S6D). ChETA-expressing mice did not develop a place preference after conditioning (Fig. 3G). To investigate whether the activation of POMC→PVT terminals is, by itself, sufficient to induce a positive valence, we performed a real-time place preference test. ChETA-expressing mice did not spend more time in the light-stimulated compartment (Fig. 3H), nor did we observe alterations in locomotor activity (fig. S6, E and F). Together, these data demonstrate that the POMC→PVT circuit is selectively important for entraining dietary preferences.

If activation of the POMC→PVT opioid circuit upon sugar detection is involved in creating a preference for high sugar–containing foods, then silencing it should diminish the formation of sugar preference. Mice were given a choice between HSD and chow diet at the onset of the dark cycle while chemogenetically inhibiting POMC neurons (Fig. 3I). CNO-treated control mice (mCherry-expressing) developed a strong preference for HSD already on the second day (Fig. 3J). By contrast, CNO- and hM4Di-mediated inhibition of POMC neurons delayed preference formation (Fig. 3J). Chemogenetic inhibition of POMC neurons did not alter total food consumption during the 4-hour experimental period (Fig. 3K). Consistent with the endogenous opioid action of the POMC→PVT circuit, administration of naloxone also delayed sugar preference formation without affecting total caloric consumption (fig. S6, G to I).

The POMC→PVT circuit drives sugar—but not fat—intake beyond caloric needs

High sugar–containing foods are not only favorably consumed after meals, when satiety is triggered through short-term feedback signals from the gut, but also in states of caloric surplus, when long-term satiety signals (such as leptin) are critical factors that determine appetite control (*1*). To test whether activity of the POMC→PVT opioid circuit also contributes to the regulation of sugar consumption in states of caloric surplus, we provided mice access to HSD at the beginning of the light cycle (Fig. 4A)—a time when mice are in a physiologically fed state from the food that they consumed during the dark cycle, accompanied by elevated levels of leptin (fig. S7A). Access to HSD for 30 min in acclimated mice induced voracious feeding (Fig. 4A and fig. S7B). Recording GCaMP6 signals in POMC→PVT neuron terminals revealed that HSD presentation and subsequent consumption resulted in a profound increase in presynaptic activity, which emerged rapidly after pellet delivery (Fig. 4B). Consistent with being in a state of caloric surplus, mice did not consume chow (Fig. 4A), and chow presentation did not elicit alterations in presynaptic activity (Fig. 4B and fig. S7C). In addition to these experiments in freely behaving mice, we also measured presynaptic activity in head-fixed animals. In fed and fully hydrated mice (fig. S7D), cue presentation and subsequent consumption of the high-sugar solution induced time-locked increases in presynaptic activity (Fig. 4C). The responses to the water cues that we observed in dehydrated mice were strongly diminished (Fig. 3, B and D, and Fig. 4C), which indicates that they specifically relate to the hydration state.

We next tested whether activity of the POMC→PVT opioid circuit is necessary for driving sugar consumption in states of caloric surplus (Fig. 4D). Chemogenetically inhibiting POMC neurons and optogenetic silencing of POMC→PVT projections diminished HSD intake at the onset of the light cycle (Fig. 4, D and E, and fig. S7, E to H). Selective chemogenetic stimulation of MOR-expressing neurons in the PVT (PVT^{MOR} neurons), which counteracts the inhibitory opioid action of the POMC→PVT circuit, also diminished HSD intake in fed mice (Fig. 4, D and E, and fig. S7, E to H).

Because high fat–containing foods are likewise consumed beyond caloric needs, we assessed the contribution of POMC→PVT circuit activity in regulating intake of a high-fat diet (HFD). Access to HFD for 30 min at the beginning of the light cycle potently stimulated feeding, with mice consuming more calories than when provided HSD (fig. S7I). Recording GCaMP6s dynamics in POMC→PVT terminals showed that HFD presentation and consumption evoked an increase in presynaptic activity; yet, this response was significantly smaller in magnitude than the response evoked by HSD presentation and consumption (Fig. 4F). In fed mice, HFD intake was not altered by chemogenetic inhibition of POMC neurons, optogenetic silencing of POMC→PVT projections, or activation of PVT^{MOR} neurons (Fig. 4G and fig. S7J). Inhibition of the POMC→PVT circuit also failed to reduce HFD intake when provided for 30 min after refeeding during the dessert period (fig. S7, K and L). We then determined the possibility that activity of the POMC→PVT opioid circuit contributes to the regulation of feeding at the onset of the dark cycle when mice are naturally energy depleted because of their circadian feeding rhythm. Chemogenetically inhibiting POMC neurons, activating PVT^{MOR} neurons, and blocking endogenous opioid signaling with naloxone all failed to acutely (within 3 hours) alter chow diet intake (fig. S7, M and N). Inhibition of the circuit also did not alter HSD intake at the onset of the dark cycle (fig. S7O). Thus, activity of the POMC→PVT opioid circuit is of particular importance in driving the specific appetite for sugar in states of satiety.

Dysregulation of the PVT by exogenous opioids mediates opioid withdrawal symptoms, and PVT neurons invigorate sugar seeking during unexpected reward omission (*39*–*41*). We therefore sought to precisely determine the relationship between endogenous opioid signaling in PVT neurons and sugar consumption. We first used fiber photometry to record the activity of PVT^{MOR} neurons expressing GCaMP6s (Fig. 5A). Consistent with the activation of the inhibitory POMC→PVT opioid circuit, presentation and subsequent consumption of HSD—but not chow diet—inhibited PVT^{MOR} neurons in fed and acutely sated mice (Fig. 5B and fig. S8, A and B), an effect that was blocked by preadministration of naloxone (Fig. 5B and fig. S8, C and D). To directly test whether POMC neurons underlie this endogenous opioid response, we recorded PVT^{MOR} neurons while selectively manipulating POMC neuron activity (Fig. 5C). We injected Cre-dependent GCaMP6s adeno-associated virus (AAV) into the PVT and Dre-dependent hM3Dq AAV into the ARC of *Oprm1-t2a-Cre; Pomc-Dre* mice and placed fiberoptic implants above the PVT (Fig. 5C). CNO- and hM3Dq-induced activation of POMC neurons significantly decreased PVT neuron activity (Fig. 5D and fig. S8E). This inhibition was abolished by naloxone pretreatment (Fig. 5D and fig. S8E). If activation of the POMC→PVT opioid circuit underlies the inhibition of PVT^{MOR} neurons, then activation of POMC neurons preceding HSD access should occlude the response. CNO administration in doubly transduced, hM3Dq-expressing mice significantly attenuated the HSD-evoked response in PVT^{MOR} neurons (fig. S8F). Because exogenous opioid action maintains seeking behavior via PVT neurons that project to the nucleus accumbens (NAc) (*39*, *41*, *42*), we used *Oprm1-t2a-cre; D1r-tdTomato* mice to assess synaptic connection characteristics between PVT^{MOR} and NAc medium spiny neurons (MSNs) expressing dopamine receptor D1 (tdTomato+) and neurons putatively expressing the D2 receptor (tdTomato−) in the NAc shell. Electrophysiological recordings revealed that PVT^{MOR} neurons provide strong excitatory input to both D1R+ and putative D2R NAc neurons with similar synaptic characteristics (fig. S9, A to G).

Sugar consumption decreases human PVT activity

We next determined whether the POMC→PVT opioid circuit is conserved in humans. To histologically assess the proximity of POMC neuron terminals and PVT^{MOR} neurons, we costained brain sections from human tissues for POMC

(IHC) and *Oprm1* (FISH). We confirmed faithful and efficient binding of the POMC antibody to POMC neurons in the human ARC as determined by FISH (Fig. 5, E and F). In the PVT, POMC-expressing terminals were directly adjacent to a large fraction of MOR-expressing cell bodies; by contrast, density of MOR-expressing cells in the terminal field was lower in the PVH (Fig. 5G). Finally, to determine activity changes in the human PVT during sugar consumption, we performed functional magnetic resonance imaging with normal-weight participants (Fig. 5H). Consumption of a high sugar–containing solution reduced the subsequent blood oxygen level–dependent (BOLD) response in the PVT relative to the baseline before consumption (Fig. 5H) (one-sampled t test for the contrast –glucose: $t = 3.47$; family-wise error corrected for multiple comparisons within the PVT mask: $P_{\text{FWE-corr}} = 0.006$; cluster size = 37; peak at $x = 4$, $y = -12$, $z = 4$), even in a direct comparison with water intake (paired t test for the contrast water > glucose: $t = 3.12$; $P_{\text{FWE-corr}} = 0.016$; cluster size = 13; peak at $x = 4$, $y = -12$, $z = 6$). The opposite contrasts (–water and glucose > water) did not reveal suprathreshold clusters, even at a more lenient statistical threshold without correction for multiple comparisons.

Discussion

POMC neurons of the hypothalamus produce numerous neuropeptides, including α-MSH and β-MSH, which exert well-established satiety-promoting and obesity-preventing actions because of their binding to the MC4R (*6*, *43*). Additionally, POMC neurons are the sole brain source of the potent MOR agonist β-endorphin (*44*), which exhibits broad effects on reward-seeking and food-intake behavior when administered into different brain regions (*14*, *45*–*48*). Thus, it is important to establish where in the brain POMC neurons use these functionally different melanocortin and opioid neuropeptides as endogenous neuronal messenger. In this work, we found that the PVT constitutes a projection area of POMC neurons, where their β-endorphin–MOR signaling selectively silenced postsynaptic neurons. The POMC→PVT circuit was rapidly engaged by sugar detection in the oral cavity and remained activated during sugar consumption. POMC→PVT activity increased upon cues instructive for sugar acquisition, which involved the learned association of environmental information with consumption. We probed the function of this rapid activity regulation, which was particularly pronounced in fed conditions. Our experiments unexpectedly revealed that POMC neurons and downstream PVT^{MOR} neurons are required to promote surplus consumption of high sugar–containing food.

Together, our data support a model where POMC neuron activation in the fed state actuates two, nearly opposing processes, namely (i) the known decrease in total food intake by activating satiety-promoting PVH neurons through MC4R signaling (*11*, *12*, *49*) and (ii) the herein described stimulation of sugar intake by inhibiting PVT neurons through MOR signaling. The orexigenic action of POMC neurons is specific to states of caloric sufficiency or surplus (Figs. 2 and 4) (*13*, *50*) and may thus act complementary to endogenous opioids from brainstem enkephalin neurons, which also promote consummatory behavior but in states of caloric deprivation (*50*). It would therefore be of interest to define how the state-dependent activity of these endogenous opioid systems interacts with dopamine signaling in the mesoaccumbens circuitry, which serves to control reward-driven behavior and association learning (*3*, *51*). Notably, MC4R-deficient mice and humans exhibit significant alterations in preferences for high sugar–containing foods (*52*, *53*), which raises the possibility that interactions between melanocortin and opioid signaling in response to POMC neuropeptide release further modulate macronutrient preferences.

The stimulation of sugar appetite by POMC neurons may have been evolutionary advantageous when food was scarce because sugars, when available, can be readily absorbed and metabolized for the synthesis of glycogen and lipids as energy reserve. However, it seems plausible that recurring activation of POMC→PVT opioid signaling when food and sugar are abundant could manifest compulsive-like eating behavior or even binge eating of sugar. The PVT has emerged as a key brain node underlying sugar seeking and feeding behavior (*20*, *21*, *40*), and its GABA-mediated inhibition evokes overeating and obesity development (*19*). Engagement of PVT neuron activity by exogenous opioids facilitates drug-seeking behavior and the expression of opioid withdrawal (*39*, *41*, *54*). Therefore, our findings may revive investigations on endogenous opioid signaling in sugar appetite regulation (*55*) and accelerate further investigations on the POMC→PVT circuit for the development of new obesity therapeutics.

REFERENCES AND NOTES

1. M. L. Andermann, B. B. Lowell, *Neuron* **95**, 757–778 (2017).
2. M. H. Tschöp, J. M. Friedman, *Sci. Transl. Med.* **15**, eadh4453 (2023).
3. I. E. de Araujo, M. Schatzker, D. M. Small, *Annu. Rev. Psychol.* **71**, 139–164 (2020).
4. E. C. O'Connor *et al.*, *Neuron* **88**, 553–564 (2015).
5. J. H. Jennings *et al.*, *Cell* **160**, 516–527 (2015).
6. M. J. Krashes, B. B. Lowell, A. S. Garfield, *Nat. Neurosci.* **19**, 206–219 (2016).
7. C. Vaisse, K. Clement, B. Guy-Grand, P. Froguel, *Nat. Genet.* **20**, 113–114 (1998).
8. G. S. Yeo *et al.*, *Nat. Genet.* **20**, 111–112 (1998).
9. L. Yaswen, N. Diehl, M. B. Brennan, U. Hochgeschwender, *Nat. Med.* **5**, 1066–1070 (1999).
10. D. Huszar *et al.*, *Cell* **88**, 131–141 (1997).
11. A. S. Garfield *et al.*, *Nat. Neurosci.* **18**, 863–871 (2015).
12. S. Q. Giraudo, C. J. Billington, A. S. Levine, *Brain Res.* **809**, 302–306 (1998).
13. M. Koch *et al.*, *Nature* **519**, 45–50 (2015).
14. L. D. McKay, N. J. Kenney, N. K. Edens, R. H. Williams, S. C. Woods, *Life Sci.* **29**, 1429–1434 (1981).
15. M. Apfelbaum, A. Mandenoff, *Pharmacol. Biochem. Behav.* **15**, 89–91 (1981).
16. J. Cleary, D. T. Weldon, E. O'Hare, C. Billington, A. S. Levine, *Psychopharmacology* **126**, 110–114 (1996).
17. A. S. Levine, D. T. Weldon, M. Grace, J. P. Cleary, C. J. Billington, *Am. J. Physiol.* **268**, R248–R252 (1995).
18. D. Wang *et al.*, *Front. Neuroanat.* **9**, 40 (2015).
19. X. Zhang, A. N. van den Pol, *Science* **356**, 853–859 (2017).
20. J. N. Betley, Z. F. H. Cao, K. D. Ritola, S. M. Sternson, *Cell* **155**, 1337–1350 (2013).
21. Y. Livneh *et al.*, *Nature* **546**, 611–616 (2017).
22. T. R. Stratford, D. Wirtshafter, *Brain Res.* **1490**, 128–133 (2013).
23. O. Gardon *et al.*, *Neuroscience* **277**, 595–609 (2014).
24. A. Dutton, R. E. J. Dyball, *J. Physiol.* **290**, 433–440 (1979).
25. C. Schöne, J. Apergis-Schoute, T. Sakurai, A. Adamantidis, D. Burdakov, *Cell Rep.* **7**, 697–704 (2014).
26. M. Cazalis, G. Dayanithi, J. J. Nordmann, *J. Physiol.* **369**, 45–60 (1985).
27. B. C. Jarvie, S. T. Hentges, *J. Comp. Neurol.* **520**, 3863–3876 (2012).
28. C. Dong *et al.*, *Nat. Neurosci.* **27**, 1844–1857 (2024).
29. H. Fenselau *et al.*, *Nat. Neurosci.* **20**, 42–51 (2017).
30. M. Ghamari-Langroudi, D. Srisai, R. D. Cone, *Proc. Natl. Acad. Sci. U.S.A.* **108**, 355–360 (2011).
31. Y. Chen, Y. C. Lin, T. W. Kuo, Z. A. Knight, *Cell* **160**, 829–841 (2015).
32. C. Brandt *et al.*, *Cell* **175**, 1321–1335.e20 (2018).
33. C. Zhan *et al.*, *J. Neurosci.* **33**, 3624–3632 (2013).
34. Y. Aponte, D. Atasoy, S. M. Sternson, *Nat. Neurosci.* **14**, 351–355 (2011).
35. J. C. Brüning, H. Fenselau, *Science* **381**, eabl7398 (2023).
36. H. E. Tan *et al.*, *Nature* **580**, 511–516 (2020).
37. I. E. de Araujo *et al.*, *Neuron* **57**, 930–941 (2008).
38. K. L. Buchanan *et al.*, *Nat. Neurosci.* **25**, 191–200 (2022).
39. Y. Zhu, C. F. R. Wienecke, G. Nachtrab, X. Chen, *Nature* **530**, 219–222 (2016).
40. F. H. Do-Monte, A. Minier-Toribio, K. Quiñones-Laracuente, E. M. Medina-Colón, G. J. Quirk, *Neuron* **94**, 388–400.e4 (2017).
41. K. M. Vollmer *et al.*, *Nat. Commun.* **13**, 6865 (2022).
42. J. M. Otis *et al.*, *Neuron* **103**, 423–431.e4 (2019).
43. Y. S. Lee *et al.*, *Cell Metab.* **3**, 135–140 (2006).
44. C. Toda, A. Santoro, J. D. Kim, S. Diano, *Annu. Rev. Physiol.* **79**, 209–236 (2017).
45. C. A. Baile, C. L. McLaughlin, M. A. Della-Fera, *Physiol. Rev.* **66**, 172–234 (1986).
46. B. A. Gosnell, J. E. Morley, A. S. Levine, *Brain Res.* **369**, 177–184 (1986).
47. M. Amalric, E. J. Cline, J. L. Martinez Jr., F. E. Bloom, G. F. Koob, *Psychopharmacology* **91**, 14–19 (1987).
48. V. P. Bakshi, A. E. Kelley, *J. Pharmacol. Exp. Ther.* **265**, 1253–1260 (1993).
49. N. Balthasar *et al.*, *Cell* **123**, 493–505 (2005).
50. D. C. Castro *et al.*, *Nature* **598**, 646–651 (2021).
51. S. J. Gershman, N. Uchida, *Nat. Rev. Neurosci.* **20**, 703–714 (2019).
52. A. A. van der Klaauw *et al.*, *Nat. Commun.* **7**, 13055 (2016).
53. B. L. Panaro, R. D. Cone, *Proc. Natl. Acad. Sci. U.S.A.* **110**, 7050–7055 (2013).
54. P. C. Keyes *et al.*, *Neuron* **107**, 1113–1123.e4 (2020).
55. P. K. Olszewski, A. S. Levine, *Physiol. Behav.* **91**, 506–512 (2007).
56. M. Minere *et al.*, Thalamic opioids from POMC satiety neurons switch on sugar appetite, version 1_28.08.2024, Zenodo (2024); https://doi.org/10.5281/zenodo.13385228.

ACKNOWLEDGMENTS

We thank M.-L. Dreisow and R. Beck for their excellent technical assistance. K. Schöfisch and R. Braun provided invaluable help for animal care. We appreciate the scientific counsel and input from P. N. Mirabella, S. Dodt, E. Ciglieri, and J. Brüning. We thank J. B. Johansen and J. Juul from Novo Nordisk A/S for technical support on human brain histology. We also acknowledge C. Smith at the Edinburgh Brain and Tissue Bank for providing human brain tissue samples. **Funding:** This study was supported by the European Research Council (ERC) under the European Union Horizon 2020 Research and Innovation Programme, grant agreement ID 851778 (H.F.); collaboration agreements with Novo Nordisk (Denmark) (H.F.); Deutsche Forschungsgemeinschaft (DFG, German Research Foundation), grants 409551513 (H.F.) and 505389599 (H.F. and P.K.); the Excellence Initiative by German Federal and State Governments (CECAD) (H.F. and M.T.); German Centre for Diabetes Research, project IDs 82DZD00502 and 82DZD05H1G (M.T.); DFG through SFB 1451, project ID 431549029, C06 (M.T.); the Mapping Autonomic Neural Interaction and Control

(MANIAC) Emerging Group by the University of Cologne Excellent Research Support Program (M.T.); and the Israel Science Foundation, grant 3015/22 (Y.L.). **Author contributions:** Conceptualization: M.M., H.F.; Funding acquisition: M.T., Y.L., H.F.; Investigation: M.M., H.W., B.Ku., A.C., S.L., D.F.; Methodology: M.M., D.F., L.T., S.S., I.T., Y.P., J.D., B.Ku., M.T., B.Ki., Y.L., H.F.; Project administration: M.M.; Supervision: P.K., M.T., Y.L., H.F.; Visualization: M.M., H.F.; Writing – original draft: M.M., H.F.; Writing – review & editing: M.M., B.Ku., J.D., S.L., B.Ki., M.T., Y.L., H.F., with input from all authors. **Competing interests:** S.L. and J.D. are Novo Nordisk employees and minor shareholders as part of an employee offering program. The authors declare no other competing interests. **Data and materials availability:** All data are available in the main text or the supplementary materials. In-house analysis scripts for fiber photometry are available at Zenodo (*56*). The human data reported in this study cannot be deposited in a public repository per General Data Protection Regulation and Institutional Review Board data protection policies. To request access, please contact the senior author (H.F.). Data provision may include processed and unprocessed data and will require a data sharing agreement. Data sharing necessitates that the purpose of data reanalysis is in line with the study aims as approved by the ethics review boards and participant consent. Furthermore, consent to data privacy must be assured by signing the agreement form accordingly. Requests will be answered within 4 weeks. **License information:** Copyright © 2025 the authors, some rights reserved; exclusive licensee American Association for the Advancement of Science. No claim to original US government works. https://www.science.org/about/science-licenses-journal-article-reuse

SUPPLEMENTARY MATERIALS

science.org/doi/10.1126/science.adp1510
Materials and Methods
Figs. S1 to S9
References (*57*–*60*)
MDAR Reproducibility Checklist

Submitted 10 March 2024; accepted 11 December 2024
10.1126/science.adp1510

GEOPHYSICS

Depth-dependent seismic sensing of groundwater recovery from the atmospheric-river storms of 2023

Shujuan Mao[1,2,*], William L. Ellsworth[1], Yujie Zheng[3], Gregory C. Beroza[1]

In early 2023, a series of intense atmospheric-river storms eased California's historic drought, yet the spatiotemporal extent of groundwater recovery remains poorly understood. We tracked two-decadal changes in groundwater in Greater Los Angeles using seismic ambient-field interferometry. The derived seismic hydrographs reveal distinct expressions of groundwater and surficial water droughts: Whereas surface and near-surface water storage nearly fully recovered in the epic wet season of 2023, only about 25% of the groundwater lost since 2006 was restored. On a decadal scale, we find substantial depletion in aquifers below 50-meter depth, with only limited storm-related recovery. Our analysis underscores the need to monitor deep aquifers for a more complete assessment of total water deficits, using high-resolution tools such as seismic sensing.

After two decades of historic droughts, California's weather drastically shifted in water year 2023. From the last day of 2022 through March 2023, the state experienced a series of storms stemming from 16 atmospheric rivers (ARs). In August 2023, Hurricane Hilary added to this "weather whiplash" (*1*, *2*) with torrential rainfall in southern California. These intense events resulted in one of the wettest water years in California's recorded history, with statewide precipitation surpassing its 1901–2000 historical annual average by 141% and snowpack reaching 247% of the average yearly maximum (*3*). In Greater Los Angeles (GLA), precipitation ranged from 150% to >300% of the historical annual average (*3*). The downpours also led to widespread flooding and landslides, affecting life safety, infrastructure, and the economy. Climate modeling predicts increasing intensity and frequency in California's precipitation volatility, shifting between prolonged, extremely dry periods and rapid, extremely wet periods (*1*). These weather extremes pose challenges to the state's water supply infrastructure and management.

California's climate adaptability could be improved through the capture and storage of stormwater during periodic intense storms to mitigate water scarcity during prolonged droughts. The natural infrastructure for stormwater storage—groundwater reservoirs—represents an environmentally friendly alternative to costly and environmentally concerning surface reservoirs. The total storage capacity of California's groundwater basins is estimated at >850 million acre-feet (~1000 km^3), which is more than 17 times that of all the major aboveground reservoirs in California (*3*, *4*). Groundwater is vital for buffering the spatiotemporal variability of surface water under weather extremes. During droughts, groundwater contributes about 60% of California's water supply, underscoring its strategic importance for a resilient water system (*5*–*8*).

Although vital to assessing drought impact and planning sustainable water use, quantifying groundwater storage changes is challenging. Groundwater storage is influenced by many interacting factors, including climatic conditions, land use, hydrogeological structure, and water management strategies. As a result, considerable variability exists in aquifers' spatiotemporal state. The expensive, point-scale well data are still spatially sparse and do not suffice to capture the heterogeneities across aquifers, especially at the basin-to-watershed scales that are crucial for water management. Recently, promising strides in aquifer monitoring have been made through noninvasive geophysical approaches such as satellite sensing and airborne surveys (*8*–*16*), yet their spatiotemporal resolution may not be adequate, and they can be costly to perform.

California's heavy precipitation in 2023 swiftly refilled surface reservoirs to 128% of their historical average (*3*); however, limited analysis is available for groundwater. In particular, the amount, rate, and spatial variability of aquifer recovery are poorly characterized. Our study examines the GLA area (fig. S1) to assess the natural recharge of groundwater from the 2023 AR storms by leveraging data from existing seismic stations. Applying advanced ambient-field interferometry, we measured small changes in seismic velocity to track changes in water storage at depth. With seismic hydrographs, we infer the temporal and spatial variations of groundwater storage and present depth profiles of groundwater depletion and recovery from observations, which allows us to evaluate how the 2023 storms contributed to replenishing the groundwater depleted during recent droughts.

Results

Seismic hydrograph

GLA is a densely populated metropolitan area that has long wrestled with challenges of water supply. The dense seismic network in GLA (*17*) (fig. S1B), designed and developed to study seismic hazards, continuously records the ambient seismic field, which is the ever-present ground vibrations resulting from natural and anthropogenic sources (*18*, *19*). Analysis of these passive seismic records enables the calculation of spatiotemporal changes in seismic velocity (*20*). Seismic velocity varies as pore pressure or water saturation (moisture) of the medium changes, and thus can serve as a measure of the total water content in the subsurface. Passive sensing of seismic velocity changes ($\Delta v/v$) is emerging as a noninvasive, cost-effective approach for the continuous monitoring of aquifers (Fig. 1A) (*21*–*31*). We used ambient seismic data recorded by 68 stations (fig. S1B) from the Southern

[1]Department of Geophysics, Stanford Doerr School of Sustainability, Stanford University, Stanford, CA, USA. [2]Department of Earth and Planetary Sciences, Jackson School of Geosciences, The University of Texas at Austin, Austin, TX, USA. [3]Department of Sustainable Earth Systems Sciences, School of Natural Sciences and Mathematics, The University of Texas at Dallas, Dallas, TX, USA.
*Corresponding author. Email: smao@jsg.utexas.edu

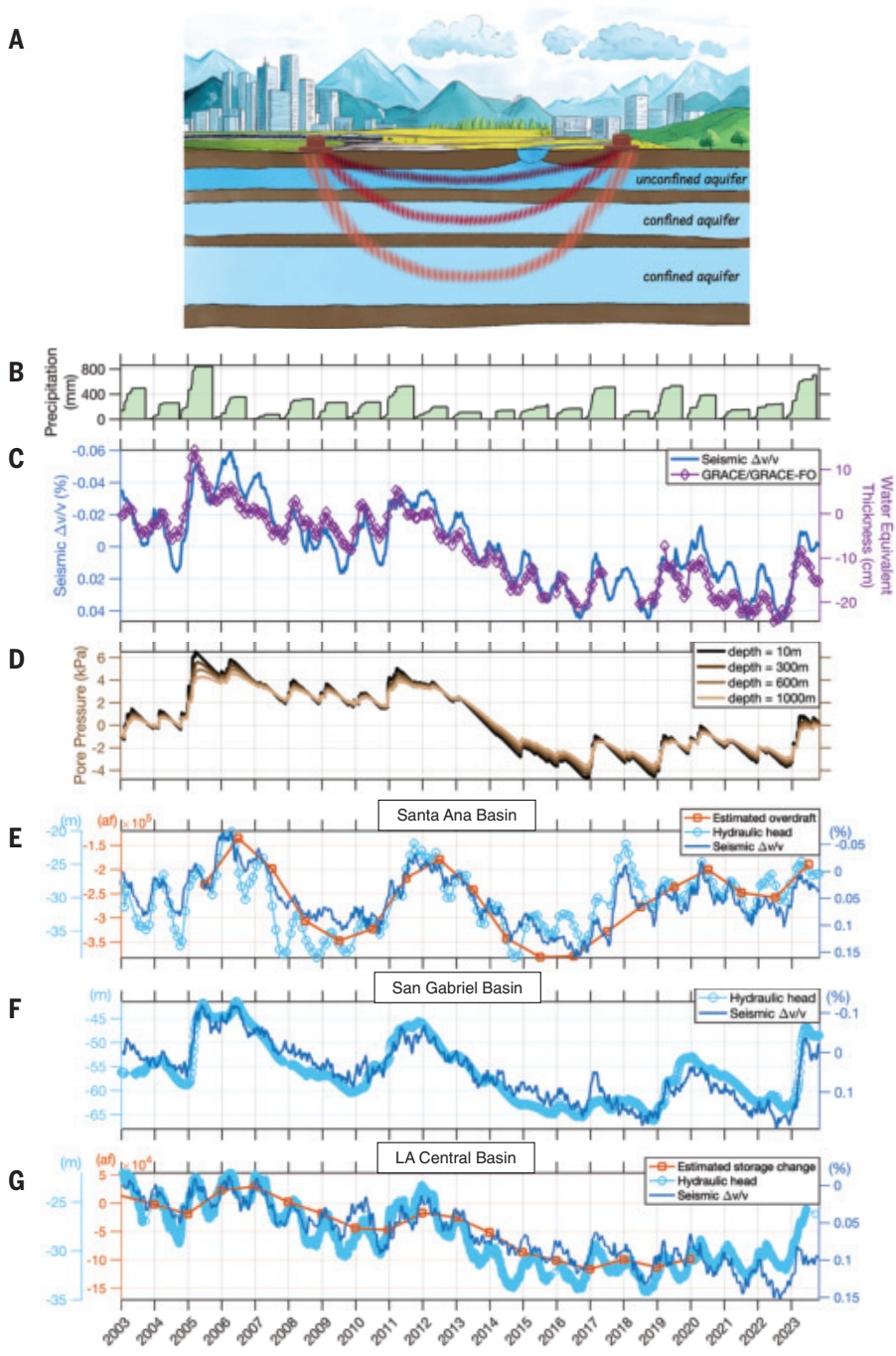


Fig. 1. The seismic sensing and different types of hydrographs from 1 January 2003 to 31 October 2023. (**A**) A schematic illustration of the depth-dependent seismic interferometric sensing. The underground portion of this figure shows a simplified aquifer model, consisting of an unsaturated vadose zone, an unconfined aquifer layer, two confined aquifer layers, and the aquitards in between. Calculating interferometry of the ambient seismic field allows us to retrieve the seismic response of the underground medium between two seismometers. Seismic waves (the reddish traces) of different frequencies travel and thus probe the underground medium properties at different depths. The above-surface portion of this figure is produced by an artificial intelligence (AI) art generation program, Midjourney. It shows objects and activities above the ground that are sources of the ambient seismic field, including wind, traffic, urban activities, and ocean waves. (**B**) Annual cumulative precipitation measured at the meteorological station WWP (Whittier Hills Wilderness Preserve; denoted in fig. S1B as a green diamond). (**C**) A comparison of the seismic hydrograph (blue) and satellite gravimetry (purple). The seismic hydrograph ($\Delta v/v$) is measured over the entire study area, calculated with a 21-day moving-window average at 1-day steps. The purple line represents the water equivalent thickness (WET) derived from GRACE and GRACE-FO missions with a monthly resolution. (**D**) Modeling of pore-pressure variations in response to diffusion of precipitation and the coupled poroelastic deformation. (**E** to **G**) Comparisons of $\Delta v/v$ (dark blue), hydraulic head (cyan), and estimated storage changes (red) in (E) the Santa Ana Basin, (F) the San Gabriel Basin, and (G) the Los Angeles Central Basin, respectively. $\Delta v/v$ in each panel is measured within the corresponding basin. Hydraulic head data are from monitoring wells located in the respective basins (locations denoted in fig. S1B). The red line in (E) is the overdraft, or the available empty storage space, estimated for the Santa Ana Basin by Orange County Water District. The red line in (G) is the aquifer storage changes estimated for the LA Central Basin based on groundwater flow simulation. See section S8 of (*32*) for more details about the various datasets and modeling. Note that (C) represents a regional average, whereas (E) to (G) are basin-scale localized measurements.

California Seismic Network (*17*) in the GLA. Applying advanced seismic interferometry techniques, we calculated the seismic velocity changes, $\Delta v/v$, in GLA over the past two decades (*32*).

The time series of $\Delta v/v$ from 1 January 2003 to 31 October 2023 is shown by the blue line in Fig. 1C, which we term a seismic hydrograph as it characterizes quantitatively the fluctuations of subsurface water storage. The seismic hydrograph is an integrated measure of water content over the space (or volume) through which seismic waves propagate (Fig. 1A). Because seismic waves sample a volume, $\Delta v/v$ differs from measurements of the hydraulic head in wells, which are point measurements.

We validated the ability of seismic hydrographs to capture groundwater fluctuations from regional to subbasin scales. This allowed us to investigate the spatiotemporal variations in $\Delta v/v$ to understand the amplitude, timing, and depth distribution of groundwater drought and the natural aquifer recharge from the AR storms of 2023.

Regional- versus subbasin-scale fluctuations

Leveraging existing seismic data (*17*), we obtained seismic hydrographs on 2-km by 2-km grid cells in GLA. This high spatial resolution allows us to retrieve both regional and localized aquifer behaviors.

We verified the regional seismic hydrograph against the water equivalent thickness (WET) changes derived from gravity observations from the GRACE and GRACE-FO missions (*33*–*35*) [see section S8 in (*32*)]. In Fig. 1C, $\Delta v/v$ (blue line) is measured across the entire study area

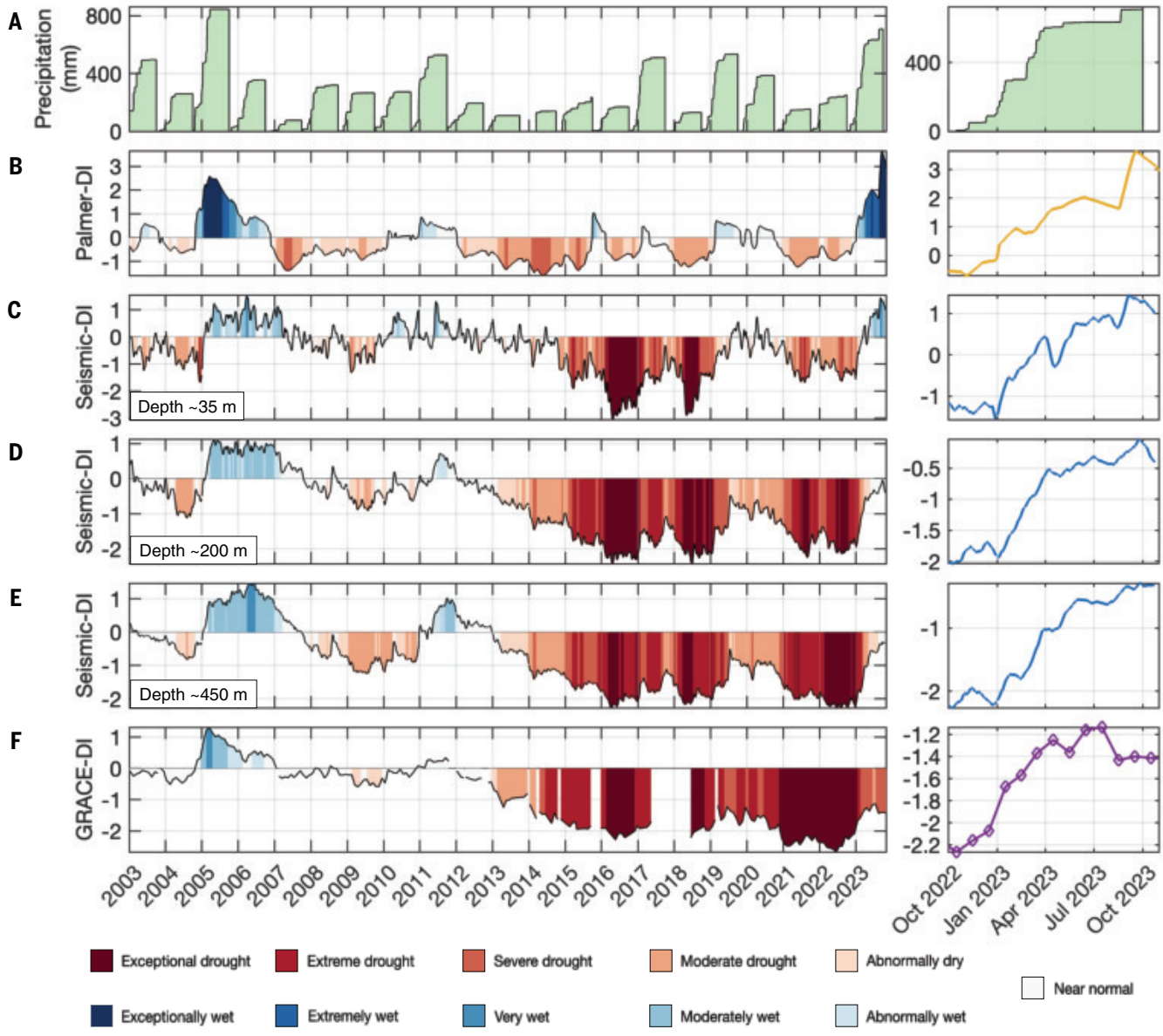


Fig. 2. Comparisons of drought indices (DIs) defined with different types of data. (**A**) Annual cumulative precipitations measured at the meteorological station WWP. (**B**) Calibrated Palmer-DI, which quantifies the severity of meteorological and soil-moisture drought. (**C** to **E**) Seismic-DI at different depths: (C) ~35 m, (D) ~200 m, and (E) ~450 m below the land surface, calculated with frequency bands (C) 1.0 to 4.0 Hz, (D) 0.5 to 2.0 Hz, and (E) 0.2 to 0.8 Hz, respectively. (**F**) Calibrated GRACE-DI. See section S3 of (*32*) for definitions and standardizations of these drought indices. The left column shows the full study period from 1 January 2003 to 31 October 2023, and the right column shows zoom-in views from 1 October 2022 to 31 October 2023.

(fig. S1A), whereas the WET (purple line) is a measurement of total mass changes over a much larger area of 3 by 3 arc degrees (shown in fig. S1C). Seismic and satellite gravimetry also differ in their temporal discretization and resolution: $\Delta v/v$ is measured almost continuously, and we show $\Delta v/v$ with a daily moving average (a 21-day moving average with 1-day steps for a stable signal-to-noise ratio). WET samples discretely in time with a monthly interval. The seismic hydrograph characterizes water content changes only in the subsurface, whereas WET represents changes in the total amount of terrestrial water, including both surface and subsurface water components.

Nevertheless, the regional seismic hydrograph and WET exhibit consistent temporal trends in the past two decades over the GLA area. They both register the seasonal and the interannual fluctuations of aquifer storage. The seasonal variations characterize the annual hydrological cycles in response to the Mediterranean climate in GLA: In winter, the seismic hydrograph and WET show increases in groundwater storage in response to stormwater replenishment and reduced pumping; in dry, hot summer months, both curves show declines in groundwater storage owing to heavy pumping to meet local water demand. The multiyear variations in seismic hydrographs and gravity document an overall decline in groundwater storage in GLA from 2003 to 2023, resulting from the combined effects of long-term drought and groundwater overdraft.

We further compare the regional measurements with simulations of pore-pressure changes in response to precipitation (Fig. 1D). Considering both the diffusion of water and its coupling with deformation (*36*–*38*) [see section S4 in

(*32*)], this simplified poroelastic model informs the overall trends of aquifer storage, which match well with the regional seismic and gravity observations.

The excellent agreement between seismic, satellite gravimetry, and pore-pressure modeling at both seasonal and interannual time scales validates the use of the seismic hydrograph to capture average hydrologic conditions at regional scales.

We also calculated and validated the seismic hydrographs at smaller spatial scales. We zoom into three primary basins in GLA: the Santa Ana Basin, the Los Angeles Central Basin, and the San Gabriel Basin (fig. S1A), which are managed by different municipal water districts. In each basin, we show comparisons (Fig. 1, E to G) of the seismic hydrographs measured within the basin, the hydraulic head measured at local groundwater monitoring wells, and storage change estimation [including the estimated storage overdraft in Santa Ana Basin and the estimated aquifer storage changes in LA Central Basin; see section S8 in (*32*)]. In these three adjacent basins, the groundwater storages exhibit long-term trends that differ considerably from each other or the regional average (Fig. 1C) owing to the spatial variability of hydrogeological conditions, local water demands, and water withdrawal and replenishment practices in different water districts. In fig. S2, we further compare the basin-scale seismic hydrographs with surface vertical deformation inferred from GPS stations. GPS measurements mirror the long-term trends in seismic hydrographs, providing further evidence for the spatial heterogeneity of aquifer fluctuations across the study area.

Across these basins, the seismic hydrographs coincide well with the hydraulic head records, aquifer storage change simulations, and GPS measurements, affirming the effectiveness of seismic sensing in capturing localized changes in aquifer storage. Minor differences exist among the various types of data mainly because (i) they gauge the water content over different spatial volumes, and (ii) they manifest physical properties that respond differently to changes in water content. These comparisons verify the usefulness of seismic sensing for assessing aquifer fluctuations at basin-to-watershed scales, which is crucial for the timely management of water resources, such as the estimation of safe yield and the planning of regional water allocation.

Vertical seismic hydrographs (VSHs)

One special benefit of $\Delta v/v$ is its depth resolution. Satellite sensing provides measurements that are integrated over vertical columns, and in situ borehole data only give point-scale measurements at certain depths. By contrast, seismic sensing allows for probing the subsurface medium as a function of depth by using different frequency content [section S2 in (*32*)]. The derived vertical seismic hydrographs (VSHs) (fig. S6, B to F) track $\Delta v/v$ across different depths between ~20 and 800 m beneath the land surface, offering a valuable opportunity to understand the vertical variability of aquifer dynamics. In this study, we show VSHs measured across the study area and investigate the averaged depth variabilities.

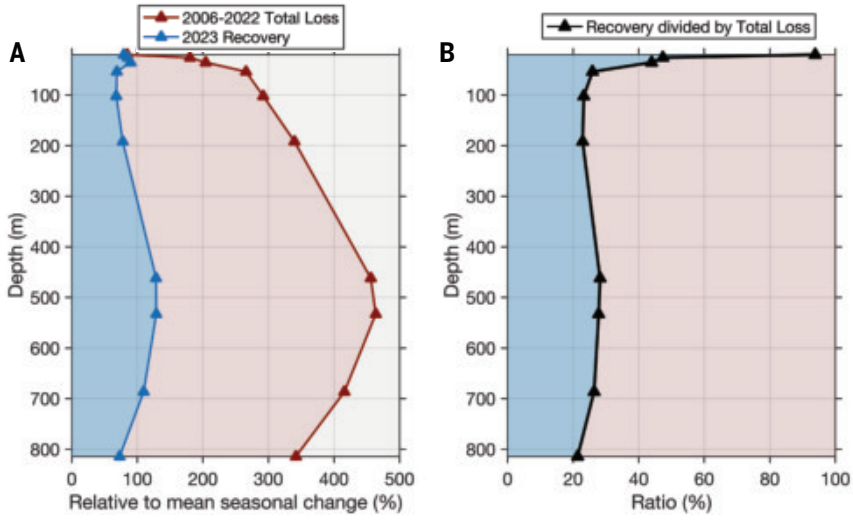


Fig. 3. Depth profiles of groundwater depletion and recovery. (**A**) The red line represents the total loss, defined as the loss accumulated over the recent droughts between the recorded high in spring 2006 and the recorded low in summer 2022. The blue line is the recovery in 2023, defined as the increase between 31 December 2022 and 30 September 2023, on the VSHs. The horizontal axis denotes the percentage relative to the mean annual change at corresponding depths. (**B**) The black line shows the recovery in 2023 [blue line in (A)] normalized by the total loss in the past two decades [red line in (A)].

The VSH focusing on October 2022 to October 2023 (fig. S6, right column) provides clear evidence of how aquifers at different depths responded to storms in 2023. In response to the consecutive AR storm series from January to March 2023, VSHs at shallower depths exhibit evident and rapid increases in groundwater storage, whereas the response at greater depths is smoother and longer lasting. By April, shallow depths were largely recovered (fig. S6, B and C, right column), whereas recovery at middle to greater depths took longer until June (fig. S6, D to F, right column). The amplitudes and time scales of the groundwater recovery at different depths, as shown by the VSHs, are comparable to those following the AR storms of water year 2005. In response to Hurricane Hilary, an intense but rapid event in August 2023, the VSH registered an immediate increase that took less than a month. This increase is only observed at relatively shallow depths, whereas deep aquifers barely change. This observation demonstrates the limited impact of rapid storm events on deeper aquifers.

From a long-term perspective, the VSH from 2003 to 2023 (fig. S6, left column) reveals varying patterns of groundwater storage at different depths. At shallower depths, the seismic hydrographs fluctuate rapidly, closely trailing precipitation events, but the net multiyear change is minute. At greater depths, the seismic hydrographs respond on seasonal to multiyear scales, and the long-term net decline is more pronounced. This suggests that the long-term depletion of groundwater is both more severe and more difficult to remediate at greater depths.

Surface-water drought versus groundwater drought

Over the past two decades, California has experienced substantial precipitation volatility, and climate modeling projects more frequent and intense shifts between extremely dry and wet conditions (*1*). To evaluate the impact of hydroclimatic extremes on water resources and inform water management decisions, the occurrence, duration, and severity of droughts are tracked regularly at national and regional scales (*39*, *40*).

Most drought indices are derived using measurements of above-surface and near-surface water, including precipitation, streamflow, surface reservoir gauge, snow cover and melt, and soil moisture (*39*, *40*). However, quantifying groundwater drought conditions remains challenging (*41*) owing to the limited resolution of groundwater monitoring data despite the overarching role of groundwater in the total water supply. Here we showcase how seismic analysis can contribute to indexing the groundwater drought.

Using VSHs, we propose a depth-dependent seismic drought index (Seismic-DI) that quantitatively characterizes subsurface water deficit

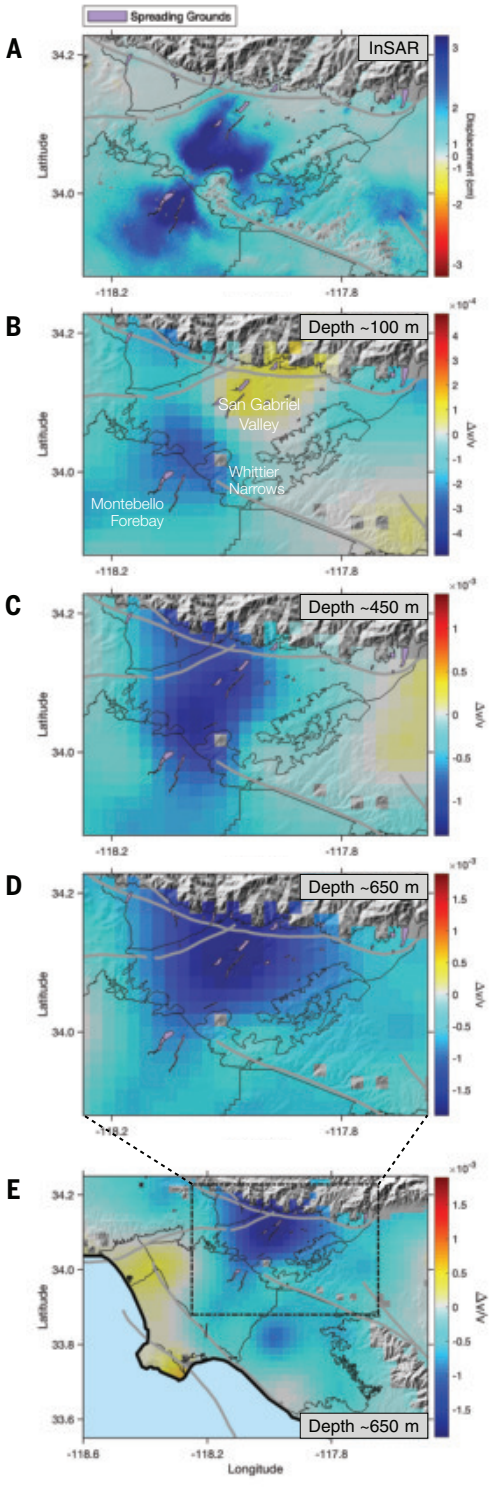


Fig. 4. The spatial variability of groundwater recovery following the 2023 atmospheric-river storms around the San Gabriel Valley. (**A** to **E**) The dashed box in (E) denotes the location of (A) to (D) with respect to the entire study area. From (A) to (D) are measurements from the ground surface to greater depths: (A) The quasi-vertical displacement derived from InSAR between 27 December 2022 and 1 June 2023. (B) to (D) show net changes of seismic velocity between 27 December 2022 and 1 June 2023, at depths of (B) ~100 m, (C) ~450 m, and (D) ~650 m below the surface. These maps are measured with frequency content of (B) 0.5 to 2.0 Hz, (C) 0.2 to 0.8 Hz, and (D) 0.12 to 0.48 Hz, respectively. Spatial images of the entire study area are shown in fig. S9. Pink areas enclosed by black lines in all maps denote the location of Spreading Grounds Facilities operated by the Department of Public Works of Los Angeles County to enhance the replenishment of groundwater.

across different depths [see section S3 in (*32*) for detailed definitions]. We show the Seismic-DI at ~35, 200, and 450 m, respectively (Fig. 2, C to E). In comparison, we also present the Palmer drought index (Palmer-DI) and a GRACE drought index (GRACE-DI) (Fig. 2) (*42*–*47*), which are both calibrated with the same reference period (2003–2012) and standardization as Seismic-DI. The Palmer-DI, based on temperature, precipitation, and a simplified water balance model, indicates water availability near and above the land surface (in shallow soils and in the atmosphere). By contrast, the Seismic-DI measures subsurface water changes (either in saturated or unsaturated zones), and the GRACE-DI measures the total changes in surface and subsurface water content.

A comparison of drought indices suggests that the groundwater deficit evolves considerably differently from that of near- and above-surface water (Fig. 2). Over the two-decadal study period, surface-water availability (indicated by Palmer-DI) varies rapidly in response to precipitation, exhibiting severe to moderate drought during dry years (for example, 2007–2010, 2012–2016, and 2020–2022) but quickly returning to wet conditions in storm years (for example, 2005, 2011, and 2023). By contrast, Seismic-DI and GRACE-DI consistently suggest much more severe conditions in groundwater drought that have continued to accumulate over the study period. Although a few storm years help mitigate the groundwater drought, their replenishment does not compensate for the substantial depletion during dry years. In the years from 2014 to 2022, the surface water recovered and reached "wet" conditions amid storms, but the deep aquifers (Fig. 2, D to F) remained persistently in moderate to extreme drought conditions.

During the most recent drought (2020–2022), the Seismic-DI (Fig. 2, C to E) yields more severe drought at deeper depths, suggesting pronounced groundwater depletion at greater depths (~450 m). An ensemble of drought periods defined by the Seismic-DI at different depths (Fig. 2, C to E) matches well with the drought periods characterized by GRACE-DI (Fig. 2F), which is a vertically integrated measure.

Depth profiles of groundwater depletion and recovery

To understand better the groundwater deficit, we used VSHs to quantify the depth distribution of groundwater loss during the past droughts and recovery from the 2023 AR storms in GLA (Fig. 3) [see section S5 in (*32*) for definitions of the lost and recovered amplitudes]. The VSHs are calculated over the entire study area. The depletion curve (red line) suggests that groundwater loss in the past two decades spans a wide depth range, reaching a maximum of >450% of its mean seasonal variation at around 500-m depth. In response to the 2023 AR storms, groundwater recovered to about 120% of its mean seasonal change. The area between the depletion and recovery curves corresponds to the net loss in stored groundwater.

We plotted the depth profile of the recovery ratio, defined as the amplitude of $\Delta v/v$ recovered in 2023 divided by the total loss during four recent droughts since 2006 (Fig. 3B). At depths shallower than 50 m, our observations imply that the groundwater storage recovered almost completely, whereas at greater depths, only about 25% of water lost since 2006 was restored by the intense AR storms of 2023.

Areal variability of the natural recharge

Basin-scale seismic hydrographs show varying magnitudes of groundwater replenishment in different basins after the AR storms of 2023 (Fig. 1, E to G). To map the spatial variability of natural recharge, we imaged the groundwater recovery in 2023 using seismic and satellite sensing (Fig. 4 and fig. S9). Displacements of land surface inferred from interferometric synthetic aperture radar (InSAR) (Fig. 4A and fig. S9A) depict strain changes integrated over vertical columns (*12*, *15*, *48*–*52*). The seismic and satellite imagery (Fig. 4) both highlight prominent groundwater replenishment (in blue areas) in the west San Gabriel Basin and near the Whittier Narrows at shallower (~100 m) to mid-depths (~450 m). These depth ranges correspond to the water-bearing layers in the San Gabriel basin. The thickness of these water-bearing deposits averages about 300 m inside the basin and about 250 m in Whittier Narrows. Toward the eastern and western perimeters of the basin, the average thickness reduces to about 100 m (*53*). Beneath these water-bearing sediments lie non–water-bearing formations that, despite their name, also contain some water, though they produce only limited quantities compared to the more permeable water-bearing layers above. Subsurface flow from the San Gabriel Mountains, as a result of the 2023 AR storms, likely caused changes in pore pressure within these deeper non–water-bearing layers (*54*, *55*). Although these small pore-pressure changes in more consolidated deep layers do not generate observable surface deformation, seismic interferometry can detect relative changes in pore pressure in the form of $\Delta v/v$. The replenishment at depths of ~650 m is most pronounced in the north San Gabriel Basin along the front of the San Gabriel Mountains and extends to the entire basin (Fig. 4D). A comparison between the seismic and satellite imagery with the locations of the Spreading Grounds Facilities (Fig. 4) suggests that human-enhanced groundwater recharge may also partly contribute to the replenishment. The ability to map the extent of aquifer recovery provides an effective new tool for groundwater management.

High-resolution seismic sensing of aquifers

Advanced seismic interferometry methods enable the continuous monitoring of aquifers with high spatial resolution (for example, a 2-km by 2-km resolution with the existing seismic network in GLA in this study). This allows an understanding of the spatial variability in hydrophysics from regional to watershed scales, which can directly assist local management and regional allocation of groundwater resources.

A key advantage of seismic sensing, compared with existing aquifer monitoring tools, is its high vertical resolution. We showcased the depth profiles of decadal and subannual aquifer fluctuations (Fig. 3), which underscore large aquifer overdrafts and the lack of replenishment at depth. A single epic year of storms proved insufficient to restore the groundwater deficit that gradually accumulated over the previous decades. The deep aquifer would require many more wet years or intentionally enhanced recharge and reduced pumping to recover fully.

These depth profiles also emphasize the distinct expressions of groundwater and surficial water droughts. Considering the critical role of groundwater (which contributes 40 to 60% of the freshwater supply in California), our study highlights the need to incorporate deep aquifers for a more complete assessment of total water deficits. The depth-dependent Seismic-DI that we proposed (Fig. 2) can serve as a cost-effective tool to inform groundwater drought in practice with high spatiotemporal resolutions.

REFERENCES AND NOTES

1. D. L. Swain, B. Langenbrunner, J. D. Neelin, A. Hall, *Nat. Clim. Chang.* **8**, 427–433 (2018).
2. C. C. Lee, *Int. J. Climatol.* **42**, 4214–4222 (2022).
3. California Department of Water Resources (DWR), Semi-Annual Update, Water Year 2023; https://cawaterlibrary.net/document/californias-groundwater-conditions-semi-annual-update-october-2023.
4. *California Department of Water Resources (DWR),* Water Resilience Portfolio (2020); https://resources.ca.gov/-/media/CNRA-Website/Files/Initiatives/Water-Resilience/Final_California-Water-Resilience-Portfolio-2020_ADA3_v2_ay11-opt.pdf.
5. R. G. Taylor *et al*., *Nat. Clim. Chang.* **3**, 322–329 (2013).
6. S. M. Gorelick, C. Zheng, *Water Resour. Res.* **51**, 3031–3051 (2015).
7. T. Gleeson, K. M. Befus, S. Jasechko, E. Luijendijk, M. B. Cardenas, *Nat. Geosci.* **9**, 161–167 (2016).
8. B. R. Scanlon *et al*., *Nat. Rev. Earth Environ.* **4**, 87–101 (2023).
9. A. Binley *et al*., *Water Resour. Res.* **51**, 3837–3866 (2015).
10. A. M. White, W. P. Gardner, A. A. Borsa, D. F. Argus, H. R. Martens, *Water Resour. Res.* **58**, WR032078 (2022).
11. A. A. Borsa, D. C. Agnew, D. R. Cayan, *Science* **345**, 1587–1590 (2014).
12. D. A. Schmidt, R. Bürgmann, *J. Geophys. Res. Solid Earth* **108**, 2416 (2003).
13. R. Knight *et al*., *Groundwater* **56**, 893–908 (2018).
14. R. G. Smith *et al*., *Water Resour. Res.* **53**, 2133–2148 (2017).
15. J. Chen, R. Knight, H. A. Zebker, W. A. Schreüder, *Water Resour. Res.* **52**, 3623–3636 (2016).
16. L. A. Blazevic *et al*., *Water* **12**, 1230 (2020).
17. SCEDC, Southern California Earthquake Center, Caltech, Dataset (2013); https://doi.org/10.7909/C3WD3xH1.
18. M. Campillo, A. Paul, *Science* **299**, 547–549 (2003).
19. N. M. Shapiro, M. Campillo, *Geophys. Res. Lett.* **31**, 2004GL019491 (2004).
20. G. Poupinet, W. L. Ellsworth, J. Frechet, *J. Geophys. Res.* **89** (B7), 5719–5731 (1984).
21. C. Sens-Schönfelder, U. Wegler, *Geophys. Res. Lett.* **33**, L21302 (2006).
22. C. Voisin, M. A. R. Guzmán, A. Réfloch, M. Taruselli, S. Garambois, *J. Water Resource Prot.* **9**, 1414–1427 (2017).
23. T. Lecocq, L. Longuevergne, H. A. Pedersen, F. Brenguier, K. Stammler, *Sci. Rep.* **7**, 14241 (2017).
24. T. Clements, M. A. Denolle, *Geophys. Res. Lett.* **45**, 6459–6465 (2018).
25. A. Mordret *et al*., *Geophys. J. Int.* **221**, 692–705 (2020).
26. L. Illien *et al*., *AGU Adv.* **2**, e2021AV000398 (2021).
27. K. F. Feng, H. H. Huang, Y. J. Hsu, Y. M. Wu, *J. Geophys. Res. Solid Earth* **126**, e2021JB022650 (2021).
28. S. Mao, A. Lecointre, R. D. van der Hilst, M. Campillo, *Nat. Commun.* **13**, 4643 (2022).
29. E. Delouche, L. Stehly, *J. Geophys. Res. Solid Earth* **128**, e2023JB026759 (2023).
30. L. A. Ermert *et al*., *Solid Earth* **14**, 529–549 (2023).
31. V. Sobolevskaia *et al*., *Water Resour. Res.* **60**, e2023WR036172 (2024).
32. Materials and methods are available as supplementary materials.
33. J. Wahr, M. Molenaar, F. Bryan, *J. Geophys. Res.* **103** (B12), 30205–30229 (1998).
34. J. S. Famiglietti *et al*., *Geophys. Res. Lett.* **38**, L03403 (2011).
35. B. R. Scanlon *et al*., *Proc. Natl. Acad. Sci. U.S.A.* **115**, E1080–E1089 (2018).
36. E. A. Roeloffs, *J. Geophys. Res.* **93**, 2107–2124 (1988).
37. P. Segall, *Earthquake and Volcano Deformation* (Princeton Univ. Press, 2010).
38. D. Rivet, F. Brenguier, F. Cappa, *Geophys. Res. Lett.* **42**, 6332–6339 (2015).
39. T. B. McKee, N. J. Doesken, J. Kleist, "The relationship of drought frequency and duration to time scales" in *Proceedings of the 8th Conference on Applied Climatology* (1993), vol. 17, pp. 179–183.
40. A. Zargar, R. Sadiq, B. Naser, F. I. Khan, *Environ. Rev.* **19**, 333–349 (2011).
41. M. E. Miro, J. S. Famiglietti, *Remote Sens.* **10**, 143 (2018).
42. R. Houborg, M. Rodell, B. Li, R. Reichle, B. F. Zaitchik, *Water Resour. Res.* **48**, W07525 (2012).
43. B. R. Scanlon *et al*., *Water Resour. Res.* **51**, 9891–9903 (2015).
44. B. F. Thomas *et al*., *Remote Sens. Environ.* **198**, 384–392 (2017).
45. M. Zhao, A. Geruo, I. Velicogna, J. S. Kimball, *J. Hydrometeorol.* **18**, 2117–2129 (2017).
46. W. Chen, C. Huang, Z. L. Yang, *J. Hydrol.* **603**, 126802 (2021).
47. A. Rateb, A. Sun, B. R. Scanlon, H. Save, E. Hasan, *Earth Space Sci.* **9**, EA002162 (2022).
48. B. Riel, M. Simons, D. Ponti, P. Agram, R. Jolivet, *Water Resour. Res.* **54**, 3557–3582 (2018).
49. G. W. Bawden, W. Thatcher, R. S. Stein, K. W. Hudnut, G. Peltzer, *Nature* **412**, 812–815 (2001).
50. R. Lanari, P. Lundgren, M. Manzo, F. Casu, *Geophys. Res. Lett.* **31**, L23613 (2004).
51. D. F. Argus, M. B. Heflin, G. Peltzer, F. Crampé, F. H. Webb, *J. Geophys. Res. Solid Earth* **110**, B04401 (2005).
52. N. Houlie, G. J. Funning, R. Bürgmann, *IEEE Trans. Geosci. Remote Sens.* **54**, 5365–5374 (2016).
53. California Department of Water Resources (DWR), 1966 Planned utilization of groundwater basins, San Gabriel Valley; Appendix A: Geohydrology.
54. K. H. Markovich, A. H. Manning, L. E. Condon, J. C. McIntosh, *Water Resour. Res.* **55**, 8278–8304 (2019).
55. D. F. Argus *et al*., *J. Geophys. Res. Solid Earth* **122**, 10559–10585 (2017).
56. The topographic data at the USGS Earth Resources Observation and Science (EROS) Center, https://www.usgs.gov/centers/eros/science/usgs-eros-archive-digital-elevation-shuttle-radar-topography-mission-srtm-1.

ACKNOWLEDGMENTS

We thank the Orange County Water District (OCWD) for providing the estimated aquifer overdraft that they derived for the Santa Ana Basin, shown in Fig. 1E in this study. We appreciate the insights from B. R. Scanlon, A. Rateb, Z.-L. Yang, and C. S. Linick on GRACE data and drought indices. We are thankful to R. Bürgmann, M. Campillo, J. C. Thompson, and R. Smith for their perspectives. We thank the three anonymous reviewers for their helpful feedback. We acknowledge the AI art generation software Midjourney for creating the aboveground portion of Fig. 1A. **Funding:** S.M. knowledges the support from the George A. Thompson Fellowship at Stanford University. Analysis of seismic data was performed on the computing cluster at the Stanford Center for Computational Earth and Environment Science (CEES). **Author contributions:** Conceptualization: S.M., G.C.B., W.L.E. Methodology: S.M. Investigation: S.M., Y.Z. Visualization: S.M. Supervision: G.C.B., W.L.E. Writing – original draft: S.M. Writing – review and editing: S.M., G.C.B., W.L.E., Y.Z. **Competing interests:** The authors declare that they have no competing interests. **Data and materials availability:** The seismic data used in this study are available from the Southern California Earthquake Data Center under network code CI (*17*). The topographic data of metropolitan Los Angeles are available from the USGS Earth Resources Observation and Science (EROS) Center (*56*). The data sources for precipitation, groundwater well, satellite gravimetry, GPS, and hydrological simulations are detailed in section S8 of (*32*). **License information:** Copyright © 2025 the authors, some rights reserved; exclusive licensee American Association for the Advancement of Science. No claim to original US government works. https://www.sciencemag.org/about/science-licenses-journal-article-reuse.

SUPPLEMENTARY MATERIALS

science.org/doi/10.1126/science.adr6139
Supplementary Text S1 to S8
Figs. S1 to S10
Tables S1 and S2
References (*57*–*98*)

Submitted 10 July 2024; accepted 17 December 2024
10.1126/science.adr6139

MARINE CONSERVATION

Elephant seals as ecosystem sentinels for the northeast Pacific Ocean twilight zone

Roxanne S. Beltran[1]*, Allison R. Payne[1], A. Marm Kilpatrick[1], Conner M. Hale[1], Madison Reed[1], Elliott L. Hazen[1,2], Steven J. Bograd[2], Joffrey Jouma'a[1], Patrick W. Robinson[1], Emma Houle[1], Wade Matern[1], Alea Sabah[1], Kathryn Lewis[1], Samantha Sebandal[1], Allison Coughlin[1], Natalia Valdes Heredia[1], Francesca Penny[1], Sophie Rose Dalrymple[1], Heather Penny[1], Meghan Sherrier[1], Ben Peterson[1], Joanne Reiter[1], Burney J. Le Boeuf[1], Daniel P. Costa[1,3]

The open ocean twilight zone holds most of the global fish biomass but is poorly understood owing to difficulties of measuring subsurface ecosystem processes at scale. We demonstrate that a wide-ranging carnivore—the northern elephant seal—can serve as an ecosystem sentinel for the twilight zone. We link ocean basin–scale foraging success with oceanographic indices to estimate twilight zone fish abundance five decades into the past, and into the future. We discovered that a small variation in maternal foraging success amplified into larger changes in offspring body mass and enormous variation in first-year survival and recruitment. Worsening oceanographic conditions could shift predator population trajectories from current growth to sharp declines. As ocean integrators, wide-ranging predators could reveal impacts of future anthropogenic change on open ocean ecosystems.

Many ecosystems are highly dynamic, with resource pulses cascading through species interactions to alter food webs. Environmental variation can cause large fluctuations in wild animal populations (*1*), with classic examples that include cone masting events affecting squirrel vital rates (*2*) and snowpack affecting ungulate recruitment (*3*). However, unlike in terrestrial ecosystems where resource pulses and their impacts on populations have been quantitatively measured, environmental variation in the deep, open ocean and its impact on the food web are rarely studied (*4*). A major unanswered question is whether deep, open ocean ecosystems, which hold the majority of global fish biomass (*5*, *6*), have similarly large and frequent fluctuations in population dynamics that cascade through trophic levels or whether populations in these relatively insulated ecosystems are more stable through time. In recent years, large fluctuations in marine predator vital rates [e.g., whales (*7*), fur seals (*8*), and penguins (*9*)] have suggested that marine ecosystems are highly variable. However, small changes at lower trophic levels can result in large variation at higher trophic levels (*10*), so large fluctuations in predator vital rates may stem from small or large changes in lower trophic levels. Unfortunately, the factors that influence prey abundance in many marine fish, and especially the population dynamics of fish in the twilight zone, are poorly understood (*11*).

[1]Department of Ecology and Evolutionary Biology, University of California Santa Cruz, Santa Cruz, CA, USA. [2]Ecosystem Science Division, Southwest Fisheries Science Center, National Oceanic and Atmospheric Administration, National Marine Fisheries Service, Monterey, CA, USA. [3]Institute of Marine Sciences, University of California Santa Cruz, Santa Cruz, CA, USA.
*Corresponding author. Email: roxanne@ucsc.edu

Technological constraints are a major limitation to understanding the scale and impact of environmental variation in three-dimensional open ocean ecosystems (*12*). Basic monitoring of a limited subset of physical and biological variables requires advanced technologies and costly research vessels, resulting in fragmented, short time series or snapshots, often collected near shore. As a result, interannual variation in the open ocean is often described using satellite-derived surface measurements (e.g., sea surface temperature) or oceanographic indices based on physical variables that are sometimes correlated with the abundance or demography of marine organisms (*13*–*18*) (e.g., North Pacific Gyre Oscillation: sea surface height variability, upwelling, strength of gyre circulation; Southern Oscillation Index: sea level pressure differences, ocean currents; Pacific Decadal Oscillation: sea surface temperature). These satellite-derived measurements are limited to the top 1 m of the ocean, which is up to 11,000 m deep (*19*). Because measurements are often constrained to single trophic levels, short durations, or limited spatial scales, it has been difficult to quantify temporal variation in fish abundance in the twilight zone. Understanding the past and future impacts of environmental variation in this region requires new tools for measuring ecological processes.

Wildlife have been proposed as sentinels for ecosystems (*20*), including as indicators of human impacts and ecosystem changes (*21*) that are otherwise difficult or impossible to measure (*22*). Some marine predators integrate broad-scale prey abundance by foraging over thousands of kilometers in the ocean each year (*23*). Monitoring interannual variation in foraging success of these marine predators could provide estimates of prey abundance in areas and at scales that are otherwise impossible to measure (*24*). Moreover, longitudinal measurements of demographic variation in these sentinel species could reveal the cascading impacts of fluctuations in lower trophic levels on top predators.

An ecosystem sentinel for the open ocean

We examined interannual variation in prey consumption of northern elephant seals (*Mirounga angustirostris*) to examine the magnitude and frequency of variability in the open ocean twilight zone. These seals predominantly consume twilight zone fish (*25*) and integrate food resources over large portions of the northeast Pacific Ocean (Fig. 1). We then quantified links between oceanographic indices and prey consumption, which provided a way to estimate the abundance of twilight zone fish four decades into the past and to make predictions 2 years into the future. We quantified four temporal scales of seal demography over four decades to examine the impact of environmental variation on both short- and long-term demographic processes. Finally, we identified links between oceanographic indices and seal demographic rates to examine whether these indices might also serve as correlates for the demography of open ocean predators. All methods are detailed in the supplementary text.

To quantify the suitability of elephant seals as ecosystem sentinels, we first estimated the ocean volume (in km^3) sampled by foraging elephant seals by multiplying the area (in km^2) of a polygon encompassing seal foraging locations for each 7-month postmolt foraging trip (June to December) by the average of the 95th percentiles of seals' dive depths (in km). Each year, seals instrumented with satellite-linked data loggers during the 7-month-long foraging trip (n = 13.8 adult female seals per year) made a total of 143,201 dives, covering 5.8 million km^2 of horizontal space and an average 0.77 km of vertical space, for a total of 4.4 million km^3 of ocean volume sampled each year (Fig. 1A). Approximately half (50.7%) of all dives were foraging dives [rather than transit, resting, or benthic dives; (*26*)] (fig. S1), and almost all dives were in the twilight zone, 200 to 1000 m below the ocean surface (96% of all dives and 99% of foraging dives; fig. S2). Previous work showed that seals make an average of 14.6 prey capture attempts per foraging dive (*27*), which suggests that instrumented seals made an average of 1,060,002 prey capture attempts per year. This vast, extensive sampling of prey in the twilight zone makes seal foraging success a valuable indicator of twilight zone fish abundance and the northern elephant seal a promising sentinel for this ecosystem.

Sentinel and oceanographic monitoring uncover multidecadal ecosystem dynamics

We examined links between seal mass gain (measured by weighing instrumented seals before

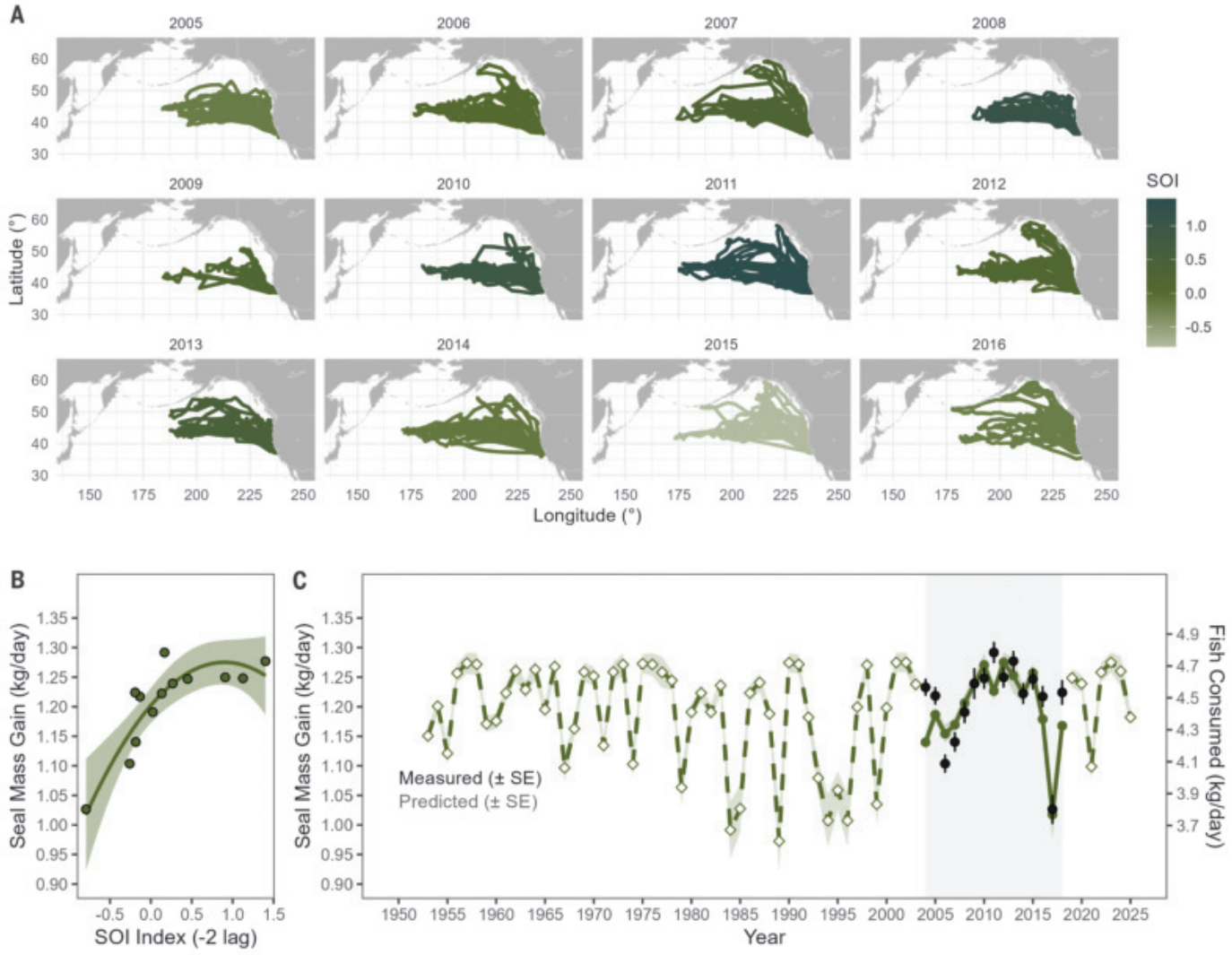


Fig. 1. Large-scale movements of elephant seals across an ocean basin make measurements of their foraging success a useful indicator of biological productivity. (**A**) Northern elephant seals (n_{avg} = 13.8 adult females per year) instrumented with satellite-linked data loggers cover a major portion of the North Pacific Ocean during migrations, traveling thousands of kilometers offshore and hundreds of meters beneath the ocean surface to consume twilight zone fish. (**B**) A very strong correlation between 2-year-lagged oceanographic conditions (SOI, Southern Oscillation Index) and average adult female mass gain {mass gain = 1.20 + [0.16 * SOI (SE = 0.033; P = 0.00065)] − [0.090 * SOI^2 (SE 0.032, P = 0.017)]; coefficient of determination (R^2) = 74%; P = 0.0012; see fig. S4 for other lags and oceanographic variables} allows for (**C**) predictions of historical and future fish consumption estimates based on oceanographic conditions (SOI). In (B) and (C), each solid point shows the average mass gain of 15.3 adult females measured in a single year, often for instrumentation. In (C), black points and error bars are measured seal mass gain (the same points as in Fig. 1B), filled colored points and the solid line are the observed and predicted seal mass gain from the study period, open colored points and dashed lines are predicted seal mass gain for the past and future, and the gray rectangle encompasses the study years. Shading in (B) shows the 95% confidence interval.

and after their 7-month postmolt foraging trip, 15.3 adult female seals per year) and annual averages of three long-term oceanographic indices (fig. S3) for biologically plausible temporal lags (fig. S4). These indices are based on surface measurements of pressure, temperature, and circulation, often with strong coastal signatures, so it was unclear whether they would provide any useful information about ecosystem dynamics in the twilight zone. Over the past two decades, seal mass gained over this vast area was quite stable, with a coefficient of variation of only 5.7% (SD/mean: 0.069/1.21 kg/day) and a range of approximately 25% (range 1.03 to 1.29 kg/day) (Fig. 1, B and C). There was one longer period of 8 years with high foraging success (2009–2016) in between two relatively sharp declines (Fig. 1C). The variability in mass gain was correlated with fluctuations in all three oceanographic indices 2 years earlier (Fig. 1B and figs. S4 and S5), which suggests that these ocean surface indices also provide an estimate of fluctuations in deeper ocean ecosystems. The very strong correlation between mass gain and the long-term Southern Oscillation Index that was observed 2 years previously (Fig. 1B) allowed us to hindcast seal mass gain 45 years into the past and predict 2 years into the future. Specifically, we used the Southern Oscillation Index to predict historic and future fish consumption after converting daily seal mass gain (left y axis in Fig. 1C) to approximate fish consumption (right y axis in Fig. 1C) using a multiplier of 0.27 from previously published daily energy ingestion rates and assimilation efficiencies (*28*). The relationship predicted low fish abundance in 2021, but higher fish abundance in 2019–2020 and 2022–2024, as well as periods of very low fish abundance in

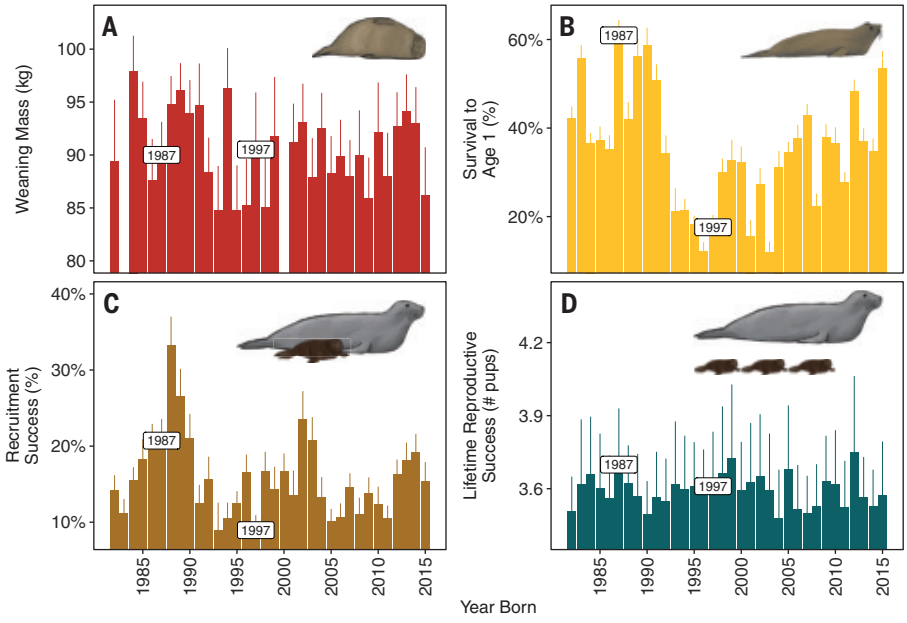


Fig. 2. Female seal demographic rates show pronounced fluctuations across years. Vital rates (±SE) from cohort studies include (**A**) weaning mass, (**B**) survival to age 1, (**C**) survival to reproduction or recruitment success, and (**D**) lifetime reproductive success for recruited seals, showing pronounced fluctuations across years. Each panel shows a demographic measure for annual cohorts of seals tagged and weighed as pups and subsequently followed. Each column shows the average value for a single year's cohort of seals, with mean sample sizes: (A) n = 86.0, (B) n = 221.7, (C) n = 242.4, and (D) n = 38.8. For (D), only seals that recruited into the reproductive population are included in each yearly cohort average lifetime reproductive success to disentangle recruitment success (C) from subsequent reproduction. Two contrasting cohorts are labeled as examples: Seals born in 1987 had higher first-year survival, recruitment success, and lifetime reproductive success after recruitment, whereas seals born in 1997 exhibited lower first-year survival, recruitment success, and lifetime reproductive success.

1984–1985 and 1994–1996, and very high abundance in 1975–1978 (Fig. 1C). The relationship also suggests that the temporal fluctuations in prey populations are often quite rapid, with peaks and troughs frequently occurring every 3 to 5 years (Fig. 1C). These estimates of fish abundance as well as the magnitude and frequency of variability in twilight zone prey populations are presently impossible to measure in any other way.

Temporal variability in predator demography and oceanography

To examine interannual variation in seal demography, we quantified among-year variation in seal offspring size, survival, and reproductive success over four decades (*29*). We marked 8485 seals (mean 242 ± 92 SD seal pups each year) in 35 cohorts born between 1982 and 2015 with unique alphanumeric flipper tags in their birth year, weighed them, and attempted to resight them each subsequent year during hundreds of days per year in the breeding and molting seasons at Año Nuevo Reserve, California, USA (*29*). We evaluated maternal mass gain as a potential mechanistic link between prey abundance and pup weaning mass using data from a subset of mother-pup pairs in which both pups and maternal mass gain were measured. We then used generalized linear models to examine links between oceanographic indices and maternal foraging success, maternal investment (pup size), and pup demographic success.

The impacts of variation in twilight zone prey abundance were amplified from smaller variation in maternal mass gain compared with variation in offspring weaning mass (fig. S5). There was even larger interannual variation in two measurements of seal survival. First-year survival and recruitment success varied sixfold and fourfold among elephant seal cohorts across four decades (Fig. 2), with very strong (e.g., 1987) and weaker (e.g., 1997) cohorts based on first-year survival (61 versus 18%) and recruitment success (21 versus 9%) (Fig. 2). By contrast, lifetime reproductive success, which integrates reproduction across many years, varied only 8% from 3.47 to 3.75 pups (Fig. 2). All four vital rates were significantly correlated with oceanographic indices (Fig. 3 and tables S1 to S4), which suggests that these indices provide some information about the oceanographic processes that affect predator demography. Weaning mass and recruitment success significantly increased with the North Pacific Gyre Oscillation in the year of birth, whereas first-year survival and lifetime reproductive success significantly increased with the Southern Oscillation Index in the year after birth (Fig. 3). Across the range of North Pacific Gyre Oscillation values observed, predicted weaning mass varied by only 6% but predicted recruitment success increased by 69%. Across the range of Southern Oscillation Index values observed, predicted first-year survival increased by 58% but predicted lifetime reproductive success varied by only 3%. The combination of variation in predicted recruitment success and predicted lifetime reproductive success resulted in 2.4 times more lifetime pups produced under the most extreme values of the oceanographic indices (766 versus 323 pups produced per 1000 seals in favorable versus unfavorable ocean conditions).

Variation in predator demography correlated with oceanographic indices could lead to large changes in seal population growth rates, λ. Across the range of oceanographic conditions during our study, estimated λ based on variation in recruitment success varied from a sharp decline (λ = 0.86 ± 0.03) when the North Pacific Gyre Oscillation was at its minimum to rapid growth (λ = 1.24 ± 0.03) when the North Pacific Gyre Oscillation was at its maximum (fig. S6). Elephant seal populations were not self-supporting (λ < 1) in 49% (17 of 35) of study years.

To evaluate the full potential impacts of fluctuations in environmental conditions (including both physical oceanographic variability and other biological phenomena such as predation and competition), we simulated seal population size and age structure after a single year of favorable or unfavorable ocean conditions and calculated the difference in the number of seals produced. We simulated the full northern elephant seal population, including all colonies [n = 220,000 seals; (*30*)] that forage in overlapping areas (*31*) and have similar population trajectories (*30*). We used an age-structured population model with a Leslie matrix parameterized with age-specific fecundity and survival values (*30*) and projected the population 20 years forward using the stable age distribution of the Leslie matrix. We calculated the difference between two scenarios: a single year of high first-year survival (61%, as in 1987) or low first-year survival (18%, as in 1997). The population pulse produced by this single year of high first-year survival would result in an additional 24,588 1-year-old seals surviving compared with a single year of low first-year survival (Fig. 4). Two years later, this high survival cohort would begin generating even more offspring through recruitment to the breeding population than the low survival cohort (2485 in the first year when ~25% of the females recruit at age 3, and 7476 in the second year when most of the remaining seals recruit at age 4) (Fig. 4). Across the 20-year simulation, a single year difference in first-year survival could result in an additional 312,812 seals added to the population. These population projections show that

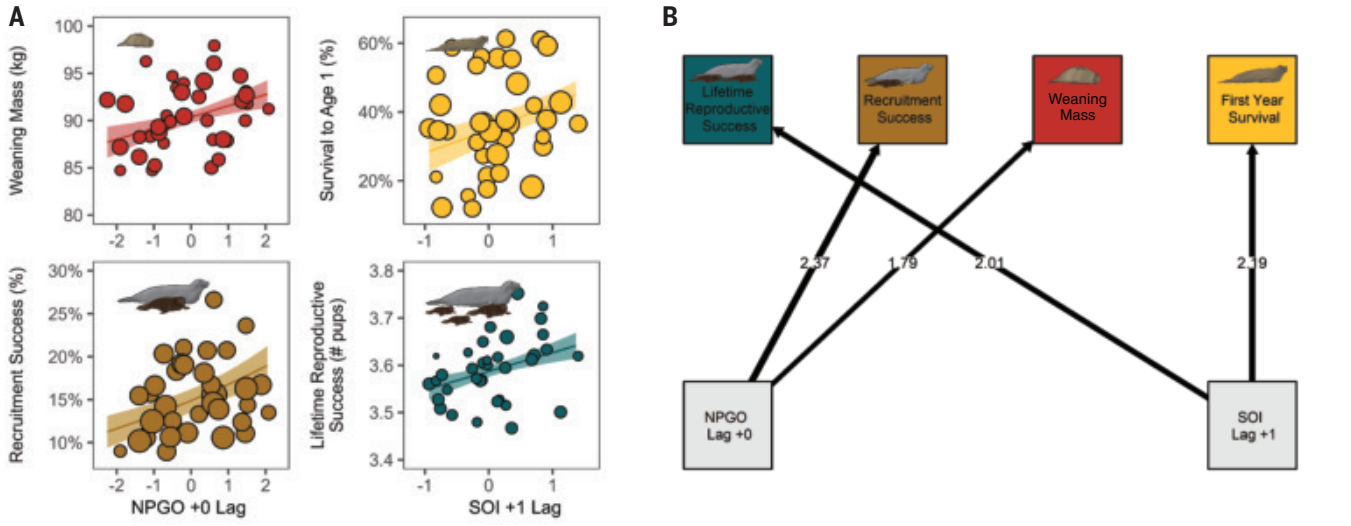
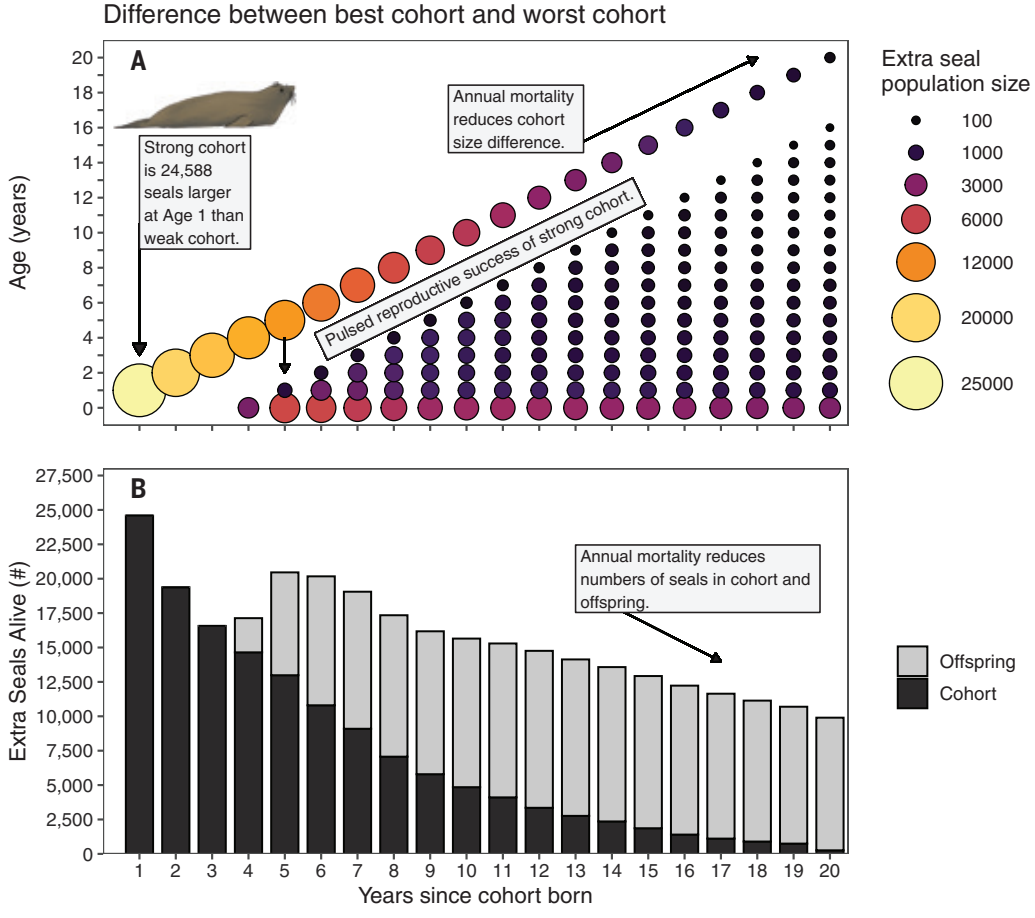


Fig. 3. Demographic success of female elephant seal cohorts varies with oceanographic conditions. (**A**) Weaning mass and recruitment success were most closely correlated with the North Pacific Gyre Oscillation (NPGO; no lag), whereas first-year survival and lifetime reproductive success were most closely tied to the Southern Oscillation Index (SOI; 1-year lag). Each dot is the mean of a cohort of seals tagged as pups (these are the same data shown as a time series in Fig. 2, where sample sizes for each panel are reported), with point sizes indicating sample sizes. Lines (with shading indicating SE) show significant relationships from fitted models (tables S1 to S4). (**B**) Conceptual diagram of relationships between lagged oceanographic metrics (gray boxes) and elephant seal demographic metrics (colored boxes). Labeled weighted arrows show *Z* values (slopes/SEs) from models (tables S1 to S4) of relationships shown in (Fig. 3A).

Fig. 4. Population simulation showing how a single year of high or low survival leads to pronounced differences in population size. Population projections of the difference between the best elephant seal cohort (1987, 61% first-year survival) and the worst cohort (1997, 18% first-year survival) resulted in substantial differences in (**A**) population age structure and (**B**) total population size, with 24,588 more seals surviving to age 1 in the first year after the population pulse and 312,812 extra seals across the 20-year simulation.



oceanographic fluctuations can produce marked demographic pulses in a large marine vertebrate and highlight the sensitivity of top predators to environmental variation.

A new tool for monitoring ecological processes in a changing world

Ecosystem sentinels are a promising way to track environmental change in food webs (*32*–*34*), but we are presently missing a sentinel for the open ocean. Large marine predators such as elephant seals can provide a valuable indicator of prey populations in important but poorly understood ecosystems by extremely-high-frequency sampling of prey over vast areas of the open ocean. The strong correlations that we found between oceanographic indices and northern elephant seal foraging success indicate that these oceanographic indices, despite being based on physical surface measurements with strong coastal signatures, also provide an estimate of fluctuations in the abundance of twilight zone (200 to 1000 m) fish. This is fortuitous because these historical indices provide a way to look into the past state of these ecosystems to provide a baseline, and also look forward as the planet warms and oceans become more acidic. Direct monitoring of open ocean sentinels such as elephant seals—and other deep-diving, far-ranging marine vertebrate species such as northern fur seals (*Callorhinus ursinus*)—will be needed to uncover the ecosystem impacts of warming in the north Pacific Ocean and will be especially critical if twilight zone fisheries develop (*35*) and interfere with correlations between oceanic indices and fish populations. In the Southern Hemisphere, individual southern elephant seals (*Mirounga leonina*) also make thousands of foraging dives over vast distances per year, which suggests that this congener may provide a counterpart sentinel species for the Southern Ocean twilight zone. The correlation between maternal mass gain and oceanographic conditions (*36*) provides an approach for understanding historic and future conditions, even if the mechanisms underlying this link are not fully understood.

Large marine predators also provide a promising platform for miniaturized instruments that will facilitate long-term, large-scale measurements of physical-biological coupling across ocean basins (*37*). Future studies could use in situ environmental data from instrumented predators such as seals, whales, and seabirds to collect coupled physical metrics and prey abundance data in three dimensions. This approach could scale to other species to monitor previously understudied ocean basins and ecosystems, such as energy seascapes that have garnered recent attention (*38*).

Our findings of oceanographic-demographic coupling show the cascading effects of oceanographic conditions several years before a seal's birth on lifelong demographic success. Notably, broad-scale indices of physical surface oceanography were linked to demographic rates of predators that forage several trophic levels above primary producers, hundreds of meters below the ocean surface, and over an entire ocean basin (*25*, *39*). Although environmental conditions and annual vital rates have been linked in terrestrial and coastal marine populations (*40*–*43*), in this work we translate vital rates forward to population growth rates and also backward to underlying prey processes in the open ocean. If future climate scenarios result in persistently weaker North Pacific Gyre circulation (as measured by the North Pacific Gyre Oscillation index), there could be a sizable negative impact on the population dynamics of seals and potentially other large marine vertebrates such as whales. We found that even one cohort of strong vital rates can substantially affect population dynamics.

Although we show that oceanographic conditions influence seal survival, mortality due to starvation, predation, disease, and competition also likely influences cohorts. In terrestrial birds and mammals, predation is a major selective force, accounting for 35% of mammalian mortality and 70% of avian mortality (*44*). Unfortunately, the causes of mortality for marine predators remain a major, unsolved mystery, as do the physiological and behavioral processes that facilitate survival (*45*, *46*). Future research in these areas will contribute to our understanding of population processes in predators that rely on marine resources.

Climate change is already altering ecosystem dynamics and presents a major challenge for conservation and management. Moreover, rapidly increasing demands for a global fish supply have driven interest in extracting fish from the twilight zone (*47*). Sustainable fishing requires estimates of fish populations, and ecosystem-based fishery management requires understanding relationships between exploited fish and their oceanographic and biological links (*48*). We have shown that monitoring foraging success of some wide-ranging predators can provide estimates of marine prey populations that are otherwise difficult or impossible to measure (*22*). In addition, climate change or fishing that leads to a small variation in foraging success can have large consequences for predator survival, population growth, and ecosystem functioning. Top predators could serve as sentinels for multiple trophic levels of marine ecosystems (*23*, *49*), which is critical in an era of human disturbance and global change.

REFERENCES AND NOTES

1. J. H. Myers, *Proc. Biol. Sci.* **285**, 20172841 (2018).
2. L. Petrullo, S. Boutin, J. E. Lane, A. G. McAdam, B. Dantzer, *Science* **379**, 269–272 (2023).
3. R. A. Garrott, L. L. Eberhardt, P. J. White, J. Rotella, *Can. J. Zool.* **81**, 33–45 (2003).
4. B. J. Le Boeuf, D. E. Crocker, *BMC Biol.* **3**, 9 (2005).
5. I. S. Iglesias, J. A. Santora, J. Fiechter, J. C. Field, *Front. Mar. Sci.* **10**, 1220088 (2023).
6. X. Irigoien *et al.*, *Nat. Commun.* **5**, 3271 (2014).
7. J. D. Stewart *et al.*, *Science* **382**, 207–211 (2023).
8. J. Forcada *et al.*, *Glob. Change Biol.* **29**, 6867–6887 (2023).
9. A. C. Lohmann, J. P. Morton, O. M. Schofield, D. P. Nowacek, *Limnol. Oceanogr.* **68**, 2668–2687 (2023).
10. R. S. Beltran *et al.*, *Ecol. Lett.* **26**, 706–716 (2023).
11. R. Swalethorp *et al.*, *Nat. Commun.* **14**, 7412 (2023).
12. A. Borja, *Front. Mar. Sci.* **1**, 1 (2014).
13. G. L. Hadley, J. J. Rotella, R. A. Garrott, *J. Anim. Ecol.* **76**, 448–458 (2007).
14. M.-A. Lea *et al.*, *Mar. Ecol. Prog. Ser.* **310**, 77–94 (2006).
15. R. Williams *et al.*, *ICES J. Mar. Sci.* **70**, 1273–1280 (2013).
16. D. M. Ware, R. E. Thomson, *Science* **308**, 1280–1284 (2005).
17. A. J. Miller, F. Chai, S. Chiba, J. R. Moisan, D. J. Neilson, *J. Oceanogr.* **60**, 163–188 (2004).
18. S. R. Hare, N. J. Mantua, *Prog. Oceanogr.* **47**, 103–145 (2000).
19. M. J. Behrenfeld *et al.*, *Nature* **576**, 257–261 (2019).
20. P. D. Boersma, *Science* **200**, 1481–1483 (1978).
21. J. A. van Gils *et al.*, *Science* **352**, 819–821 (2016).
22. T. J. Clark-Wolf *et al.*, *J. Appl. Ecol.* **61**, 1638–1648 (2024).
23. E. L. Hazen *et al.*, *Annu. Rev. Environ. Resour.* **49**, 573–598 (2024).
24. D. Ellis-Soto, M. Wikelski, W. Jetz, *Nat. Clim. Chang.* **13**, 1042–1054 (2023).
25. C. Goetsch *et al.*, *Front. Mar. Sci.* **5**, 430 (2018).
26. D. D. Costa *et al.*, *Sci. Data* **11**, 1357 (2024).
27. Y. Naito *et al.*, *Funct. Ecol.* **27**, 710–717 (2013).
28. T. Maresh *et al.*, *Mov. Ecol.* **3**, 22 (2015).
29. B. Le Boeuf, R. Condit, J. Reiter, *Can. J. Zool.* **97**, 1203–1217 (2019).
30. M. S. Lowry *et al.*, *Aquat. Mamm.* **40**, 20–31 (2014).
31. S. E. S. Kienle, thesis, University of California Santa Cruz (2019).
32. S. C. Doney *et al.*, *Annu. Rev. Mar. Sci.* **4**, 11–37 (2012).
33. G. T. Pecl, A. J. Hobday, S. Frusher, W. H. H. Sauer, A. E. Bates, *Rev. Fish Biol. Fish.* **24**, 409–413 (2014).
34. É. Plagányi, *Science* **363**, 930–931 (2019).
35. K. Fjeld, R. Tiller, E. Grimaldo, L. Grimsmo, I.-B. Standal, *Mar. Policy* **147**, 105359 (2023).
36. C. R. McMahon, R. G. Harcourt, H. R. Burton, O. Daniel, M. A. Hindell, *J. Anim. Ecol.* **86**, 359–370 (2017).
37. R. Harcourt *et al.*, *Front. Mar. Sci.* **6**, 326 (2019).
38. M. C. Arostegui *et al.*, *Sci. Adv.* **9**, eadi8200 (2023).
39. P. W. Robinson *et al.*, *PLOS ONE* **7**, e36728 (2012).
40. M. L. Feddern, G. W. Holtgrieve, E. J. Ward, *Ecology* **104**, e3865 (2023).
41. J. F. Le Galliard, O. Marquis, M. Massot, *J. Anim. Ecol.* **79**, 1296–1307 (2010).
42. P. M. Thompson, J. C. Ollason, *Nature* **413**, 417–420 (2001).
43. U. Shimabukuro *et al.*, *Mar. Ecol. Prog. Ser.* **708**, 177–189 (2023).
44. J. E. Hill, T. L. DeVault, J. L. Belant, *Glob. Ecol. Biogeogr.* **28**, 680–689 (2019).
45. C. D. Braun *et al.*, *Annu. Rev. Mar. Sci.* **14**, 129–159 (2022).
46. J. Harwood, A. Hall, *Trends Ecol. Evol.* **5**, 254–257 (1990).
47. M. Hidalgo, H. I. Browman, *ICES J. Mar. Sci.* **76**, 609–615 (2019).
48. L. C. Scopel, A. W. Diamond, S. W. Kress, A. R. Hards, P. Shannon, *Can. J. Fish. Aquat. Sci.* **75**, 1215–1229 (2018).
49. E. L. Hazen *et al.*, *Front. Ecol. Environ.* **17**, 565–574 (2019).
50. R. Beltran, D. Costa, B. Le Boeuf, R. Condit, An ecosystem sentinel for the northeast Pacific Ocean twilight zone. Dryad (2024); https://doi.org/10.5061/dryad.hdr7sqvpp.

ACKNOWLEDGMENTS

This research was completed at the University of California Natural Reserve System's Año Nuevo Reserve; conceptualization occurred during an inquiry-based undergraduate field course at the University of California Santa Cruz, BIOE128L (2022 cohort). We thank R. Condit, dozens of field leaders, and hundreds of field assistants who have contributed to the elephant seal research program over many years, along with the Abrahms and Prugh Labs, B. Abrahms, L. Prugh, M. Savoca, and A. Nisi for invaluable brainstorming. Elephant seal handling and sampling was approved by the University of California Santa Cruz Institutional Animal Care and Use Committee. Fieldwork was carried out under National Marine Fisheries Service permits 786-1463, 87-143, 14636, 14535, 19108, and 23188. **Funding:** This work was funded by the Office

of Naval Research (R.S.B., D.P.C., B.J.L.B., and P.W.R.), the Tagging of Pacific Predators Program (D.P.C.), the National Science Foundation (B.J.L.B., R.S.B., D.P.C., A.M.K.), a Packard Fellowship in Science and Engineering (R.S.B.), a Beckman Young Investigator Award (R.S.B.), Strategic Environmental Research and Development Program grant RC20-C2-1284 (D.P.C.), the National Oceanic and Atmospheric Administration's Integrated Ecosystem Assessment program (D.P.C.), the Bureau of Land Management (B.J.L.B.), the National Geographic Society (B.J.L.B.), and gifts from G. Malloch (B.J.L.B.). **Author contributions:** Conceptualization: R.S.B., A.M.K., A.R.P., M.R.; Investigation: All authors; Visualization: R.S.B., A.R.P., A.M.K., J.J.; Funding acquisition: R.S.B., B.J.L.B., D.P.C., P.W.R., A.M.K.; Supervision: R.S.B., A.R.P., P.W.R., A.M.K., D.P.C., B.J.L.B.; Writing – original draft: R.S.B., A.M.K., A.R.P., C.M.H., M.R.; Writing – review & editing: All authors. **Competing interests:** The authors declare that they have no competing interests. **Data and materials availability:** Code and data are available on Dryad (*50*). **License information:** Copyright © 2025 the authors, some rights reserved; exclusive licensee American Association for the Advancement of Science. No claim to original US government works. https://www.science.org/about/science-licenses-journal-article-reuse

SUPPLEMENTARY MATERIALS

science.org/doi/10.1126/science.adp2244
Materials and Methods
Figs. S1 to S6
Tables S1 to S4
References (*51*–*56*)
MDAR Reproducibility Checklist

Submitted 14 March 2024; resubmitted 19 June 2024
Accepted 8 November 2024
10.1126/science.adp2244

CATALYSIS

Thermal catalytic reforming for hydrogen production with zero CO_2 emission

Mi Peng[1]†, Yuzhen Ge[1]†, Rui Gao[2]†, Jie Yang[3]†, Aowen Li[4]†, Zhiheng Xie[1], Qiaolin Yu[1], Jie Zhang[1], Hiroyuki Asakura[5], Hui Zhang[6], Zhi Liu[7], Qi Zhang[8], Jin Deng[3], Jihan Zhou[1]*, Wu Zhou[4]*, Graham J. Hutchings[9]*, Ding Ma[1]*

Carbon-neutral hydrogen production is of key importance for the chemical industry of the future. We demonstrate a new thermal catalytic route for the partial reforming of ethanol into hydrogen and acetic acid with near-zero carbon dioxide emissions. This reaction is enabled by a catalyst containing a high density of atomic Pt_1 and Ir_1 species supported on a reactive alpha-molybdenum carbide substrate, achieving a hydrogen production rate of 331.3 millimoles of hydrogen per gram catalyst per hour and an acetic acid selectivity of 84.5% at 270°C, and is therefore more energy-efficient compared with standard reforming. Techno-economic analysis of partial ethanol reforming demonstrates the potential profitability for operation at an industrial scale, presenting the opportunity to produce hydrogen and acetic acid with a substantially reduced carbon dioxide footprint.

The reforming of fossil fuels is currently the predominant route for industrial hydrogen (H_2) production (*1*, *2*), but it is associated with considerable CO_2 emissions (*3*). Greener alternatives such as water electrolysis (*4*) and biomass gasification (*5*) could reduce the carbon footprint of H_2 production, but these face bottlenecks in efficiency, cost-effectiveness, and scalability. Partial oxidation ($C_2H_5OH + 1.5O_2 = 2CO_2 + 3H_2$) and full steam reforming ($C_2H_5OH + 3H_2O = 2CO_2 + 6H_2$) (*6*, *7*) of ethanol have also been actively explored for possible carbon-neutral H_2 production, especially using bio-derived renewable ethanol. Although these processes show some advantages over conventional H_2 production routes (Fig. 1A) (*8*), partial oxidation is intrinsically limited by the stoichiometrically low H_2 production rate (*9*), whereas the highly endothermic nature of full steam reforming (Fig. 1B) (*10*, *11*) requires high operating temperatures that promote undesired side reactions (*12*). Notably, both pathways convert 100% of the carbon atoms into CO_2, depleting the carbon resources.

[1]Beijing National Laboratory for Molecular Science, New Cornerstone Science Laboratory, College of Chemistry and Molecular Engineering, Peking University, Beijing, China. [2]School of Chemistry and Chemical Engineering, Inner Mongolia University, Hohhot, China. [3]CAS Key Laboratory of Urban Pollutant Conversion, Anhui Province Key Laboratory of Biomass Clean Energy, Department of Applied Chemistry, University of Science and Technology of China, Hefei, China. [4]School of Physical Sciences, University of Chinese Academy of Sciences, Beijing, China. [5]Department of Applied Chemistry, Faculty of Science and Engineering, Kindai University, Osaka, Japan. [6]Shanghai Synchrotron Radiation Facility, Shanghai Advanced Research Institute, Chinese Academy of Sciences, Shanghai, China. [7]Center for Transformative Science, Shanghai Tech University, Shanghai, China. [8]SINOPEC Shanghai Research Institute of Petrochemical Technology Co., Ltd., Shanghai, China. [9]Max Planck-Cardiff Centre on the Fundamentals of Heterogeneous Catalysis, FUNCAT, Cardiff Catalysis Institute, School of Chemistry, Cardiff University, Cardiff, UK.
***Corresponding author. Email: dma@pku.edu.cn (D.M.); wuzhou@ucas.ac.cn (W.Z.); jhzhou@pku.edu.cn (J.Z.); hutch@cardiff.ac.uk (G.J.H)**
†These authors contributed equally to this work.

Reaction pathway and catalyst design

A comprehensive exploration of the ethanol reforming process revealed a complex reaction network (Fig. 1C). An ideal H_2 production pathway from ethanol reforming should both be thermodynamically favorable and minimize net carbon emission (*13*). We propose selective partial reforming of ethanol with water to form acetic acid and H_2 ($C_2H_5OH + H_2O = CH_3COOH + 2H_2$) as the more valuable route (rust red in Fig. 1C). It offers multiple benefits: (i) the reforming process extracts H_2 from both ethanol and water, producing more H_2 than the dehydrogenation process from a stoichiometric perspective; (ii) carbon atoms remain in the liquid phase, generating a valuable chemical product and minimizing CO_2 emissions; (iii) the co-produced acetic acid fulfills rising global demand and serves as a critical intermediate for the production of additional chemicals, including cellulose acetate, vinyl acetate monomer, and polyvinyl acetate (*14*). By contrast, conventional catalysts for ethanol reforming, including noble metal catalysts (such as Pt and Pd) and non-noble metal catalysts (such as, Ni, Cu, and Co) (*15*–*21*), tend to convert the carbon atoms in ethanol into CO_x, leading to a net carbon-positive process with CO_x emission (without taking into account the origin of ethanol).

Designing a new catalyst that enables the reforming reaction while preventing C-C bond breakage (*22*) is crucial for selectively facilitating this partial reforming route into acetic acid. We developed a highly dispersed Pt/Ir metal catalyst supported on alpha-molybdenum carbide (α-MoC) that efficiently promoted the partial steam reforming of ethanol into H_2 and acetic acid under temperatures considerably lower than that required in conventional ethanol steam reforming. We selected α-MoC as a reactive support to construct the interfacial catalysts in view of its unprecedented capability of activating water at low temperatures (*23*, *24*) and its strong interactions with noble metals, which created a high density of interfacial active sites for methanol reforming (*25*, *26*).

Compared with methanol reforming, ethanol reforming is thermodynamically less favored (*27*, *28*) and requires a higher density of reforming sites to facilitate the reaction. More importantly, to achieve a high selectivity toward acetic acid, the cleavage of the C-C bond in the ethanol backbone, which leads to the formation of undesired C_1 products such as CO, CO_2, or CH_4, (see Fig. 1C) must be suppressed. Because C-C bond cleavage typically requires a di-σ carbon-metal configuration, large metal catalytic ensembles that contain abundant metal-metal bonds must be eliminated (*29*). Previous studies on Ir/α-MoC and Pt/α-MoC catalysts revealed that Ir has a stronger interaction with α-MoC (*26*, *30*, *31*), which leads to much higher dispersion than Pt under the same metal loading, although the intrinsic dehydrogenation activity of Ir is lower than

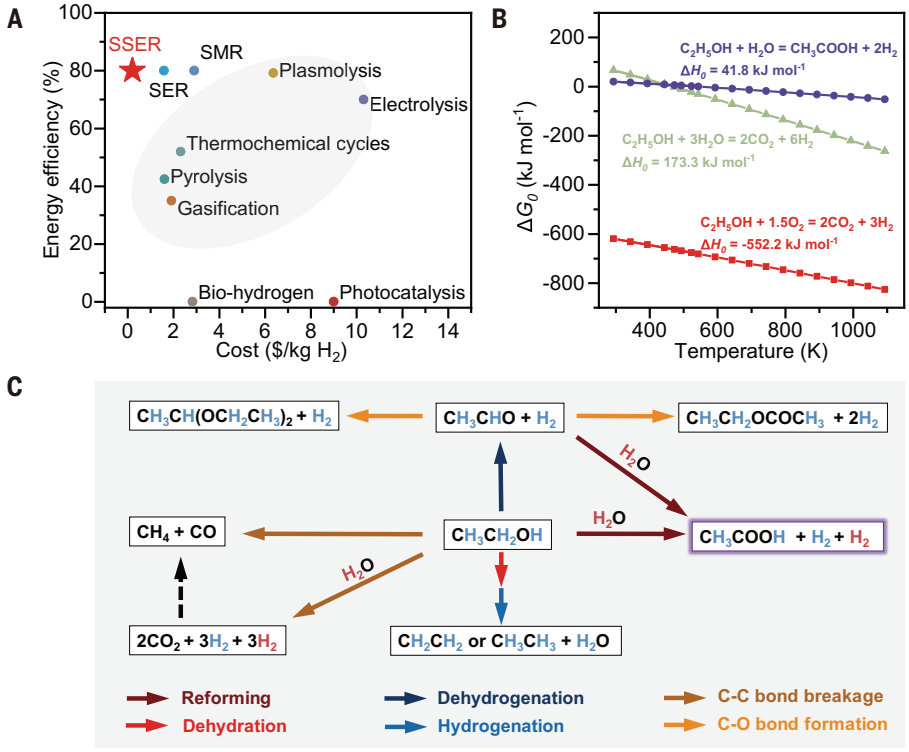


Fig. 1. Survey of H_2 production routes. (**A**) Comparison of energy efficiency and costs of various H_2 production routes. Detailed references listed in table S1. SMR, steam methanol reforming; SER, steam ethanol reforming; SSER, selective steam ethanol reforming. (**B**) Thermodynamic evaluation of different ethanol conversion routes. (**C**) Schematics of the reaction network for ethanol reforming: (i) ethanol is converted into acetaldehyde through dehydrogenation and forms the corresponding (hemi)acetal through condensation, with the latter not contributing to net H_2 production; (ii) ethanol goes through dehydration/hydrogenation to form ethylene and ethane, neither generating H_2; (iii) ethanol can produce CO_2 and CO/CH_4 through C-C bond breakage, a side reaction consuming H_2; (iv) ethanol goes through full reforming with water and produces H_2 and CO_2. Although this process produces the most H_2, it requires higher temperatures and does not preserve the carbon resource at all. (v) Ethanol selectively reforms with water to produce H_2 from both reactants while preserving high-value C_2 products such as acetic acid.

that of Pt (*26*, *32*). We expected co-loading of Ir and Pt onto α-MoC improve Pt dispersion, thereby constructing a catalyst (M/α-MoC, M = Pt/Ir) with a high density of atomic interfacial sites (i.e., active interfaces formed by atomic-scale Pt or Ir species, including Pt or Ir single atoms as well as fully exposed clusters (*33*), over the reactive α-MoC support) that are beneficial for the efficient and selective reforming of ethanol into acetic acid.

Catalyst synthesis and characterization

We synthesized a series of Pt/Ir-based catalysts supported on α-MoC using the incipient wetness impregnation method (see methods for details; the number before Pt or Ir denotes the weight percentage of the metal loading). X-ray diffraction (XRD) revealed the formation of Pt particles (2θ = 39.8°) in 3Pt/α-MoC, and the diffraction for crystalline Pt became more pronounced in 6Pt/α-MoC (Fig. 2A and fig. S1). By contrast, Ir particles were not detected even at a metal loading of 6 weight percent (wt%) (Fig. 2A and fig. S2). Importantly, with the addition of Ir, 3Pt3Ir/α-MoC did not show obvious XRD peaks for either Pt or Ir crystals at a total metal loading of 6 wt%, confirming that Ir indeed enhanced the dispersion of Pt species. Loading the Pt and Ir species with equal concentration onto an inert SiO_2 support ($3Pt3Ir/SiO_2$) produced metal particles that were resolved by XRD (Fig. 2A). This $3Pt3Ir/SiO_2$ catalyst served as a reference catalyst containing abundant large metal ensemble sites.

The metal dispersions were further analyzed using extended x-ray absorption fine-structure (EXAFS). For the 1Pt/α-MoC catalyst, the Pt-Pt coordination number (CN) was 1.0, indicating the formation of small Pt clusters even at a low Pt loading. The average $CN_{Pt\text{-}Pt}$ increased with higher Pt loading, reaching 4.9 for 6Pt/α-MoC (Fig. 2B, figs. S3 to S8, and tables S2 and S3), suggesting the formation of a substantial number of Pt ensemble sites. By contrast, no Ir-Ir coordination was detected in the 1Ir/α-MoC and 3Ir/α-MoC catalysts, and the average $CN_{Ir\text{-}Ir}$ for 6Ir/α-MoC was only 1.9, indicating a much higher dispersion of Ir on α-MoC compared with Pt (Fig. 2B). At a total metal loading of 6 wt%, the 3Pt3Ir/α-MoC catalyst showed no Ir-Ir scattering and a $CN_{Pt\text{-}Pt}$ of 2.3, suggesting atomic dispersion of Ir species and enhanced dispersion of Pt compared with 3Pt/α-MoC.

We used atomic number (Z) contrast imaging and electron energy-loss spectroscopy (EELS) mapping on aberration-corrected scanning transmission electron microscopy (STEM) to visualize the atomic-scale structures of the 3Pt/α-MoC and 3Pt3Ir/α-MoC catalysts. For 3Pt/α-MoC, STEM Z-contrast image combined with EELS mapping revealed the coexistence of atomically dispersed Pt species and Pt clusters with a diameter of ~1 nm (Fig. 2, C and D, and fig. S9 and S10). For 3Pt3Ir/α-MoC, the Z-contrast imaging could not differentiate Pt and Ir (fig. S10), but the EELS mapping in Fig. 2F, in combination with the Z-contrast image in Fig. 2E, revealed the coexistence of atomically dispersed Pt and Ir species, as well as small Pt clusters on the α-MoC support. The Pt and Ir EELS signals extracted from Fig. 2F were highly confined to single pixels, demonstrating that the elemental-sensitive EELS mapping has single-atom sensitivity (*34*). In addition, comparison of Fig. 2D and Fig. 2F revealed a much-improved dispersion of Pt species in 3Pt3Ir/α-MoC than that in 3Pt/α-MoC, consistent with the conclusion drawn from XAS.

Atomic electron tomography (AET) (*35*, *36*) was used to investigate the three-dimensional (3D) distribution and coordination of Pt (and Ir) atoms in metal clusters in the 3Pt/α-MoC and 3Pt3Ir/α-MoC catalysts (see methods and figs. S11 to S13). Although sampling is limited with AET, it still provides valuable insights into the 3D distribution of the Pt(Ir) species on the α-MoC support, and the local metal-metal CNs calculated from the reconstructed atomic coordinates can be informative. In 3Pt/α-MoC, for a 1495-atom motif containing 48 Pt atoms, most Pt atoms had $CN_{Pt\text{-}Pt}$ ranging from 3 to 9 (Fig. 2G and movie S1). By contrast, in the 3Pt3Ir/α-MoC catalyst, most of the Pt/Ir atoms were present as single atoms distributed at point defect sites on α-MoC, with only a small portion of Pt/Ir atoms showing a CN between 1 and 5 (Fig. 2H and movie S2). These comprehensive structural analysis results consistently demonstrate that Ir species promoted the dispersion of Pt species on α-MoC to create a high density of interfacial active sites.

Catalytic evaluation

In situ spectroscopy experiments were performed to examine the potential of the 3Pt3Ir/α-MoC catalyst for activating water and ethanol by tracking the adsorption and evolution of surface species. The O 1s x-ray photoelectron spectroscopy (XPS) under ultrahigh vacuum showed two peaks at 530.3 and 531.6 eV that

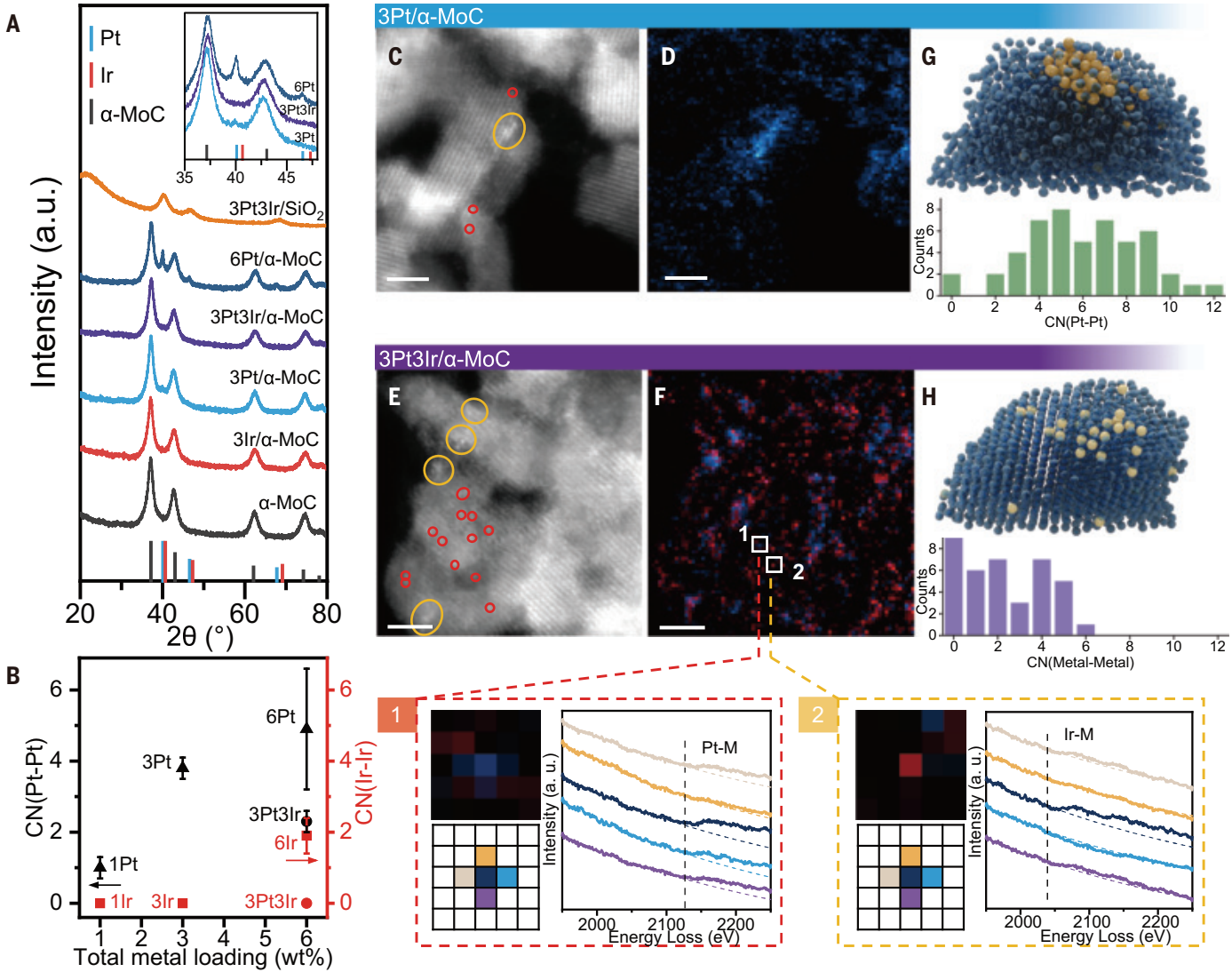


Fig. 2. Structural characterization of the PtIr/α-MoC catalysts. (**A**) XRD profiles of α-MoC supported Pt/Ir catalysts with different metal loadings. Inset notes the enlarged region of the Pt(111) diffraction peak. (**B**) Coordination numbers (CN) of Pt-Pt and Ir-Ir in different catalysts obtained from EXAFS fitting. Triangles indicate Pt/α-MoC; squares, Ir/α-MoC; circles, PtIr/α-MoC. (**C**) and (**D**) High-angle annular dark-field (HAADF) image (C) and the corresponding EELS mapping (D) of 3Pt/α-MoC. (**E**) and (**F**) HAADF image (E), and the corresponding EELS mapping (F) of 3Pt3Ir/α-MoC. Metal clusters and atomically dispersed species are marked with yellow and red circles, respectively. Pt is presented in blue and Ir in red in the EELS mapping. The bottom panels present the enlarged Pt/Ir elemental maps and the corresponding pixel indexes of the areas marked by the white squares 1 and 2 in (F) and the EELS spectra extracted from the pixels with the corresponding colors. (**G**) and (**H**) The metal atom distribution in 3Pt/α-MoC (G) and 3Pt3Ir/α-MoC (H) is obtained through 3D reconstruction from tomographic tilt series. The blue spheres show Mo atoms and the golden spheres represent Pt/Ir atoms. The bar charts show the M-M (M = Pt or Ir) coordination number distribution calculated from the reconstructed 3D structural model. Scale bars in (C) to (F) are 2 nm.

we attributed to residual oxygen and hydroxyl groups, respectively, on the surface of α-MoC (Fig. 3A and fig. S14) (*31*). After dosing water onto the catalyst at room temperature (RT) in near-ambient-pressure XPS (NAP-XPS) experiments, an adsorbed water peak at 533.2 eV (*37*) emerged, accompanied by an increase in the hydroxyl group peak (531.6 eV). This observation suggests that water dissociates into hydroxyl species over 3Pt3Ir/α-MoC at RT, consistent with previous reports on other α-MoC based catalysts (*38*).

In addition, dosing ethanol onto the 3Pt3Ir/α-MoC catalyst at RT caused increases in the two peaks at 531.8 eV and 533.2 eV, attributed to adsorbed oxygenates and ethanol (*39*), respectively (Fig. 3B and fig. S14), indicating the dissociative adsorption of ethanol. As the temperature increased, the peak assigned to adsorbed oxygenates increased, indicating enhanced activation of ethanol, despite the Pt and Ir species remaining unchanged during this process (figs. S15 and S16). Meanwhile for 3Pt3Ir/SiO_2, feeding water and ethanol does not lead to dissociation at RT (fig. S17). The dissociation of ethanol over the 3Pt3Ir/α-MoC catalysts was further confirmed by transient kinetic analysis (figs. S18 and 19). When C_2H_5OD was fed to the pretreated 3Pt3Ir/α-MoC surface at RT, both H_2 and hydrogen deuteride were detected in the outlet gas, suggesting that the catalyst could dissociate both C-H and O-H bonds of ethanol at RT.

To assess the feasibility of ethanol-water partial reforming over these catalysts, we used in situ Fourier-transforming infrared (FTIR) spectroscopy (Fig. 3C) to monitor the adsorption

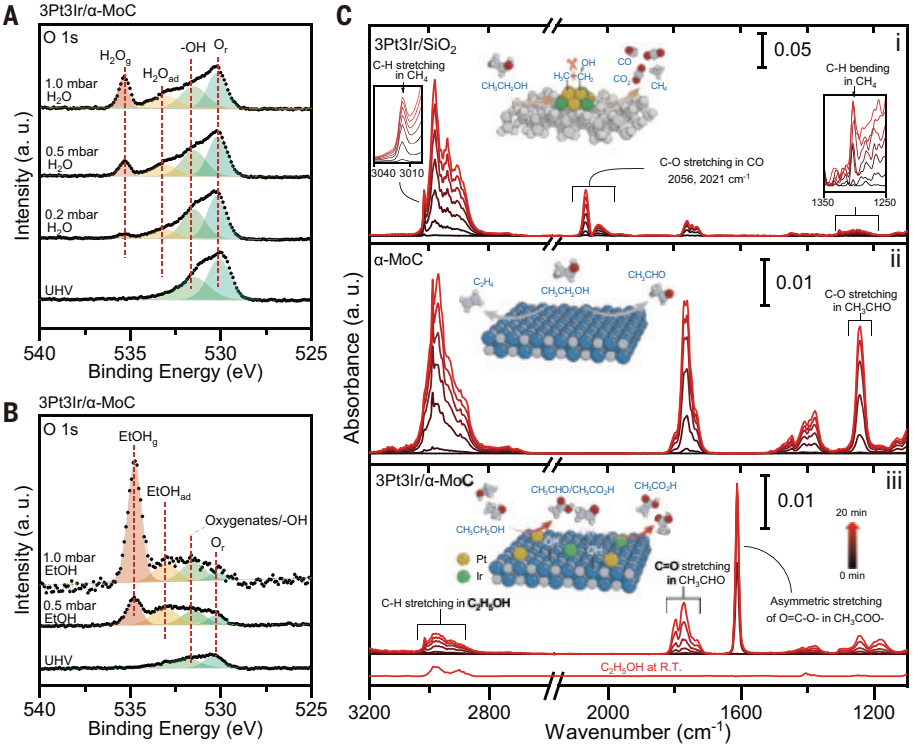


Fig. 3. Reaction network and site requirement studies for partial reforming of ethanol. (**A**) and (**B**) NAP-XPS results of the 3Pt3Ir/α-MoC catalyst under different pressure of H_2O (A) and ethanol (B). The samples were treated in the corresponding environments noted in the figure for 30 min before measuring. O_r represents residual oxygen; H_2O_g and H_2O_{ad} denote water in the gas phase and water adsorbed on the catalyst surface, respectively; $EtOH_g$ and $EtOH_{ad}$ refer to ethanol in the gas phase and ethanol adsorbed on the catalyst surface, respectively. (**C**) In situ FTIR spectra of water and ethanol adsorption over (i) 3Pt3Ir/SiO_2, (ii) α-MoC, and (iii) 3Pt3Ir/α-MoC catalysts at 270°C. The fresh catalysts after pretreatment were followed by Ar flushing for 30 min at 270°C, and then exposed to ethanol and water atmosphere. Inset includes schematic illustration of possible dominant reaction pathways on each catalyst.

(evident by the presence of C-H stretching in ethanol at 2981 cm^{-1}), the effective dehydrogenation of ethanol (evident by the increase of C=O stretching at 1758 cm^{-1}, C-O bending mode at 1377 cm^{-1}, and C-O stretching mode at 1242 cm^{-1} in acetaldehyde) (*40*) and the overall reactivity (formation of acetic acid) among α-MoC, 3Pt3Ir/α-MoC, and 3Pt3Ir/SiO_2 catalysts. For the 3Pt3Ir/SiO_2 catalyst containing large metal ensembles, the peaks associated with carbon monoxide (C-O stretching at 2063 cm^{-1}) and methane (C-H stretching at 3016 cm^{-1}, degenerate bending mode at 1303 cm^{-1}) were clearly resolved (Fig. 3C, i) once the vapor of ethanol/water mixture was introduced over the catalyst. This result indicated that large ensembles of noble metals were highly active for C-C bond cleavage (*41*), making them unfavorable for partial ethanol reforming.

By contrast, ethanol dehydrogenation was particularly effective on α-MoC (Fig. 3C, ii), as evidenced by the appearance of bands associated with acetaldehyde at 1242 cm^{-1} and 1758 cm^{-1} after the introduction of the ethanol/water vapor mixture onto the catalyst at 270°C. Although C-C bond breakage was not observed, we were unable to resolve the peak associated with CH_3COO- over α-MoC, possibly because of its inability to further transform acetaldehyde into the corresponding acid. Notably, only on the 3Pt3Ir/α-MoC catalyst containing abundant atomic-scale interfaces between Pt_1 or Ir_1 and α-MoC, could the asymmetric stretching mode of O=C-O- in CH_3COO- at 1612 cm^{-1} (*42*) be resolved, even from the early stages of reforming (Fig. 3C, iii). Thus, these interfaces were critical for the formation of acetic acid. These results demonstrated that the surface of 3Pt3Ir/α-MoC could readily activate both water and ethanol in the initial stage of the reaction, following the pathway shown in Fig. 3C, indicating potentially excellent catalytic performance in steady-state reactions.

The pristine α-MoC sites favored the dehydrogenation of ethanol into acetaldehyde and the dissociation of H_2O into hydroxyls (*31*, *43*), whereas the interfaces between atomic-scale Pt or Ir species and α-MoC were pivotal for the partial reforming of ethanol with water. Importantly, eliminating the formation of Pt(Ir)-Pt(Ir) ensembles was crucial for preventing C-C bond cleavage and for the low selectivity toward CO_x and methane in the reaction.

We evaluated the selective reforming performance using a continuous-flow fixed-bed reactor (the mass balance, calculated based on the number of carbon atoms, ranged from 101 to 109% for all catalysts, see methods for details). Ethanol reforming typically follows a dehydrogenation-reforming sequential pathway (*44*), so the performance of acetaldehyde reforming with water was evaluated first on α-MoC-based catalysts (Fig. 4A). Pure α-MoC shows negligible activity toward acetaldehyde reforming, which is in good agreement with the in-situ FTIR results. By contrast, with the loading of Pt or Ir, the activity increased substantially, suggesting that noble metals or metal/carbide interfaces played a vital role in the reforming process. Although 3Pt/α-MoC showed a higher H_2 production rate than 3Ir/α-MoC, its selectivity toward undesired C_1 products was much higher (~38 versus ~8%), primarily because of its tendency to aggregate under high metal loadings that promoted C-C bond cleavage. The co-loading of Pt and Ir boosted activity toward H_2 production and high selectivity, exceeding 80%, toward acetic acid. These results supported our proposal that a high density of Pt_1 and Ir_1 single atoms on molybdenum carbide would facilitate H_2 production through reforming while suppressing C-C cleavage.

We then evaluated ethanol reforming with water on these catalysts. Pure α-MoC showed a H_2 production rate of 51.3 $mmol_{H2}/(g_{cat}{\cdot}h)$ at 543 K, with acetaldehyde as the main product (selectivity ~53.0%) (Fig. 4B and table S4) and ethylene/ethane accounting for ~20% selectivity. Loading either Pt or Ir onto α-MoC substantially increased the H_2 generation rate (figs. S20 and S21). A comparison of the reforming activity of Pt/α-MoC and Ir/α-MoC at a low metal loading of 1% (fig. S22) revealed higher intrinsic ethanol reforming activity for Pt/α-MoC and the essential role of atomic-scale noble-metal/carbide interface in reforming, similar to what we observed for acetaldehyde reforming. For comparison, supporting atomically dispersed Pt species on an inert carbon support yielded neglectable reforming activity, highlighting the essential role of the Pt(or Ir)/α-MoC interface. At a higher metal loading of 3%, both 3Pt/α-MoC and 3Ir/α-MoC demonstrated superior H_2 generation activity 147.3 $mmol_{H2}/(g_{cat}{\cdot}h)$ and 176.0 $mmol_{H2}/(g_{cat}{\cdot}h)$, respectively) and a high acetic acid selectivity exceeding 50%. Further increasing the individual metal loading to 6% did not improve the activity or selectivity toward acetic acid (figs. S20 and S21).

Notably, with co-loading of Pt and Ir, 3Pt3Ir/α-MoC exhibited the highest efficiency, achieving a H_2 generation rate of 331.3 $mmol_{H2}/(g_{cat}{\cdot}h)$ after optimizing reaction condition (figs S23

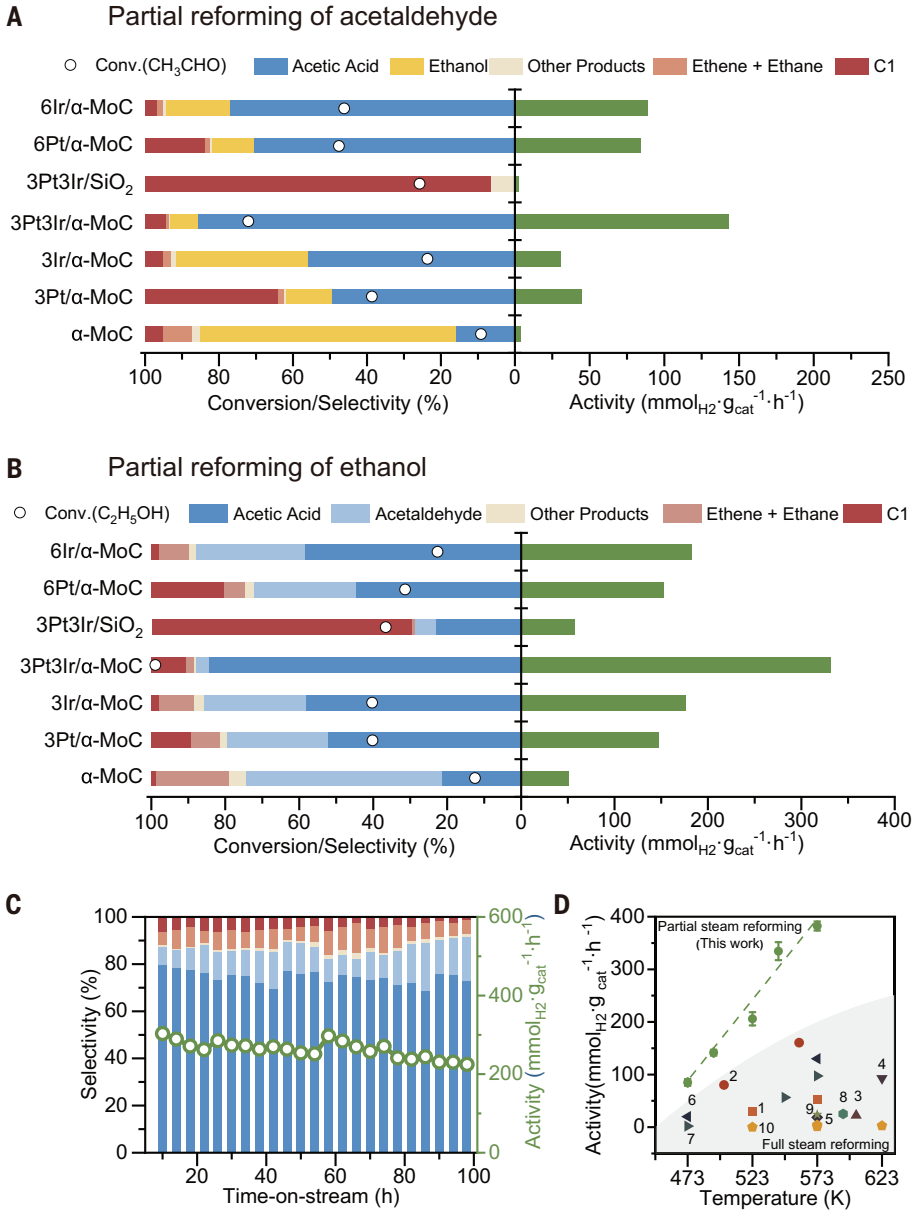


Fig. 4. Catalytic performance for partial reforming of ethanol. (**A**) Catalytic performance of supported Pt/Ir catalysts for partial reforming of acetaldehyde. Reaction conditions: 543 K, weight-hourly space velocity (WHSV) of acetaldehyde = 10.6 $g_{acetaldehyde}/(g_{cat} \cdot h)$, flow rate of the carrier gas (5% Ar in N_2) = 60 mL/min, n (acetaldehyde): n (H_2O) = 1: 9. (**B**) Catalytic performance of supported Pt/Ir catalysts for partial reforming of ethanol. Reaction conditions: 543 K, $WHSV_{ethanol}$ = 10.6 $g_{ethanol}/(g_{cat} \cdot h)$, flow rate of the carrier gas (5% Ar in N_2) = 60 mL/min, n (ethanol): n (H_2O) = 1: 9. (**C**) Long-term stability test of 3Pt3Ir/α-MoC for partial reforming of ethanol with water. The reaction condition is the same as in (B). (**D**) Comparison of H_2 production activity through ethanol steam reforming in literature and in this work. The same symbol indicates data from the same reference (detailed references are listed in table S7).

and 24), and surpassed previously reported results in thermocatalysis, photocatalysis, and electrocatalysis (Fig. 4D and tables S5 and S6). A high water-to-ethanol ratio was used (9:1) under the optimal condition, which is critical for both thermodynamic and kinetic reasons, as detailed in the theoretical investigation section below. Additionally, 3Pt3Ir/α-MoC demonstrated a high selectivity of 84.5% toward acetic acid, with less than 10% toward C_1 products (CO, CO_2, and CH_4), showing better performance than fully reforming processes under similar reaction temperatures (Fig. 4D and table S7). The presence of a high density of interfacial M_1/α-MoC (M_1 = Pt_1 or Ir_1) sites effectively blocked the undesired reaction routes, such as the formation of acetaldehyde and other byproducts.

A durability test on the 3Pt3Ir/α-MoC catalyst demonstrated promising stability in both activity and selectivity over a 100-hour run (Fig. 4C). The activity for H_2 production decreased by 21% from its initial level within the first 100 hours of reaction, but the rate of decline gradually slowed as testing proceeded. Over this period, the catalyst achieved a cumulative H_2 production of 27.3 mol per gram of catalyst, accompanied by the generation of 19.2 mol of acetic acid. Furthermore, XRD characterization revealed no obvious structural change of the catalyst after usage (fig. S25), suggesting a potentially much longer life span.

Theoretical investigation

To better understand the enhanced catalytic performance of the 3Pt3Ir/α-MoC catalyst, we performed density functional theory (DFT) calculations to explore the ethanol reforming paths and reaction mechanisms (Fig. 5 and figs. S26 to S37). With inputs from structural characterizations, we constructed five structural models to represent different catalytic sites: Mo-terminated α-MoC(111) as pristine α-MoC; Pt(111) and Pt(210) representing the flat surface sites and step sites of Pt clusters/particles, respectively; Pt_1/MoC(111) and Ir_1/MoC(111) for atomically dispersed Pt and Ir on α-MoC, respectively.

We first explored the reaction pathways of ethanol decomposition on the α-MoC(111) surface. Figure 5A and fig. S26 show that on α-MoC(111) the terminal C-H bond of ethanol first dissociated into surface $*CH_2CH_2OH$ and then went through two favored routes. One involved the dissociation of C-O bond to form ethylene with an effective energy barrier of 0.80 eV, and the other generated the most thermodynamically stable intermediate CH_2CO with an effective energy barrier of 0.78 eV. However, subsequent transformation of this intermediate into acetaldehyde and acetic acid required a much higher energy barrier (>1.3 eV), suggesting that ethanol reforming would be hindered on α-MoC by the accumulation of C_2 species. However, this result did not fully align with the high acetaldehyde selectivity we observed in our experiment (Fig. 4B), signaling the strong influence from surface hydroxyls.

Note that under our experimental conditions, a high surface hydroxyl coverage was expected during the reaction because of the high feedstock ratio of water to ethanol (9:1) and the high activity of α-MoC for water dissociation (*31*). To unveil the interaction between carbon intermediates and hydroxyls, we performed calculations of CH_2CH_2OH dissociation on the α-MoC(111) surface with low and high hydroxyl coverages of 1/3 ML and 5/9 ML, respectively (fig. S27). The rate-determining steps of ethanol decomposition under 5/9 ML hydroxyl coverage are presented in Fig. 5D. A comparison of Fig. 5A and Fig. 5D revealed

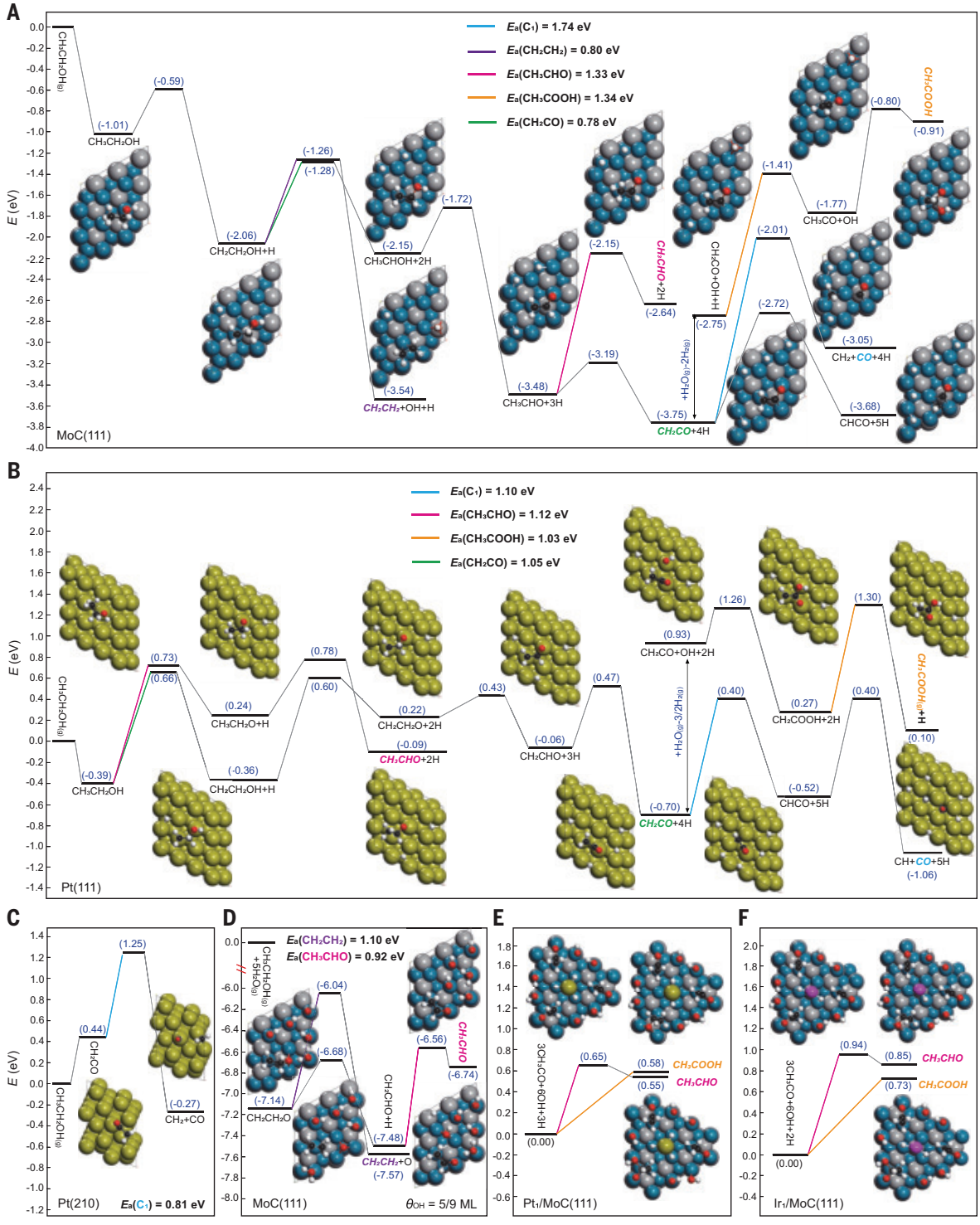


Fig. 5. Reaction pathways of ethanol reforming on PtIr/α-MoC catalysts. (**A**) Energy profiles for ethanol conversion pathways on the pure α-MoC (111) surface. (**B**) Energy profiles for ethanol conversion pathways on the flat Pt(111) surface. (**C**) Energy profile for the conversion pathway of the most stable intermediate CH_2CO on the Pt(210) step surface. (**D**) Energy profiles for the corresponding formation pathways of C_2H_4 and CH_3CHO on the α-MoC(111) surface with a hydroxyl coverage of 5/9 ML. (**E**) and (**F**) The energy profiles for the rate-determining steps of CH_3CHO and CH_3COOH formation from the most stable intermediate CH_2CO and hydroxyl on the Pt_1/MoC(111) (E) and Ir_1/MoC (111) (F) interfaces (CH_2CO/OH = 1:2, their total coverage = 9/16 ML). The Pt, Ir, Mo, C, O, and H atoms are shown in gold, pink, dark cyan, gray, red, and white, respectively; C atoms from ethanol are marked in black.

that the overall energy barrier toward the formation of acetaldehyde was lowered to 0.92 eV at higher hydroxyl coverage, whereas the barrier toward ethylene formation increased to 1.10 eV. This result suggested that ethylene formation could be to some extent inhibited by the increased hydroxyl coverage from water dissociation on α-MoC, consistent with the experimental selectivity.

For comparison, the pathways of ethanol decomposition on Pt particles were also investigated (Fig. 5B and fig. S28). The results showed that the reforming process on the Pt(111) flat surface did not exhibit a specific preference for any single product, as the calculated energy barriers toward acetaldehyde, acetic acid, CH_2CO intermediate, and C_1 products were similar. However, on the Pt(210) step surface, the energy barrier for C-C bond breakage of the most stable CH_2CO intermediate was reduced to 0.81 eV (Fig. 5C and fig. S29), suggesting that Pt particles, containing rich step surfaces, favored the formation of C_1 products. This result aligned well with the experimental findings on catalysts containing large metal ensembles, such as the 3Pt3Ir/SiO_2, 3Pt/α-MoC, and 6Pt/α-MoC (Fig. 4B, fig. S20, and table S4).

To investigate the catalytic effects of atomic M_1/α-MoC (M_1 = Pt_1 or Ir_1) interfacial sites, we calculated the pathways for the reaction of CH_2CO (the most stable C_2 intermediate on α-MoC, Fig. 5A) into acetic acid and acetaldehyde on Pt_1/MoC(111) and Ir_1/MoC(111) at high hydroxyl coverage (Fig. 5, E and F, and fig. S30,). The energy barriers toward the formation of acetic acid were reduced to 0.58 eV on Pt_1/MoC(111) and 0.73 eV on Ir_1/MoC(111), substantially lower than those on pristine α-MoC and metallic Pt surfaces. Thus, the interfacial structure formed by atomically dispersed Pt (or Ir) and α-MoC facilitated the selective generation of acetic acid, aligning well with experimental observations, highlighting the importance of a high density of interfacial M_1/α-MoC sites in turning the reaction pathway toward partial reforming into acetic acid. Our calculations also suggest that small fully exposed metal clusters on MoC exhibit structural and adsorption characteristics (figs. S31 to S37 and movies S3 and S4) akin to those of Pt_1/MoC or Ir_1/MoC sites, thus also contribute to the overall catalytic activity. However, when large Pt or Ir particles form on α-MoC surface, C-C bond cleavage is considerably facilitated, leading to the formation of undesired products like CO_2 and CH_4.

Techno-economic analysis

Having demonstrated the outstanding catalytic performance of 3Pt3Ir/α-MoC in selective partial ethanol reforming, we further conducted an exhaustive techno-economic analysis and life cycle assessment to evaluate its prospect in an industry-scale plant for the production of H_2 and acetic acid (fig. S31, analysis detailed shown in tables S8 to S11). The evaluation indicates that the reforming plant can potentially achieve an attractive return on sales (ROS) ratio (table S12), surpassing the average ROS of the chemical industry (*45*) and demonstrating the economic viability of this process. Moreover, over the life span of the catalyst, carbon emissions for the production of H_2, and acetic acid are reduced by 21.9 and 38.6%, respectively, compared with conventional routes (fig. S32, analysis details shown in table S13). The decrease in fossil energy consumption is even more significant, with reductions of 51 and 86%, respectively. These results provide robust support for the sustainable attributes and feasibility of scaling up this process. Note that this process is still in its primary stage, more research and development efforts are required to further improve its efficiency and adaptability (see table S12 and associated discussions).

Outlook

In summary, we report a new thermal catalytic process for the selective partial reforming of ethanol with water to produce H_2 and acetic acid, which preserves the carbon resources in a high-valued liquid product and substantially cuts net carbon emissions. A rational design and construction of a high density of atomic M_1/α-MoC interfacial sites while avoiding the formation of large metal ensembles is demonstrated to be crucial for tuning the reforming pathway toward a high selectivity of acetic acid and for achieving an unprecedented H_2 generation activity of 331.3 $mmol_{H2}/(g_{cat}{\cdot}h)$ at low temperatures. This process could be scalable and profitable at an industrial scale, offering a promising avenue for sustainable green H_2 production with zero CO_2 emissions.

REFERENCES AND NOTES

1. G. Chen, X. Tu, G. Homm, A. Weidenkaff, *Nat. Rev. Mater.* **7**, 333–334 (2022).
2. E. Lewis *et al*., "Comparison of commercial, state-of-the-art, fossil-based hydrogen production technologies" (National Energy Technology Laboratory, report DOE/NETL-2022/3241, 2022).
3. International Energy Agency (IEA), "The Future of Hydrogen" (IEA, 2019).
4. A. J. Shih *et al*., *Nat. Rev. Methods Primers* **2**, 84 (2022).
5. H. de Lasa, E. Salaices, J. Mazumder, R. Lucky, *Chem. Rev.* **111**, 5404–5433 (2011).
6. G. A. Deluga, J. R. Salge, L. D. Schmidt, X. E. Verykios, *Science* **303**, 993–997 (2004).
7. L. V. Mattos, G. Jacobs, B. H. Davis, F. B. Noronha, *Chem. Rev.* **112**, 4094–4123 (2012).
8. A. Palanisamy, N. Soundarrajan, G. Ramasamy, *Environ. Sci. Pollut. Res. Int.* **28**, 63690–63705 (2021).
9. W. J. Wang, Y. Q. Wang, *Int. J. Hydrogen Energy* **33**, 5035–5044 (2008).
10. D. Pashchenko, *Int. J. Hydrogen Energy* **44**, 30865–30875 (2019).
11. M. Nielsen *et al*., *Nature* **495**, 85–89 (2013).
12. S. Ogo, Y. Sekine, *Fuel Process. Technol.* **199**, 106238 (2020).
13. E. Balaraman, E. Khaskin, G. Leitus, D. Milstein, *Nat. Chem.* **5**, 122–125 (2013).
14. A. C. Dimian, A. A. Kiss, *Chem. Eng. Res. Des.* **159**, 1–12 (2020).
15. A. L. M. da Silva *et al*., *J. Catal.* **318**, 67–74 (2014).
16. A. L. M. da Silva *et al*., *Catal. Today* **164**, 262–267 (2011).
17. A. H. Braga *et al*., *ACS Catal.* **11**, 2047–2061 (2021).
18. M. Martinelli *et al*., *Appl. Catal. A Gen.* **610**, 117947 (2021).
19. M. Kourtelesis *et al*., *Appl. Catal. B* **284**, 119757 (2021).
20. H. Meng *et al*., *Nat. Commun.* **14**, 3189 (2023).
21. W. Shi *et al*., *Adv. Energy Mater.* **13**, 2301920 (2023).
22. M. H. Haider *et al*., *Nat. Chem.* **7**, 1028–1032 (2015).
23. Y. Deng *et al*., *Acc. Chem. Res.* **52**, 3372–3383 (2019).
24. Y. Ge *et al*., *J. Am. Chem. Soc.* **143**, 628–633 (2021).
25. L. Lin *et al*., *J. Am. Chem. Soc.* **143**, 309–317 (2021).
26. L. Lin *et al*., *Nature* **544**, 80–83 (2017).
27. M. Compagnoni, A. Tripodi, I. Rossetti, *Appl. Catal. B* **203**, 899–909 (2017).
28. S. M. de Lima *et al*., *J. Catal.* **268**, 268–281 (2009).
29. P. S. Kirlin, B. C. Gates, *Nature* **325**, 38–40 (1987).
30. S. Li *et al*., *Natl. Sci. Rev.* **9**, nwab026 (2021).
31. X. Zhang *et al*., *Nature* **589**, 396–401 (2021).
32. L. Sun *et al*., *ACS Catal.* **11**, 5942–5950 (2021).
33. M. Peng *et al*., *ACS Cent. Sci.* **7**, 262–273 (2021).
34. Z. Gao, A. Li, D. Ma, W. Zhou, *Top. Catal.* **65**, 1609–1619 (2022).
35. J. Miao, P. Ercius, S. J. L. Billinge, *Science* **353**, aaf2157 (2016)
36. Z. Li *et al*., *Nat. Commun.* **14**, 2934 (2023).
37. Z. Liu *et al*., *Science* **368**, 513–517 (2020).
38. S. Yao *et al*., *Science* **357**, 389–393 (2017).
39. Z. Liu *et al*., *Phys. Chem. Chem. Phys.* **18**, 16621–16628 (2016).
40. K. I. Hadjiivanov *et al*., *Chem. Rev.* **121**, 1286–1424 (2021).
41. V. Muravev *et al*., *Science* **380**, 1174–1179 (2023).
42. X. Q. Tang *et al*., *Spectrochim. Acta A Mol. Biomol. Spectrosc.* **175**, 11–16 (2017).
43. S. Hanukovich, A. Dang, P. Christopher, *ACS Catal.* **9**, 3537–3550 (2019).
44. T. Hou, S. Zhang, Y. Chen, D. Wang, W. Cai, *Renew. Sustain. Energy Rev.* **44**, 132–148 (2015).
45. National Bureau of Statistics China (NBS China), The Profit of Industrial Enterprises above Designated Size in 2023 (NBS China, 2024); https://www.stats.gov.cn/english/PressRelease/202402/t20240201_1947130.html.

ACKNOWLEDGMENTS

NAP-XPS experiments were conducted at BL02B of the Shanghai Synchrotron Radiation Facility and the Analytical Instrumentation Center of Peking University. The authors thank Y. Xu for helping with the NAP-XPS experiments. XAFS experiments were conducted at BL39XU of SPring-8 with the approval of the Japan Synchrotron Radiation Research Institute (JASRI) (proposal 2019B1237) and Beijing Synchrotron Radiation Facility. This research benefited from resources and supports from the Electron Microscopy Center at the University of Chinese Academy of Sciences. The authors thank the Electron Microscopy Laboratory and the Analytical Instrumentation Center at Peking University for the use of aberration-corrected electron microscopes for AET experiment, and the High-performance Computing Platform of Peking University for 3D reconstruction. D.M. acknowledges support from the New Cornerstone Science Foundation through the XPLORER PRIZE and New Cornerstone Investigator Program. The authors thank Mark Howard, Jie Su, and Yi Qiu for the helpful discussion. **Funding:** This work was supported by the following: National Key R&D Program of China 2023YFA1506602 (to M.P.); 2021YFA1501102 (to D.M.); CAS Project for Young Scientists in Basic Research (YSBR-003) (to W.Z.); National Natural Science Foundation of China 22232001 (to D.M.); 22202004 (to M.P.); 22172003 (to J.Z.); 22172083 (to R.G.); XPLORER Prize of Tencent Foundation (to D.M.); New Cornerstone Science Foundation of Tencent Foundation (to D.M.); Liaoning Binhai Laboratory LBLF-2023-02 (to D.M.). **Author contributions:** Conceptualization: D.M., G.J.H., and W.Z. Methodology: W.Z., J.Z., A.H., J.D., J.Y., R.G., H.Z., and L.Z. Investigation: M.P., Y.G., A.L., Z.X., Q.Y. Visualization: M.P., A.L., Z.X., J.Z., and Q.Z. Funding acquisition: D.M., W.Z., M.P., and J.Z. Project administration: D.M. Supervision: D.M. and W.Z. Writing – original draft: M.P., J.Z., and A.L. Writing – review and editing: M.P., J.Z., A.L., Y.G., W.Z., and D.M. **Competing interests:** A Chinese patent that covers the PtIr/α-MoC catalysts reported in this paper was filed by Peking University (application 202411426363.1). All other authors declare that they have no competing interests. **Data and materials availability:** All data supporting the findings of this study are available within the paper and its supplementary materials.

License information: Copyright © 2025 the authors, some rights reserved; exclusive licensee American Association for the Advancement of Science. No claim to original US government works. https://www.science.org/content/page/science-licenses-journal-article-reuse

SUPPLEMENTARY MATERIALS

science.org/doi/10.1126/science.adt0682
Materials and Methods
Figs. S1 to S39
Tables S1 to S13
References (*46*–*89*)
Movies S1 to S4

Submitted 10 September 2024; accepted 14 January 2025
10.1126/science.adt0682

MEMBRANES

Engineering grain boundaries in monolayer molybdenum disulfide for efficient water-ion separation

Jie Shen[1,2]†, Areej Aljarb[3]†, Yichen Cai[1,4,5]†, Xing Liu[6]†, Jiacheng Min[7,8]†, Yingge Wang[1], Qingxiao Wang[9], Chenhui Zhang[1], Cailing Chen[1], Mariam Hakami[10], Jui-Han Fu[10], Hui Zhang[11,12], Guanxing Li[1], Xiaoqian Wang[1], Zhuo Chen[1], Jiaqiang Li[1], Xinglong Dong[1,13], Kaimin Shih[8], Kuo-Wei Huang[1,4], Vincent Tung[1,10,14]*, Guosheng Shi[6,15,16]*, Ingo Pinnau[1]*, Lain-Jong Li[7]*, Yu Han[11,12]*

Two-dimensional (2D) materials have long been considered as ideal platforms for developing separation membranes. However, it is difficult to generate uniform subnanometer pores over large areas on 2D materials. We report that the well-defined eight-membered ring (8-MR) pores, typically formed at the boundaries of two antiparallel grains of monolayer molybdenum disulfide (MoS_2), can serve as molecular sieves for efficient water-ion separation. The density of grain boundaries and, consequently, the number of 8-MR pores can be tuned by regulating the grain size. Optimized MoS_2 membranes outperformed the state-of-the-art membranes in forward osmosis tests by demonstrating both ultrahigh water/sodium chloride selectivity and exceptional water permeance. Creating precise pore structures on atomically thin films through grain boundary engineering presents a promising route for producing membranes suitable for various applications.

Selective molecular transport through nanoporous membranes forms the basis of many important separation and purification processes (*1*–*4*). In principle, two-dimensional (2D) materials, such as graphene, are ideal for preparing high-performance separation membranes. This is because they are extremely thin, thereby maximizing the molecular transport efficiency in the presence of nanopores (*5*–*7*). Theoretical studies have suggested that membranes based on 2D materials could be considerably superior to the conventional polymeric membranes in terms of permeability and selectivity in water desalination and gas separation (*8*–*10*). However, it is difficult to generate nanopores with precise molecular dimensions on 2D materials, especially over large areas, as required for practical applications.

Various methods, including ion or electron irradiation (*11*–*13*) and chemical or plasma etching (*6*, *14*, *15*), have been used to create nanopores on 2D materials. However, these methods offer limited control of pore size and pore density. The obtained membranes typically have a nonuniform distribution of pore size, resulting in low permeability or poor selectivity when used for molecular separation (*12*, *16*, *17*).

Compared with these posttreatment methods, direct generation of nanopores during the synthesis of 2D materials is more promising for achieving precise pore size control and high pore density. The synthesis of 2D materials through chemical vapor deposition (CVD) typically involves the simultaneous growth of multiple grains having different orientations. As the growth progresses, the grains are connected through grain boundaries (GBs) to form an extensive polycrystalline thin film. The formation of GBs in 2D materials induces structural inhomogeneity, which usually adversely affects the properties in comparison to single-crystalline ones. However, the presence of local structures at GBs may also create opportunities for specific applications. For example, eight-membered rings (8-MRs) formed at graphene GBs can act as pores that allow Li^+ ions to pass through (*18*), whereas the perfect graphene lattice comprising 6-MRs is impermeable to Li^+. Although 8-MRs in graphene have demonstrated considerable potential for ionic transport, such pores are randomly produced by the uncontrolled growth of graphene, thereby limiting the pore density and, in turn, the permeability of the membrane. The GB structure is primarily determined by the relative orientation of adjacent grains, with the number of pores being directly proportional to the GB density. Hence, controlling the grain orientation and size during the growth of 2D materials is necessary for optimizing the desired pore structure on the GB.

We intentionally generated a large number of GBs with predesigned porous structures in monolayer molybdenum sulfide (MoS_2) by precisely controlling MoS_2 grains to adopt one of two specific antiparallel orientations, with a consistent 60° relationship between them. This arrangement leads to the formation of several predictable GB structures, among which the 8-MR is dominant. The size of 8-MR in monolayer MoS_2 matches the requirement to enable rapid water transport while blocking various hydrated ions. Hence, the prepared films exhibit high water flux and water/ion selectivity when used as separation membranes. The number of 8-MRs can be increased by reducing the average grain size.

GB engineering in monolayer MoS_2

A single-crystalline defect-free monolayer MoS_2 comprising 6-MRs is impermeable to any atoms or molecules (*19*). Structural defects with ring sizes exceeding the intrinsic 6-MR can provide channels for selective molecular transport. However, to achieve high selectivity, the generated structural defects should have appropriate channel diameters (i.e., ring sizes) to match the required application. Molecular dynamics (MD) simulations were performed to explore appropriate MoS_2 ring sizes for water-ion separation based on the density functional theory (DFT)–optimized structural models (fig. S1). The results revealed that 7-MR is still too small to transport water molecules or ions (Fig. 1A), whereas 8-MR exhibits the desired pore size (~4.2 × 2.4 Å), allowing fast water permeation while completely rejecting hydrated Na^+ and Cl^- ions (Fig. 1B). The MD simulations also revealed the single-file transport of water in MoS_2 8-MRs. The average number of hydrogen bonds (H-bonds) per water molecule in 8-MRs was considerably lower than that of bulk water (1.6 versus 3.3, respectively; Fig. 1C), similar to water transport through protein aquaporin channels (*20*, *21*).

[1]Physical Sciences and Engineering Division (PSE), King Abdullah University of Science and Technology (KAUST), Thuwal, Saudi Arabia. [2]School of Materials Science and Engineering, Nanyang Technological University, 50 Nanyang Avenue, Singapore, Singapore. [3]Department of Physics, King Abdulaziz University, Jeddah, Saudi Arabia. [4]KAUST Catalysis Center, King Abdullah University of Science and Technology (KAUST), Thuwal, Saudi Arabia. [5]Key Laboratory of Flexible Electronics (KLOFE) and Institute of Advanced Materials (IAM), Nanjing Tech University (NanjingTech), Nanjing, China. [6]Shanghai Applied Radiation Institute, Shanghai Key Laboratory of Atomic Control and Application of Inorganic 2D Supermaterials, Shanghai University, Shanghai, China. [7]Department of Mechanical Engineering, University of Hong Kong, Pok Fu Lam Road, Hong Kong, China. [8]Department of Civil Engineering, University of Hong Kong, Pok Fu Lam Road, Hong Kong, China. [9]Imaging and Characterization Core Lab, King Abdullah University of Science and Technology (KAUST), Thuwal, Saudi Arabia. [10]Department of Chemical System Engineering, School of Engineering, The University of Tokyo, Tokyo, Japan. [11]Center for Electron Microscopy, South China University of Technology, Guangzhou, China. [12]School of Emergent Soft Matter, South China University of Technology, Guangzhou, China. [13]Catalyst Center of Excellence (CCoE), Research and Development Center, Saudi Aramco, Dhahran, Saudi Arabia. [14]Center for Sustainability and Energy Technologies, Chang Gung University, Taoyuan, Taiwan. [15]Key Laboratory of Comprehensive and Highly Efficient Utilization of Salt Lake Resources, Qinghai Institute of Salt Lakes, Chinese Academy of Sciences, Xining, Qinghai, China. [16]Wenzhou Institute, University of Chinese Academy of Sciences, Wenzhou, China. [17]Department of Materials Science and Engineering, National University of Singapore, Singapore, Singapore. [18]State Key Laboratory of Pulp and Paper Engineering, South China University of Technology, Guangzhou, China.
*Corresponding author. Email: vincent@g.ecc.u-tokyo.ac.jp (V.T.); gsshi@shu.edu.cn (G.S.); ingo.pinnau@kaust.edu.sa (I.P.); lance.li@nus.edu.sg (L.-J.L.); hanyu@scut.edu.cn (Y.H.)
†These authors contributed equally to this work.

8-MR is a typical defect structure of polycrystalline monolayer MoS_2, which is commonly found at the boundaries between two grains with a 60° orientation relationship (*22*, *23*). To gain insights into this phenomenon, we performed DFT calculations to compare the formation energies of the GB structures that were previously observed between grains with a 60° orientation relationship, including 4, 8-4, 8-4-8-4, 12-4, 12-4-12-4, and 4-8-4-4-12 structures (the numbers refer to ring sizes; see Fig. 1D). The calculation results showed that 8-4 (i.e., 8-MR combined with 4-MR) is the most stable configuration with the lowest formation energy, regardless of the sulfur concentration; moreover, structures involving 12-MR generally exhibited high formation energies, suggesting that the formation of 12-MR is energetically less favorable than the formation of 8-MR (Fig. 1E). Therefore, polycrystalline monolayer MoS_2 films exclusively comprising grains with a fixed orientation relationship (0° or 60°) are expected to have abundant 8-MRs suitable for water-ion separation.

We successfully fabricated such films on sapphire [α-Al_2O_3 (0001)] substrates using an established method that features a step of aligning MoS_2 seeds before further growth (*24*). For comparison, we also prepared monolayer MoS_2 films with randomly oriented grains by omitting the prior alignment step (fig. S2). Experimental details can be found in the materials and methods section of the supplementary materials. The films with controlled and random grain orientations are denoted as C-MoS_2 and R-MoS_2, respectively. The difference in grain orientation

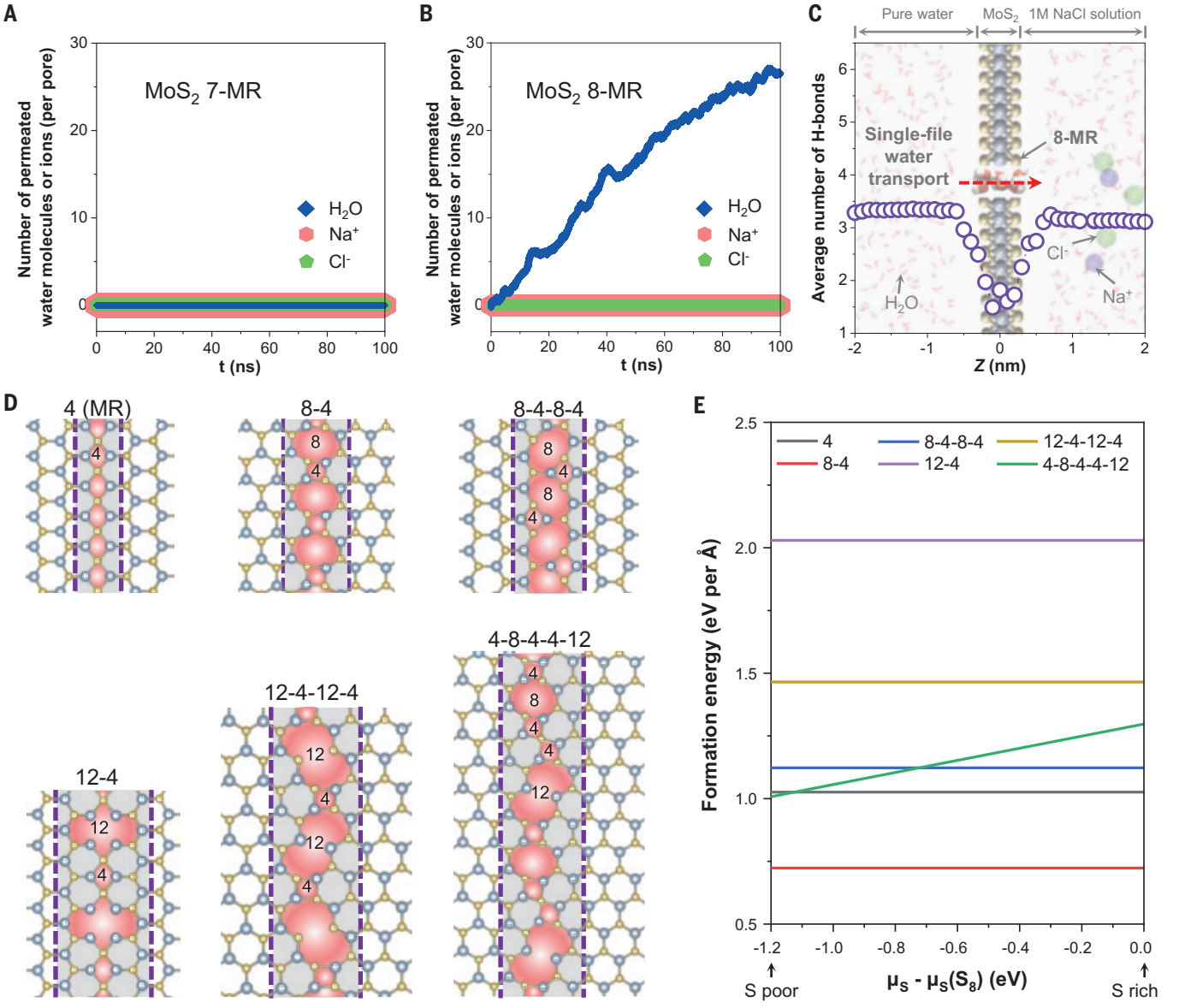


Fig. 1. Defect structures at MoS_2 grain boundaries. (**A** and **B**) MD simulations of water and ion transport through MoS_2 defect structures, (A) 7-MR and (B) 8-MR. t, time. (**C**) MD simulations reveal the single-file water transport through the 8-MR pore and the consequent change in the average number of H-bonds per water molecule as a function of its *Z* coordinate, which represents different locations within the studied region. In the simulation, pure water and 1 M NaCl aqueous solution were placed on the left and right sides of a monolayer MoS_2 film, respectively. The red dashed arrow indicates the direction of water transport. Water molecules outside the 8-MR are shown by red lines for clarity. (**D**) Common mirror-twin grain boundary structures in MoS_2. Blue and yellow spheres represent Mo and S atoms, respectively. (**E**) Formation energies of the structures shown in (D), as determined by the DFT calculations. The formation energy changes with the chemical potential per sulfur atom in ring structures (μ_s). The maximum and minimum values of μ_s correspond to sulfur-rich and sulfur-poor situations, respectively. The constant $\mu_s(S_8)$ represents the chemical potential per sulfur atom in S_8 molecules in the gas phase.

between C-MoS_2 and R-MoS_2 can be identified from optical microscopy images showing triangular MoS_2 flakes recorded at an early stage of the CVD process (Figs. 2, A and D). As the CVD process proceeded, the triangular MoS_2 flakes continued to grow and connected to each other through GBs, eventually forming continuous films (Figs. 2, B and E). The as-prepared MoS_2 films exhibited excellent uniformity throughout the substrate (diameter = 5.08 cm), as seen from the Raman and photoluminescence spectra and atomic force microscopy (AFM) images (figs. S3 to S5).

We used annular dark-field scanning transmission electron microscopy (ADF-STEM), commonly used for probing local structures in 2D transition metal dichalcogenides (TMDs) (*25*–*31*), to investigate C-MoS_2 and R-MoS_2 films. The obtained images revealed that 7-MR is the main defect structure of R-MoS_2, prevalent at GBs between grains with non-60° orientation relationships. Figure 2C shows a typical example, where numerous 7-MRs are observed along the boundary between two grains misaligned by 19°. This finding aligns with the conclusion of previous theoretical and experimental studies that 7-5 rings are a preferential configuration at non–mirror twin boundaries in TMD monolayers (*25*, *26*, *32*). Notably, when the two interconnected grains had a 60° orientation relationship, as in the case of C-MoS_2, a string of 8-MRs was observed along the mirror-twin boundaries (Fig. 2F and fig. S6). This observation was consistent with the expectation that building GBs with MoS_2 grains with a 60° orientation relationship can yield abundant 8-MRs in the film (*28*, *29*). Statistics based on ADF-STEM imaging revealed that 8-MRs accounted for ~97% of all the pores observed in the GBs of C-MoS_2 (4-MRs were not included in the statistics because of their impermeability), whereas pores of sizes >1 nm were rare, accounting for only <2.3% of all the observed pores (fig. S6). We determined that the duration of the MoS_2 grain growth step at 800°C is crucial for the formation of uniform interfacial 8-MRs. An inadequate duration leads to the presence of numerous irregular large pores (2 to 7 nm) at mirror-twin boundaries (fig. S7), attributed to an insufficient supply of Mo.

The grain sizes and grain boundary numbers in C-MoS_2 and R-MoS_2 films can be roughly determined by visualizing GBs using an established method. Specifically, heating the films at 100°C for 1 hour in humid air (60% relative humidity) caused the accumulation of contaminants (water, oxygen, and hydrocarbon molecules) along the GB, allowing the easy identification of GBs with scanning electron microscopy (SEM) (*33*). The SEM results showed that R-MoS_2 and C-MoS_2 films grown under standard conditions exhibit similar average grain sizes of ~8 and ~7.2 μm^2, respectively; however, the intersection of multiple GBs was observed in R-MoS_2 but not in C-MoS_2, confirming the difference in grain orientation (i.e., random versus fixed) between the two films (fig. S8). Electron diffraction analysis and dark-field imaging based on 4D STEM datasets further corroborated the random grain orientations in R-MoS_2 and the exclusive presence of two grain orientations at a 60° relationship in C-MoS_2 (figs. S9 and S10).

We fabricated three other C-MoS_2 films exhibiting different average grain sizes by

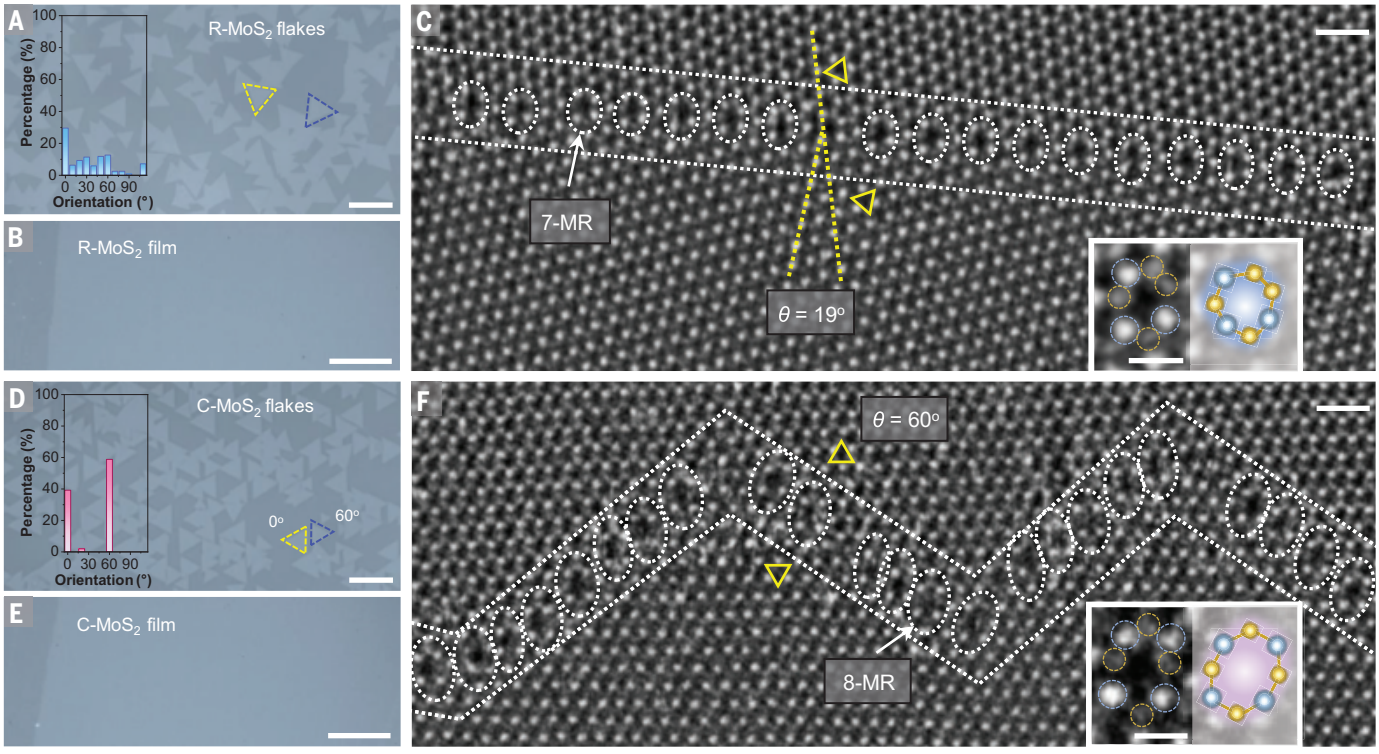


Fig. 2. Microscopic characterization of R-MoS_2 and C-MoS_2. (**A** and **B**) Optical microscopy images taken at (A) early and (B) late stages of the R-MoS_2 film growth process. In (A), triangular MoS_2 flakes with random orientations were observed, as exemplified by the dashed yellow and blue triangles. The orientation distribution is shown in the inset. (**C**) Atomic-resolution ADF-STEM image of a monolayer R-MoS_2 film, showing two grains with a misorientation of 19°. The dashed lines outline the grain boundary, and dashed circles highlight 7-MR pores. Yellow triangles indicate the orientations of the two grains. The inset shows a magnified image of a single 7-MR pore and the corresponding schematic structural model. (**D** and **E**) Optical microscopy images taken at (D) early and (E) late stages of the C-MoS_2 film growth process. In (D), triangular MoS_2 flakes with a fixed-orientation relationship (0° or 60°) were observed, as exemplified by the dashed yellow and blue triangles. The orientation distribution is shown in the inset. (**F**) Atomic-resolution ADF-STEM image of a monolayer C-MoS_2 film, showing two grains with a 60° orientation relationship. Yellow triangles indicate the orientations of the two grains. The dashed lines outline the grain boundary, and dashed circles highlight 8-MR pores. The inset shows a magnified image of a single 8-MR pore and the corresponding schematic structural model. Scale bars: 2 μm [(A) and (D)], 20 μm [(B) and (E)], 1 nm [(C) and (F)], and 5 Å [insets, (C) and (F)].

modulating the nucleation density. Their average grain sizes, which were determined by using the aforementioned method, were ~443.4, ~87.3, and ~0.26 μm^2, respectively (fig. S11). Thus, a total of five films were fabricated, hereinafter denoted as "C-MoS_2-X" or "R-MoS_2-X," where X indicates the average grain size. The 8-MR density of the film increases with decreasing grain size. From the ADF-STEM imaging results, the density of 8-MR pores in C-MoS_2-0.26 was estimated to be ~6.5 × 10^{11} cm^{-2}. Details on the estimation method are provided in the supplementary materials.

The control of grain orientation, grain size, and pore structure in C-MoS_2 films relies on several critical factors. Firstly, initiating the deposition of MoS_2 at 750°C, rather than directly heating to 800°C, is essential for controlling the orientation of MoS_2 grains (fig. S2B). This step maintains a relatively high S/Mo ratio, which helps stabilize the MoS_2 seeds at small sizes. These small seeds are sufficiently mobile to rotate and align themselves into the most energetically favorable orientations, specifically at 0° or 60° relative to the lattice of the sapphire substrate, before further growth (*24*). Secondly, the average grain size in the MoS_2 film is controlled by adjusting the temperature of the sulfur zone between 145° and 175°C. Higher sulfur vapor pressure promotes MoS_2 nucleation, which, in turn, lead to the formation of smaller grains. Thirdly, it is crucial to expose armchair (AC) edges during grain stitching, as 8-MR pores preferentially form at mirror twin boundaries (MTBs) at AC edges rather than at zigzag (ZZ) edges. Unlike fully developed MoS_2 flakes, which typically exceed 20 μm and are terminated with ZZ edges (*31*, *34*, *35*), C-MoS_2 films exhibit significantly smaller grains, ranging

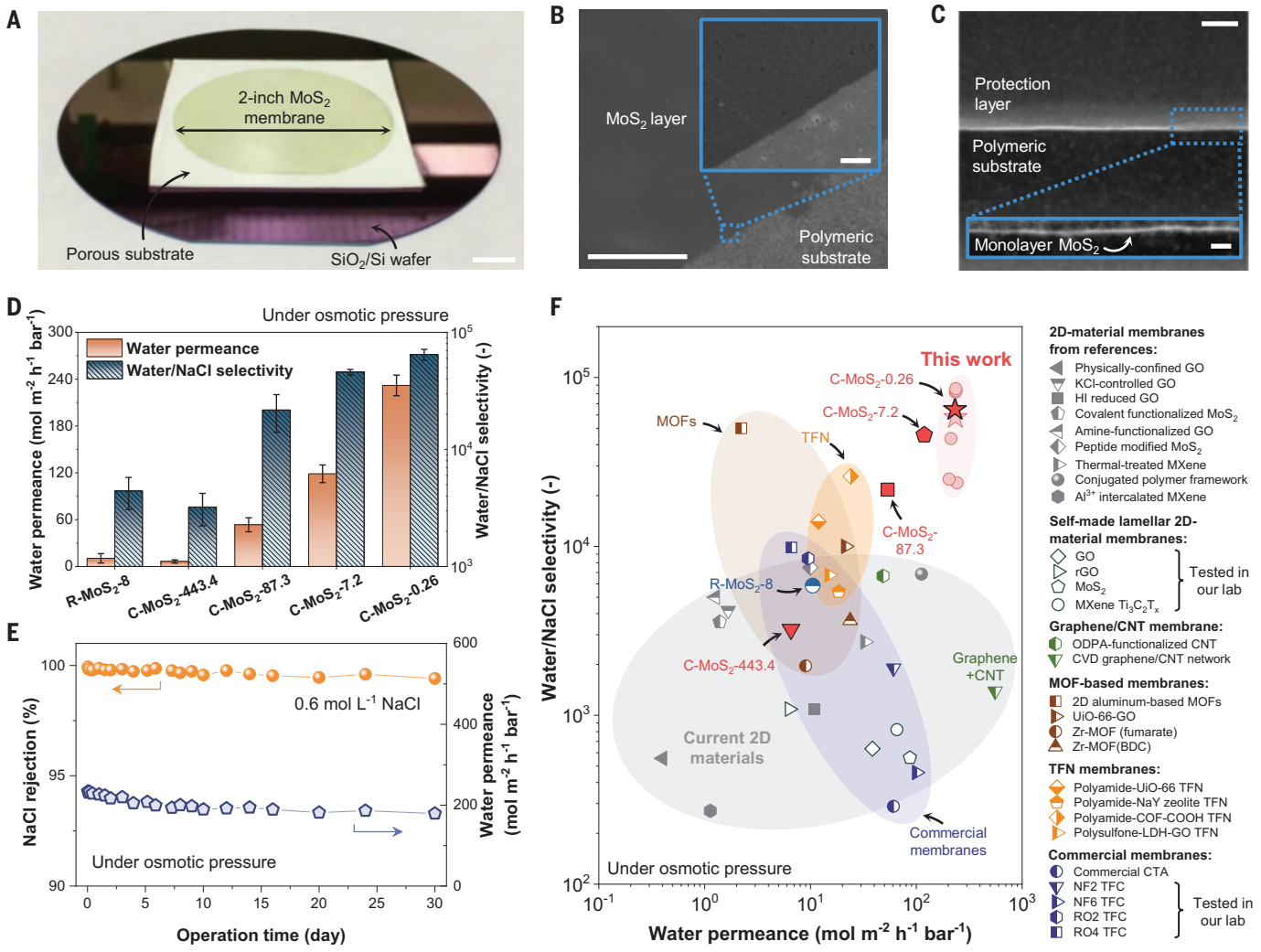


Fig. 3. Water-ion separation of C-MoS_2 membranes. (**A**) Photograph of a C-MoS_2 film (diameter = 5.08 cm) supported on a PC substrate. (**B**) Top-view SEM image of a C-MoS_2-7.2 membrane. (**C**) Cross-sectional ADF-STEM images of the membrane shown in (B), confirming the monolayer nature of the MoS_2 film. (**D**) Water-NaCl separation performance of R-MoS_2 and C-MoS_2 membranes. Feed side, 0.1-M NaCl solution; draw side, 2-M sucrose solution. Error bars denote the standard deviations from three different samples. On the *y* axis, - represents the unitless nature of water/NaCl selectivity. (**E**) NaCl rejection (0.6-M in feed solution) and water permeance of the C-MoS_2-0.26 membrane during a 30-day continuous forward osmosis test. (**F**) Comparison of MoS_2 membranes with state-of-the-art membranes reported for water-NaCl separation driven by osmotic pressure. TFC, thin-film composite; TFN, thin-film nanocomposite; ODPA, octadecylphosphonic acid; CTA, cellulose triacetate. Data points in red color indicate C-MoS_2 with different domain size tested under cocurrent mode with 0.1-M NaCl as the feed solution and 2-M sucrose as the draw solution. The five-pointed pink star indicates the C-MoS_2-0.26 membrane tested under 0.6-M NaCl as the feed solution and 2-M sucrose as the draw solution. All the pink solid circles indicate the C-MoS_2-0.26 membranes tested under countercurrent mode with different NaCl concentration (feed side, deionized water; draw side, NaCl solutions with concentrations ranging from 0.2 to 2 M). See table S1 for details. Scale bars: 1 cm (A), 50 μm (B), 1 μm [(B), inset], 10 nm (C), and 2 nm [(C), inset].

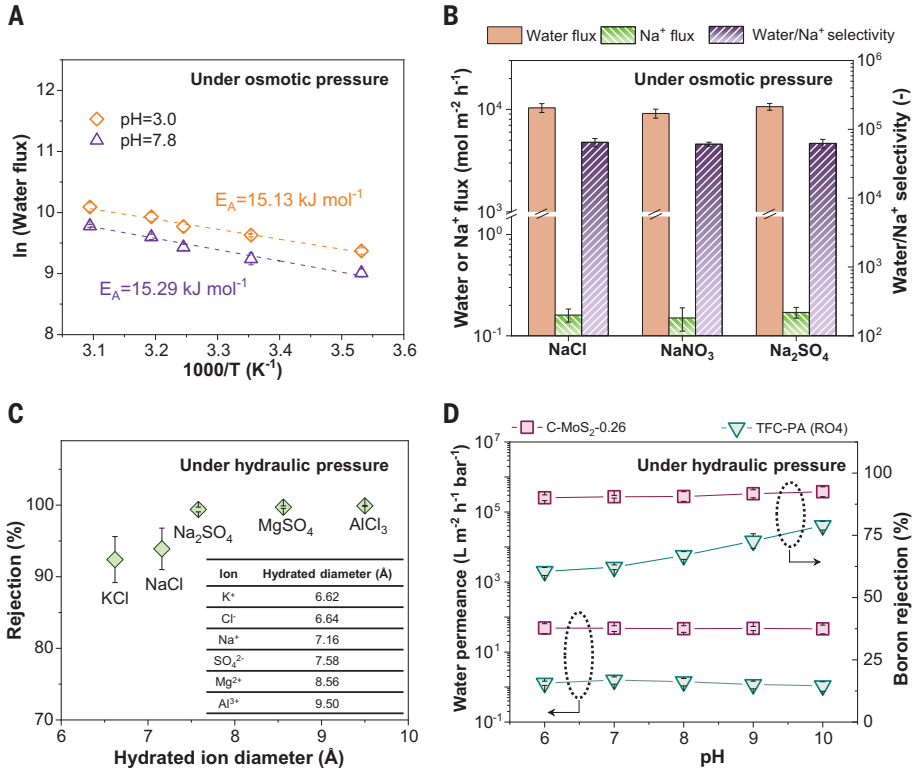


Fig. 4. Mechanism of water-ion separation by the C-MoS$_2$-0.26 membrane. (**A**) Arrhenius plots of water flux versus temperature under pH of 3.0 and 7.8. Feed side, 0.1-M NaCl; draw side, 2-M sucrose solution. The pH values were adjusted using 0.1-M HCl and 0.1-M $NaHCO_3$ solution. (**B**) Effect of anions on the water and Na^+ fluxes. Feed side, 0.1-M NaCl, $NaNO_3$ or Na_2SO_4 solution; draw side, 2-M sucrose solution. (**C**) Rejection for various salts driven by hydraulic pressure at 13 bar using 2000-ppm salt solutions (with KCl, NaCl, Na_2SO_4, $MgSO_4$, or $AlCl_3$) as the feed. (Inset) Hydrated diameters of ions. (**D**) Comparison of the water permeance and boron rejection driven by hydraulic pressure (5 ppm, 10 bar, 25°C, dead-end operation) between the C-MoS$_2$-0.26 membrane and a commercial polyamide thin-film composite (TFC) membrane (Sepro RO4) at different pH values. The pH values were adjusted using 0.1 to 1 M $NaHCO_3$ solutions. Error bars denote standard deviations from three different samples.

from several hundred nanometers to a few micrometers, achieved through a high nucleation density. The stitching of these less-mature grains gives rise to abundant AC-type MTBs in the resultant film (see figs. S11 and S12 for a detailed analysis).

MoS$_2$ membranes for water-ion separation

To fabricate separation membranes, the CVD-grown monolayer MoS_2 films were transferred from sapphire to porous polycarbonate (PC) substrates by using the polydimethylsiloxane-assisted technique (*33*) (Fig. 3A and fig. S13). PC was chosen as the substrate because its smooth surface and high surface energy (~40 mJ m^{-2}) can provide a strong adhesion with the supported MoS_2 film (*36*, *37*). The top-view SEM image showed that the MoS_2 film is continuous and devoid of cracks (Fig. 3B and fig. S14), whereas the cross-sectional ADF-STEM image confirmed the monolayer nature and homogeneity of the film (Fig. 3C).

The water and ion transport properties of the fabricated MoS_2 membranes were first verified by using a forward osmosis (FO) configuration, typically with an effective membrane area of 0.28 cm^2 unless otherwise specified. When pure water was used as the feed solution and 2-M NaCl was used as the draw solution, the C-MoS$_2$-7.2 membrane exhibited a water flux of ~1.2 × 10^4 mol m^{-2} h^{-1} (fig. S15A). Its water-ion separation capability was evaluated by using various salt solutions (K^+, Na^+, Ca^{2+}, Mg^{2+}, and Al^{3+}; 0.1 M) as the feed solution and a sucrose solution (2 M) as the draw solution. In all the tests, the ion flux of the C-MoS$_2$-7.2 membrane was ultralow; it was more than five orders of magnitude lower than that of the bare PC substrate (fig. S15B), corresponding to extremely high water/ion selectivity. For example, when tested with 0.1 M NaCl, the membrane had a water permeance of ~118.9 mol m^{-2} h^{-1} bar^{-1} and a water/NaCl selectivity of ~4.6 × 10^4. The nonzero ion fluxes (<0.16 mol m^{-2} h^{-1}) can be attributed to the presence of a few large pores (fig. S6), which are only occasionally observed along the GBs (fig. S16) but are absent inside the MoS_2 grains (fig. S17). Under identical test conditions, the R-MoS$_2$-8 membrane showed considerably lower water permeance (~10.5 mol m^{-2} h^{-1} bar^{-1}) and water/NaCl selectivity (~4418) than the C-MoS$_2$-7.2 membrane despite having similar average MoS_2 grain sizes (Fig. 3D). This result is consistent with the expectations and is attributed to the presence of the impermeable 7-MR as the primary defect structure on the randomly grown MoS_2 film.

The C-MoS$_2$-87.3 and C-MoS$_2$-443.4 membranes showed lower water permeance and water/NaCl selectivity compared with the C-MoS$_2$-7.2 membrane, whereas the C-MoS$_2$-0.26 membrane outperformed all the tested membranes, exhibiting a water permeance of ~232 mol m^{-1} h^{-1} bar^{-1} and a water/NaCl selectivity of ~6.5 × 10^4 (Fig. 3D). These results demonstrate that the water-ion separation performance of the C-MoS$_2$ membranes is dependent on the number of 8-MRs, which increases as the grain size decreases. Unlike the conventional water desalination membranes that have a tradeoff between water permeance and water/ion selectivity, C-MoS$_2$ membranes show positively correlated water permeance and water/ion selectivity, suggesting a molecular sieving–based separation mechanism (*38*). The observed rise in water/NaCl selectivity with the reduction in grain size is attributed to the enhanced water flux, a result of the increased number of 8-MR pores. This observation also suggests that the formation of nonselective large pores is effectively minimized, irrespective of the grain sizes. The nonlinear enhancement in water permeance demonstrated by C-MoS$_2$ membranes with decreased grain size stems from the constraints imposed by the low porosity (less than 2%) of the PC substrates (see fig. S18 for analysis) (*1*). Stacking multiple layers of C-MoS$_2$-0.26 on the PC support led to membranes with greatly reduced water permeation compared with the monolayer version (fig. S19). This decrease in permeation is attributed to the misaligned 8-MRs across the layers and the nonpermeable gap between MoS_2 layers, which measures ~0.18 nm (*39*). This result underscores the pivotal role of 8-MRs as the primary transport channels for water and the necessity of maintaining monolayer thickness for optimal membrane performance.

The monolayer C-MoS$_2$-0.26 membrane underwent comparative analysis with a range of high-performance membranes (Fig. 3F), including various lamellar 2D-material membranes (fig. S20) and commercial polyamide thin-film composite membranes. Under identical conditions, the C-MoS$_2$-0.26 membrane demonstrated superior performance in terms of water/NaCl selectivity and water permeance compared with all other evaluated membranes, regardless of the testing mode used (cocurrent mode, 0.1-M NaCl versus 2-M sucrose, or countercurrent mode, deionized water versus 1-M NaCl) (figs. S19B and S21 and table S1).

These findings further underscore the salt rejection capacity of the C-MoS_2-0.26 membrane across varying operating modes and high salt concentrations. Seven membranes fabricated with C-MoS_2-0.26 collected from different regions of a sapphire substrate (diameter = 5.08 cm) showed consistent water-ion separation properties (fig. S22), demonstrating the structural homogeneity of monolayer MoS_2 and reliability of the water separation tests. Increasing the effective membrane area from 0.28 to 2.54 cm^2 did not result in a noticeable alteration in membrane performance (fig. S22C).

During 30 days of continuous testing with 0.6-M NaCl in the feed (similar to the ionic strength of seawater) and 2-M sucrose as the draw solution, the C-MoS_2-0.26 membrane showed a steady NaCl rejection of >99% and only slightly reduced water permeance. When synthetic seawater (containing KCl, NaCl, Na_2SO_4, $CaCl_2$, and $MgCl_2$; ionic strength: ~1.15 M) was used as the feed, it exhibited >99.9% ion rejection and a water permeance of ~214 mol m^{-2} h^{-1} bar^{-1} (fig. S23). Mechanical strength assessment through AFM indentation revealed that the C-MoS_2-0.26 film can withstand a pressure of at least 9 MPa (fig. S24). Moreover, after prolonged treatments simulating permeation experiments, it retained its characteristic 8-MR pores along the GBs, as evidenced by ADF-STEM imaging (fig. S25). These findings collectively demonstrate the enduring mechanical and chemical stability of the C-MoS_2-0.26 membrane.

Exploration of the separation mechanism

The excellent water-ion separation ability of C-MoS_2 membranes is believed to originate from the size-exclusion effect of 8-MR, as hydrated ions encounter a considerably higher energy barrier than water molecules when entering the subnanometer-sized pores (*40*, *41*). To gain more insight into the separation mechanism, we calculated the Arrhenius activation energy (E_A) for water transport through the C-MoS_2-0.26 membrane based on the water fluxes measured at different temperatures. The results showed that E_A is barely affected by the system pH (e.g., E_A = 15.1 and 15.3 kJ mol^{-1} at pH 3.0 and 7.8, respectively; Fig. 4A); this finding indicates a lack of proton concentration–governed water-pore interactions. Therefore, it is more likely that the energy barrier is associated with the drastic change in the H-bond configuration when water molecules are transported from the bulk solution into the 8-MR pores. Likewise, different anion species did not have considerable impact on the water-Na^+ separation performance of the C-MoS_2-0.26 membrane (Fig. 4B), confirming the irrelevance of solution chemistry to the separation.

The C-MoS_2-0.26 membrane was also evaluated under pressure-driven conditions. For these tests, membranes with an effective membrane area of 2.54 cm^2 were fabricated by supporting monolayer C-MoS_2-0.26 films on highly porous anodized aluminum oxide (AAO) substrates (fig. S26). The use of AAO substrates inevitably resulted in the generation of pinholes in the membrane; these pinholes could be sealed subsequently through an interfacial polymerization strategy (*13*, *16*) (see details in materials and methods). At a feed salt concentration of 2000 ppm and an operating pressure of 13 bar, the C-MoS_2-0.26 membrane exhibited the following ion diameter–dependent rejection (R) sequence: R ($AlCl_3$) > R ($MgSO_4$) > R (Na_2SO_4) > R (NaCl) > R (KCl) (Fig. 4C). The fact that $MgSO_4$ is rejected to a greater extent than Na_2SO_4 rules out the Donnan exclusion as the main separation mechanism (*6*, *42*, *43*). Notably, the membrane recorded a water permeance of 44.3 L m^{-2} h^{-1} bar^{-1} and $MgSO_4$ rejection of 99.7%. This surpassed the performance of commercial nanofiltration membranes, such as FilmTec NF270, Sepro NF2, and NF6, tested under similar conditions (fig. S27). The tests were not conducted at higher hydraulic pressures primarily owing to the mechanical limitations of the AAO substrate. It is anticipated that using porous substrates with greater mechanical strength than AAO will improve the membrane's maximum pressure tolerance, provided that there is strong adhesion between the MoS_2 film and the selected substrates.

In addition to common cations, C-MoS_2 membranes can effectively exclude boron, which exists as $B(OH)_3$ in neutral solutions with a low molecular weight of 61.8 g mol^{-1}. Compared with the commercial polyamide thin-film composite membrane Sepro RO4, the C-MoS_2-0.26 membrane exhibited a higher boron rejection (~90.5 versus ~63% at pH 7) and an approximately 40-fold increase in water permeance (Fig. 4D). Furthermore, unlike RO4, whose boron rejection is pH sensitive, the high boron rejection of the C-MoS_2-0.26 membrane remained almost constant in the pH range of 6 to 10. These results collectively indicated that the strong molecular-sieving effect of 8-MR pores, rather than the surface charge, is the primary mechanism responsible for the exceptional water/ion selectivity of C-MoS_2 membranes, regardless of the type of driving force (osmotic or hydraulic pressure) for the water transport.

Conclusions

This study demonstrates that water-ion separation can be achieved by using a monolayer MoS_2 membrane with specially designed structural defects. Precise control of the orientation and size of MoS_2 grains is important for the successful preparation of high-performance separation membranes. When all MoS_2 grains have a fixed-orientation relationship (0° or 60°), the desired 8-MR defects dominate at the GBs, resulting in the formation of membranes with high water/ion selectivity. Additionally, the grain size determines the number of GBs and, thus, the density of the 8-MR pores. The synthesis method reported in this work offers a strategic approach for the controlled generation of local structures in 2D materials to modulate their properties. Compared with other methods with similar objectives (*22*, *44*, *45*), this approach distinctly enables the simultaneous achievement of high-density grain boundaries, precise control over pore structures, and the growth of large-area continuous films.

REFERENCES AND NOTES

1. H. B. Park, J. Kamcev, L. M. Robeson, M. Elimelech, B. D. Freeman, *Science* **356**, eaab0530 (2017).
2. R. Epsztein, R. M. DuChanois, C. L. Ritt, A. Noy, M. Elimelech, *Nat. Nanotechnol.* **15**, 426–436 (2020).
3. Z. Jiang *et al*., *Nature* **609**, 58–64 (2022).
4. B. Sengupta *et al*., *Science* **381**, 1098–1104 (2023).
5. L. Wang *et al*., *Nat. Nanotechnol.* **12**, 509–522 (2017).
6. Y. Yang *et al*., *Science* **364**, 1057–1062 (2019).
7. P. R. Kidambi, P. Chaturvedi, N. K. Moehring, *Science* **374**, eabd7687 (2021).
8. D. E. Jiang, V. R. Cooper, S. Dai, *Nano Lett.* **9**, 4019–4024 (2009).
9. D. Cohen-Tanugi, J. C. Grossman, *Nano Lett.* **12**, 3602–3608 (2012).
10. M. Heiranian, A. B. Farimani, N. R. Aluru, *Nat. Commun.* **6**, 8616 (2015).
11. J. Feng *et al*., *Nature* **536**, 197–200 (2016).
12. K. Celebi *et al*., *Science* **344**, 289–292 (2014).
13. C. Cheng, S. A. Iyengar, R. Karnik, *Nat. Nanotechnol.* **16**, 989–995 (2021).
14. S. P. Surwade *et al*., *Nat. Nanotechnol.* **10**, 459–464 (2015).
15. J. Feng *et al*., *Nano Lett.* **15**, 3431–3438 (2015).
16. S. C. O'Hern *et al*., *Nano Lett.* **15**, 3254–3260 (2015).
17. J. Zhao *et al*., *Sci. Adv.* **5**, eaav1851 (2019).
18. E. Griffin *et al*., *ACS Nano* **14**, 7280–7286 (2020).
19. S. Hu *et al*., *Nature* **516**, 227–230 (2014).
20. W. Song *et al*., *Nat. Nanotechnol.* **15**, 73–79 (2020).
21. R. H. Tunuguntla *et al*., *Science* **357**, 792–796 (2017).
22. P. Man, D. Srolovitz, J. Zhao, T. H. Ly, *Acc. Chem. Res.* **54**, 4191–4202 (2021).
23. F. Bertoldo *et al*., *ACS Nano* **15**, 2858–2868 (2021).
24. A. Aljarb *et al*., *ACS Nano* **11**, 9215–9222 (2017).
25. S. Najmaei *et al*., *Nat. Mater.* **12**, 754–759 (2013).
26. Y. Han *et al*., *Nat. Mater.* **17**, 129–133 (2018).
27. J. Chen *et al*., *Small* **15**, e1902590 (2019).
28. A. M. van der Zande *et al*., *Nat. Mater.* **12**, 554–561 (2013).
29. S. Wang *et al*., *ACS Nano* **12**, 5626–5636 (2018).
30. X. Zhang *et al*., *Nano Lett.* **18**, 1049–1056 (2018).
31. W. Zhou *et al*., *Nano Lett.* **13**, 2615–2622 (2013).
32. N. Gao, Y. Guo, S. Zhou, Y. Bai, J. Zhao, *J. Phys. Chem. C Nanomater. Interfaces* **121**, 12261–12269 (2017).
33. H. Yu *et al*., *ACS Nano* **11**, 12001–12007 (2017).
34. T. H. Ly *et al*., *Nat. Commun.* **7**, 10426 (2016).
35. Q. Wang *et al*., *Nano Lett.* **20**, 7193–7199 (2020).
36. A. J. Watson, W. Lu, M. H. D. Guimarães, M. Stöhr, *2D Mater.* **8**, 032001 (2021).
37. Y. Cao *et al*., *IEEE Access* **8**, 70488–70495 (2020).
38. J. Abraham *et al*., *Nat. Nanotechnol.* **12**, 546–550 (2017).
39. Y. Liu, Y. Huang, X. Duan, *Nature* **567**, 323–333 (2019).
40. L. Ries *et al*., *Nat. Mater.* **18**, 1112–1117 (2019).
41. W.-H. Zhang *et al*., *Nat. Nanotechnol.* **16**, 337–343 (2021).
42. J. Shen *et al*., *Nat. Mater.* **21**, 1183–1190 (2022).
43. Y. Zhang *et al*., *Science* **382**, 202–206 (2023).
44. J. Zhu *et al*., *Innovation (Camb.)* **4**, 100502 (2023).
45. O. V. Yazyev, Y. P. Chen, *Nat. Nanotechnol.* **9**, 755–767 (2014).

ACKNOWLEDGMENTS

We acknowledge P. Guo and Y. Ma for helpful discussions.
Funding: The financial support for this work was provided by the GJYC program of Guangzhou City (2024D03J0001); the National Key Research and Development Project of China (2022YFE0113800); Baseline Fund (BAS/1/1323-01-01) from King Abdullah University of Science and Technology (KAUST); Research Grant of the Council of Hong Kong (CRS_PolyU502/22); the National Key R&D Project of China (2022YFB4044100); the National Natural Science Foundation of China (U1932123, 12105166); Kunlun Talent Program of Qinghai Province, China; KAUST Office of Sponsored Research (OSR) Award (CCF-3079); JST, CREST Grant (JPMJCR24A3); Japan Society for the Promotion

of Science (JSPS, 23H00253 and 24K21233). **Author contributions:** Y.H., L.-J.L., I.P., and G.S. conceived the idea. J.S., A.A., Y.C., Y.W., Q.W., C.Z., C.C., M.H., J.-H.F., H.Z., G.L., X.W., Z.C., J.L., and X.D. synthesized and characterized the materials and carried out transport measurements. X.L. performed MD simulations, and J.M. conducted the DFT calculations. K.S., K.-W.H., and V.T. provided constructive opinions and suggestions. All authors were involved in the analysis and discussion of the results. Y.H., L.-J.L., I.P., G.S., and J.S. wrote the manuscript, and all authors commented on it. **Competing interests:** The authors declare that they have no competing interests. **Data and materials availability:** All data needed to evaluate the conclusions in the paper are present in the paper and/or the supplementary materials. **License information:** Copyright © 2025 the authors, some rights reserved; exclusive licensee American Association for the Advancement of Science. No claim to original US government works. https://www.science.org/about/science-licenses-journal-article-reuse

SUPPLEMENTARY MATERIALS
science.org/doi/10.1126/science.ado7489
Materials and Methods
Figs. S1 to S27
Table S1
References (*46*–*72*)

Submitted 19 February 2024; accepted 17 January 2025
10.1126/science.ado7489

HYDROLOGY

Variability of flowing stream network length across the US

Jeff P. Prancevic[1,2]*†‡, Hansjörg Seybold[2]†, James W. Kirchner[1,2,3]

The aggregate length of flowing streams in a drainage network lengthens and shortens as landscapes become wetter and drier. However, direct measurements of stream network variability have been limited to a handful of small drainage basins. We estimated the variability of stream network length for 14,765 gauged basins across the contiguous United States using measured streamflow distributions and topography-based estimates of how sensitive each stream network is to changing landscape wetness (the network's elasticity). We find that the median US stream network is five times longer during annual high-flow conditions than during annual low-flow conditions. Stream networks are more dynamic in some regions than in others, driven by regional differences in both hydroclimatology and the networks' elasticity in response to hydroclimatic forcing.

Although stream networks have often been treated as static features of the landscape, their total wetted length can vary by more than an order of magnitude seasonally or during storm events, as the shallow subsurface fills and drains (*1*–*8*). As streams lengthen and shorten, so does their ability to transport sediment, carbon, and nutrients (*9*–*12*); exchange gases with aquifers and the atmosphere (*13*); and provide habitat to aquatic organisms (*14*, *15*). Many of these functional roles depend on streams' total wetted surface area and thus on both their width and their length. Field observations show that wetted stream widths have a consistent distribution across different flow conditions and different landscapes, such that the total wetted surface area can be estimated (*16*) if the network length is known. The dynamics of stream length, however, are more difficult to predict, limiting our ability to estimate greenhouse gas fluxes from terrestrial surface waters (*17*) and understand the impact of climate change on riparian habitat (*14*).

The lengthening and shortening of streams are driven by changes in landscape wetness. Intuitively, rainstorms and snowmelt wet the landscape, causing streamflow to increase and streams to lengthen. The total amount of stream lengthening in a network depends on the surface topography and three-dimensional structure of subsurface permeability, which route water through rock and soil and eventually to the surface to create streamflow. This topographic and subsurface structure determines the sensitivity of stream length to changes in wetness; we term this sensitivity the "network elasticity." Thus, changes in stream length are determined both by network elasticity and by the change in landscape wetness (which can be inferred, at the scale of whole drainage basins, from changes in streamflow).

Repeated mapping under different flow conditions has shown that the total wetted length of stream networks, L, typically scales nonlinearly with the streamflow, Q, measured at the catchment outlet:

$$L \propto Q^{\beta} \quad (1)$$

where β, a site-specific elasticity coefficient, expresses the sensitivity of stream-network length to variations in landscape wetness as reflected in streamflow Q [e.g., (*3*–*5*)]. If the value of β is known, changes in length can be estimated from real-time, historical, or forecasted future changes in streamflow [e.g., (*18*)] (Fig. 1).

Measurements of stream network length at multiple wetness states are rare, but the measurements that do exist show that β varies substantially from site to site. For example, the 12 stream networks mapped by Jensen *et al.* (*3*) exhibit β values ranging from 0.04 to 0.71, even though they all lie within humid, forested, mountainous catchments of the Appalachian Highlands of the eastern US. Direct measurements of β require extensive fieldwork and thus are likely to remain rare for the foreseeable future. Nevertheless, given the importance of stream network elasticity for aquatic habitats and biogeochemical cycles, estimates—even if approximate—of how β varies at continental scales could find widespread application.

In this study, we estimated stream network elasticity for the entire contiguous US, using a previously published semimechanistic model (*19*) that relates topography to stream network dynamics. We then combined those estimates of elasticity with streamflow measurements to estimate the variability of stream network length for 14,765 gauged basins across the country, revealing regional patterns in stream network dynamics.

Estimating stream network elasticity

Several recent studies suggest that β can potentially be estimated from other landscape properties (*19*–*21*). In a regression analysis of their 12 catchments, Jensen *et al.* (*3*) found that stream networks with narrow channels and little base flow tend to be more elastic than those with wide channels and high base flows. Using a more mechanistic approach, Ward *et al.* (*20*) modeled changes in the spatial distribution of surface flow, on the basis of soil and topographic properties that control the capacity of valley bottoms to transport water through the subsurface. Although this model can predict the detailed stream dynamics in individual study catchments, it requires estimates of subsurface permeability, which are not widely available.

In a semimechanistic approach, Prancevic and Kirchner (*19*) showed that the basin-averaged behavior of stream networks can be estimated without any direct hydrologic measurements by considering how topography modulates the spatial pattern of shallow groundwater flow through soil and rock. This approach is based on the simple conceptual framework proposed by Godsey and Kirchner (*5*), which states that flow will emerge at the surface wherever the water supply from the landscape (which will depend on its wetness and the upslope drainage area) just exceeds the local subsurface

[1]Department of Earth & Planetary Science, University of California, Berkeley, Berkeley, CA, USA. [2]Department of Environmental Systems Science, ETH Zürich, Zürich, Switzerland. [3]Swiss Federal Institute for Forest, Snow and Landscape Research WSL, Birmensdorf, Switzerland.
***Corresponding author. Email: jeff.prancevic@gmail.com**
†These authors contributed equally to this work.
‡Present address: Earth Research Institute, University of California, Santa Barbara, Santa Barbara, CA, USA.

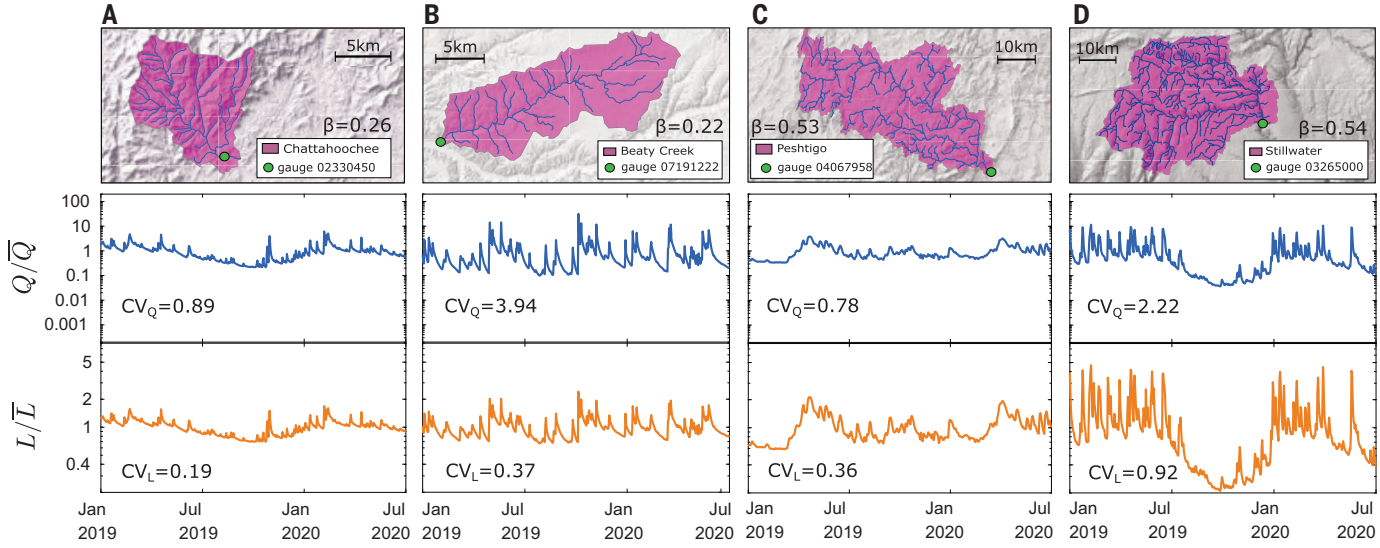


Fig. 1. Four drainage basins and their predicted variability in network length. (Top) Ten-meter hillshade DEMs with the drainage basin (highlighted in purple) and its predicted elasticity coefficient β (based on Eq. 2). (Middle) Plots show 1.5 years of normalized streamflow. (Bottom) Time series of normalized network length, calculated from the basin's β and the streamflow measurements from the corresponding middle panel using Eq. (1). The associated coefficients of variation of discharge and length, measured over the entire period of record (CV_Q and CV_L), are displayed as insets. Chattahoochee (column **A**) is an example of a basin with small β and small CV_Q, causing the stream network to be very stable (low CV_L). Stillwater Creek (column **D**) is an example where both β and CV_Q are high, causing a very dynamic stream network. Columns (**B**) and (**C**) both have moderately dynamic stream networks but for different reasons: Peshtigo (C) has relatively stable streamflow (small CV_Q), but its hydrogeologic properties predict high network elasticity (large β). Streamflow in Beaty Creek (B) is 5 times more variable than in Peshtigo, but its morphology predicts much lower elasticity, which stabilizes flowing stream network length to nearly match Peshtigo's CV_L.

transport capacity of the valley bottom (which will depend on its permeability, slope, and cross-sectional area). Prancevic and Kirchner (*19*) argue that downvalley changes in both water supply and subsurface transport capacity can be estimated from three topographic scaling parameters:

$$\beta = \frac{\alpha}{k_1\delta + k_2 + \theta + 1} \quad (2)$$

where k_1 = 1.6 ± 0.2 km and k_2 = −0.51 ± 0.53 are empirical constants based on β measurements from 17 basins (*1*–*5*, *22*) and α, δ, and θ are topographic scaling parameters that can be measured directly from digital elevation models (DEMs). For the 17 basins examined in that study, the root mean square error (RMSE) of β predictions from Eq. (2) was 0.12. Excluding two outlier basins, both of which are smaller than 1 km^2, the RMSE of β predictions drops to 0.04, suggesting that β, whose measured values range from 0.04 to 0.71, can be estimated with meaningful accuracy.

Each of the topographic parameters included in Eq. (2) has a mechanistic relationship to stream network dynamics. The convergence exponent α characterizes how long flowpaths need to be to achieve substantial increases in contributing drainage area. α is always positive, and larger values are characteristic of planar landscapes that tend to have more dynamic flowheads (fig. S1A). The concavity index θ measures the concavity of longitudinal stream profiles and is generally positive in stream networks [e.g., (*23*)]. Larger values of θ indicate stronger decreases in downstream gradient that can locally slow subsurface flow and stabilize flowheads (fig. S1B). The curvature coefficient δ describes how the valley-bottom curvature changes downstream. δ values are generally positive in ephemeral channel segments, where broad hillslopes transition to incised valleys, and can be considered a measure of downstream valley constriction. Larger values indicate greater constriction, which can squeeze water to the surface and make stream networks less elastic (fig. S1C).

There are several limitations to this approach of estimating stream network dynamics from Eqs. (1) and (2). Because Eq. (2) assumes that runoff is generated by first saturating the shallow subsurface, it only applies to stream network dynamics that result from shallow groundwater exfiltration. Lengthening of the stream network caused by flash flooding, in which intense rainfall exceeds surface infiltration rates, should not be modeled with Eq. (2). Similarly, stream segments in impervious terrain, including bedrock outcrops or urban landscapes, will not be well described by Eq. (2). Lastly, Eq. (1) implicitly assumes that streamflow is a proxy for landscape wetness throughout the catchment, so it should not be applied where streamflows are substantially altered by dams. Similarly, in very large basins, flow at the outlet can become decoupled from wetness in the headwaters. For these reasons, we limited our analysis to basins <10,000 km^2 in area, with less than 10% of their drainage area affected by dams.

US stream elasticity coefficients

To estimate elasticity coefficients (β) at high resolution with nearly continuous coverage across the contiguous US, we split the national 10-m DEM into 83,015 individual subcatchments using hydrologic unit code (HUC)-12 polygons and then applied Eq. (2) to each of those ~100-km^2 subcatchments (fig. S2) (*24*, *25*) (supplementary materials (SM), materials and methods; and data S1). We then averaged the resulting β values over 14,765 gauged basins, with drainage areas ranging from 1 km^2 to 10,000 km^2 (SM, materials and methods). Over 99.7% of gauged basins had average elasticity coefficients between β = 0 and β = 1 (Fig. 2B and data S2), which is similar to the range of β values that have been measured using field mapping (fig. S3) (*3*, *4*, *19*). Values of β = 0 indicate that the stream network maintains a constant length even as landscape wetness and streamflow vary (Eq. 1). Values of β = 1 indicate that changes in stream length are proportional to changes in streamflow at the outlet (Eq. 1).

Estimated elasticity coefficients β vary regionally across the US, with stream networks generally being less elastic (smaller β) in steeper terrain and more elastic (larger β) in lower-gradient terrain (Figs. 2 and 3A and fig. S2). Gentle, low-gradient landscapes are found in a variety of geomorphic settings across the US: The California Central Valley and the Ogallala

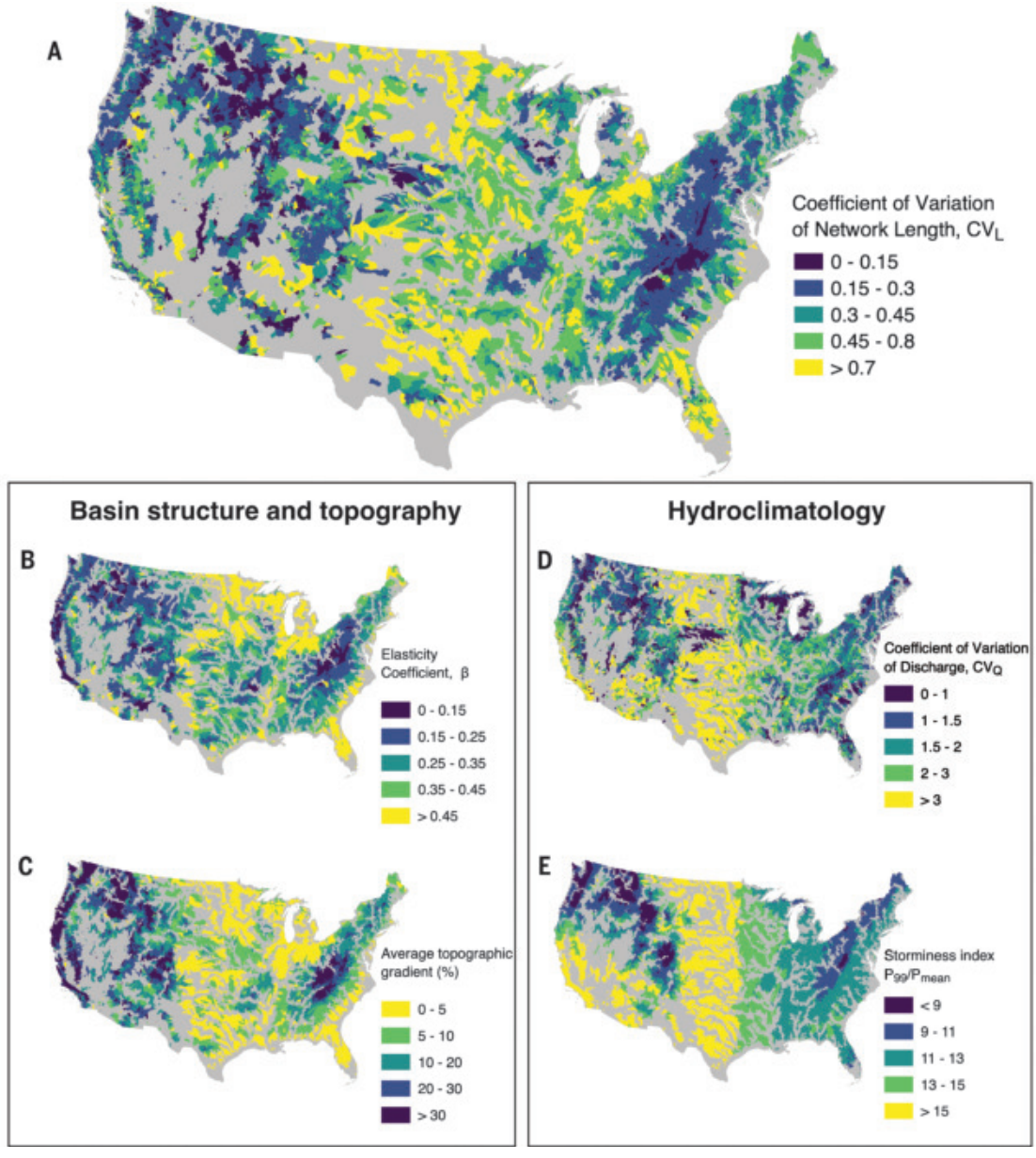


Fig. 2. Maps of stream network dynamics for 14,765 gauged stream basins. In all panels, colder colors indicate basins that have attributes of stable stream networks, whereas warmer colors indicate attributes of more dynamic stream networks. (**A**) Predicted variability of stream network length, CV_L, resulting from the combined effect of streamflow variability and network elasticity (e.g., Fig. 1). (**B**) Elasticity coefficients β as estimated from topography using Eq. (2) (see also fig. S2A for a more granular β map using HUC-12 basins). (**C**) Average topographic slope of each basin, measured from its 10-m DEM, displaying a similar spatial pattern to β as shown in (B). (**D**) Measured coefficient of variation for streamflow, CV_Q, over the period of record. Discharge is more variable in regions of greater storminess, as measured by the ratio of extreme precipitation events relative to mean precipitation, $P99/\bar{P}$ (**E**). The map of stream network length variability (A) has greater similarity to the map of network elasticity (B) than that of streamflow variability (C), suggesting that the geologic and topographic structures of basins are critical to predicting the expansion and contraction of stream networks.

megafan were formed by sediment deposition in foreland basins; Florida and the Atlantic Coastal Plain have been resurfaced by shallow marine erosion (*26*); and much of the north-central and northeastern parts of the country were resurfaced by the Laurentide Ice Sheet during the last glacial maximum (*27*) (fig. S2B). Regardless of their origins, these lower-gradient landscapes tend to have topographic properties that imply greater stream network elasticity (higher β) (Figs. 2 and 3A and fig. S2A). Values of β in low-gradient landscapes can exceed previously measured elasticity coefficients (fig. S3), which have historically only been measured directly in steeper terrain, and thus large β values (β > 0.6) should be considered an extrapolation of the calibrated model Eq. (2). In steeper terrain, topography is predominantly shaped by the competition between diffusive processes on hillslopes and fluvial incision in the valley network (*28*). This hillslope-to-valley transition leads to strong downslope gradients in cross-valley curvature (e.g., fig. S5C), thus stabilizing streamheads and leading to small β values (*19*). This transition (as measured by δ) is more pronounced in steeper terrain, giving rise to a strong correlation between β and the average topographic slope of a basin (Fig. 3A).

US stream length variability

Elasticity coefficients describe how stream network length varies with landscape wetness, as reflected in streamflow. To quantify how much streams will lengthen and shorten over time, we must scale these elasticities by the variability in streamflow. Therefore, we combined daily streamflows Q in 14,765 gauged basins with their basin-averaged elasticity coefficients β to estimate daily stream network lengths L, using Eq. (1) (Fig. 1) (data S2). For each basin, we estimated the ratio of stream network length for annual high-flow conditions relative to annual low-flow conditions by dividing the 99th-percentile length by the 1st-percentile length ($L99/L1$). The ratio of high-flow and low-flow stream lengths is typically between 1 and 10, with a median value of $L99/L1 = 4.90$ (fig. S4), meaning that that the length of a median US stream network varies by a factor of five over the course of a year; i.e., the nonperennial

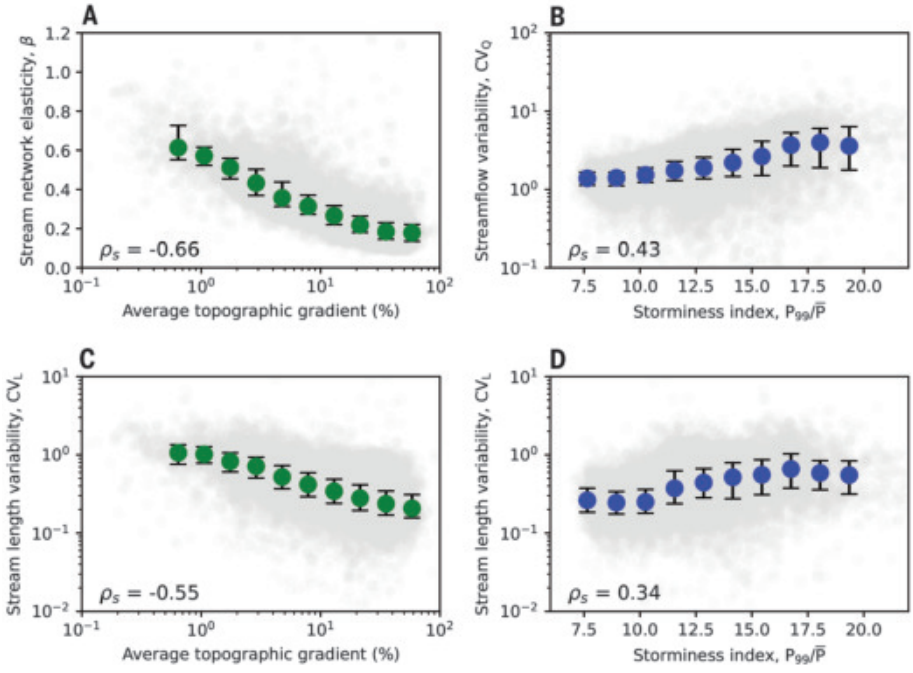


Fig. 3. Factors driving differences in stream length variability across the US. In these scatter plots, transparent gray circles indicate values for individual gauged basins, colored circles indicate binned median values, and error bars indicate the interquartile range of the binned data. Insets display the Spearman rank correlation coefficient between the plotted parameters (not their binned values) in each panel. (**A**) The elasticity coefficient β is strongly correlated with the average topographic gradient of the basin. (**B**) Streamflow variability depends, in part, on precipitation variability (storminess). Consequently, the variability of stream length in a drainage basin is correlated with the basin's topographic gradient (**C**) and storminess (**D**), with CV_L more closely related to a basin's topography than to its storminess.

fraction of the channel network varies substantially from place to place, but in most basins, the nonperennial network is many times longer than the perennial network.

We also evaluated regional variability in stream network dynamics and investigated whether those regional patterns are driven more by stream network elasticity (variability in β as reflected in topography) or hydroclimatic factors (variability in Q as resulting from precipitation patterns). The length ratio $L99/L1$ is useful and intuitive for comparing high-flow and low-flow conditions, but if streamflow vanishes at the gauge for at least 1% of the record, as it does for 3368 stream gauges, then that ratio goes to infinity and ceases to resolve the variability of stream network length. For a more robust analysis of stream network dynamics, we calculated the coefficient of variation for both streamflow and stream network length (the ratio of the standard deviation to the mean, $CV = \frac{\sigma}{\mu}$) and used those measures to evaluate regional patterns.

Maps of streamflow variability reflect climatological patterns across the US (Fig. 2, D and E). We quantified precipitation storminess of each gauged basin as the ratio of the 99th percentile daily rainfall to the average daily rainfall using PRISM (Parameter-Elevation Regressions on Independent Slopes Model) data ($P99/\bar{P}$) (*29*). Regional trends in streamflow variability are broadly consistent with regional patterns in precipitation storminess (Figs. 2, D and E, and 3B). The coefficient of variation of streamflow is high, either where precipitation and streamflow are highly variable (e.g., because of convective storms and atmospheric rivers), or in dry landscapes, where mean streamflow is low. Conversely, streamflows have smaller coefficients of variation in more humid regions and those with more consistent rainfall, including the East Coast, the Pacific Northwest, and the Upper Midwest.

Maps of the variability of flowing stream length (Fig. 2A) show the combined effects of variability in landscape wetness (Fig. 2D) and stream network elasticity (Fig. 2B). Across the country, stream network elasticity varies substantially, as does the temporal variability in streamflow (a proxy for variation in landscape wetness), and both contribute significantly to regional patterns in stream network length variability. Much of the eastern US—including Florida, the East Coast, and the Appalachian Mountains—exhibits similar degrees of streamflow variability (Fig. 2A) but also exhibits strong contrasts in stream network elasticity (Fig. 2B) due to contrasts in topographic form (mountains versus coastal plains). Consequently, in this region, spatial patterns of stream network dynamics (Fig. 2C) predominantly reflect differences in elasticity between basins. By contrast, stream networks along the West Coast have similar elasticities, but streamflow variability differs substantially across the region, driving large differences in the variability of stream network length. Across the nation as a whole, both network elasticity and streamflow variability strongly influence the variability of stream network length, and thus CV_L is strongly correlated with both topography and climate (Fig. *3*).

Outlook

Our results show that a basin's topography and subsurface structure, and thus its network elasticity, are at least as important as climatological factors for predicting how much flowing streams will lengthen and shorten. The values of stream-length variability presented here can be used to better understand how much the extents of aquatic habitats may vary over time (*14*, *15*) or to more accurately predict biogeochemical cycling over continental scales (*11*–*13*, *17*). These results also provide a foundation to forecast how different climate scenarios may alter stream networks. For example, if climate predictions imply substantial increases in storminess, the values of stream network elasticity presented here can be used to estimate the consequences for stream network dynamics. Such an analysis would require long-term forecasts of streamflow statistics to couple with β values, and such datasets are just beginning to emerge (*30*). Although our results are limited to the continental US (Fig. 2), our analysis only requires reliable digital elevation models and streamflow data and thus could be more widely applied.

Conclusions

There is growing recognition that flowing stream networks are dynamic features of the landscape, but quantifying their extension and retraction over time has required laborious field mapping under different flow conditions. Our results illustrate how the growth and decay of stream networks can be estimated using only topographic analysis and stream gauge data. Our compilation of such estimates for most of the gauged basins in the continental US reveals regional differences in stream network dynamics that are driven by variations in both hydroclimatology and network elasticity. Our results further indicate that variations in network elasticity are at least as important as variations in landscape wetness in explaining regional patterns in stream network dynamics across the continental US.

REFERENCES AND NOTES

1. M. C. Roberts, P. C. Klingeman, in *22nd International Geographical Congress*, Montreal, Canada, 25 July to 5 September, 1972 (Univ. of Toronto Press, 1972), pp. 189–191.

2. S. M. Lovill, W. J. Hahm, W. E. Dietrich, *Water Resour. Res.* **54**, 5702–5726 (2018).
3. C. K. Jensen, K. J. McGuire, P. S. Prince, *Hydrol. Processes* **31**, 3350–3363 (2017).
4. J. A. Whiting, S. E. Godsey, *Hydrol. Processes* **30**, 2305–2316 (2016).
5. S. E. Godsey, J. W. Kirchner, *Hydrol. Processes* **28**, 5791–5803 (2014).
6. D. G. Day, *J. Hydrol.* **22**, 3–17 (1983).
7. K. J. Gregory, D. E. Walling, *Hydrol. Sci. J.* **13**, 61–68 (1968).
8. K. Blyth, J. C. Rodda, *Water Resour. Res.* **9**, 1454–1461 (1973).
9. D. von Schiller, S. Bernal, C. N. Dahm, E. Martí, *Nutrient and Organic Matter Dynamics in Intermittent Rivers and Ephemeral Streams* (Elsevier, 2017).
10. K. L. Jaeger, N. A. Sutfin, S. Tooth, K. Michaelides, M. Singer, *Geomorphology and Sediment Regimes of Intermittent Rivers and Ephemeral Streams* (Elsevier, 2017).
11. T. J. Battin *et al*., *Nature* **613**, 449–459 (2023).
12. M. A. Zimmer, B. L. McGlynn, *Water Resour. Res.* **54**, 1576–1598 (2018).
13. A. K. Aufdenkampe *et al*., *Front. Ecol. Environ.* **9**, 53–60 (2011).
14. A. Clarke, R. Mac Nally, N. Bond, P. S. Lake, *Freshw. Biol.* **53**, 1707–1721 (2008).
15. R. Stubbington *et al*., in *Intermittent Rivers and Ephemeral Streams: Ecology and Management*, T. Datry, N. Bonada, A. Boulton, Eds. (Elsevier, 2017), pp. 217–243.
16. G. H. Allen *et al*., *Nat. Commun.* **9**, 610 (2018).
17. J. P. Benstead, D. S. Leigh, *Nat. Geosci.* **5**, 678–679 (2012).
18. A. Dai, T. Qian, K. E. Trenberth, J. D. Milliman, *J. Clim.* **22**, 2773–2792 (2009).
19. J. P. Prancevic, J. W. Kirchner, *Geophys. Res. Lett.* **46**, 2084–2092 (2019).
20. A. S. Ward, N. M. Schmadel, S. M. Wondzell, *Adv. Water Resour.* **114**, 64–82 (2018).
21. C. K. Jensen, K. J. McGuire, Y. Shao, C. Andrew Dolloff, *Earth Surf. Process. Landf.* **43**, 2762–2778 (2018).
22. S. B. Shaw, *Hydrol. Processes* **30**, 479–492 (2016).
23. J. J. Flint, *Water Resour. Res.* **10**, 969–973 (1974).
24. D. B. Gesch, G. A. Evans, M. J. Oimoen, S. Arundel, in *Digital Elevation Model Technologies and Applications: The DEM Users Manual*, D. Maune, A. Nayegandhi, Eds. (American Society for Photogrammetry and Remote Sensing, ed. 3, 2018), pp. 83–110.
25. L. McKay, T. Bondelid, C. Johnston, R. Moore, A. Rea, NHDPlus Version 2: User guide (US Environmental Protection Agency, 2012); https://www.epa.gov/waterdata/nhdplus-national-data.
26. K. G. Miller, G. S. Mountain, B. Tucholke, *Geology* **13**, 10–13 (1985).
27. D. E. Sugden, *Arct. Alp. Res.* **9**, 21–47 (1977).
28. J. T. Perron, P. W. Richardson, K. L. Ferrier, M. Lapôtre, *Nature* **492**, 100–103 (2012).
29. PRISM Climate Group, PRISM Climate Data (Oregon State Univ., 2014); https://prism.oregonstate.edu.
30. O. V. Müller, P. C. McGuire, P. L. Vidale, E. Hawkins, *Hydrol. Earth Syst. Sci.* **28**, 2179–2201 (2024).

ACKNOWLEDGMENTS

Funding: J.P.P. was funded by Swiss National Science Foundation Postdoc.Mobility grant P400P2-183929. **Author contributions:** Conceptualization: J.P.P., H.S., J.W.K.; Methodology: J.P.P., H.S., J.W.K.; Investigation: J.P.P., H.S.; Visualization: J.P.P., H.S., J.W.K.; Supervision: J.W.K.; Writing – original draft: J.P.P.; Writing – reviewing & editing: J.P.P., H.S., J.W.K. **Competing interests:** The authors declare that they have no competing interests. **Data and materials availability:** All data presented in Figs. 2 and 3 are included in data S2. Data presented in fig. S2 are included in data S1. Corresponding geospatial polygons for HUC basins (data S1) and gauged drainage basins (data S2) can be downloaded at http://www.hydroshare.org/resource/d4b4922f81c44ccabfd2753111fbfad2. **License information:** Copyright © 2025 the authors, some rights reserved; exclusive licensee American Association for the Advancement of Science. No claim to original US government works. https://www.science.org/about/science-licenses-journal-article-reuse

SUPPLEMENTARY MATERIALS

science.org/doi/10.1126/science.ado2860
Materials and Methods
Figs. S1 to S5
Table S1
Data S1 and S2
References (*31*–*42*)

Submitted 7 February 2024; accepted 14 January 2025
10.1126/science.ado2860

QUANTUM MATERIALS

Good plasmons in a bad metal

Francesco L. Ruta[1,2]*, Yinming Shao[1], Swagata Acharya[3], Anqi Mu[1], Na Hyun Jo[4,5], Sae Hee Ryu[4], Daria Balatsky[6,7]†, Yifan Su[1], Dimitar Pashov[8], Brian S. Y. Kim[1,9]‡, Mikhail I. Katsnelson[10], James G. Analytis[7,11,12], Eli Rotenberg[4], Andrew J. Millis[1,13], Mark van Schilfgaarde[3,14], D. N. Basov[1]*

Correlated metals may exhibit unusually high resistivity that increases linearly in temperature, breaking through the Mott-Ioffe-Regel bound, above which coherent quasiparticles are destroyed. The fate of collective charge excitations, or plasmons, in these systems is a subject of debate. Several studies have suggested that plasmons are overdamped, whereas other studies have detected propagating plasmons. In this work, we present direct nano-optical images of low-loss hyperbolic plasmon polaritons (HPPs) in the correlated van der Waals metal $MoOCl_2$. HPPs are plasmon-photon modes that waveguide through extremely anisotropic media and are remarkably long-lived in $MoOCl_2$. Photoemission data presented here reveal a highly anisotropic Fermi surface, reconstructed and made partly incoherent, likely through electronic interactions as explained by many-body theory. HPPs remain long-lived despite this, revealing previously unseen imprints of many-body effects on plasmonic collective modes.

Electrons may experience a breakdown of quasiparticle coherence in metals with substantial electron-electron interactions (*1*), leading to mean free paths shorter than the interatomic spacing: the so-called Mott-Ioffe-Regel limit (*2*). The conceptual breakdown of an electronic mean free path of Bloch states at well-defined energy and momentum is accompanied by nonsaturating, linear-in-temperature resistivity with frequency-dependent scattering (*3*, *4*). This phenomenology has been broadly observed across high–critical temperature (T_c) superconductors (*5*), density wave materials (*6*), and heavy-electron systems (*7*). One might naively expect for collective modes, or plasmons, of correlated electrons to likewise propagate short distances. Results on this topic are mixed, however. Some studies suggest that a quantum critical continuum extends to all frequencies and momenta (*8*), explaining observations of overdamped plasmons in non–Fermi-liquid systems (*9*, *10*). Other experiments detected well-defined propagating plasmons qualitatively explained by noninteracting theories (*11*, *12*), arguing that long-wavelength plasmons are less sensitive to local correlations.

In this work, we present direct nano-optical images of low-loss hyperbolic plasmon polaritons (HPPs) in the correlated metal $MoOCl_2$. HPPs are waveguiding plasmon-photon modes in materials with oppositely signed dielectric tensor components (*13*, *14*). HPPs tend to be very lossy (*15*, *16*) relative to their phononic analogs (*17*–*19*). Unexpectedly, we found that HPPs in $MoOCl_2$ can propagate for several micrometers, up to about 10 cycles at room temperature—breaking records for HPP lifetimes and rivaling graphene surface plasmons (*20*)—without electrostatic gating or chemical doping. Furthermore, $MoOCl_2$ is found to have an ultrabroad hyperbolic band that spans the near-infrared and visible spectrum, so HPPs can be studied in previously inaccessible frequency regimes.

$MoOCl_2$ belongs to the oxychloride family of van der Waals materials, which is generally characterized by weak interlayer coupling and lattice distortions, enabling exotic anisotropic physics (*21*–*23*). In the case of $MoOCl_2$, an orbital-selective Peierls distortion produces one-dimensional dimerized Mo chains, rendering Mo-d_{xy} bands essentially dispersionless and splitting them away from the Fermi surface (FS), whereas $d_{xz/yz}$ bands disperse through the Fermi level E_F but with strong in-plane anisotropy (*24*). Computational studies have suggested that this electronic structure gives $MoOCl_2$ optical hyperbolicity with interband transitions pushed to higher energies (*25*), enabling HPPs (*26*). Furthermore, transport studies (*27*) indicate that $MoOCl_2$ may be regarded as a "bad" metal, with appreciable electron-electron interactions. Its poor room-temperature resistivity

[1]Department of Physics, Columbia University, New York, NY, USA. [2]Department of Applied Physics and Applied Mathematics, Columbia University, New York, NY, USA. [3]National Renewable Energy Laboratory, Golden, CO, USA. [4]Advanced Light Source, E.O. Lawrence Berkeley National Laboratory, Berkeley, CA, USA. [5]Department of Physics, University of Michigan, Ann Arbor, MI, USA. [6]Department of Chemistry, University of California, Berkeley, CA, USA. [7]Department of Physics, University of California, Berkeley, CA, USA. [8]Theory and Simulation of Condensed Matter, King's College London, London, UK. [9]Department of Mechanical Engineering, Columbia University, New York, NY, USA. [10]Institute for Molecules and Materials, Radboud University, Nijmegen, Netherlands. [11]CIFAR Quantum Materials, Toronto, ON, Canada. [12]Kavli Energy Nanoscience Institute, Berkeley, CA, USA. [13]Center for Computational Quantum Physics, Flatiron Institute, New York, NY, USA. [14]Department of Physics, University of Colorado, Boulder, CO, USA.
***Corresponding author. Email: fr2441@columbia.edu (F.L.R.); db3056@columbia.edu (D.N.B.)**
†Present address: Alga Biosciences, San Francisco, CA, USA.
‡Present address: Department of Materials Science and Engineering, University of Arizona, Tucson, AZ, USA.

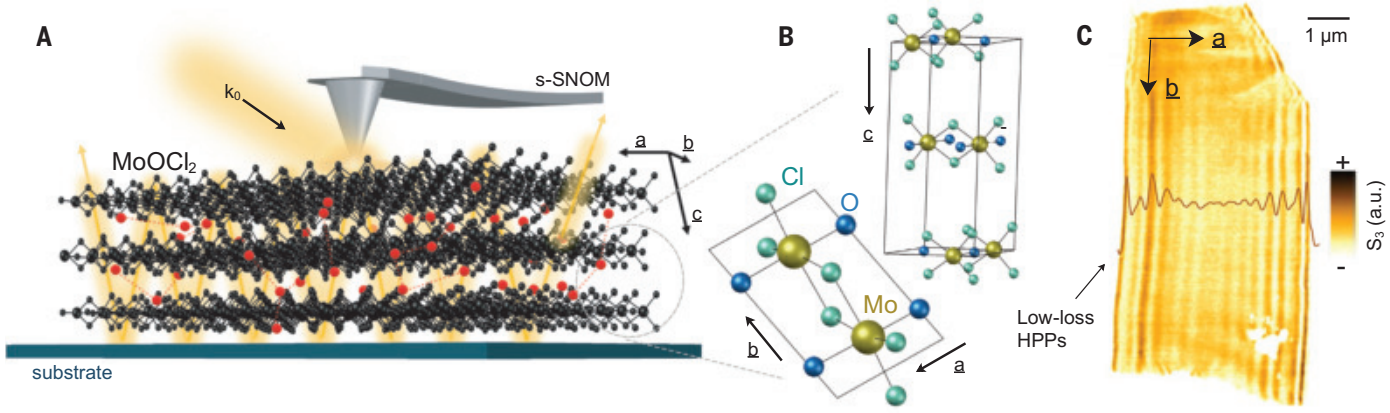


Fig. 1. Hyperbolic plasmon polaritons in $MoOCl_2$. (**A**) Experiment schematic showing cantilever and tip of a scattering-type s-SNOM scanning a metallic slab of $MoOCl_2$. Free-space light with momentum $k_0 = \omega/c$ scatters off the s-SNOM tip, exciting hyperbolic plasmon polaritons: waveguiding quasiparticles composed of light and electrons. (**B**) Bulk $MoOCl_2$ *C2/m* crystal structure showing Peierls-distorted cell with Mo dimers along *b* axis below. (**C**) Near-field amplitude (ω = 1.312 eV) image of an 18-nm-thick $MoOCl_2$ microcrystal. Several unidirectional interference fringes attributable to low-loss hyperbolic plasmon polaritons (HPPs) are observed.

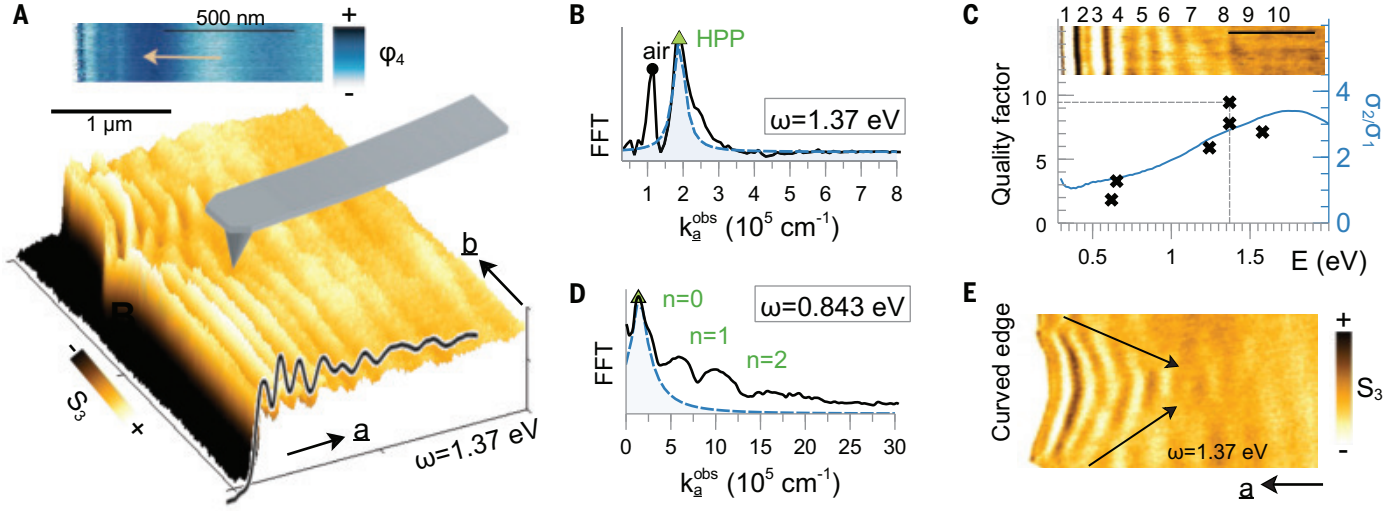


Fig. 2. Properties of hyperbolic plasmon polaritons. (**A**) Near-field amplitude image of a 30 nm $MoOCl_2$ microcrystal showing low-loss propagation of hyperbolic plasmon polaritons (HPPs) along the *a* axis. (Inset) A near-field phase image displaying ultraconfined higher-order modes in real-space. (**B**) FFT spectrum at ω = 1.37 eV showing HPP and air mode peaks. Complex momenta are extracted from Lorentzian fits (dashed blue line). (**C**) HPP quality factors $Q = \mathrm{Re}k/\mathrm{Im}k$ reach ~10 and have strong energy dependence as expected from optical conductivity ratio (blue line). (Inset) Highest-quality image showing ten fringes. Scale bar, 1 μm. (**D**) FFT spectrum of complex near-field profile with ω = 0.843 eV. Three dispersive peaks (dotted line) correspond to fundamental (n = 0) and higher-order (n = 1, 2) HPPs. (**E**) Planar focusing of HPPs at a curved edge.

corresponds to a sheet resistance per plane of ~8.5 kilohms, which is twice the resistance quantum $h/e^2 \approx 4$ kilohms (where h is the reduced Planck's constant and e is the charge on the electron), and $MoOCl_2$ exhibits colossal nonsaturating magnetoresistance along with T^2 behavior, transitioning to T-linear transport above 133 K.

In this context, the record-breaking HPP lifetimes in $MoOCl_2$ are even more noteworthy: We found that a metal with high electrical resistivity supports HPPs with lower damping than previously seen in "good" metals with low resistivity. In this work, we used HPPs to probe the intraband electrodynamics of $MoOCl_2$ and unravel this paradox. First, we discovered that the HPP dispersion differs from predictions by noninteracting theories. Angle-resolved photoemission spectroscopy (ARPES) interpreted with quasiparticle self-consistent *GW* (QS*GW*) theory revealed incoherent $d_{xz/yz}$ bands. The observed HPP dispersion can be explained by calculating optics of an incoherent $MoOCl_2$ electronic structure. Last, reconciling the high-frequency dielectric function implied by HPPs with transport measurements requires strongly frequency-dependent scattering, which partially accounts for apparent conflicts between plasmons and transport.

Optical imaging and spectroscopy

To access subdiffractional HPPs, we used a scattering-type scanning near-field optical microscope (s-SNOM). A schematic of the experiment is shown in Fig. 1A, in which a metallic s-SNOM tip was illuminated by laser light with wave vector k_0. The tip launches waveguiding HPPs with wave vector k that reflect or

transmit at the edge of a $MoOCl_2$ crystal (Fig. 1B) and then outcouple to far-field. Outcoupled modes will interfere with tip- or edge-scattered light, creating standing wave fringes in real-space scans. A room-temperature s-SNOM image of a thin $MoOCl_2$ microcrystal is shown in Fig. 1C. Subdiffractional interference fringes attributed to propagating HPPs extend unidirectionally across the entire span of the crystal, highlighting their low damping.

We quantified HPP lifetimes and verified that HPPs display the distinctive features of hyperbolic modes (Fig. 2). The edge of a 30-nm-thick $MoOCl_2$ microcrystal was imaged under illumination by a near-infrared laser with photon energy ω = 1.37 eV (Fig. 2A). The near-field amplitude shows interference fringes with multiple periodicities corresponding to a superposition of air modes, free-space standing waves between tip and sample, and tip-launched HPPs. The corresponding fast Fourier transform (FFT) spectrum is shown in Fig. 2B. By fitting Lorentzian parameters to the HPP peak (Fig. 2B, dashed line) or simply counting fringes in real-space images (Fig. 2C), we could extract the quality factor Q = Re k/Im k (*28*), which expresses the number of propagation cycles above the noise floor. We counted 10 fringes and estimated Q = 9.45. Similar quality was measured between ω = 1.305 and 1.771 eV, reducing at lower energy, at which the fringe wavelength also increases substantially. Energy dependence of the quality factor tracks the ratio of imaginary to real optical conductivity, σ_2/σ_1 (Fig. 2C, blue line).

In contrast to evanescent surface plasmons, HPPs behave like waveguide modes, with strong thickness dependence and infinite higher-order branches (*16*, *18*). Near-field line profiles from samples with thicknesses d = 10 to 40 nm are shown in fig. S1. HPP fringe wavelengths shorten, or increase momentum k, with decreasing thickness, which is characteristic of hyperbolic modes (*16*, *18*, *19*). FFT amplitudes of complex near-field profiles at ω = 0.620 to 1.033 eV are shown in Fig. 2D. Three dispersive peaks were detected, corresponding to fundamental (n = 0) and higher-order (n = 1, 2) HPP modes. n = 2 HPPs reached confinement factors k/k_0 ~ 10 in our experiments, which is an order of magnitude tighter than other reported near-infrared modes (*29*, *30*). Last, HPP wavefronts at a curved edge, demonstrating planar focusing, are shown in Fig. 2E. In-plane hyperbolic phonon polaritons exhibit similar behavior (*31*), which can be explained with Huygen's principle (fig. S2).

The appearance of HPPs can be understood by studying the dielectric tensor of $MoOCl_2$, which can be extracted from Fourier transform infrared (FTIR) spectroscopy (*28*). Bulk $MoOCl_2$ is monoclinic (space group $C2/m$), with lattice parameters a = 3.755 Å, b = 6.524 Å, c = 12.721 Å, and β = 104.86° (*27*), which permits anisotropy between diagonal dielectric tensor components. Shown in Fig. 3A are room-temperature FTIR reflectance spectra on bulk $MoOCl_2$ for light polarized along the orthogonal in-plane a and b axes. Reflectance data show intraband responses and the onset of interband transitions, which can be well fit by an anisotropic Drude-Lorentz model. The

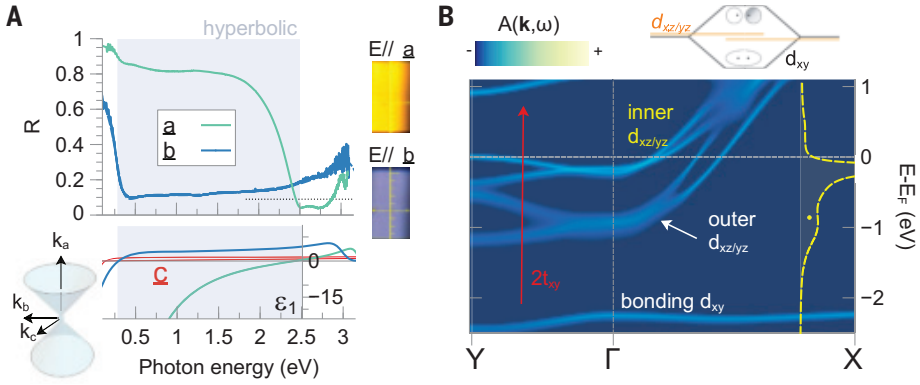


Fig. 3. Dielectric function and electronic structure of $MoOCl_2$. (**A**) (Top) Polarization-resolved $MoOCl_2$ reflectance spectra reveal large plasma frequency anisotropy, enabling (bottom) a wide hyperbolic window where $\varepsilon_1^a\varepsilon_1^b < 0$ and $\varepsilon_1^a\varepsilon_1^c < 0$ so that (left inset) the isofrequency surface is hyperboloidal. Hyperbolicity extends into the visible spectrum, attested to by (right inset) optical anisotropy observable by eye and polarizer. (**B**) Theoretical spectral function $A(\mathbf{k}, \omega)$ showing outer Mo-$d_{xz/yz}$ bands becoming more incoherent at higher binding energy (white arrow). Inner $d_{xz/yz}$ bands have an incoherent shoulder (yellow dot). (Inset) Peierls distortion causes large bonding-antibonding splitting of d_{xy} band (red arrow, $2t_{xy}$ = 2.8 eV), whereas $d_{xz/yz}$ have weaker bonding character.

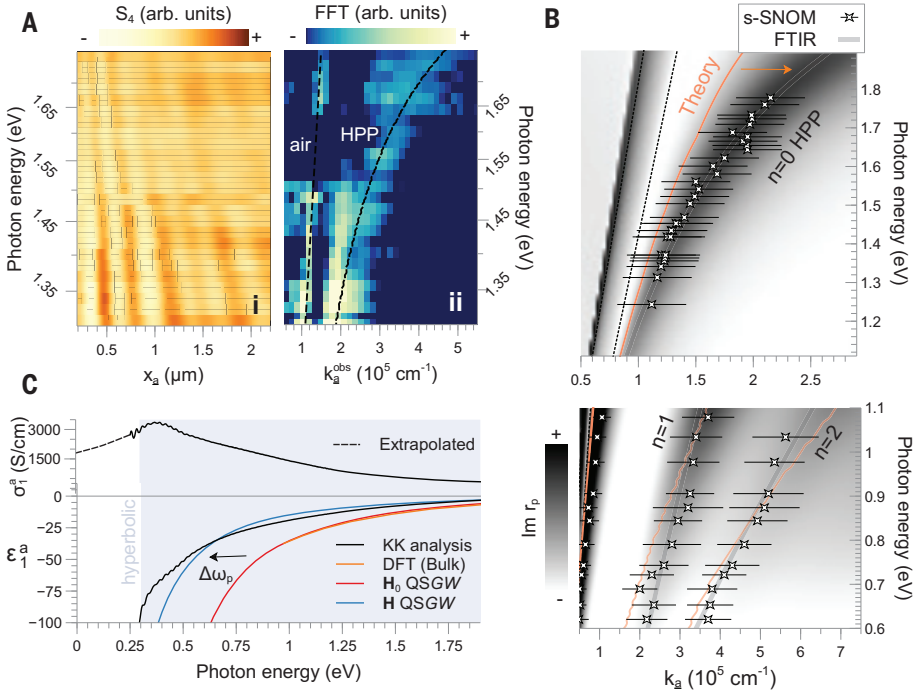


Fig. 4. Electronic interactions renormalize hyperbolic plasmon dispersion. (**A**) (i) Averaged a axis near-field amplitude profiles and (ii) corresponding FFTs for ω = 1.305 to 1.771 eV. FFT spectra show vacuum light cone (air) and fundamental (n = 0) HPP dispersions. Dashed black lines are guides to the eye. (**B**) Geometry-corrected HPP momenta k (error bars are rescaled FFT full widths at half maxima) overlaid on dispersions calculated with FTIR optical constants (gray) and noninteracting theory (orange). Colormap is Imr_p loss function. Observed plasmon dispersion is renormalized to higher momenta compared with noninteracting calculations (orange arrow). Low-energy data with n = 1, 2 higher-order modes agree with calculated dispersions. (**C**) Plasma frequency ω_p^a obtained from Kramers-Kronig (KK) analysis (black) of measured reflectance and many-body theory (**H** QSGW, blue) is reduced relative to noninteracting theories (DFT, orange, and quasiparticalized GW, **H**$_0$ QSGW, red). Extrapolating real a axis optical conductivity to static value forces shifting of Drude peak.

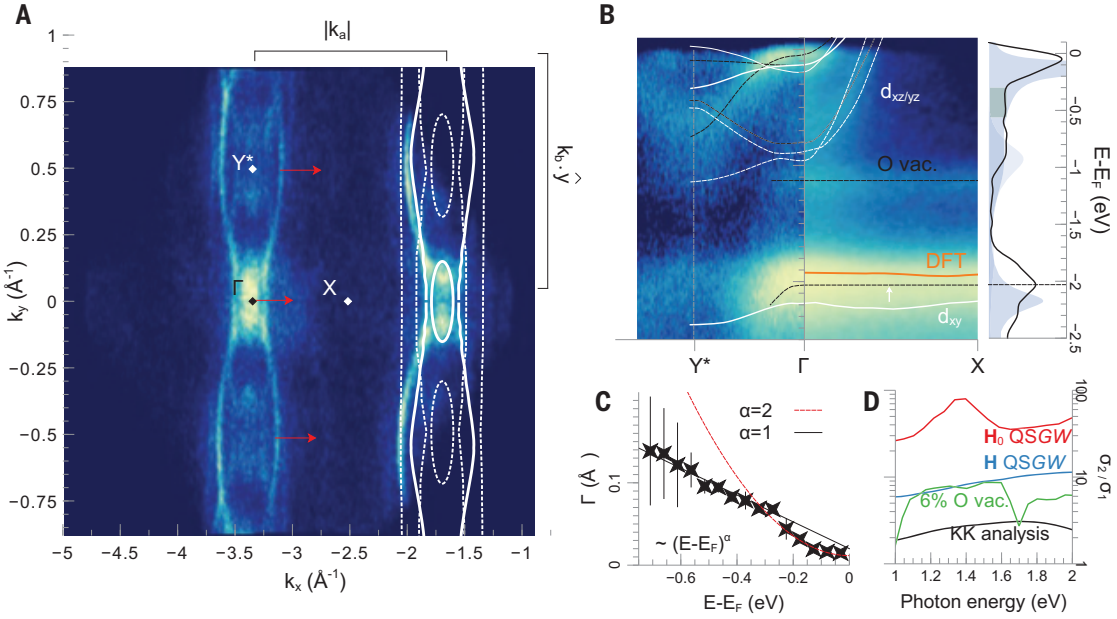


Fig. 5. Angle-resolved photoemission spectroscopy of $MoOCl_2$. (**A**) Fermi surfaces measured with ARPES at T = 11 K. White lines are guides to the eye. Prominent open and closed Fermi surface orbits indicated by the solid white lines are inner $d_{xz/yz}$ bands. Faded bands and Y^* pockets indicated with dashed white lines are outer $d_{xz/yz}$ bands. Faint replica bands are shifted by ~0.3 Å^{-1} (red arrows). (**B**) ARPES (black) and QSGW (white) band dispersions along $\Gamma - X$ and $\Gamma - Y^*$. DFT (orange) underestimates energy of the d_{xy} bonding band (−2 eV). Nondispersive −1 eV band likely comes from localized oxygen vacancy states. (Right) Spectral function (blue) overlaid on photoemission intensity in region without −1 eV band (black). (**C**) Momentum distribution curve analysis at k_y = −0.5 Å^{-1} reveals nonlinearities in energy dependence of $d_{xz/yz}$ linewidths. (**D**) Computed quality factors in interacting theory (blue) and noninteracting theory with (green) and without (red) oxygen vacancies.

model dielectric function $\varepsilon^{\alpha} = \varepsilon_1^{\alpha} + i\varepsilon_2^{\alpha}$ along the $\alpha \in \{a, b\}$ axis is

$$\varepsilon^{\alpha}(\omega) = \varepsilon_{\infty}^{\alpha} - \frac{\left(\omega_{\mathrm{p}}^{\alpha}\right)^2}{\omega^2 + i\gamma^{\alpha}\omega} + \sum_n \frac{f_n^{\alpha}}{\left(\omega_n^{\alpha}\right)^2 - \omega^2 - i\gamma_n^{\alpha}\omega} \quad (1)$$

where the plasma frequency ω_{p} describes oscillations of the electron density, ε_{∞} is the high-frequency permittivity, f_n are oscillator strengths, ω_n are resonance energies, and γ_n are scattering rates. We focused on room-temperature results because dielectric functions do not change substantially with temperature (fig. S3). Anisotropy of ω_{p} is the primary driver of hyperbolicity in $MoOCl_2$, causing ε_1^a to go negative whereas ε_1^b and ε_1^c stay positive (Fig. 3A, bottom) over ω = 0.3 to 2.45 eV. In this range, $MoOCl_2$ is a quasi–one-dimensional metal: It has a hyperboloidal isofrequency surface (Fig. 3A, left inset) that constrains propagation of high-momentum extraordinary electromagnetic waves to a conoid around the a axis. Plasmon polaritons will thus display waveguiding hyperbolic wavefronts. The hyperbolic band extends to visible frequencies (Fig. 3A, dotted line) so that even the human eye can detect optical anisotropy with the help of polarizers (Fig. 3A, right inset). Moreover, interband transitions do not appear until ω > 2.5 eV, so that dielectric losses from interband transitions are suppressed within the hyperbolic band. And estimated intraband losses are lower than previously observed in this frequency range (fig. S4), enabling low-loss propagation of HPPs.

Electronic and plasmonic dispersions

The large optical anisotropy in $MoOCl_2$ originates in part from an orbital-selective Peierls distortion (*24*). Mo is in the d^2 electronic configuration. In its MoO_6 edge-sharing octahedral environment, the d_{xy} orbital is occupied by one electron, and $d_{xz/yz}$ orbitals share the other. The d_{xy} orbital in such a crystal field environment forms a one-dimensional chain (Mo–Mo dimer) along the b axis and a singlet in the b-c plane. Mo–Mo bonds are strongly distorted from dimerization: Intra- and interdimer bond lengths are 2.7792 and 3.73648 Å^{-1}, respectively. As a consequence, the d_{xy} band, which would cross E_{F} along $\Gamma - Y$ in the undistorted state, picks up strong bonding-antibonding character and splits off from the FS. Meanwhile, intradimer hopping between $d_{xz/yz}$ orbitals is too small to form a molecular orbital. $d_{xz/yz}$ bands thus have weaker bonding-antibonding character and still disperse strongly through E_{F} along $\Gamma - Y$, giving $MoOCl_2$ global metallic behavior in transport (*27*).

The $MoOCl_2$ spectral function $A(\mathbf{k}, \omega)$ is shown in Fig. 3B, calculated by using QSGW (*28*)

$$A(\mathbf{k}, \omega) = -\frac{1}{\pi}\mathrm{Im}[\omega + \mu - \mathbf{H}_0(\mathbf{k}) - \Sigma(\mathbf{k}, \omega)]^{-1} \quad (2)$$

where μ is the chemical potential, $\mathbf{H}_0$ is the one-particle Hamiltonian with the static self-energy Σ_0, and $\Sigma(\mathbf{k}, \omega)$ is the dynamical part of the self-energy. $A(\mathbf{k}, \omega)$ shows flat d_{xy} bands split by $2t_{xy}$ = 2.8 eV (Fig. 3B, red arrow), whereas dispersive $d_{xz/yz}$ bands cross E_{F}. QSGW bands qualitatively resemble noninteracting density functional theory (DFT) eigenvalues, modulo a larger $2t_{xy}$ (fig. S5). However, in contrast to DFT, QSGW is a many-body approach capable of incorporating the long-range nature of charge scattering. Re Σ accounts for energy- and momentum-dependent mass renormalization, whereas the imaginary part contributes to quasiparticle lifetimes and spectral weight redistribution. When including many-body effects beyond the quasiparticle approximation into Σ, $d_{xz/yz}$ bands display some degree of incoherence—spectral broadening through Im Σ. The outer $d_{xz/yz}$ bands broaden as they move away from E_{F} (Fig. 3B, white arrow). Inner $d_{xz/yz}$ bands also broaden (fig. S6); in particular, their spectral peaks develop a characteristic shoulder (Fig. 3B, yellow dot). The quasiparticle weight $Z = (1 - d\mathrm{Re}\Sigma/d\omega)^{-1}$ of $d_{xz/yz}$ bands, representing the overlap between interacting and noninteracting wavefunctions, is ~0.5.

Plasmons serve as highly sensitive, self-referenced probes of intraband electrodynamics (*16*, *20*). We refined our optical parameters by testing our model dielectric function against the near-field HPP dispersion in addition to FTIR spectroscopy. Plasmon momenta k can be extracted from observed fringe momenta k^{obs} by applying geometrical corrections (supplementary text, section S1). Shown in Fig. 4A are (i) averaged near-field profiles with ω = 1.305-1.771 eV and (ii) corresponding FFTs displaying two dispersive peaks (Fig. 4A, black dashed lines). Low-momenta peaks correspond to background air modes at the vacuum light cone. Higher-k^{obs} peaks are attributed to the fundamental HPP. The two HPP branches below

1.5 eV (fig. S7) correspond to different paths taken by HPPs to the detector. HPPs were observed to the ends of our near-infrared laser range, only disappearing at mid-infrared energies (fig. S8), which confirms the ultrabroadband hyperbolicity of $MoOCl_2$.

As shown in Fig. 4B, we computed the HPP dispersion $k_a(\omega)$ using the a axis FTIR dielectric function and our theoretical ε^c. Geometry-corrected k (Fig. 4B, stars) are overlaid on the calculated dispersion, showing reasonable agreement. $k_a(\omega)$ computed from the optics of a noninteracting electronic structure (Fig. 4B, orange line), however, systematically underestimates observed plasmon momenta at higher energies. This result was reproduced on several samples (fig. S9). At lower energies, high-order $n = 1, 2$ modes were mostly sensitive to ε^c and showed good agreement with theoretical ε^c. To build intuition, we considered a simplified model for the HPP dispersion (supplementary text, section S3)

$$k_a(\omega) = -\frac{2}{d}\left[1-\left(\frac{\omega_p^a}{\omega}\right)^2\right]^{-\frac{1}{2}} \times \operatorname{arctanh}\left[1-\left(\frac{\omega_p^a}{\omega}\right)^2\right]^{-\frac{1}{2}} \quad (3)$$

Because k_a and ω_p^a are inversely proportional, the HPP renormalization can be attributed to a reduced plasma frequency. Plotting ε_1 in Fig. 4C, the $\sim(\omega_p^a/\omega)^2$ decay of noninteracting theories (quasiparticalized $\mathbf{H}_0$ QSGW and DFT) implies $\omega_p^a \approx 6.4$ eV. $\omega_p^a \approx 5.9$ eV may also be obtained directly from the electronic structure (*28*). By contrast, Kramers-Kronig analysis (Fig. 4C, black line) of the FTIR spectrum, which also fits the HPP momenta, implies $\omega_p^a \approx 5$ eV (supplementary text, section S2).

Electronic structure from photoemission spectroscopy

To gain insight into mechanisms behind the HPP renormalization, we performed ARPES (*28*). Fermi surfaces in the third and second Brillouin zones and electronic band dispersions measured at $T = 11$ K are shown in Fig. 5, A and B, respectively. One closed and one open FS orbit can be clearly observed around Γ (Fig. 5, A and B, solid white lines) corresponding to the inner $d_{xz/yz}$ bands. Fermi surfaces corresponding to outer $d_{xz/yz}$ bands are less prominent but may be observed around $k_y = \pm 0.5$ Å^{-1}, along with faint pockets around Y^* (Fig. 5, A and B, dotted white lines). Further, a faint FS replica can be observed along the k_x shifted by ~0.3 Å^{-1} (Fig. 5A, red arrows). Replicas appearing on either side of the FS with half the bandwidth of the $d_{xz/yz}$ band are shown in fig. S10. Last, the –1 eV flat band likely corresponds to localized oxygen vacancy states (*32*) along the direction reciprocal to the Mo–O bond (fig. S11).

Many-body effects enhanced bonding-antibonding splitting and introduced some degree of incoherence. The measured d_{xy} bonding band energy (–2 eV) was below the DFT prediction (Fig. 5B, orange line). QSGW (Fig. 5B, white line) puts the bonding band even below the measurement, but accounting for the excitonic vertex (*33*) would likely bring band energies into agreement. Furthermore, incoherence effects seen in the QSGW spectral function $A(\mathbf{k}, \omega)$ were also apparent in ARPES. In Fig. 5B, right, we overlaid the calculated Γ-point spectral function (Fig. 5B, blue) onto measured photoemission intensity (Fig. 5B, black). Spectral weight observed between –0.3 and –0.6 eV (Fig. 5B, green) cannot be attributed to any coherent band but corresponds closely to the shoulders of incoherent inner $d_{xz/yz}$ bands. As further evidence, the inner $d_{xz/yz}$ band linewidth (fig. S12) broadens to higher binding energy, with a distinctive kink at –0.275 eV (Fig. 5C), marking a sudden change in coherence (*34*). Also, the Y^* pockets observed in ARPES appear in $A(\mathbf{k}, \omega)$ at E_F (fig. S13) but not band calculations, suggesting that incoherent spectra below E_F are leaking onto the FS. Last, outer $d_{xz/yz}$ bands (Fig. 5, A and B, dotted white lines) are weaker than inner $d_{xz/yz}$ bands (Fig. 5, A and B, solid white lines), which is consistent with fig. S13. However, the outermost $d_{xz/yz}$ band is sometimes not as weak (fig. S14), which suggests that photoemission matrix element effects are partly responsible for this contrast.

We can account for incoherence revealed with ARPES into our optics calculations by convolving our spectral function $A(\mathbf{k}, \omega)$ with Fermi velocities (*35*). As shown in Fig. 4C, ε_1^a calculated with many-body interactions (Fig. 4C, blue line, $\mathbf{H}$ QSGW) was renormalized from the noninteracting picture (Fig. 4C, red line) and represents experimental ε_1 (Fig. 4C, black line) more faithfully. Incoherence broadens $A(\mathbf{k}, \omega)$ (fig. S6), reducing the quasiparticle weight near E_F and effectively decreasing the number of coherent carriers available for intraband transitions to quasiparticle states. Plasma oscillations downshift and renormalize ε_1 (*36*). By similar reasoning, incoherence should increase losses; yet $MoOCl_2$ hosts low-loss plasmons. Interactions do come with enhanced electron-electron scattering (Fig. 5D). However, electron-electron scattering alone is insufficient to overdamp plasmons while other loss mechanisms are suppressed. For one, the orbital-selective Peierls distortion modifies interband transitions to avoid substantial overlap with the plasmonic energy range. And we found that defects—particularly oxygen vacancies—have minimal impact on quasiparticles. Even an unrealistic 6% concentration (Fig. 5D, green) will only mildly degrade σ_2/σ_1. The structure of $MoOCl_2$ admits a low-energy manifold so that matrix elements between Mo-d and O-p states are weak because of the π* character of the overlap matrix.

Moreover, correlated metals are often described by generalizing the constant Drude scattering to a complex function representing frequency-dependent scattering and mass enhancement of electronic excitations from many-body interactions (*37*). Transport measurements fix the $MoOCl_2$ static conductivity to a lower value than our measured optical conductivity. This constraint forces the Drude peak to shift away from zero frequency (Fig. 4C), indicating frequency-dependent scattering. One explanation is that a fluctuating charge density wave (CDW) suppresses low-energy conductivity without fully opening a gap because phase fluctuations prevent complete stabilization of charge order (*6*). In support of this, the momentum shift of the FS replica in ARPES (Fig. 5A, red arrows) is consistent with a predicted charge instability in the static dielectric response at $k_x = 0.27$ Å^{-1} (*28*). High-frequency HPPs will be immune to low-frequency CDW scattering, explaining high HPP quality in the face of poor transport properties.

Conclusions and outlook

We have directly observed unidirectional, steady-state HPPs with record-breaking lifetimes in $MoOCl_2$. We confirmed the hyperbolic character of $MoOCl_2$ plasmons and obtained consistent HPP dispersions between near-field measurements of high-Q modes and FTIR optical parameters, which allowed us to pin down a precise near-infrared dielectric function: found to be renormalized relative to noninteracting theory. The high-frequency dielectric function was reproduced from first principles by including many-body interactions that introduce incoherence and enhanced bonding-antibonding splitting, as seen in our ARPES measurements. Further, reconciling our high-frequency dielectric function with transport requires frequency-dependent scattering, implying low-frequency absorption attributable to fluctuating CDWs, which is congruent with FS replicas seen in ARPES.

$MoOCl_2$ is an air-stable, exfoliatable van der Waals crystal that hosts long-lived, ultrabroadband HPPs without electrostatic gating or chemical doping, which makes it an attractive material for technologically important near-infrared nanophotonics. For example, a hyperlens that exploits $MoOCl_2$ HPPs (*38*) may find applications in photolithography (*39*) or super-resolution imaging (*40*). Enhancing propagation lengths through cryogenic temperatures (*41*), isotopic enrichment (*42*), or integration into tailored nanostructures (*43*, *44*) will enable further advancements. $MoOCl_2$ HPPs are long-lived despite a prevalence of electron-electron scattering and incoherent conductivity. $MoOCl_2$ is thus an ideal platform for studying plasmons formed by correlated electrons. Shedding light

on the physics of "bad" metals could lead to transformative insights into correlated systems, paving the way for unprecedented technologies.

Note added in proof: We became aware of concurrent work (*45*) upon completion of this manuscript.

REFERENCES AND NOTES

1. J. A. N. Bruin, H. Sakai, R. S. Perry, A. P. Mackenzie, *Science* **339**, 804–807 (2013).
2. N. E. Hussey, K. Takenaka, H. Takagi, *Philos. Mag.* **84**, 2847–2864 (2004).
3. R. Jaramillo, S. D. Ha, D. M. Silevitch, S. Ramanathan, *Nat. Phys.* **10**, 304–307 (2014).
4. A. Pustogow *et al.*, *Nat. Commun.* **12**, 1571 (2021).
5. V. J. Emery, S. A. Kivelson, *Phys. Rev. Lett.* **74**, 3253–3256 (1995).
6. L. V. Delacrétaz, B. Goutéraux, S. A. Hartnoll, A. Karlsson, *SciPost Phys.* **3**, 025 (2017).
7. M. A. Chernikov *et al.*, *Phys. Rev. B Condens. Matter* **56**, 1366–1375 (1997).
8. A. Romero-Bermúdez, A. Krikun, K. Schalm, J. Zaanen, *Phys. Rev. B* **99**, 235149 (2019).
9. M. Mitrano *et al.*, *Proc. Natl. Acad. Sci. U.S.A.* **115**, 5392–5396 (2018).
10. A. A. Husain *et al.*, *Nature* **621**, 66–70 (2023).
11. N. Nücker, U. Eckern, J. Fink, P. Müller, *Phys. Rev. B Condens. Matter* **44**, 7155–7158 (1991).
12. M. Knupfer, F. Jerzembeck, N. Kikugawa, F. Roth, J. Fink, *Phys. Rev. B* **106**, L241103 (2022).
13. J. S. Gomez-Diaz, M. Tymchenko, A. Alù, *Phys. Rev. Lett.* **114**, 233901 (2015).
14. A. Nemilentsau, T. Low, G. Hanson, *Phys. Rev. Lett.* **116**, 066804 (2016).
15. C. Wang *et al.*, *Nat. Commun.* **11**, 1158 (2020).
16. Y. Shao *et al.*, *Sci. Adv.* **8**, eadd6169 (2022).
17. S. Dai *et al.*, *Science* **343**, 1125–1129 (2014).
18. W. Ma *et al.*, *Nature* **562**, 557–562 (2018).
19. Z. Zheng *et al.*, *Sci. Adv.* **5**, eaav8690 (2019).
20. G. X. Ni *et al.*, *Nature* **557**, 530–533 (2018).
21. T. Zhang *et al.*, *ACS Nano* **13**, 11353–11362 (2019).
22. H. Ai, X. Song, S. Qi, W. Li, M. Zhao, *Nanoscale* **11**, 1103–1110 (2019).
23. Q. Guo *et al.*, *Nature* **613**, 53–59 (2023).
24. Y. Zhang, L.-F. Lin, A. Moreo, E. Dagotto, *Phys. Rev. B* **104**, 060102 (2021).
25. J. Zhao *et al.*, *Phys. Rev. B* **102**, 245419 (2020).
26. H. Gao, C. Ding, L. Sun, X. Ma, M. Zhao, *Phys. Rev. B* **104**, 205424 (2021).
27. Z. Wang *et al.*, *Phys. Rev. Mater.* **4**, 041001 (2020).
28. Materials and methods are available as supplementary materials.
29. F. L. Ruta *et al.*, *Nat. Commun.* **14**, 8261 (2023).
30. F. Hu *et al.*, *Nat. Photonics* **11**, 356–360 (2017).
31. J. Martín-Sánchez *et al.*, *Sci. Adv.* **7**, eabj0127 (2021).
32. S. Backes *et al.*, *Phys. Rev. B* **94**, 241110 (2016).
33. B. Cunningham, M. Grüning, D. Pashov, M. van Schilfgaarde, *Phys. Rev. B* **108**, 165104 (2023).
34. D. R. Garcia, A. Lanzara, *Adv. Condens. Matter Phys.* **2010**, 807412 (2010).
35. J. M. Tomczak, S. Biermann, *Phys. Rev. B Condens. Matter Mater. Phys.* **80**, 085117 (2009).
36. E. G. C. P. van Loon, H. Hafermann, A. I. Lichtenstein, A. N. Rubtsov, M. I. Katsnelson, *Phys. Rev. Lett.* **113**, 246407 (2014).
37. A. V. Puchkov, D. N. Basov, T. Timusk, *J. Phys. Condens. Matter* **8**, 10049–10082 (1996).
38. I. I. Smolyaninov, Y.-J. Hung, C. C. Davis, *Science* **315**, 1699–1701 (2007).
39. J. Sun, N. M. Litchinitser, *ACS Nano* **12**, 542–548 (2018).
40. P. Li *et al.*, *Nat. Commun.* **6**, 7507 (2015).
41. G. Ni *et al.*, *Nano Lett.* **21**, 5767–5773 (2021).
42. J. F. Schultz, S. Krylyuk, J. J. Schwartz, A. V. Davydov, A. Centrone, *Nanophotonics* **13**, 1581–1592 (2024).
43. S. G. Menabde *et al.*, *Adv. Opt. Mater.* **10**, 2201492 (2022).
44. H. H. Sheinfux *et al.*, *Nat. Mater.* **23**, 499–505 (2024).
45. G. Venturi, A. Mancini, N. Melchioni, S. Chiodini, A. Ambrosio, *Nat. Commun.* **15**, 9727 (2024).

ACKNOWLEDGMENTS

We thank Y. Zhang from the University of Tennessee for sharing DFT and Wannierization files, which we used to sanity check our own initial noninteracting theory. Also, we thank R. Scholtens at HQ Graphene for taking on the R&D project of synthesizing $MoOCl_2$, which was later made commercially available. **Funding:** Research on hyperbolic polaritons is supported by DOE-BES DE-SC0018426. The development of nano-imaging capabilities and the analysis of the electronic bands structure of $MoOCl_2$ is supported as part of Programmable Quantum Materials, an Energy Frontier Research Center funded by the US Department of Energy (DOE), Office of Science, Basic Energy Sciences (BES), under award DE-SC0019443. N.H.J., S.H.R., E.R., J.G.A., and D.B. were supported by the Quantum Systems Accelerator (QSA), supported by the DOE, Office of Science, National Quantum Information Science Research Centers. This research used resources of the Advanced Light Source, which is a DOE Office of Science User Facility under contract DE-AC02-05CH11231. S.A., D.P., and M.v.S. are supported by the Computational Chemical Sciences program within the DOE, Office of Science, BES, under award DE-AC36-08GO28308. This research used resources of the National Energy Research Scientific Computing Center (NERSC), under contract DE-AC02-05CH11231 using NERSC award BES-ERCAP0021783, and the computational resources sponsored by the DOE's Office of Energy Efficiency and Renewable Energy and located at the National Renewable Energy Laboratory. D.N.B. is a Moore Investigator in Quantum Materials EPIQS 9455. M.I.K. is supported by the ERC Synergy Grant, project 854843 FASTCORR (ultrafast dynamics of correlated electrons in solids). The Flatiron Institute is a division of the Simons Foundation. **Author contributions:** F.L.R., Y.Sh., and Y. Su performed near- and far-field optical measurements. F.L.R. conceived the experiment and did electrodynamics calculations. S.A., D.P., and M.v.S. performed QS*GW* calculations. N.H.J., S.H.R., and E.R. performed angle-resolved photoemission spectroscopy. B.S.Y.K. and F.L.R. prepared samples for optical measurements. D.B. and J.G.A. synthesized the $MoOCl_2$ crystals. M.I.K., A.M., and A.J.M. helped to interpret the data. F.L.R. and D.N.B. wrote the manuscript with input from all coauthors. **Competing interests:** The authors declare no competing financial interests. **Data and materials availability:** All data are available in the manuscript or the supplementary materials. **License information:** Copyright © 2025 the authors, some rights reserved; exclusive licensee American Association for the Advancement of Science. No claim to original US government works. https://www.science.org/about/science-licenses-journal-article-reuse

SUPPLEMENTARY MATERIALS

science.org/doi/10.1126/science.adr5926
Materials and Methods
Supplementary Text
Figs. S1 to S21
Tables S1 to S3
References (*46*–*50*)

Submitted 9 July 2024; resubmitted 19 November 2024
Accepted 16 January 2025
10.1126/science.adr5926

ELECTROCHEMISTRY

Ultrastable supported oxygen evolution electrocatalyst formed by ripening-induced embedding

Wenjuan Shi[1]†‡, Tonghao Shen[2]†, Chengkun Xing[1], Kai Sun[1], Qisheng Yan[1], Wenzhe Niu[1], Xiao Yang[1], Jingjing Li[1], Chenyang Wei[1], Ruijie Wang[1], Shuqing Fu[1], Yong Yang[1], Liangyao Xue[1], Junfeng Chen[1], Shiwen Cui[1], Xiaoyue Hu[1], Ke Xie[3], Xin Xu[2,4]*, Sai Duan[2]*, Yifei Xu[1]*, Bo Zhang[1]*

The future deployment of terawatt-scale proton exchange membrane water electrolyzer (PEMWE) technology necessitates development of an efficient oxygen evolution catalyst with low cost and long lifetime. Currently, the stability of the most active iridium (Ir) catalysts is impaired by dissolution, redeposition, detachment, and agglomeration of Ir species. Here we present a ripening-induced embedding strategy that securely embeds the Ir catalyst in a cerium oxide support. Cryogenic electron tomography and all-atom kinetic Monte Carlo simulations reveal that synchronizing the growth rate of the support with the nucleation rate of Ir, regulated by sonication, is pivotal for successful synthesis. A PEMWE using this catalyst achieves a cell voltage of 1.72 volts at a current density of 3 amperes per square centimeter with an Ir loading of just 0.3 milligrams per square centimeter and a voltage degradation rate of 1.33 microvolts per hour, as demonstrated by a 6000-hour accelerated aging test.

Water electrolysis can convert electricity harvested from renewable but intermittent solar or wind energy into "green" (i.e., environmentally sustainable) hydrogen (*1*). Large-scale and cost-effective generation of green hydrogen is considered a key to the future clean energy industry with net-zero carbon emissions (*2*). Presently, the proton exchange membrane water electrolyzer (PEMWE) stands out as the most promising technology for green hydrogen production owing to its high current density, rapid system response, and low gas crossover rate (*3*, *4*). Central to the functioning of PEMWE is the anodic oxygen evolution reaction (OER), which provides the protons and electrons needed

[1]State Key Laboratory of Molecular Engineering of Polymers, Department of Macromolecular Science, Fudan University, Shanghai, China. [2]Collaborative Innovation Center of Chemistry for Energy Materials, Shanghai Key Laboratory of Molecular Catalysis and Innovative Materials, MOE Key Laboratory of Computational Physical Sciences, Department of Chemistry, Fudan University, Shanghai, China. [3]Department of Chemistry and Department of Electrical and Computer Engineering, Northwestern University, Evanston, IL, USA. [4]Hefei National Laboratory, Hefei, China.
***Corresponding author. Email: xxchem@fudan.edu.cn (X.X.); duansai@fudan.edu.cn (S.D.); xyf@fudan.edu.cn (Y.X.); bozhang@fudan.edu.cn (B.Z.)**
†These authors contributed equally to this work.
‡Present address: School of Marine Science and Engineering, State Key Laboratory of Marine Resource Utilization in South China Sea, Hainan University, Haikou, China.

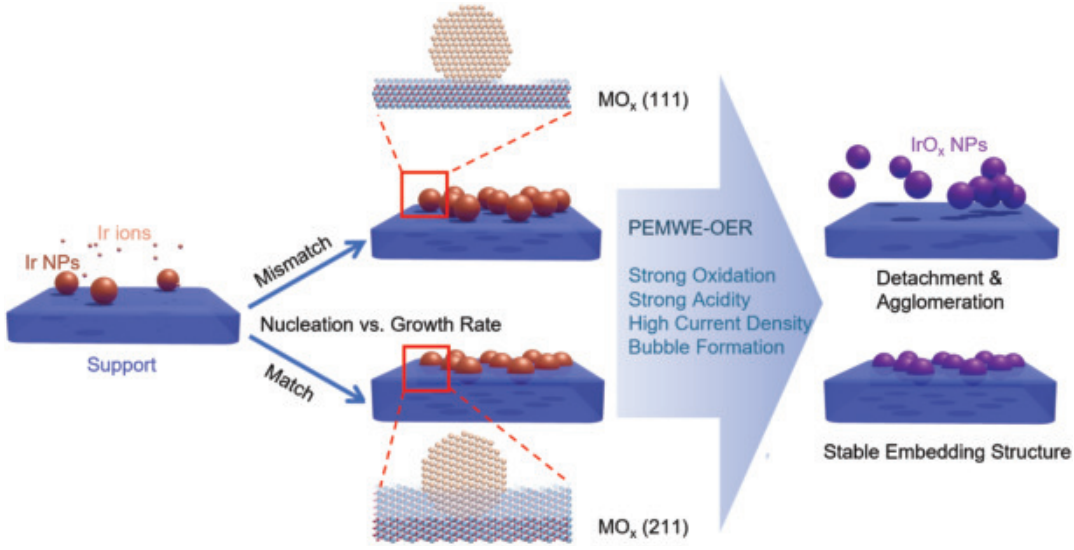


Fig. 1. Schematic illustration of the embedding strategy. Identical parameters of Ir NP nucleations are applied to the KMC simulations on the growth of the (111) and (211) surfaces of metal oxide supports (MO$_x$).

for PEMWE. Enhancement in the activity and stability of OER catalysts has a deep impact on the overall efficiency and economic viability of the device (*5*, *6*). Iridium oxide (IrO$_x$) is so far the only practical OER catalyst that can work continuously in PEMWE (*7*). Nevertheless, the high cost [>$180 per gram (*8*)] and scarce reserve [only 3×10^{-6} parts per million in Earth's crust (*9*)] of Ir pose substantial barriers to the future terawatt-scale deployment of PEMWE (*10*).

To enhance the activity and stability of the catalyst while reducing the Ir content, various approaches have been explored, such as alloying (*11*, *12*) and compositing with perovskites (*13*–*15*) or mixed oxides (*16*, *17*). An efficient and commonly used strategy is loading IrO$_x$ nanoparticles (NPs) with high surface areas onto different supports, typically metal oxides (*18*–*24*). Activities of the resultant supported catalysts are often comparable to or even superior to that of pure IrO$_x$, owing to the strong catalyst-support interactions that tune the electronic structure of Ir and its adsorption energy to OER intermediates (*22*, *24*). This strategy has led to PEMWE performance improvements, realizing cell voltages of <1.9 V at a current density of 2 A cm^{-2} with Ir loading of <0.5 mg cm^{-2} (*23*, *24*). Nonetheless, the primary challenge confronting the supported catalysts is stability; even the best reported results for cell voltage degradation rate with Ir loading of <0.5 mg cm^{-2} remains ~100 μV hour^{-1} (*23*, *24*), which is about 50 times too high as compared with the ambitious 2.3 μV hour^{-1} target set by the United States Department of Energy (DOE) for the year 2026 (*25*).

It has been demonstrated that the primary causes for the instability of the aforementioned supported catalysts are the dissolution, redeposition, detachment, and agglomeration of the IrO$_x$ NPs (*18*, *21*, *26*). The dissolution and redeposition issues could be mitigated by suppressing the overoxidation of Ir through electron donation from metal oxide supports, as observed for many oxides with rich oxygen vacancies, such as antimony-doped tin oxide (*18*), TaO$_x$ (*24*), and CeO$_x$ (*27*, *28*). Intuitively, a solution to the problems of detachment and aggregation would be to firmly anchor the working Ir sites into the supports. A recent advance in this direction has entailed the atomic loading of Ir^{VI} sites into MnO$_2$ through oxidative ligand substitution, achieving <1 μV hour^{-1} potential degradation in PEMWE. However, the cell voltage at a current density of 3 A cm^{-2} was 1.88 V, 80 mV higher than the DOE 2026 target, which compromises the desired activity (*29*). The gap in activity is probably due to the low amount of loaded Ir^{VI} owing to the requirement of complete ligand replacement, limiting the number of available active sites and thus curtailing the catalyst's performance. Consequently, finding a catalyst that can fulfill all DOE 2026 targets continues to represent an unresolved pursuit for PEMWE.

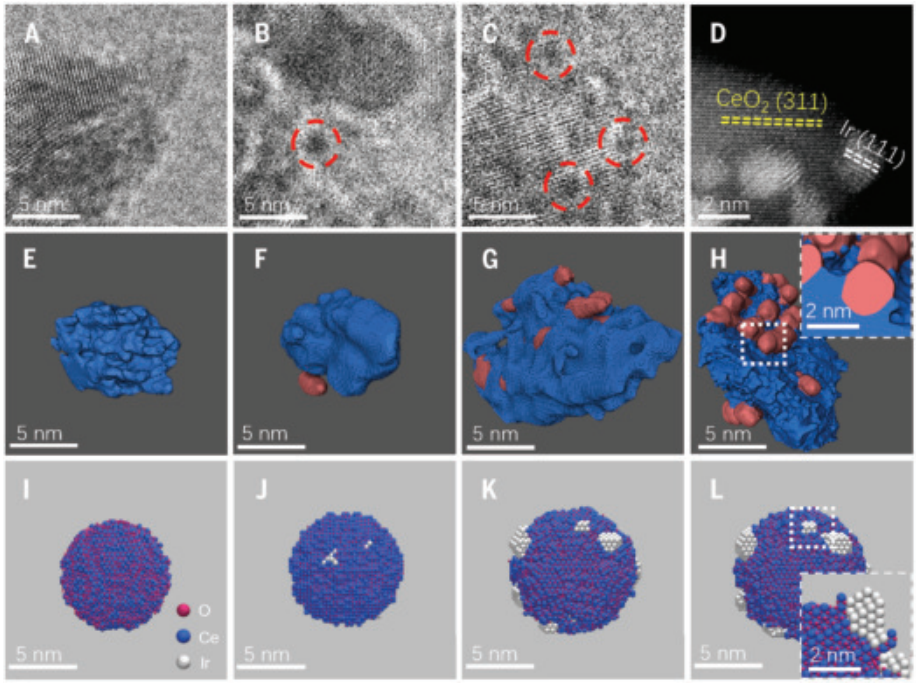


Fig. 2. Formation process of supported catalysts with RIE. (**A** to **C**) (Cryo-)TEM images of the CeO$_x$ support particles after 0, 5, and 60 min of Ir loading, respectively, with Ir NPs highlighted by dashed red circles. (**D**) Cs-corrected HAADF-STEM images of CeO$_x$ after 180 min of Ir loading. (**E** to **H**) (Cryo-)ET reconstructed 3D models of the samples shown in (A) to (D). CeO$_x$ and Ir NPs are colored in blue and pink, respectively. Inset of (H) shows the cross section of the area in the box. (**I** to **L**) KMC simulation of the formation process of RIE-Ir/CeO$_x$ at time points corresponding to (A) to (D).

In this work, we integrated the advantages of high-density Ir sites per unit area offered by NPs with the stability imparted by anchoring the working catalyst on metal oxide supports. We developed a ripening-induced embedding (RIE) strategy to securely embed IrO_x NPs into CeO_x support. Extra sonication processes were adopted to ensure matchable rates between support growth and Ir nucleation, leading to an ultrastable and efficient catalyst characterized by embedding depths optimally at half of the particle diameter. PEMWE based on this RIE catalyst can attain a cell voltage of 1.72 V at a current density of 3 A cm^{-2} with a voltage degradation rate of 1.33 μV $hour^{-1}$, and the total platinum group metal (PGM) loading (both anode and cathode) is 0.4 mg cm^{-2}, satisfying all DOE 2026 targets. Furthermore, this RIE strategy has proven versatile in extensions to other combinations of metal NPs and metal oxides that exhibit increased stability as effective catalysts under different reaction conditions, thereby charting a distinct path in the design of highly resilient catalyst systems.

Design of the RIE strategy

We conceived of a strategy to securely embed the working catalysts into supports by initiating the formation of Ir NPs directly on the surface of the growing support. Practically, this RIE strategy is accomplished through a polyol method (*30*), where an iridium salt is reduced into monodispersed Ir NPs and loaded onto the metal oxide support by heating in ethylene glycol. In this protocol, the applied heating facilitates the growth of the unaged support particles through Ostwald ripening (*31*), making the embedding possible.

A successful RIE process, however, requires a fast ripening of the support, to match the rapid nucleation of the Ir NPs. According to the theorem of Lifshitz and Slyozov (*32*), in a diffusion-controlled scenario, the growth rate of ripening particles is proportional to their surface energy. In other words, the supports with higher surface energies are expected to exhibit a faster increase of their average sizes. Indeed, preliminary simulations using density function theory (DFT)–based kinetic Monte Carlo (KMC) affirm this expectation (Fig. 1 and table S1). Specifically, stable facets, such as the (111) surface of a face-centered cubic metal oxide support, exhibit only submonolayer growth in a reasonable synthesis time of a few hours, which is inadequate for embedding the fast-nucleating NPs. In contrast, high-energy facets such as the (211) surface grow faster, resulting in a successful embedding of the Ir NPs during the synthesis process. Under the PEMWE-OER condition, these Ir NPs are rapidly oxidized into IrO_x. During this process, the lattice constant would be increased, and the Ir dissolution would be suppressed by electron donation from the support, such as the aforementioned CeO_x (*27*), resulting in a net expansion of the NPs and enhancing their anchoring in the support. In light of these considerations, it is imperative that the growth rate of high-energy facets of the support be both fast and sustainable, aligning with the rapid nucleation rate of Ir NPs, to successfully synthesize the intended embedded catalysts.

Experimental synthesis of supported catalysts with RIE

We applied a sonication-assisted polyol method to promote the growth of the high-energy facets by first synthesizing sub-10-nm CeO_x particles with rough surface morphology. Sonication created a transient (<1 ms) (*33*) local high temperature (5000 to 5500 K, as indicated by sonoluminescence spectra; see fig. S1) (*34*) upon the collapse of acoustic cavitation bubbles. This intense heat, along with local high pressure, shock wave, and other effects, can erode the surface of CeO_x and facilitate the exposure of high energy facets (*35*, *36*). Moreover, carbon substrate was used to facilitate the dispersion of CeO_x, which was removed at the end of synthesis by calcination in air (figs. S2 to S5 and tables S2 and S3) (*37*). The size of the as-synthesized CeO_x NPs ranged from 4 to 10 nm, averaging 7.9 ± 1.3 nm (Fig. 2A and fig. S2), in line with the broad peaks in the x-ray diffraction spectrum (see figs. S6 to S8 for detailed characterizations). According to the Ostwald ripening theorem, smaller particles dissolve and recondense onto larger ones (*31*). Our intentionally broad size distribution of CeO_x was thus expected to amplify the driving force for ripening. Electron tomography (ET; Fig. 2E and movie S1) confirmed the rough morphology of CeO_x, which should further enhance the growth rate as predicted by the theorem of Lifshitz and Slyozov (*32*).

Subsequently, Ir NPs were nucleated onto the prepared CeO_x support particles using the polyol method. Regrettably, no desired embedding was observed in the product (figs. S9 to S15), implying an imbalance between the CeO_x growth kinetics and the fast nucleation of Ir NPs. Indeed, closer scrutiny of the synthesis process uncovered that Ir nucleation reached completion within the first hour, whereas the CeO_x ripening process persisted even after 3 hours (fig. S22). This finding underscored the necessity to further accelerate the growth rate of the support.

To address this challenge, sonication was reintroduced during the Ir loading process, which was expected to expedite the dissolution of smaller particles and accelerate the ripening process. In this scenario, it was found that the ripening rate of the CeO_x support was tripled by sonication (figs. S16 to S22). Cryo–transmission electron microscopy (cryo-TEM) and cryo–electron tomography (cryo-ET) were used to monitor the synthesis process. These techniques permit high-resolution three-dimensional (3D) imaging of solution samples without drying or washing (*38*, *39*), which is essential for accurately studying the Ir nucleation and embedding kinetics (see discussions in figs. S15 and S16). Cryo-TEM revealed that a few Ir NPs were deposited on the roughened CeO_x support after 5 min of reaction (Fig. 2B, dashed red circle; also in movie S2). At this initial stage, the cryo-ET image confirmed that the Ir NPs were not yet embedded into the CeO_x support (Fig. 2F), with the particle size of CeO_x remaining virtually unchanged (fig. S18). In the hours that followed, more Ir NPs nucleated onto the CeO_x surface (Fig. 2C, dashed red circles), with the particle size of CeO_x expanding to 10.4 ± 1.1 nm (fig. S20). Notably, the Ir NPs were embedded into the CeO_x support, as clearly shown in the cryo-ET 3D reconstruction (Fig. 2G; see also movie S3), reaching an embedding depth of ~1.0 nm, nearly equivalent to the expanded radius of CeO_x. Although most of the ripening process was complete within the first hour (fig. S22), the reaction was prolonged to 3 hours to optimize the embedding process. The final product, designated RIE-Ir/CeO_x, was examined by spherical aberration–corrected scanning TEM (Cs-corrected STEM). The high-angle annular dark field (HAADF) image (Fig. 2D) illustrates clearly the embedding of Ir NPs into the CeO_x lattice to a depth of ~1 nm, occurring indiscriminately across crystallographic orientations. The embedding was further corroborated by the cross section of the ET results (Fig. 2H; see also movie S4).

As illustrated in Fig. 2, the ripening rate of the support is proportional to its surface energy, and a high support surface energy is essential for the successful execution of the RIE process. To exemplify this point, a control experiment was conducted using ~30-nm commercial CeO_2 crystallites as the support. These crystallites predominantly expose well-defined and thermodynamically stable (111) facets (fig. S23; see detailed characterizations in figs. S6 to S8) (*40*). Ir NPs were then nucleated onto these crystallites using the same sonication-assisted polyol method for 3 hours. The final product, namely C-Ir/CeO_2 (fig. S28; see also movie S5), was detected, where no embedding was observed, and the average size of the CeO_2 crystallites remained largely unchanged (figs. S24 to S28). Moreover, we also measured the size of CeO_x before and after heating and sonication without Ir loading. A similar level of particle growth was observed (fig. S29 and table S3), confirming that the ripening of the CeO_x is not affected by Ir loading.

The mechanisms underlying the RIE process were further investigated using KMC simulations on top of DFT calculations (fig. S30), a powerful approach enabling atomic-scale simulations of crystallization phenomena over hours-long timescales (*41*). A random removal

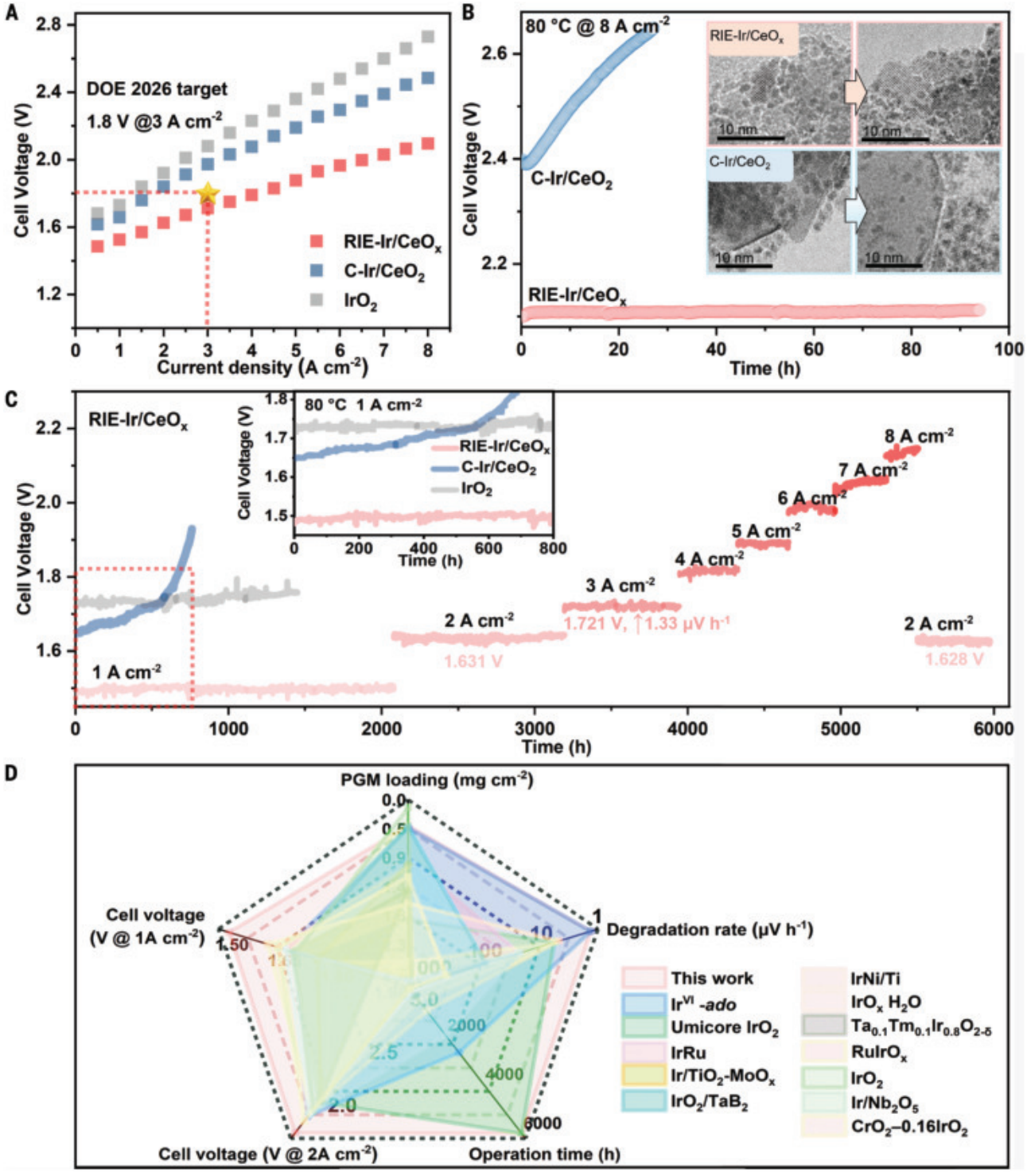


Fig. 3. PEMWE performances of the supported RIE catalyst. (**A**) Polarization curves of the PEMWE. (**B**) Chronopotentiometric curves of the PEMWE using RIE-Ir/CeO_x and C-Ir/CeO_2 catalysts operated at 8 A cm^{-2}. The inset shows TEM images of the catalysts taken before and after the operation. (**C**) Chronopotentiometric curves of the PEMWE using RIE-Ir/CeO_x catalyst at a sequential current density of 1, 2, 3, 4, 5, 6, 7, 8, and 2 A cm^{-2}. Inset shows chronopotentiometry curves using RIE-Ir/CeO_x, C-Ir/CeO_2, and IrO_2 catalysts operated at 1 A cm^{-2}, respectively. (**D**) Comparisons between RIE-Ir/CeO_x and other Ir-based PEMWE-OER catalysts.

of surface atoms was applied to the surface of CeO_x during the simulations, to mimic the surface erosion caused by sonication. The KMC simulation results excellently reproduced the growth and embedding processes during synthesis (Fig. 2, I to L; see also figs. S31 to S33). Further theoretical analysis revealed that the growth rate of the CeO_x support was profoundly influenced by the concentration of CeO_x species released by surface erosion, which accelerated the ripening of CeO_x and facilitated the Ir NP embedding. Moreover, the rough morphology of CeO_x, dominated by high-energy surfaces, sustained a higher concentration of CeO_x in solution and fostered a rapid species exchange

with solution, thereby amplifying the ripening rate, a phenomenon that is in line with the Lifshitz and Slyozov theorem (*32*). Indeed, inductively coupled plasma mass spectrometry (ICP-MS) confirmed that the concentration of Ce species in solution was increased upon sonication (table S5). In contrast, the simulated growth rate of a CeO_2 crystallite consisting of stable (111) facets was very slow even with sonication, confirming its incapacity to embed Ir NPs (figs. S28C, S34, and S35 and table S4), again in good agreement with the experimental observations.

PEMWE performance of the supported RIE catalyst

The electrical and proton conductivities of RIE-Ir/CeO_x were measured to be 0.893 and 0.010 S cm^{-1} (figs. S36 to S39 and tables S6 to S8), respectively, which allow its use in the PEMWE devices with high current densities (*42*, *43*). The OER catalytic activity and stability of RIE-Ir/CeO_x were then assessed under practical working conditions in a PEMWE, using an anode with 0.3 mg cm^{-2} of Ir loading complemented by a cathode with 0.1 mg cm^{-2} of platinum (Pt) loading. Polarization curves verified the heightened OER activity of the catalyst, achieving a cell voltage of 1.72 V at a 3 A cm^{-2} current density (Fig. 3A), accompanied by ~99 and ~98% Faraday efficiencies for H_2 and O_2 generation, respectively (figs. S40 and S41). This performance not only exceeded C-Ir/CeO_2 and commercial IrO_2 but also surpassed the corresponding DOE 2026 target (1.8 V at 3 A cm^{-2}), suggesting a higher mass activity of RIE-Ir/CeO_x, considering its lower Ir content (15.6 wt %; table S9) than that of C-Ir/CeO_2 (17.2 wt %) and commercial IrO_2 (87.7 wt %). Using a quasi–membrane electrode assembly method (figs. S42 and S43), the mass activity of RIE-Ir/CeO_x at 3 A cm^{-2} was quantified at 777.4 A g_{Ir}^{-1} (fig. S44 and table S10), representing a 6.32-fold increase over C-Ir/CeO_2 (122.9 A g_{Ir}^{-1}) and a 17.04-fold improvement compared with commercial IrO_2 (45.6 A g_{Ir}^{-1}) operating at equivalent potentials. After normalization with surface areas determined by the Brunauer-Emmett-Teller method or electrochemical active surface area, the specific activity of RIE-Ir/CeO_x maintained its superiority over both C-Ir/CeO_2 and commercial IrO_2 (figs. S45 to S47). Comparable enhancements in activity have been reported for other Ir-based supported catalysts, attributed to Ir-support electronic interactions (*18*, *28*), although not to such a large extent, hinting at a more profound interaction facilitation in the case of RIE-Ir/CeO_x.

The long-term stability of the catalyst in PEMWE-OER was tested in an accelerated aging experiment that lasted for >6000 hours (Fig. 3C), with the current density stepped up from 1 A cm^{-2} to 8 A cm^{-2} and then reverted to 2 A cm^{-2}. The flat plateaus at each current density signify the exceptional stability of the RIE-Ir/CeO_x catalyst across a wide range of the current density in PEMWE. Notably, the cell voltage at 2 A cm^{-2} remained virtually unchanged from the commencement to the termination of the experiment, while the decay rate at 3 A cm^{-2} was evaluated to be 1.33 μV $hour^{-1}$ (table S18). In contrast, the control catalyst C-Ir/CeO_2 exhibited a much higher voltage decay rate of 3.1 mV $hour^{-1}$ during the 1 A cm^{-2} to 8 A cm^{-2} aging test (fig. S48). Marked disparities were also observed in constant current density tests, where a 200 mV voltage increase occurred within 800 hours at 1 A cm^{-2} (Fig. 3C, inset) or 30 hours at 8 A cm^{-2} (Fig. 3B). We also tested the performance of CeO_x loaded with Ir by only heating, and it also cannot work stably at 1 A cm^{-2} (fig. S49). These results strongly suggest that the exceptionally high stability of the RIE catalyst can be ascribed to the distinctive embedding structure, which effectively prevents the detachment and agglomeration of Ir NPs, as initially hypothesized (Fig. 1). TEM images, taken before and after the 8 A cm^{-2} constant current density test, clearly demonstrate the well-preserved embedding structure in RIE-Ir/CeO_x, contrasting starkly with the evident NP detachment and aggregation in C-Ir/CeO_2 (Fig. 3B, insets; see also figs. S50 and S51). Inhibition of Ir dissolution and detachment in RIE-Ir/CeO_x was further validated by ICP-MS

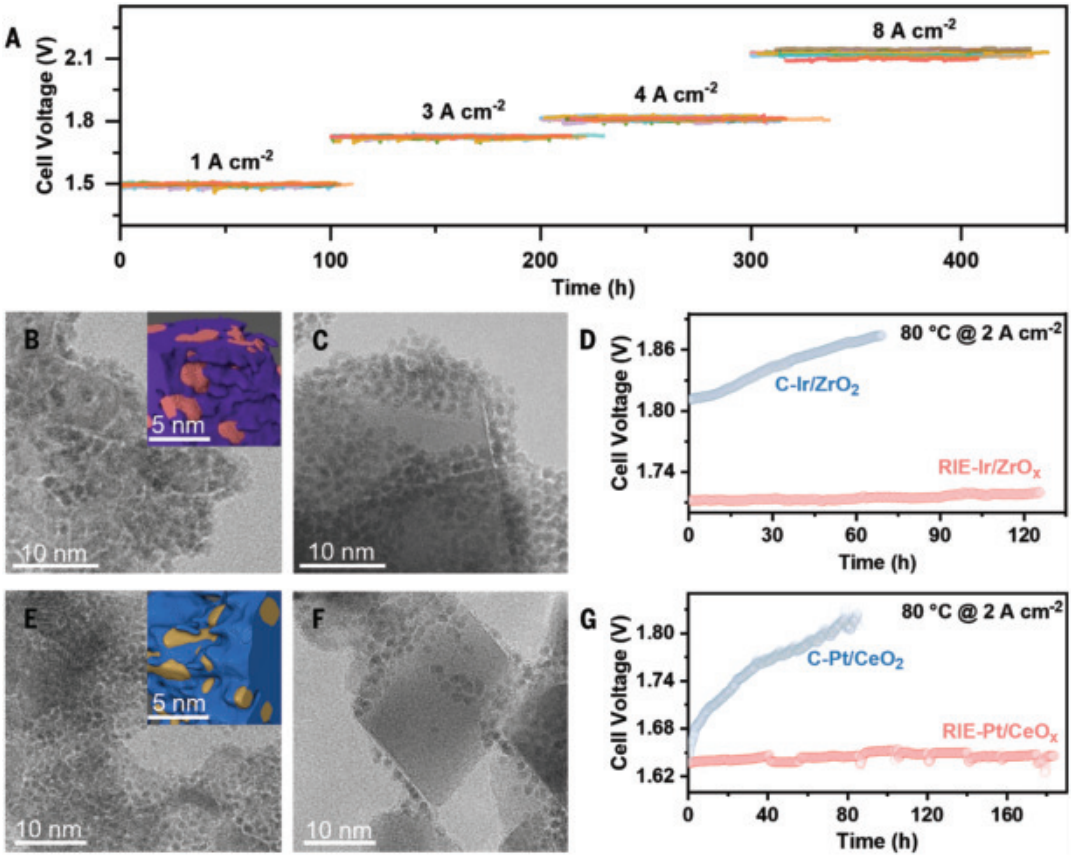


Fig. 4. Reliability and extensibility of the RIE catalysts. (**A**) Chronopotentiometric curves of 10 different PEMWE devices using RIE-Ir/CeO_x catalyst, at a sequential current density of 1, 3, 4, and 8 A cm^{-2}. The curves are plotted in 10 different colors. (**B** and **E**) TEM images of RIE-Ir/ZrO_x and RIE-Pt/CeO_x. Insets show ET reconstructed 3D models. Different materials are labeled as follows: ZrO_x, purple; CeO_x, blue; Ir, pink; and Pt, yellow. (**C** and **F**) TEM images of C-Ir/ZrO_2 and C-Pt/CeO_2. (**D**) PEMWE chronopotentiometric curves operated at 2 A cm^{-2}, using RIE-Ir/ZrO_x or C-Ir/ZrO_2 as the anode catalysts, and commercial Pt/C as the cathode catalyst, respectively. (**G**) PEMWE chronopotentiometric curves operated at 2 A cm^{-2}, using RIE-Pt/CeO_x or C-Pt/CeO_2 as the cathode catalysts, and RIE-Ir/CeO_x as the anode catalyst, respectively.

measurements (figs. S52 to S54 and tables S11 and S12), where the physical confinement of the embedded structure and electron donation effect of CeO_x may both make important contributions (see detailed characterizations in figs. S55 to S68 and tables S14 and S15). The NP size in RIE-Ir/CeO_x expanded from 2.2 ± 0.1 nm to 2.3 ± 0.3 nm. This expansion is logically attributed to the aforementioned oxidation of Ir to IrO_x (Fig. 2), a transformation that is beneficial to the stability of the embedding structure, as anticipated.

As stated above, the RIE-Ir/CeO_x displays high cell activity (1.72 V at 3 A cm^{-2}) and stability (potential degradation rate of 1.33 μV $hour^{-1}$) with a low PGM loading (0.4 mg cm^{-2}). This performance satisfies the stringent DOE 2026 targets of cell activity (1.8 V at 3 A cm^{-2}), potential degradation rate (2.3 μV $hour^{-1}$), and total PGM content (0.5 mg cm^{-2}) for a single PEMWE device. Notably, the potential degradation rate already meets the DOE's ultimate target (2.0 μV $hour^{-1}$) (*25*), guaranteeing >10 years of catalyst lifetime (table S13). The performance of RIE-Ir/CeO_x was compared with other state-of-the-art Ir-based PEMWE-OER catalysts (Fig. 3D) (*17*, *22*–*24*, *29*, *44*–*50*), clearly showing the superior overall performance of the catalyst. The potential degradation rate of the RIE catalyst is lower than most of the other Ir-based catalysts, including commercial IrO_2 (Umicore). Very recently, a <1.0 μV $hour^{-1}$ PEMWE potential degradation rate was reported for atomically dispersed Ir^{VI} oxide (table S16) (*29*), using between 0.38 and 0.48 g cm^{-2} of PGM loaded onto a Nafion 115 membrane (active area of 1 cm^2), but the cell activity (1.88 V at 3 A cm^{-2}) did not meet the DOE 2026 target. All these comparisons highlight the advantage of RIE-Ir/CeO_x in balancing activity, stability, and cost.

Reliability and extensibility of the RIE catalysts

The reliability of the RIE-Ir/CeO_x catalyst was tested on 10 different PEMWE devices (Fig. 4A), confirming its catalytic activity and stability at different current densities (figs. S69 to S74 and tables S17 and S18). As the RIE strategy does not rely on a certain element or compound, it can be used to enhance the activity and stability for other combinations of metal and metal oxide supported catalysts. The performances of these catalysts in the anode OER and cathode hydrogen evolution reaction (HER) of PEMWE, as well as hydrogen generation from $NaBH_4$ hydrolysis, were tested. ZrO_x (fig. S75A), another Earth-abundant metal oxide, was used as the support for OER in PEMWE. The RIE-Ir/ZrO_x (Fig. 4B) displays enhanced stability in comparison with the unembedded control sample (Fig. 4, C and D). Probably because of the weaker electron donation ability of ZrO_x, its activity is not as impressive as that of RIE-Ir/CeO_x. For the cathode in PEMWE, the effective HER catalyst is Pt. In this case, the RIE-Pt/CeO_x was found to display a higher stability as well (Fig. 4, E to G), showing again that the embedding structure can stabilize the supported catalyst under rapid bubble flushing. Similar results were observed for a completely different combination from the above catalysts, that is, RIE-Ru/TiO_2 (fig. S75B), for catalyzing $NaBH_4$ hydrolysis (fig. S76). All these examples demonstrate that the RIE strategy can efficiently enhance the stability of supported catalysts in harsh conditions with rapid bubble formation, showing the broad adaptability of our method.

Conclusions

This work has successfully tackled the stability challenge faced by the supported PEMWE-OER Ir catalyst through the development of a straightforward yet effective RIE strategy. This approach prevents the detachment and agglomeration of Ir NPs by synchronizing the ripening rate of the support with the nucleation rate of Ir. This was achieved by using sonication to generate CeO_x particles with rough surfaces and further accelerate their ripening by enhancing the dissolution of the smaller particles. The resultant RIE-Ir/CeO_x not only meets the DOE 2026 targets of activity and Ir loading but also attains DOE's ultimate goal of unparalleled stability, marking a milestone in the development of PEMWE-OER catalysts. The relatively low price of CeO_x ($1740 per metric ton) (*51*) allows the large-scale deployment of the catalyst in the future. Furthermore, the RIE strategy can be extended to other catalyst systems, which paves the way for designing the next generation of supported catalysts with superior stabilities.

REFERENCES AND NOTES

1. A. Ursua, L. M. Gandia, P. Sanchis, *Proc. IEEE* **100**, 410–426 (2012).
2. A. M. Oliveira, R. R. Beswick, Y. Yan, *Curr. Opin. Chem. Eng.* **33**, 100701 (2021).
3. M. Carmo, D. L. Fritz, J. Mergel, D. Stolten, *Int. J. Hydrogen Energy* **38**, 4901–4934 (2013).
4. S. Shiva Kumar, V. Himabindu, *Mater. Sci. Energy Technol.* **2**, 442–454 (2019).
5. S. Wang, A. Lu, C.-J. Zhong, *Nano Converg.* **8**, 4 (2021).
6. J. Song *et al*., *Chem. Soc. Rev.* **49**, 2196–2214 (2020).
7. C. Wang, L. Feng, *Energy Adv.* **3**, 14–29 (2024).
8. Strategic Metals Invest, Iridium prices; https://strategicmetalsinvest.com/iridium-prices/.
9. C. Minke, M. Suermann, B. Bensmann, R. Hanke-Rauschenbach, *Int. J. Hydrogen Energy* **46**, 23581–23590 (2021).
10. M. A. Hubert, L. A. King, T. F. Jaramillo, *ACS Energy Lett.* **7**, 17–23 (2021).
11. Y. Zhao *et al*., *Nano Energy* **59**, 146–153 (2019).
12. Y.-T. Kim *et al*., *Nat. Commun.* **8**, 1449 (2017).
13. L. C. Seitz *et al*., *Science* **353**, 1011–1014 (2016).
14. O. Diaz-Morales *et al*., *Nat. Commun.* **7**, 12363 (2016).
15. Y. Chen *et al*., *Nat. Commun.* **10**, 572 (2019).
16. F. Zhao *et al*., *J. Am. Chem. Soc.* **143**, 15616–15623 (2021).
17. S. Hao *et al*., *Nat. Nanotechnol.* **16**, 1371–1377 (2021).
18. H.-S. Oh *et al*., *J. Am. Chem. Soc.* **138**, 12552–12563 (2016).
19. E. Oakton *et al*., *ACS Catal.* **7**, 2346–2352 (2017).
20. H. Ohno, S. Nohara, K. Kakinuma, M. Uchida, H. Uchida, *Catalysts* **9**, 74 (2019).
21. F. Claudel *et al*., *ACS Catal.* **9**, 4688–4698 (2019).
22. Z. Shi *et al*., *Angew. Chem. Int. Ed.* **61**, e202212341 (2022).
23. S. Ge *et al*., *Energy Environ. Sci.* **16**, 3734–3742 (2023).
24. Y. Wang *et al*., *Nat. Commun.* **14**, 5119 (2023).
25. United States Department of Energy, Technical targets for proton exchange membrane electrolysis; https://www.energy.gov/eere/fuelcells/technical-targets-proton-exchange-membrane-electrolysis/.
26. H. Yu, L. Bonville, J. Jankovic, R. Maric, *Appl. Catal. B* **260**, 118194 (2020).
27. W. Gou *et al*., *Nano Energy* **104**, 107960 (2022).
28. Z. Dong *et al*., *Adv. Funct. Mater.* **34**, 2400809 (2024).
29. A. Li *et al*., *Science* **384**, 666–670 (2024).
30. F. Bonet *et al*., *Nanostruct. Mater.* **11**, 1277–1284 (1999).
31. W. Ostwald, *Z. Phys. Chem.* **22U**, 289–330 (1897).
32. I. M. Lifshitz, V. V. Slyozov, *J. Phys. Chem. Solids* **19**, 35–50 (1961).
33. D. Sunartio, M. Ashokkumar, F. Grieser, *J. Am. Chem. Soc.* **129**, 6031–6036 (2007).
34. K. S. Suslick, E. B. Flint, *Nature* **330**, 553–555 (1987).
35. H. Wang *et al*., *Phys. Chem. Chem. Phys.* **4**, 3794–3799 (2002).
36. D. G. Shchukin, E. Skorb, V. Belova, H. Möhwald, *Adv. Mater.* **23**, 1922–1934 (2011).
37. W. Shi, A.-H. Park, H.-U. Park, Y.-U. Kwon, *J. Catal.* **384**, 22–29 (2020).
38. Y. Zhu *et al*., *Adv. Mater.* **35**, e2301549 (2023).
39. P. Zhang, H. Du, S. Cui, P. Zhou, Y. Xu, *Responsive Mater.* **1**, e20230025 (2023).
40. J. Conesa, *Surf. Sci.* **339**, 337–352 (1995).
41. M. Kotrla, *Comput. Phys. Commun.* **97**, 82–100 (1996).
42. M. Bernt *et al*., *J. Electrochem. Soc.* **168**, 084513 (2021).
43. L. Chen, Q. Xu, S. Z. Oener, K. Fabrizio, S. W. Boettcher, *Nat. Commun.* **13**, 3846 (2022).
44. L. Tao *et al*., *Joule* **8**, 450–460 (2024).
45. E.-J. Kim *et al*., *Appl. Catal. B* **280**, 119433 (2021).
46. K.-R. Yeo, K.-S. Lee, H. Kim, J. Lee, S.-K. Kim, *Energy Environ. Sci.* **15**, 3449–3461 (2022).
47. J. Xu *et al*., *Sci. Adv.* **9**, eadh1718 (2023).
48. K. J. Choi, S.-K. Kim, *Int. J. Hydrogen Energy* **48**, 849–863 (2023).
49. S. Siracusano, V. Baglio, N. Van Dijk, L. Merlo, A. S. Aricò, *Appl. Energy* **192**, 477–489 (2017).
50. W. J. Shi *et al*., Ultrastable supported oxygen evolution electrocatalyst formed by ripening-induced embedding, Dryad (2024); https://doi.org/10.5061/dryad.dr7sqvb7g.
51. Statista, Cerium oxide price worldwide from 2009 to 2020 with a forecast from 2021 to 2030; https://www.statista.com/statistics/450146/global-reo-cerium-oxide-price-forecast/.

ACKNOWLEDGMENTS

We thank G. Zhou and L. Yao (Fudan University) for help with the ultramicrotomy and energy dispersive spectroscopy experiments. **Funding:** This work was supported by National Nature Science Foundation of China grant 22279019 (B.Z.), Shanghai Municipal Science and Technology Commission grants 21DZ1207102 and 21DZ1207103 (B.Z.), National Nature Science Foundation of China grant 22205038 (Y.X.), Shanghai Pujiang Program grant 21PJ1401300 (Y.X.), National Natural Science Foundation of China grant 22393911 (X.X. and S.D.), Innovation Program for Quantum Science and Technology grant 2021ZD0303301 (S.D.), Innovation Program for Quantum Science and Technology grant 2021ZD0303305 (X.X.), and National Nature Science Foundation of China grant 22273011 (T.S.). **Author contributions:** Conceptualization: B.Z., Y.X., S.D., X.X. Methodology: B.Z., Y.X., S.D., X.X., W.S., T.S. Investigation: W.S., Y.X., T.S., C.X., Q.Y., W.N. Visualization: W.S., Y.X., C.X., K.S., Q.Y., W.N., X.Y., J.L., C.W., R.W., S.F., Y.Y., L.X., J.C., S.C., X.H. Funding acquisition: B.Z., Y.X., S.D., X.X. Project administration: B.Z., Y.X., S.D., X.X. Supervision: B.Z., Y.X., S.D., X.X. Writing – original draft: W.S., Y.X., S.D., B.Z. Writing – review & editing: Y.X., W.S., T.S., S.D., B.Z., X.X., K.X. **Competing interests:** An international patent application based on this work has been filed (PCT/CN2024/130325). **Data and materials availability:** Numerical data of the electrochemistry and simulation results and TEM images for the particle size statistics are available from Dryad (*50*). Other data are available in the main text or the supplementary materials.

License information: Copyright © 2025 the authors, some rights reserved; exclusive licensee American Association for the Advancement of Science. No claim to original US government works. https://www.science.org/about/science-licenses-journal-article-reuse

SUPPLEMENTARY MATERIALS

science.org/doi/10.1126/science.adr3149
Materials and Methods
Figs. S1 to S76
Tables S1 to S18
References (*52*–*75*)
Movies S1 to S5

Submitted 25 June 2024; accepted 12 December 2024
10.1126/science.adr3149

ARE YOU THE KIND WHO WORKS TO HELP ALL HUMANKIND?



Find your next job at ScienceCareers.org

The relevance of science is at an all-time high these days. For anyone who's looking to get ahead in—or just plain get into—science, there's no better, more trusted resource or authority on the subject than *Science* Careers. Here you'll find opportunities and savvy advice across all disciplines and levels. There's no shortage of global problems today that science can't solve. Be part of the solution.

ScienceCareers

FROM THE JOURNAL SCIENCE AAAS

ScienceCareers.org

ScienceCareers

By **Salahuddin Mohammed**

Rethinking success

Late one evening, I stared at a rejection email for yet another grant proposal. I had hoped that securing independent funding would improve my chances of landing a tenure-track position at a research-focused university; years of training had ingrained the belief that such institutions were the only place one could make a meaningful contribution to science. Yet, after countless job applications, I hadn't been invited to a single interview, and the rejection of my latest grant proposal added salt to the wound. My career objective felt increasingly out of reach. I still wanted to conduct impactful research and foster students' critical thinking and scientific curiosity, but maybe it was time to look for another path toward those goals.

I had started my academic journey as a university instructor in Ethiopia, where I found immense satisfaction in mentoring students. However, the limited resources and opportunities there made it difficult to pursue my own growth, so I went to the United States for my Ph.D. and postdoc. As I progressed in my training, I internalized the dominant narrative that success meant securing a faculty position at a research-intensive R1 institution.

But during my postdoc, I realized I needed to change my perspective. I am a husband and father of two daughters, one of whom requires ongoing medical care. My modest salary and limited benefits made every day feel like walking a tightrope over an abyss of financial instability and emotional exhaustion. Professional stress bled into my home life, where I couldn't be fully present for my family. In turn, the weight of my personal responsibilities made professional setbacks feel even more crushing. Trapped in this exhausting cycle, I began to reconsider my career path.

I read articles and browsed job postings. LinkedIn and academic networking platforms provided insights into the experiences of faculty at non-R1 institutions. I was particularly drawn to smaller universities that, although they still support research, place a greater emphasis on teaching. I reached out to professors at these institutions and gleaned invaluable insights. I liked that these universities emphasize expertise and vision, along with the opportunity to build meaningful academic programs. They also offered adequate pay and comprehensive benefits—factors that were becoming increasingly important as I considered my long-term career stability. The fog began to lift. This wasn't about settling for a less prestigious or less impactful institution—it was about finding a space where I could thrive. It was about choosing an environment that would allow me to pursue my professional aspirations while also attending to my personal life.



"This wasn't about settling ... it was about finding a space where I could thrive."

I applied to several positions—and was relieved and delighted when I started to receive invitations to interview. The campus visits, which included teaching demonstrations, discussions about mentoring, and an emphasis on how I would integrate research into a student-centered environment, were challenging but invigorating, helping confirm that I was heading in the right direction.

Once I started my current position, any lingering doubts quickly faded. The rhythm of my days shifted: Instead of spending long, uninterrupted hours in the lab, I had to balance lecture preparation, student advising, and scattered moments for research. But with my institution's ample support, I felt clarity for the first time in years. The students' engagement and curiosity reignited my passion for mentorship. And research didn't disappear—it evolved. Summers became dedicated windows for focused experiments and writing manuscripts, and during the academic year I delved into analysis.

Now, 2 years into my position, I've learned to redefine success. For me, it isn't solely about high-impact publications or prestigious grants—it's about creating opportunities for students to thrive, asking meaningful research questions, and maintaining a balance between professional aspirations and personal well-being. In this space—where teaching, research, and mentorship converge—I've discovered not just success, but significance. ■

Salahuddin Mohammed is an assistant professor at Notre Dame of Maryland University. Send your career story to SciCareerEditor@aaas.org.

ILLUSTRATION: ROBERT NEUBECKER

QUALITY CONTENT FOR THE GLOBAL SCIENTIFIC COMMUNITY

Multiple ways to stay informed on issues related to your research

Posters

Podcasts

Sponsored Collection Booklets

Sponsored Feature

Webinars

Science
AAAS

Brought to you by the *Science*/AAAS Custom Publishing Office.

Scan the code and start exploring the latest advances in science and technology innovation!

Science.org/custom-publishing

YOUR RESEARCH HAS ITS REWARDS.



Submit an essay by 3/15/25 to enter to win $25K.

The *Science* & PINS Prize seeks to recognize researchers who ask fundamental questions in the field of neuromodulation. It is awarded to scientists who conduct research at the intersection between engineering and clinical neurology to develop innovative neuromodulation approaches to advance our understanding of human health and disease or to guide therapeutic interventions.

To enter, just write a 1000-word essay about your research performed in the last three years. The Grand Prize winner will be presented a US$25,000 award, as well as have their essay published in *Science* magazine and online. A runner-up will have their essay published online.

For additional inquiries,
email SciencePINSPrize@aaas.org.

SCIENCE-PINS PRIZE FOR NEUROMODULATION
SCIENCE-PINS

SCIENCE.ORG/PINS